

COMBINED FLEXURAL AND CABLE-LIKE BEHAVIOR OF  
DUCTILE STEEL BEAMS

by

Yunus Alp

A thesis submitted to the Graduate Faculty of  
Auburn University  
in partial fulfillment of the  
requirements for the Degree of  
Master of Science

Auburn, Alabama  
December 18, 2009

Keywords: steel beams, progressive collapse, cable action,  
catenary action, ductile behavior

Copyright 2009 by Yunus Alp

Approved by

Hassan H. Abbas, Chair, Assistant Professor of Civil Engineering  
James S. Davidson, Associate Professor of Civil Engineering  
Mary L. Hughes, Instructor of Civil Engineering

## ABSTRACT

In addressing the propensity of steel building structures to experience progressive collapse due to extreme loading conditions (e.g., blast), current design guidelines propose the use of a threat-independent approach that is commonly referred to in the literature as “the missing column scenario”. Under this scenario, a column from a given story is assumed to be removed and the resulting structure is analyzed to determine if it could sustain the loads by activating one or more alternate load carrying mechanisms, with the idea of mitigating the potential for progressive structural collapse. This study specifically focuses on the ability of ductile steel beams to carry loads by transitioning from flexural behavior to cable-like behavior. Theoretical fundamentals of this behavior are described for rectangular and W-shaped steel beams with idealized boundary conditions and presumed fully ductile behavior. Two theoretical analysis approaches are used to model the beam behavior: rigid-plastic analysis and cable analysis. The main factors affecting the behavior, such as material and geometric properties as well as boundary conditions are described and corroborating nonlinear finite element (FE) analyses are presented and compared to the theoretical results. *Open System for Earthquake Engineering Simulation*, OpenSees was used in the FE analysis studies. Based upon theoretical and FE analysis results, a set of equations are proposed that can be used to predict the deflection at the onset of pure cable behavior.

Additionally, the effect of elastic boundary restraints on the beam behavior was studied using FE analysis. An approach to evaluate the boundary restraints offered by the

surrounding members in a given frame is also presented. It is shown that axial restraints have a much more significant effect on the behavior than rotational restraints.

The theory presented in this thesis can serve as basis for designing ductile steel beams undergoing transition from flexural to cable-like behavior.

## ACKNOWLEDGMENTS

I would first like to express my gratitude to Dr. Hassan H. Abbas for giving me the chance to work with him. I am thankful for his continuous support, invaluable guidance, inspiration and patience throughout the course of my studies at Auburn University. I would like to thank my committee members Dr. Mary L. Hughes and Dr. James S. Davidson for their time and support. I would also like to thank other Structures Faculty members for providing valuable coursework during my study.

I take this opportunity to convey my additional thanks to all my family members for their endless love and support.

Finally, my special thanks go to all my friends who made my stay in Auburn to be an unforgettable experience.

Style manual used The Chicago Manual of Style

---

Computer Software Used Microsoft Word, Microsoft Excel, Microsoft PowerPoint,  
AutoCAD 2008, OpenSees

---

## TABLE OF CONTENTS

LIST OF TABLES.....	xi
LIST OF FIGURES .....	xii
Chapter 1. INTRODUCTION .....	1
1.1 Overview.....	1
1.2 Motivation.....	4
1.3 Research Objectives and Scope .....	4
1.4 Approach.....	5
1.5 Organization of Thesis.....	5
1.6 Notation.....	6
Chapter 2. BACKGROUND .....	7
2.1 Introduction.....	7
2.2 Existing Methodologies for Design against Progressive Collapse .....	8
2.2.1 Indirect Method.....	9
2.2.2 Direct Methods.....	15
2.2.2.1 Specific Local Resistance (SLR) .....	15
2.2.2.2 Alternate Path Method (APM).....	16
2.3 Recent Relevant Research.....	21
2.4 Static Plastic Behavior of Simple Beams.....	25
2.4.1 Rigid–Plastic Behavior .....	25

2.4.2	Effect of Finite Displacements.....	26
2.4.3	$M-N$ Interaction at Cross-Sectional Level.....	27
2.4.4	Equilibrium Equations .....	30
2.4.5	Deflected Shape Configuration.....	31
2.4.6	Load–Deflection .....	32
Chapter 3.	THEORETICAL MODELS .....	39
3.1	Overview and Scope .....	39
3.2	Rigid–Plastic Analysis .....	39
3.2.1	Simply Supported Beam with a Concentrated Load at Midspan.....	43
3.2.2	Fully Fixed Beam with a Concentrated Load at Midspan .....	51
3.2.3	Fully Fixed Beam with Uniformly Distributed Load along the Length ...	59
3.2.3.1	Beam with Rectangular Cross–Section.....	61
3.2.3.1.1	Theory I.....	61
3.2.3.1.2	Theory II .....	65
3.2.3.2	Beam with W–Shaped Cross–Section .....	74
3.2.3.2.1	Theory I.....	74
3.2.3.2.2	Theory II .....	76
3.2.4	Summary .....	81
3.3	Cable Analysis .....	82
3.3.1	Concentrated Load Case .....	83
3.3.2	Uniformly Distributed Load Case.....	85
3.3.3	Summary .....	88
3.4	Conclusion and Expected Behavior .....	89

Chapter 4.	ANALYTICAL MODELS .....	92
4.1	Introduction.....	92
4.2	Modeling Concepts .....	92
4.2.1	Fiber Section Discretization.....	92
4.2.2	Corotational Transformation.....	93
4.2.3	Selection of Beam Element.....	94
4.2.4	Material .....	94
4.2.5	Loading and Analysis .....	95
4.3	Preliminary FE Analyses .....	96
4.3.1	Approach.....	96
4.3.2	Description of Preliminary FE Models .....	98
4.3.3	Comparison of Results with Rigid–Plastic Theory.....	99
4.3.3.1	Concentrated Load Case .....	100
4.3.3.1.1	Beam with Rectangular Cross–Section.....	100
4.3.3.1.2	Beam with W–Shape Cross–Section .....	103
4.3.3.2	Distributed Load Case.....	107
4.3.3.2.1	Beam with Rectangular Cross–Section.....	107
4.3.3.2.2	Beam with W–Shape Cross–Section .....	112
4.3.4	Comparison of Results with Cable Theory.....	117
4.3.4.1	Concentrated Load Case .....	118
4.3.4.2	Distributed Load Case.....	121
4.3.5	Summary and Conclusion .....	125
4.4	Parametric Study.....	126



4.4.1	Approach.....	127
4.4.2	Description of Beam Models .....	129
4.4.3	Concentrated Load Case .....	129
4.4.3.1	Constant $\delta_p$ .....	129
4.4.3.2	Constant $\delta_p / d$ .....	132
4.4.3.3	Constant $\delta_p / 2L$ .....	142
4.4.3.4	Constant $L / d$ .....	149
4.4.4	Distributed Load Case.....	156
4.4.5	Summary and Conclusions .....	162
Chapter 5.	EQUATIONS FOR THE ONSET OF PURE CABLE BEHAVIOR .....	164
5.1	Overview.....	164
5.2	Concentrated Load Case .....	165
5.2.1	Formulation I .....	165
5.2.2	Formulation II.....	169
5.2.3	Formulation III.....	172
5.3	Distributed Load Case.....	175
5.3.1	Formulation I .....	175
5.3.2	Formulation II.....	179
5.3.3	Formulation III.....	180
5.4	Discussion.....	182
5.5	Conclusion .....	187
Chapter 6.	EFFECT OF ELASTIC BOUNDARY CONDITIONS .....	189
6.1	Overview.....	189

6.2	Effect of Elastic Restraint .....	191
6.2.1	Effect of Translational Restraint .....	191
6.2.2	Effect of Rotational Restraint .....	197
6.2.3	Combined Effect of Translational and Rotational Restraints .....	206
6.3	Relationship between Beam Models and Frame Models.....	211
6.3.1	Quantification of Elastic Spring Constants.....	212
6.3.2	Comparison between Frame and Beam Models .....	214
6.4	Summary and Conclusions .....	220
Chapter 7. SUMMARY, CONCLUSIONS AND RECOMMENDATIONS FOR FUTURE STUDY.....		221
7.1	Summary .....	221
7.2	Conclusions.....	222
7.3	Recommendations.....	223
REFERENCES .....		224
APPENDICES .....		228
APPENDIX A: Notation.....		229
APPENDIX B: Typical Input Files in OpenSees .....		232
APPENDIX B.1: Centrally Loaded Beam Fixed at Supports.....		232
APPENDIX B.2: Fixed Beam with Uniformly Distributed load along the Length.....		236
APPENDIX B.1: Beam with Elastic Boundary Conditions .....		240

## LIST OF TABLES

Table 2-1 Strength of Ties (Ellingwood et al. 2007) .....	13
Table 2-2 Load Combinations for Progressive Collapse Analysis .....	20
Table 2-3 Definition of Local Collapse (Ellingwood et al. 2007) .....	21
Table 3-1 $W_{cat}$ predicted by Rigid-Plastic Theory.....	81
Table 4-1 Summary of Model Parameters in Preliminary FE Models .....	99
Table 4-2 Elasticity Modulus.....	99
Table 4-3 Beam Models Considered with constant $\delta_p$ .....	130
Table 4-4 FE Models with Rectangular Shapes (Constant $\delta_p / d$ ) .....	134
Table 4-5 FE Models with W-Shapes (Constant $\delta_p / d$ ).....	134
Table 4-6 FE Models with Rectangular Shapes (Constant $\delta_p / 2L$ ) .....	143
Table 4-7 FE Models with W-Shapes (Constant $\delta_p / 2L$ ).....	143
Table 4-8 FE Models with Rectangular Shapes (Constant $L / d$ case).....	149
Table 4-9 FE Models with W-Shapes (Constant $L / d$ case) .....	150
Table 4-10 FE Models with Rectangular Sections (Uniform Loading).....	156
Table 4-11 FE Models with W-Shapes (Uniform Loading) .....	157
Table 6-1 W14x53 Beam Models with Translational Springs only .....	192
Table 6-2 W14x53 Beam Models with Rotational Springs only .....	199
Table 6-3 Beam Models with Combined Spring Constant Cases.....	207

## LIST OF FIGURES

Figure 2-1 Schematic of Tie Forces in a Frame Structure (UFC 2005).....	10
Figure 2-2 Calculation of Upper Bound on the Basic Strength (UFC 2005).....	14
Figure 2-3 Removal of Column (UFC 2005).....	17
Figure 2-4 Double Span Condition in a Traditional Moment Frame (GSA 2003).....	18
Figure 2-5 Element Removal Considerations for Framed Structure (GSA 2003).....	19
Figure 2-6 Behavior Idealizations (Jones 1989).....	26
Figure 2-7 Centrally Loaded Simple Beam under Finite Displacements .....	27
Figure 2-8 Combination of Axial force and Moment on a Rigid-Perfectly Plastic Beam with a Rectangular Cross-section (Jones 1989).....	28
Figure 2-9 Yield Condition Relating $M$ and $N$ required for a Rectangular Cross-Section	29
Figure 2-10 Element of a beam subjected to loads which produce finite transverse displacements (Jones 1989) .....	30
Figure 2-11 Plastic flow of a rigid-perfectly plastic beam with rectangular cross- section (Jones 1989).....	34
Figure 2-12 Forces at Midspan ( $x=0$ ) at Fully Plastic Phase.....	37
Figure 2-13 Normalized Load–Deflection curve for simple beam with a rectangular cross-section (Jones 1989).....	38
Figure 3-1 Stress distributions in the cross-section based on the location of neutral axis	41
Figure 3-2 $M$ – $N$ interaction for W–Shapes (W30x124) .....	42

Figure 3-3 W-Shaped Rigid-Plastic Simple Beam with a Concentrated load at Midspan .....	43
Figure 3-4 Normalized Axial Force-Deflection Relationship (Midspan) .....	49
Figure 3-5 Normalized Moment-Deflection Relationship (Midspan).....	49
Figure 3-6 Normalized $M-N$ interaction for W-Shape cross-section (Midspan).....	50
Figure 3-7 Normalized Load-Deflection Relationship.....	51
Figure 3-8 Centrally loaded, fully fixed beam with W-Shape cross-section .....	53
Figure 3-9 Normalized Axial Force-Deflection Relationship (Midspan) .....	58
Figure 3-10 Normalized Moment-Deflection Relationship (Midspan).....	58
Figure 3-11 Normalized Force-Deflection Relationship (Midspan) .....	59
Figure 3-12 Change in Deflected Shape Configuration Under Uniform Loading.....	60
Figure 3-13 Schematics of Theory I .....	62
Figure 3-14 Equilibrium of Forces at Pure Cable State .....	64
Figure 3-15 Schematics of Theory II.....	66
Figure 3-16 Length of Arc Approximation.....	69
Figure 3-17 Equilibrium of forces at pure catenary state .....	71
Figure 3-18 Normalized Load-Deflection relationship.....	73
Figure 3-19 Normalized Axial Force-Deflection relationship .....	73
Figure 3-20 Normalized Moment - Deflection Relationship .....	74
Figure 3-21 Normalized Load-Deflection relationship.....	79
Figure 3-22 Normalized Axial Force-Deflection relationship .....	80
Figure 3-23 Normalized Moment-Deflection relationship.....	80
Figure 3-24 Material idealization used in Cable analysis.....	82

Figure 3-25 Free body diagram under concentrated load .....	84
Figure 3-26 Free body diagram under uniform loading.....	86
Figure 3-27 $\alpha - \omega$ relationship.....	88
Figure 3-28 Expected behavior representation on $M-N$ interaction .....	90
Figure 4-1 Schematic of Fiber Section Discretization of Cross-Sections.....	93
Figure 4-2 Uniaxial Elastic-perfectly plastic material .....	95
Figure 4-3 Schematic of preliminary FE beam models .....	98
Figure 4-4 Normalized Load-Deflection Plot .....	101
Figure 4-5 Normalized Axial Force-Deflection Plot (Midspan).....	101
Figure 4-6 Normalized Moment-Deflection Plot (Midspan) .....	102
Figure 4-7 Normalized $M-N$ interaction Plot (Midspan).....	103
Figure 4-8 Normalized Load-Deflection Plot .....	104
Figure 4-9 Normalized Axial Force-Deflection Plot (Midspan).....	105
Figure 4-10 Normalized Moment-Deflection Plot (Midspan) .....	105
Figure 4-11 Normalized $M-N$ interaction Plot (Midspan).....	106
Figure 4-12 Normalized Load-Deflection Plot .....	108
Figure 4-13 Normalized Axial Force-Deflection Plot (End) .....	109
Figure 4-14 Normalized Moment-Deflection Plot (End).....	109
Figure 4-15 Normalized $M-N$ interaction (End).....	111
Figure 4-16 Normalized $M-N$ interaction (Midspan) .....	112
Figure 4-17 Normalized Load-Deflection Plot .....	114
Figure 4-18 Normalized Axial Force-Deflection Plot (End) .....	114
Figure 4-19 Normalized Moment-Deflection Plot (End).....	115

Figure 4-20 Normalized $M-N$ interaction (End).....	116
Figure 4-21 Normalized $M-N$ interaction (Midspan).....	117
Figure 4-22 External Load – Normalized Deflection Plot.....	118
Figure 4-23 Normalized Axial Force – Deflection Plot (Midspan).....	119
Figure 4-24 Normalized $M-N$ interaction (REC Section, Midspan) .....	120
Figure 4-25 Normalized $M-N$ interaction (W-Shape, Midspan).....	121
Figure 4-26 Normalized Load–Deflection Plot .....	122
Figure 4-27 Normalized Axial Force–Deflection Plot.....	123
Figure 4-28 Normalized $M-N$ interaction (REC Section, End).....	124
Figure 4-29 Normalized $M-N$ interaction (W-Shape, End).....	125
Figure 4-30 $\delta_p$ Definition .....	128
Figure 4-31 Normalized Load–Deflection Plot for Constant $\delta_p$ .....	131
Figure 4-32 Normalized Axial Force–Deflection Plot for Constant $\delta_p$ (Midspan).....	131
Figure 4-33 Normalized Moment–Deflection Plot for Constant $\delta_p$ .....	131
Figure 4-34 Typical Normalized Axial Force–Deflection plot used to determine $W_{cat}$ for .....	133
Figure 4-35 $W_{cat} / \delta_p - \delta_p / d$ Relationship (Constant $\delta_p / d$ within each group) .....	137
Figure 4-36 $W_{cat} / \delta_p - \delta_p / 2L$ Relationship (Constant $\delta_p / d$ within each group).....	137
Figure 4-37 $W_{cat} / \delta_p - L / d$ relationship (Constant $\delta_p / d$ within each group) .....	138
Figure 4-38 $W_{cat} / d - \delta_p / d$ Relationship (Constant $\delta_p / d$ within each group) .....	139
Figure 4-39 $W_{cat} / d - \delta_p / 2L$ Relationship (Constant $\delta_p / d$ within each group) .....	139
Figure 4-40 $W_{cat} / d - L / d$ Relationship (Constant $\delta_p / d$ within each group).....	140
Figure 4-41 $W_{cat} / 2L - \delta_p / d$ Relationship (Constant $\delta_p / d$ within each group).....	141

Figure 4-42 $W_{cat} / 2L - \delta_p / 2L$ Relationship (Constant $\delta_p / d$ within each group).....	141
Figure 4-43 $W_{cat} / 2L - L / d$ Relationship (Constant $\delta_p / d$ within each group) .....	142
Figure 4-44 $W_{cat} / \delta_p - \delta_p / d$ Relationship (Constant $\delta_p / 2L$ within each group).....	144
Figure 4-45 $W_{cat} / \delta_p - \delta_p / 2L$ Relationship (Constant $\delta_p / 2L$ within each group).....	145
Figure 4-46 $W_{cat} / \delta_p - L / d$ Relationship (Constant $\delta_p / 2L$ within each group) .....	145
Figure 4-47 $W_{cat} / d - \delta_p / d$ Relationship (Constant $\delta_p / 2L$ within each group).....	146
Figure 4-48 $W_{cat} / d - \delta_p / 2L$ Relationship (Constant $\delta_p / 2L$ within each group) .....	146
Figure 4-49 $W_{cat} / d - L / d$ Relationship (Constant $\delta_p / 2L$ within each group).....	147
Figure 4-50 $W_{cat} / 2L - \delta_p / d$ Relationship (Constant $\delta_p / 2L$ within each group) .....	147
Figure 4-51 $W_{cat} / 2L - \delta_p / 2L$ Relationship (Constant $\delta_p / 2L$ within each group) .....	148
Figure 4-52 $W_{cat} / 2L - L / d$ Relationship (Constant $\delta_p / 2L$ within each group) .....	148
Figure 4-53 $W_{cat} / \delta_p - \delta_p / d$ Relationship (Constant $L / d$ within each group) .....	151
Figure 4-54 $W_{cat} / \delta_p - \delta_p / 2L$ Relationship (Constant $L / d$ within each group).....	152
Figure 4-55 $W_{cat} / \delta_p - L / d$ Relationship (Constant $L / d$ within each group).....	152
Figure 4-56 $W_{cat} / d - \delta_p / d$ Relationship (Constant $L / d$ within each group) .....	153
Figure 4-57 $W_{cat} / d - \delta_p / 2L$ Relationship (Constant $L / d$ within each group) .....	153
Figure 4-58 $W_{cat} / d - L / d$ Relationship (Constant $L / d$ within each group).....	154
Figure 4-59 $W_{cat} / 2L - \delta_p / d$ Relationship (Constant $L / d$ within each group) .....	154
Figure 4-60 $W_{cat} / 2L - \delta_p / 2L$ Relationship (Constant $L / d$ within each group).....	155
Figure 4-61 $W_{cat} / 2L - L / d$ Relationship (Constant $L / d$ within each group) .....	155
Figure 4-62 $W_{cat} / \delta_p - \delta_p / d$ Relationship (Constant $L / d$ within each group) .....	158
Figure 4-63 $W_{cat} / \delta_p - \delta_p / 2L$ Relationship (Constant $L / d$ within each group).....	158
Figure 4-64 $W_{cat} / \delta_p - L / d$ Relationship (Constant $L / d$ within each group).....	159



Figure 4-65 $W_{cat} / d - \delta_p / d$ Relationship (Constant $L / d$ within each group) .....	159
Figure 4-66 $W_{cat} / d - \delta_p / 2L$ Relationship (Constant $L / d$ within each group) .....	160
Figure 4-67 $W_{cat} / d - L / d$ Relationship (Constant $L / d$ within each group).....	160
Figure 4-68 $W_{cat} / 2L - \delta_p / d$ Relationship (Constant $L / d$ within each group).....	161
Figure 4-69 $W_{cat} / 2L - \delta_p / 2L$ Relationship (Constant $L / d$ within each group).....	161
Figure 4-70 $W_{cat} / 2L - L / d$ Relationship (Constant $L / d$ within each group) .....	162
Figure 5-1 Comparison with FE results (REC Shapes) .....	167
Figure 5-2 Comparison with FE results (W-Shapes: Constant $\delta_p / d$ case).....	168
Figure 5-3 Comparison with FE results (W-Shapes: Constant $\delta_p / 2L$ case) .....	168
Figure 5-4 Comparison with FE results (W-Shapes: Constant $L / d$ case).....	169
Figure 5-5 Comparison with FE results (Constant $\delta_p / d$ case).....	171
Figure 5-6 Comparison with FE results (Constant $\delta_p / 2L$ case).....	171
Figure 5-7 Comparison with FE results (Constant $L / d$ case).....	172
Figure 5-8 Comparison with FE results (Constant $\delta_p / d$ case).....	174
Figure 5-9 Comparison with FE results (Constant $\delta_p / 2L$ case).....	174
Figure 5-10 Comparison with FE results (Constant $L / d$ case).....	175
Figure 5-11 Comparison with FE results (REC Shapes) .....	178
Figure 5-12 Comparison with FE results (W Shapes) .....	178
Figure 5-13 Comparison with FE results (Constant $L / d$ within each group).....	180
Figure 5-14 Comparison with FE results (Constant $L / d$ within each group).....	182
Figure 5-15 Distribution of the Difference for Rectangular Shaped Beams .....	184
Figure 5-16 Distribution of the Difference for W-Shaped Beams.....	185
Figure 5-17 Distribution of the Difference for Rectangular Shaped Beams .....	186

Figure 5-18 Distribution of the Difference for W-Shaped Beams.....	187
Figure 6-1 Schematics of Beam Model with Elastic Boundary Conditions .....	190
Figure 6-2 Beam model with translational springs only .....	192
Figure 6-3 Dependency of $W_{cat} / d$ on Translational Spring Constant, $k_{\Delta}$ .....	193
Figure 6-4 Normalized Load–Deflection Plot (Midspan).....	194
Figure 6-5 Normalized Axial Force–Deflection Plot (Midspan).....	195
Figure 6-6 Normalized Moment–Deflection Plot (Midspan) .....	195
Figure 6-7 Normalized $M$ – $N$ interaction (Midspan) .....	196
Figure 6-8 Normalized $M$ – $N$ Interaction (End) .....	197
Figure 6-9 Beam with Rotational Springs Only .....	198
Figure 6-10 Dependency of $W_{cat} / d$ on Rotational Spring Constant, $k_{\theta}$ .....	199
Figure 6-11 Normalized Load–Deflection Plot (Midspan).....	201
Figure 6-12 Normalized Axial Force–Deflection Plot (Midspan).....	201
Figure 6-13 Normalized Moment–Deflection Plot (Midspan) .....	202
Figure 6-14 Normalized Moment–Deflection Plot (End).....	202
Figure 6-15 Normalized $M$ – $N$ Interaction (Midspan).....	203
Figure 6-16 Normalized $M$ – $N$ Interaction Plot (End).....	204
Figure 6-17 Classification of moment–rotation response of fully restrained (FR), partially restrained (PR) and simple connections (AISC 2005).....	205
Figure 6-18 Moment–Rotation Response of Elastic Springs in FE Beam Models.....	206
Figure 6-19 Normalized Load–Deflection Plot .....	208
Figure 6-20 Normalized Axial Force–Deflection Plot (Midspan).....	209
Figure 6-21 Normalized Moment–Deflection Plot (Midspan) .....	209

Figure 6-22 Normalized $M-N$ Interaction (Midspan).....	210
Figure 6-23 Normalized $M-N$ Interaction (End) .....	211
Figure 6-24 Reference Frame .....	212
Figure 6-25 Schematic of Frame Analysis.....	213
Figure 6-26 Schematic for the Quantification of Linear–Elastic Spring Constants .....	214
Figure 6-27 Frame and Beam Models .....	215
Figure 6-28 Normalized Load–Deflection Plot (Beam Midspan) .....	216
Figure 6-29 Normalized Moment–Deflection Plot (Beam Midspan).....	217
Figure 6-30 Normalized Axial Force–Deflection Plot (Beam Midspan).....	217
Figure 6-31 Normalized $M-N$ Interaction (Beam Midspan).....	218
Figure 6-32 Normalized $M-N$ Interaction (Beam End) .....	219

## Chapter 1. INTRODUCTION

### 1.1 Overview

In May 16, 1968, 23-story Ronan Point Apartments in London, U.K partially collapsed due to a gas explosion at the 18<sup>th</sup> story. The loss of load-bearing precast concrete walls caused the upper floors to collapse and eventually led to progressive collapse of the entire corner of the building (Figure 1-1).



**Figure 1-1** Ronan Point Apartments collapse (Copyright Daily Telegraph 1968:

[http://apps.newham.gov.uk/History\\_canningtown/pic47.htm](http://apps.newham.gov.uk/History_canningtown/pic47.htm))

Progressive collapse can be defined as an initial local failure triggering a spread of failure in a disproportionately large part of the structure. There has been a considerable effort to develop design guidelines and criteria to decrease or eliminate the vulnerability of buildings to this kind of failure (Nair 2004). These efforts usually have tended to concentrate on ensuring a level of redundancy, continuity and ductility in buildings to prevent such a collapse in case of a local failure.

One of the main methods of analysis for design against progressive collapse in current design guidelines involves the so-called “missing column scenario”. In this method, a designated column from a given floor is hypothetically removed and the damaged system is expected to bridge over the beam above the removed column (Figure 1-2(a)). With this “immaculate” removal of the column, the structure seeks an alternate path to re-distribute the loads without failure. One of the key load-resisting mechanisms that is believed to assist the damaged system to achieve this is often referred to as “Catenary Action”. As illustrated in Figure 1-2 (b), the beam cannot resist the vertical loads with flexural action alone and the new equilibrium state is reached by development of axial catenary forces through a formation of catenary-like mechanism (Figure 1-2 (c)) (Khandelwal and El-Tawil 2007).

In spite of many debates, this formation is widely used in most common progressive collapse design guidelines. For example, *Progressive Collapse Analysis and Design Guidelines for New Federal Office Buildings and Major Modernization Projects* (GSA 2003) clearly states that the capability of the beam or girder to accommodate the “double span condition” resulting from the missing column scenario is essential.

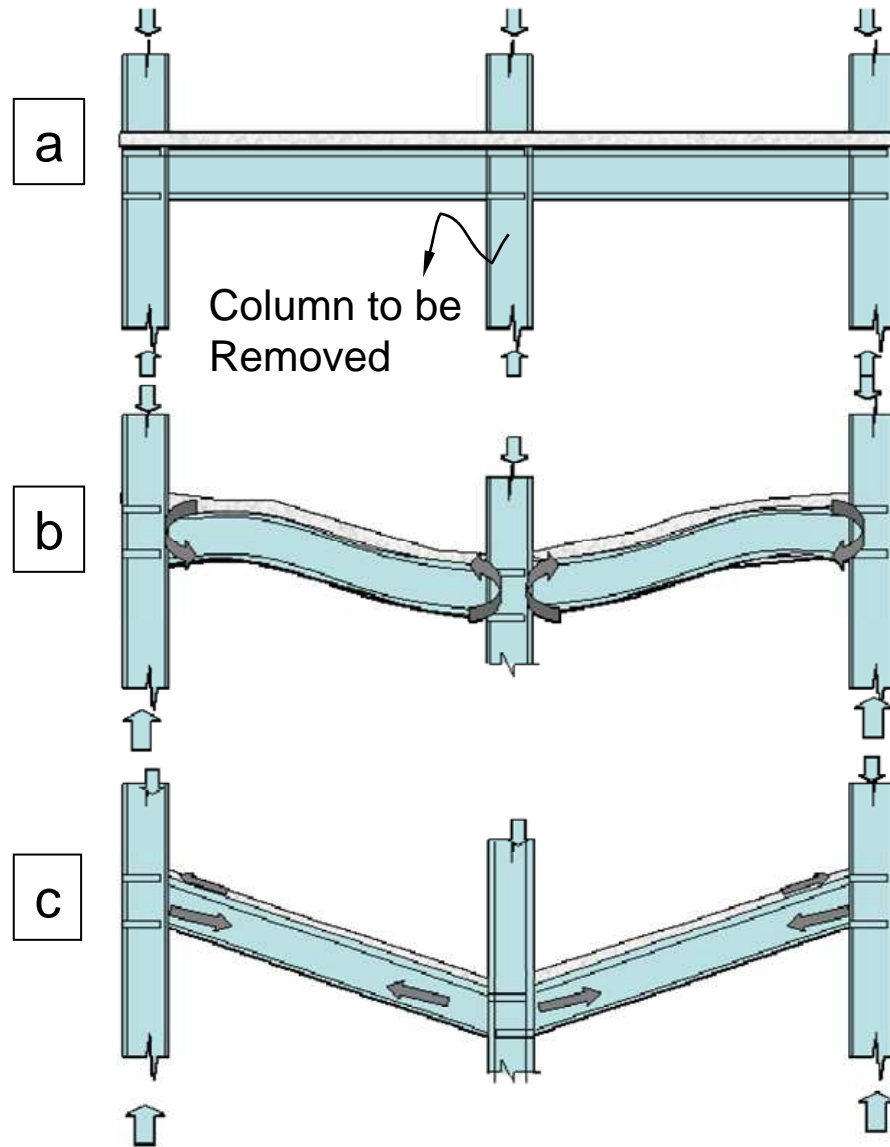


**Figure 1-2** Load-resisting mechanism upon column removal

(Adopted from Hamburger and Whittaker 2004)

The term “catenary” refers to a theoretical curved shape of a hanging chain or flexible wire supported at the ends under its own weight (Weisstein 2009). However, it is evident from Figure 1-2 (c) that the shape is more like a cable subjected to a concentrated load at midspan. Therefore, “cable-like action” is considered more rigorous describing

this behavior. However, since the terminology “catenary action” is widely used, the words “cable” and “catenary” are used interchangeably throughout this study.

## **1.2 Motivation**

Current design guidelines provide a number of prescriptive methods to prevent or limit this failure by progressive collapse. However, the theory behind the key load resisting mechanism of beams resulting from “double span condition” remains poorly understood and has not been rigorously studied.

The study presented in this thesis is intended to develop a rigorous description of the fundamental behavior of ductile steel beams undergoing a transition from a flexural to a cable-like behavior, as illustrated in Figure 1-2.

## **1.3 Research Objectives and Scope**

The overall objectives of this study are as follows:

- Develop rigorous theoretical models that describe the behavior of ductile steel beams undergoing a transition from flexural to cable-like behavior.
- Develop analytical models that can be used to evaluate and assess the theoretical models as well as help identify the main parameters affecting the behavior.
- Assess the effect of boundary conditions on the behavior.

The scope of this study is limited to ductile steel beams with idealized boundary conditions. Factors related to the potential for instability, fracture and connection behavior are beyond the scope of this research. It is believed that a thorough understanding of the behavior at this fundamental level is essential to understanding the behavior in the presence of other complex factors.

The idealized boundary conditions used include simple, fully fixed and partially restrained supports. Theoretical models are developed for the first two support types whereas finite element (FE) analysis is used for all support types. Studies related to the effect of partially restrained supports are limited to elastic boundary conditions.

#### **1.4 Approach**

The beam over which the remaining structural system is desired to bridge upon removal of a supporting column is isolated and modeled with idealized boundary conditions to study fundamental behavior. Two theoretical approaches are used to model the beam behavior: rigid-plastic analysis and cable analysis. Rigid-plastic analysis assumes that the beam behaves rigidly until a flexural collapse mechanism is reached, whereas cable analysis assumes that the beam does not offer any flexural resistance. These two theoretical models will serve as bounds to the actual behavior.

In order to verify the theoretical results from the two approaches mentioned above, preliminary FE analyses were conducted. Following this study, another parametric FE analysis was conducted in order to identify the main factors affecting the behavior.

OpenSees (McKenna et al. 2000), *Open System for Earthquake Engineering Simulation* software was used in the FE analyses.

#### **1.5 Organization of Thesis**

Chapter 2 provides background information including: current methodologies used for design against progressive collapse, a description of recent relevant research studies and a review of rigid-plastic analysis procedure. Chapter 3 presents theoretical results using rigid-plastic and cable analyses. FE analysis results are presented in Chapter



4. In Chapter 5, an equation is developed and proposed that can be used to predict the midspan deflection at the onset of pure cable behavior. In Chapter 6, the effect of elastic boundary conditions on the beam behavior is investigated. Finally, a summary of the study, along with conclusions and recommendations for future directions, are provided in Chapter 7.

## **1.6 Notation**

The notation used in this thesis follows *AISC Steel Construction Manual 13<sup>th</sup> Edition* (2005) and is listed in Appendix A.

## Chapter 2. BACKGROUND

### 2.1 Introduction

Progressive collapse is a failure mode that may not only occur unexpectedly in buildings but can also be seen in building demolitions (Bazant and Verdure 2007). Due to the relative rareness of the events and situations that cause progressive collapse, it is one of the least researched areas in structural engineering (Mohamed 2006). *ASCE Standard 7* (ASCE 2005) defines progressive collapse as “The spread of an initial failure from element to element, eventually resulting in the collapse of entire structure or a disproportionately large part of it”. The keyword “disproportionate” is widely adopted since the resulting collapse is generally out of proportion to the initial failure.

The Ronan Point apartment collapse (Figure 1-1) is a landmark case of this phenomenon in recent history that instigated code changes. In fact, a reform in British codes started in early 1970’s and has been intensively referenced in literature produced in the U. S. (Mohamed 2006). Despite the fact that eager interest has continued throughout the decades, the majority of resources were developed during the first several years after this event. A second increase in interest was aroused by the attack on the Alfred P. Murrah Federal Building in 1995. Various reports were produced to investigate the damage and progressive collapse of the building and design-specific recommendations were provided. Now, the interest has reached its peak level after 9 / 11 tragedy occurred in New York in 2001 (Dusenberry 2002).

A comprehensive survey of all the efforts mentioned above is beyond the scope of this study. Therefore, a brief review of commonly used concepts and approach methods for design against progressive collapse is presented in Section 2.2. Recent relevant research is reviewed in Section 2.3. Finally, a review of rigid–plastic analysis of beams undergoing finite displacements as provided by Jones (1989) is presented in Section 2.4.

## **2.2 Existing Methodologies for Design against Progressive Collapse**

It is usually not practical to design a structure to an abnormal loading condition unless it is a special protective system. Nevertheless, local failure effects and progressive collapse can be limited or mitigated by taking precautions in the design process (ASCE 2005).

There exist a considerable amount of reference documents that address the problem of progressive collapse. However, most common public sector codes and standards largely regard general structural integrity and progressive collapse in a qualitative manner, whereas governmental documents explicitly address the issue (Dusenberry 2002). In fact, a good engineering judgment, design and construction practices in order for increased structural robustness and integrity are addressed in a number of standards (Ellingwood et al. 2007). The most commonly used approaches for design against progressive collapse are indirect and direct design methods. In general, the indirect design method is a prescriptive method that requires a minimum level of connectivity between the structural members. Direct design, on the other hand, largely depends on structural analysis to ensure that the structure resists an abnormal event (Ellingwood et al. 2007).

The following sections provide a review of these two methods with an emphasis on steel structures for the purpose of this study.

### **2.2.1 Indirect Method**

Indirect design refers to implicit considerations to be taken during the design process for resistance to progressive collapse by means of requiring minimum levels of strength, continuity and ductility (ASCE 2005). The main purpose of those provisions is to provide an alternate path within the structure to re-distribute the loads in case of an abnormal loading condition. ASCE 7-05 gives the following key concepts to be considered for improving general structural integrity:

- Good plan layout
- Provide integrated ties among the principal elements within the structures
- Returns on walls
- Changing directions of floor spans
- Usage of load-bearing interior partitions
- Catenary action of floor framing (slab)
- Beam action of walls
- Ductile detailing
- Consideration of load reversals
- Compartmentalized construction

While most of practices listed above may be considered as examples of precautions to be considered in the design process, the second concept, which is commonly referred to as the “Tie Force Method” was introduced in British codes after

Ronan Point collapse and then was adopted by some of the governmental bodies in the U. S. In this approach, both vertical and horizontal members in buildings are desired to be tied together at each principal floor level as illustrated in Figure 2-1. Furthermore, these tensile tie forces are typically provided by the elements and their connections within the structure that are designed conventionally (UFC 2005). The types of ties are peripheral, internal, horizontal and vertical ties (Figure 2-1).

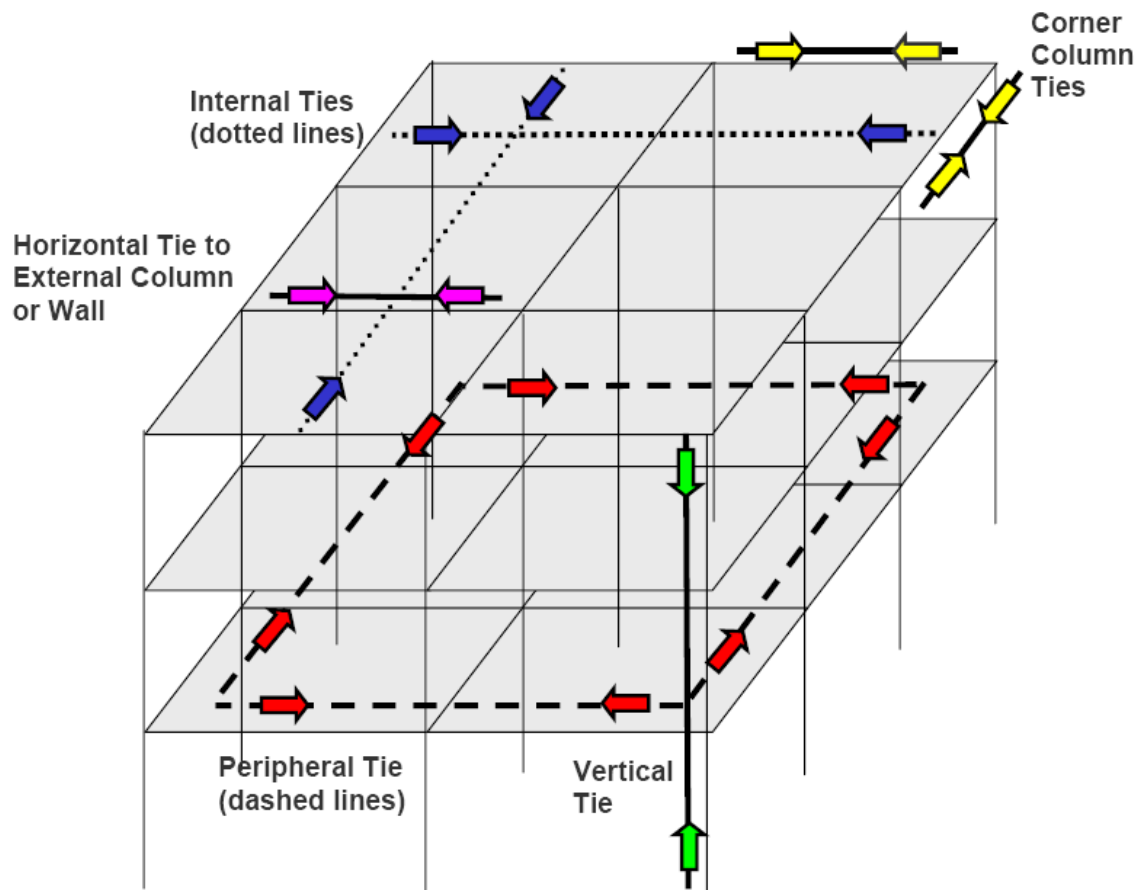


**Figure 2-1** Schematic of Tie Forces in a Frame Structure (UFC 2005)

The only standard that explicitly utilizes this approach in the U. S. is the Department of Defense document: Unified Facilities Criteria (UFC) *Design of Buildings to Resist Progressive Collapse* (2005). It is noted that the tie force requirements are

almost identical to British Standards, and it is assumed that they are applicable to U. S. construction. Tie force requirements in various design guidelines are summarized in Table 2-1; the loads generally need not be considered as additive to other loads (e. g. dead and live loads).

Even though the tie approach does not incorporate intensive calculations of the structural response to extreme load conditions, it provides a reserve capacity to members and connections within reinforced concrete and steel–framed structures through either flexure or membrane action. This event-independent approach is relatively easy to apply and convenient for all projects (Ellingwood et al. 2007).

The mechanics behind this approach are not well explained. In fact, the fundamental assumption for the efficiency of this method is that the structural members and their connections have sufficient rotational ductility to develop axial capacity in the form of catenary action under large deflections (Marchand and Alfawakhiri 2005). For the purpose of this study, horizontal tie force requirements which pertain to beams and girders will be thoroughly presented. According to Ellingwood et al. (2007), the form of horizontal steel tie force requirement given in UFC (2005) and British Code (BS 5950-I 2000) as detailed in Table 2-1 can simply be obtained with use of the one–half beam shown in Figure 2-2 in the following way: in case of a column removal, the span length is now doubled and the slab hangs in a catenary shape with a maximum sag of  $a$  (denoted by  $S$  in Figure 2-2). In addition to vertical reactions at the ends, horizontal reaction force  $F$  must also be developed. Therefore, the moment equilibrium requires:

$$F \cdot a = \frac{w \cdot (2L)^2}{8} \quad [2.1]$$

where  $w$  is load per unit length,  $L$  is the bay length. The magnitude of the horizontal force reactions that must be provided by ties, with transverse spacing  $s$ , can be expressed as:

$$F = \frac{q \cdot s \cdot L}{2 \cdot (a/L)} \quad [2.2]$$

where  $q$  is the floor load (i.e.  $q = \frac{w}{s}$ )

UFC (2005) points out that the theory behind this concept is based on research conducted by Burnett (1975), who discussed the logic and theoretical background used to develop the British tie force requirements. However, the details are limited to reinforced concrete structures and similar descriptions were not revealed for steel design in the development of UFC (2005). An illustration of this discussion is given in Figure 2-2.

$F_T$  in Table 2-1 and Figure 2-2 is defined as “Basic Strength” and according to UFC (2005), the upper limit (60 kN / m) can be obtained from two cases. The first method is to consider  $F_T$  as the internal member force developed by catenary action of the floor in case a vertical load bearing element is removed to produce a presumed transverse deflection of 10% of the span length (Figure 2-2). The second method for determining  $F_T$  is to consider the forces applied to a typical wall panel under a static pressure of 34 kN/m<sup>2</sup> (5 psi), which is thought to be the overpressure that occurred in the Ronan Point explosion. The first approach (catenary action) is the mechanism that the tie forces are intended to withstand based on the debates with British engineers (UFC 2005). It should be noted that  $F$  provided to obtain the form of steel tie force requirements (Equation 2.2) has units of force and should not be confused with  $F_T$  (force per unit length) in the context of calculations for reinforced concrete as given in Figure 2-2.

**Table 2-1** Strength of Ties (Ellingwood et al. 2007)

BS Steel 2000	BS Concrete 1997	BS Masonry 1992	Eurocode 2-2002	PCI 1976
<b>Interior</b> $0.5 (1.4 g_k + 1.6 q_k) s_t L \geq 75 \text{ kN}$	Greater of $\frac{g_k + q_k}{7.5} \frac{l_r}{5} F_t$ or $1.0 F_t$ , where $F_t =$ the lesser of $(20 + 4 n_0)$ or $60 \text{ kN}$	Greater of $F_t$ or $\frac{G_k + Q_k}{7.5} \frac{L_a}{5} F_t \text{ kN/m}$	$F_{tie, int} = 20 \text{ kN/m}$ . For ties grouped at beam lines: $f_{tie} = (l_1 + l_2) q_4 / 2$ $\leq q_5$ where $q_4 = 20 \text{ kN/m}$ and $q_5 = 70 \text{ kN}$	Horizontal $\geq 22 \text{ kN/m}$ (1500 lb/ft)
<b>Peripheral</b> $0.25 (1.4 g_k + 1.6 q_k) s_t L \geq 75 \text{ kN}$	$1.0 F_t$	$F_t \text{ kN}$	$F_{tie, per} = l_i q_5 \leq q_4$ where $q_5 = 10 \text{ kN/m}$ and $q_4 = 70 \text{ kN}$	$\geq 71 \text{ kN}$ (16 000 lb)
<b>Edge Columns</b> 1 % of the maximum factored vertical dead and imposed load in the column adjacent to that level or same as for interior ties, whichever is more.	Greater of $[2.0 F_t$ or $(l_c / 2.5) F_t$ if less], or 3 % of total ultimate vertical load carried by column at that level	Lesser of $2 F_t$ or $(h / 2.5) F_t \text{ kN}$	$F_{tie, col} = 150 \text{ kN}$	
<b>Corner Columns</b>	Same as for edge columns, but in 2 perpendicular directions		Corner columns should be tied in two directions.	
<b>Walls</b>	Greater of $[2.0 F_t$ or $(l_c / 2.5) F_t$ per meter if less], or 3 % of the total ultimate vertical load carried by the wall at that level	Lesser of $2 F_t$ or $(h / 2.5) F_t \text{ kN/m}$	$F_{tie, facade} = 20 \text{ kN/m}$	2.5 % of service load on wall, but $\geq 22 \text{ kN/m}$ (1500 lb/ft)
<b>Vertical</b> Largest factored vertical dead and imposed load reaction applied to the column at a single floor level	Maximum design ultimate dead and imposed load received by the column from any one story	Greater of $\frac{34A}{8000} \left( \frac{h_a}{t} \right)^2 \text{ N per column}$ or $100 \text{ kN/m}$ of wall length		$\geq 44 \text{ kN/m}$ (3000 lb/ft) of wall

$A$  = horizontal cross sectional area of column or wall;

$g_k, G_k$  = characteristic dead load per unit area of the floor or roof;

$h$  = clear story height;

$h_a$  = clear height of a column or wall between restraining surfaces;

$L$  = span;

$L_a$  = the lesser of:  $5 h$ , or the greatest distance in the direction of the tie, between the centers of columns or other vertical loadbearing members, whether this distance is spanned by a single slab or by a system of beams and slabs;

$l_i$  = length of end span;

$l_1, l_2$  = span length of floor slabs on either side of the beam;

$n_0, N_s$  = number of stories including ground and basement;

$q_k, Q_k$  = characteristic imposed floor or roof load per unit area;

$s_t$  = mean transverse spacing of the ties adjacent to that being checked;

$t$  = thickness of column or wall.



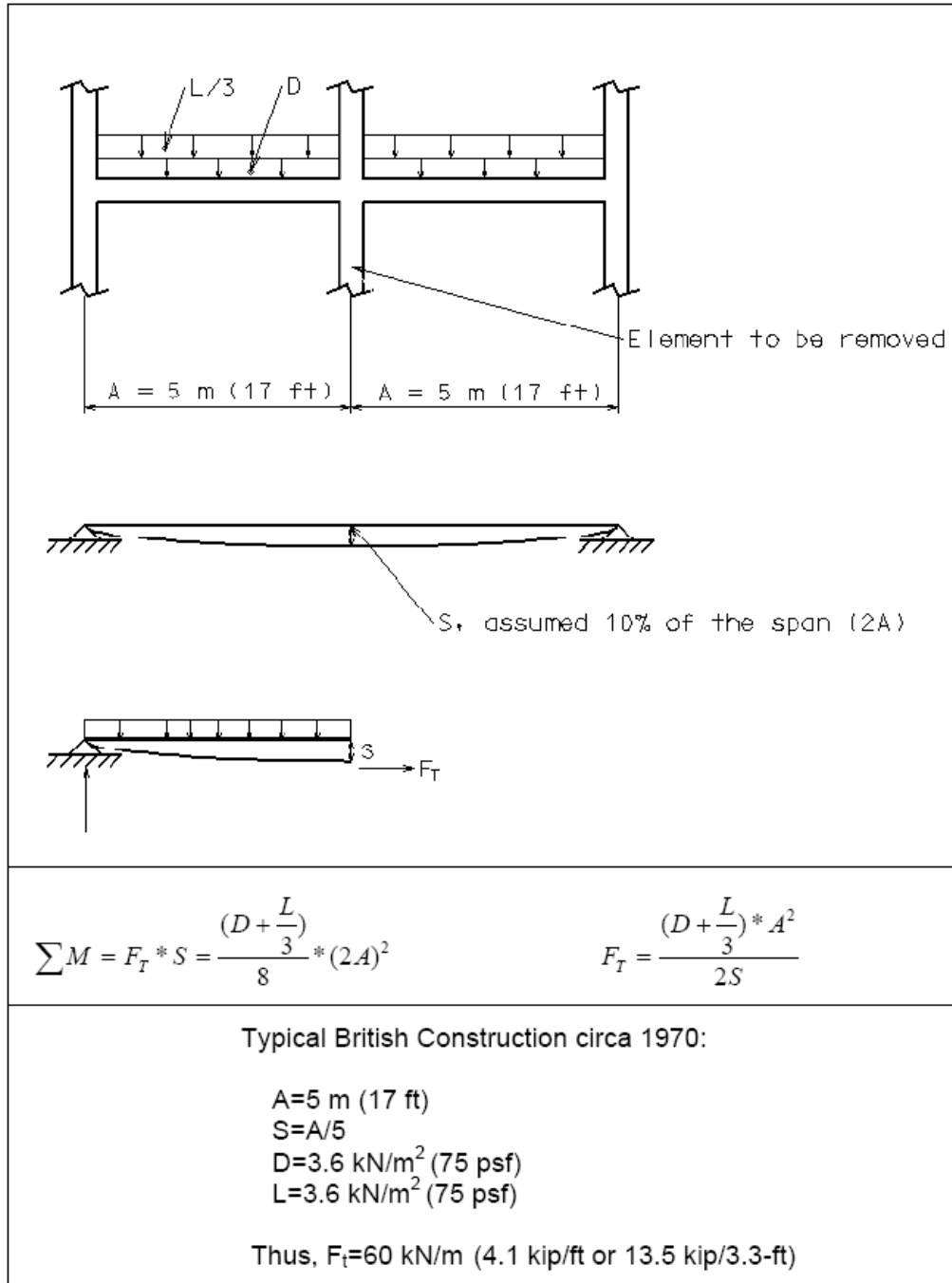


**Figure 2-2** Calculation of Upper Bound on the Basic Strength (UFC 2005)

There has been some discussion of the approximate deflection level to use in the calculation of the tie force requirements; beam and slab tests conducted by Creasy (1972) suggested that the sag of the double span over the missed support should not exceed 20%

of single span length. However, Breen (1980) stated that the British calculations are based on  $a/L$  of 0.15. For steel buildings, on the other hand, Marchand and Alfawakhiri (2005) claim that the required tie forces specified by design guidelines are “minimum” catenary forces that develop under a sag of 10 percent of “double span”.

## 2.2.2 Direct Methods

Direct design is an explicit consideration of a structure’s resistance to progressive collapse and damage absorption ability during the design phase. It consists of two approaches: Specific Local Resistance (SLR) and Alternate Path Method (APM). The first refers to providing adequate strength to resist an extreme loading condition and requires that the triggering event be identified so the local resistance can be related to a particular limit state (Krauthammer et al. 2002). Alternate Path Method, on the other hand, allows for local failure but requires the availability of alternate load paths to redistribute the loads within the remaining structure (ASCE 2005).

### 2.2.2.1 Specific Local Resistance (SLR)

SLR approach implies the design of critical vertical load bearing elements to a specific threat. These critical elements are often referred as “key elements” and are explicitly designed to withstand abnormal load conditions (e.g., blast pressure).

Therefore, this approach is threat – dependent (Ellingwood et al. 2007).

*ASCE Standard 7* (ASCE 2005) provides the following load combinations to check the capacity of a structure or structural element to resist an abnormal event:

$$\blacksquare 1.2D + A_k + (0.5L \text{ or } 0.2S + 0.2W) \quad [2.3]$$

$$\blacksquare (0.9 \text{ or } 1.2)D + A_k + 0.2W \quad [2.4]$$

where  $A_k$  represents extreme load condition such as blast pressure and  $D, L, S, W$  represents dead load, live load, snow load, wind load, respectively.

In spite of many debates regarding this method because of the difficulties in defining the magnitude of the extreme event, this approach is relatively less expensive in many cases (Mohamed 2006). In fact, this approach is often considered to be more practical for retrofitting an existing structure because the cost might be significant to have the structure meet the requirements of other approaches (Ellingwood et al. 2007).

### **2.2.2.2 Alternate Path Method (APM)**

The Alternate Path Method (APM) is based on supplying an alternate load path in order to limit the local damage and prevent major collapse in case of a local failure (Khandelwal and El-Tawil 2007). This threat – independent method addresses the performance of the structure after some elements are compromised. It is performed by assuming that the primary structural elements, sequentially one element at a time, are rendered ineffective and investigating the consequent structural behavior (Dusenberry 2002). The APM relies on continuity and ductility to redistribute the forces in case of a local damage. Therefore, APM attracts people because the limit state considered is explicitly related to overall structural performance and, in contrast to SLR method, the triggering event does not need to be identified specifically (Krauthammer et al. 2002)

In this methodology, key structural elements (typically a column or wall), are hypothetically removed and the structure is analyzed to evaluate its capacity to bridge over that removed member (Marchand and Alfawakhiri 2004). Therefore, it is important that beams and floor girders are able to at least accommodate the double span condition.

This necessitates not only beam-to-beam continuity but also requires that girders and beams deflect further than their elastic limit in flexure without undergoing structural collapse across the removed element (GSA 2003).

Even though it is not likely to occur in an actual event, the vertical load bearing elements are notionally removed without degradation of the abilities of the joint above the removed member. This so called “immaculate removal” is not necessarily intended to represent an actual event (UFC 2005). The removal procedure, as well as the response of the framing scheme, after loss of primary column support in a traditional moment frame is illustrated in Figures 2-3 and 2-4.

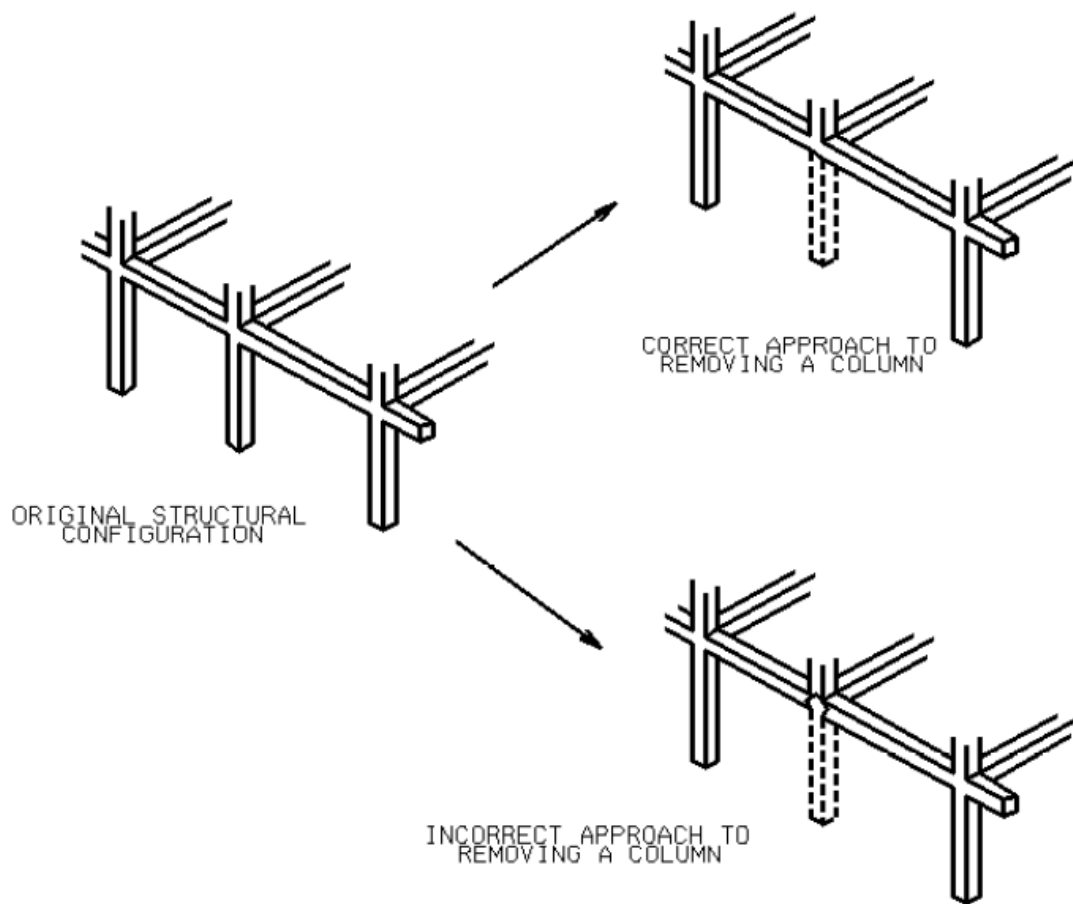


**Figure 2-3** Removal of Column (UFC 2005)

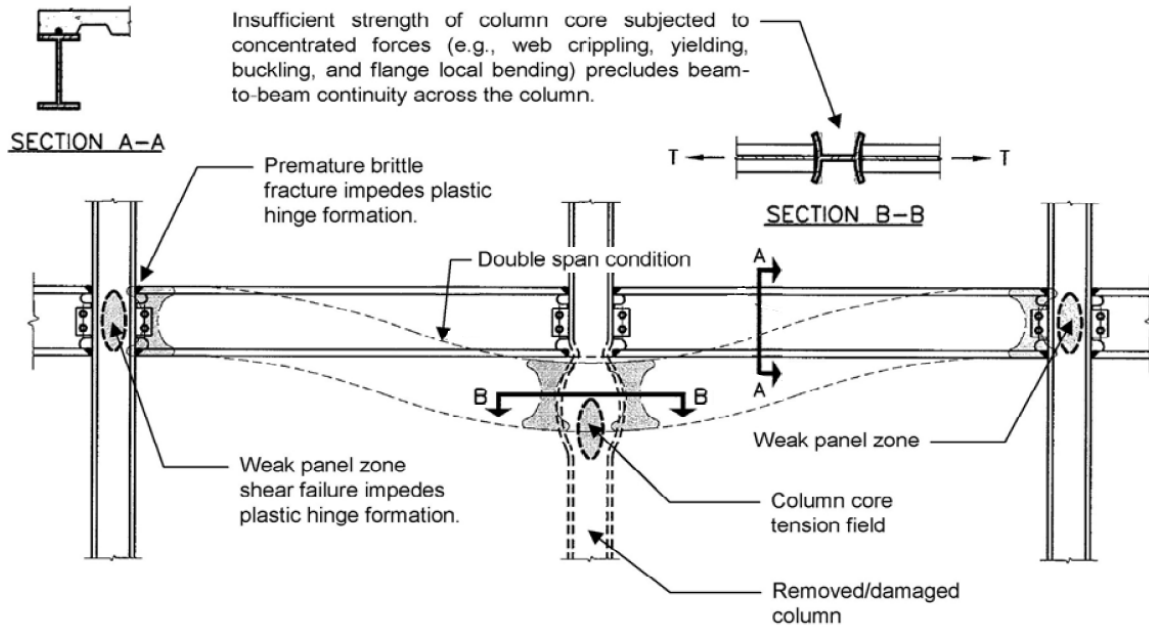


**Figure 2-4** Double Span Condition in a Traditional Moment Frame (GSA 2003)

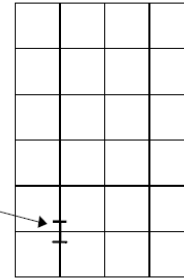
A theoretical damage state as depicted in Figure 2-3 is assumed in the application of APM and all other damages that may occur as a result of loss of vertical support are ignored. The transition is assumed to be instantaneous and dynamic effects are considered depending on the analysis procedure used (Ellingwood et al. 2007). The following analysis procedures can be conducted:

- Linear Static
- Nonlinear Static
- Linear Dynamic
- Nonlinear Dynamic

Vertical member removal considerations are generally common. Interior and exterior considerations are illustrated in Figure 2-5 for framed structures. A similar but more detailed set of considerations are also available for shear / load bearing structures.

**Interior Considerations**

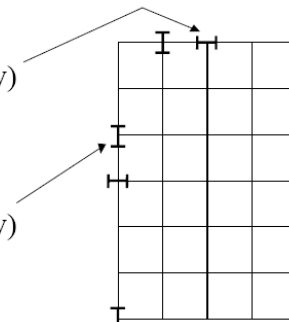
- 1 Analyze for the instantaneous loss of 1 column that extends from the floor of the underground parking area or uncontrolled public ground floor area to the next floor (1 story). The column considered should be interior to the perimeter column lines.



Plan View

**Exterior Considerations**

- 1 Analyze for the instantaneous loss of a column for one floor above grade (1 story) located at or near the middle of the short side of the building.
- 2 Analyze for the instantaneous loss of a column for one floor above grade (1 story) located at or near the middle of the long side of the building.
- 3 Analyze for the instantaneous loss of a column for one floor above grade (1 story) located at the corner of the building.



Plan View

**Figure 2-5** Element Removal Considerations for Framed Structure (GSA 2003)

Load combinations used for this method in different guidelines are summarized in Table 2-2. It can be seen that a factor 2.0 is used in DoD UFC 4-023-03 (2005) and GSA (2003) when a linear-static analysis is performed. Powell (2005) states that the maximum deflection for a linear structure is twice the static deflection, therefore, an “impact” or “load amplification” factor is commonly used in the existing design guidelines. There has been a significant amount of effort on progressive collapse assessment of both RC and

steel-framed buildings using these different analysis procedures. Advantages and disadvantages of each are discussed in detail by Powell (2005).

**Table 2-2** Load Combinations for Progressive Collapse Analysis

(Ellingwood et al. 2007)

Standards	Load combinations after notional member removal
BS	$(1 \pm 0.5) D + L / 3 + W_n / 3$
Eurocode 2003 draft	
Canada 1977	$D + L / 3 + W_n / 3$
ASCE 7-98, 02, 05	$(0.9 \text{ or } 1.2) D + (0.5 L \text{ or } 0.2 S) + 0.2 W_n$ (with member removal) $1.2 D + A_k + (0.5 L \text{ or } 0.2 S)$ (specific local resistance method) $(0.9 \text{ or } 1.2) D + A_k + 0.2 W_n$ (specific local resistance method)
DOD UFC 4-010-01	$D + 0.5 L$ net floor uplift
DOD UFC 4-023-03	$D + 0.5 L$ net floor uplift $(0.9 \text{ or } 1.2) D + (0.5 L \text{ or } 0.2 S) + 0.2 W_n$ (nonlinear dynamic analysis) $2.0 [(0.9 \text{ or } 1.2) D + (0.5 L \text{ or } 0.2 S)] + 0.2 W$ (static analysis)
NYC 1998, 2003	$2 D + 0.25 L + 0.2 W_n$
GSA	$2 (D + 0.25 L)$ static analysis $D + 0.25 L$ dynamic analysis
Sweden	$G_k + \Psi Q_k$

$D, L, W_n, S$  = dead, live, wind and snow loads;

$Q_{ak}$  = characteristic value of accidental action;

$G_k, Q_k$  = characteristic dead, imposed loads per unit area of the floor or roof;

$\Psi$  is a load reduction factor which, when multiplied with  $Q_k$ , gives the frequent value of a variable action.

$A_k$  = extraordinary load.

Two governmental documents in the U. S. explicitly use this methodology.

Department of Defense's; Unified Facilities Criteria (UFC) *Design of Buildings to Resist Progressive Collapse* (2005) and *Progressive Collapse Analysis and Design Guidelines for New Federal Office Buildings and Major Modernization Projects* developed by the General Services Administration (GSA) (2003). However, acceptance criteria used in the process vary in each. UFC (2005) uses *Load and Resistance Factor Design (LRFD)*

methodology and refers to material specific codes whereas GSA (2003) provides its own procedure.

In addition to the acceptance criteria for structural members and their connections, regardless of the analytical method used, it is required that the designer quantify structural damage during and at the end of the analysis. Table 2-3 provides the damage definitions and limits stipulated by various design guidelines.

**Table 2-3** Definition of Local Collapse (Ellingwood et al. 2007)

BS 5950-1: 2000	Canada -NBCC 1977	NYC 1998, 2003	DOD UFC 4-023-03 2005	GSA 2003
<i>Horizontal Spread</i>				
Lesser of 15 % of floor or roof area or 100 m <sup>2</sup> (1000 ft <sup>2</sup> ).	Truss, beam, floor strip or floor panel of initial damage plus one same on either side; one bay; two bay-sized slabs may hang together as a catenary if support at one end of slab is removed.	Lesser of 20 % of floor or roof area or 1000 ft <sup>2</sup> (100 m <sup>2</sup> ).	<i>Exterior:</i> Damage to floor above lost member shall be lesser of 70 m <sup>2</sup> (750 ft <sup>2</sup> ) or 15 % of total floor area; <i>Interior:</i> Lesser of 140 m <sup>2</sup> (1500 ft <sup>2</sup> ) or 30 % of total floor area. Damage must not spread beyond structure tributary to failed element (exterior) or beyond the bays adjacent to removed element (interior).	The structural bay associated with the removed member.
<i>Vertical Spread</i>				
Level of initial damage, plus one adjacent level, either above or below.	Level of initial damage, plus one adjacent level, either above or below.	≤ 3 stories	Floor directly beneath failed element should not fail	1800 ft <sup>2</sup> (170 m <sup>2</sup> ) at the floor directly above a removed <i>exterior</i> column; or 3600 ft <sup>2</sup> (330 m <sup>2</sup> ) at the floor directly above a removed <i>interior</i> column.

### 2.3 Recent Relevant Research

“Structural integrity” is a trendy term that prompted important arguments regarding inclusion of provisions into design codes for the purpose of enhanced structural



robustness (Gustafson 2009). After the September 11<sup>th</sup> attacks, research interest in progressive collapse intensified. Because of the lack of design-specific provisions in existing codes, a majority of recent considerations have more likely been intended to find quick answers for structural design practice.

For design of structural steel buildings, AISC has published “Fact for Steel Buildings 2: *Blast and Progressive Collapse*” by Marchand and Alfawakhiri (2005). The need for careful research is highlighted in regard to assessing whether or not beams and their connections as currently designed have adequate robustness to develop imperative plastic rotations and large tensile forces during catenary action, which is considered to be promising for steel structure design (Hamburger and Whittaker, 2004).

Foley et al. (2007) investigated the level of robustness that structural steel buildings naturally possess. An application of the Alternate Path Method for steel moment resisting frames with varying number of stories is presented; the inherent robustness is evaluated by means of assessing internal force demands in members and their connections after loss of an exterior column. In addition, the study goes beyond framework analysis, and the effect of catenary and membrane action in floor systems is investigated for more accurate quantification of robustness. Gravity load analyses of various floor sub-assemblages are performed assuming full fixity at the perimeter of the panels. Recommendations are made for detailing considerations to provide inherent robustness enhancement for structural systems.

The question of the reliability of catenary action to redistribute forces resulting from column damage has been studied on particular structural systems. A case study of a steel-framed building was performed by Byfield and Paramasivam (2007) with regard to

the ability of beams to exhibit catenary behavior. The results showed that industry standard simple beam–column connections have inadequate ductility to exhibit large floor displacements during catenary action. Furthermore, the absence of rotation capacity in the tie force method is emphasized and the effect of prying action is also underlined in regard to the connection performance.

Due to the natural toughness of earthquake resistant construction, which contributes to alternate load paths and distribution, a widespread notion has arisen that earthquake resistant design will improve collapse resistance (Khandelwal and El-Tawil 2007). To that end, a research study was carried out by El-Tawil and his co-workers to investigate the collapse behavior of seismically-designed steel moment resisting frames and connections. Sub- assemblages of an eight–story special moment resisting perimeter frame were taken under investigation, which is widely used in the U.S. west coast. The effect of a number of key design variables on catenary action formation was investigated and the results indicated that connection ductility and strength are adversely affected by an increase in beam depth and YUSR (yield to ultimate strength ratio). A set of practical implications are also provided based on numerical results. However, it should be remarked that the boundary conditions considered in the sub–assemblages involved seismic behavior characteristics which may not necessarily reflect actual behavior. The ensuing effort of this group focused on the development of computationally adequate, so-called “macro models” to investigate progressive collapse resistance of seismically designed moment frame buildings including RC and steel–framed structures (Khandelwal et al. 2008).

As far as recent demand to incorporate design-specific provisions into building codes, the upcoming *International Building Code* (IBC) will include new section for structural integrity. Gustafson (2009) presents these new provisions with an emphasis on structural steel requirements. According to Gustafson (2009), minimum connection requirements for beams are as follows:

“End connections of all beams and girders shall have a minimum nominal axial tensile strength equal to the required vertical shear strength for Allowable Strength Design (ASD) or 2/3 of the required shear strength for Load and Resistance Factor Design (LRFD) but not less than 10 kips (45 kN). For the purpose of this section, the shear force and the axial tensile force need not be considered to act simultaneously.”

It is emphasized that based on the last sentence of the section provided above, the proposed procedure is to design the beam end connection conventionally and then to check for the horizontal force required. Moreover, this force is not intended to be the force that is required to be redistributed within the structure (Gustafson, 2009). Instead, it can be considered as a minimum level of structural integrity within the structure.

Finally, the behavior of axially-restrained beams subjected to extreme transverse loading was studied by Izzuddin (2005), focusing on static response under ambient and elevated temperature in which beams exhibit large displacements and develop axial forces. However, the model developed in this study used a linear idealization of the yield condition under combined bending moment and axial force. Thus, the behavior of W-shaped beams could not be described rigorously.

## 2.4 Static Plastic Behavior of Simple Beams

Static plastic behavior of a centrally-loaded simple beam with a rectangular cross-section experiencing finite, but not necessarily large, displacements was presented by Jones (1989). Due to its relevance, for the purposes of the study presented in this thesis, the procedure employed by Jones (1989) is reviewed in the remainder of this chapter.

### 2.4.1 Rigid-Plastic Behavior

Elastic-perfectly plastic and rigid perfectly plastic idealizations on a material (stress versus strain) level are depicted in Figure 2-6 (a). The corresponding idealizations on the cross-sectional level (moment versus curvature) are shown in Figure 2-6 (b). Jones (1989) used the rigid-perfectly plastic idealization on a cross-sectional level for his analyses, so the effect of elastic deformations is fully ignored. In other words, no cross-sectional deformations occur until a plastic hinge forms (e.g., when the moment at any section reaches the plastic moment,  $M_p$  for the case shown in Figure 2-7). Once a flexural collapse mechanism is reached, the beam starts to deflect. As transverse deflection increases, the beam starts to develop axial force,  $N$  as discussed next.

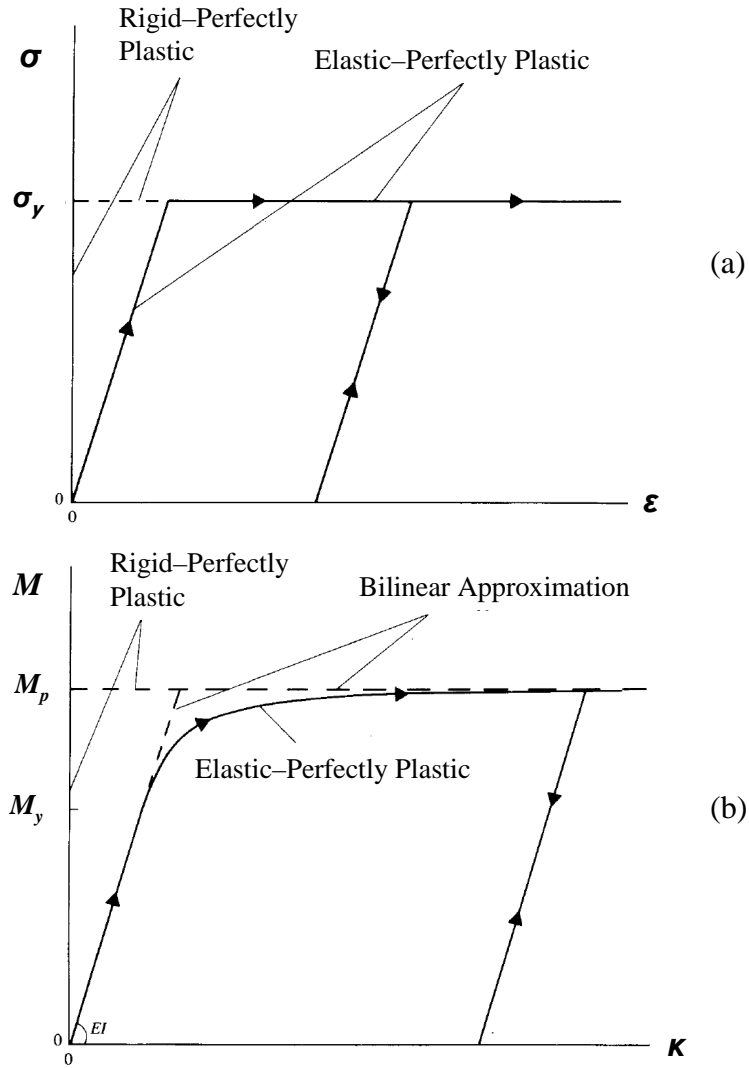


**Figure 2-6** Behavior Idealizations (Jones 1989)

### 2.4.2 Effect of Finite Displacements

Conventional beam theory is developed assuming small displacements, and hence it is possible to write the equilibrium equations for the undeformed original shape. For the case illustrated in Figure 2-7, the line through the longitudinal axis of the beam needs to be longer in the deflected shape configuration due to finite transverse displacements,  $W$ . This extension results in development of an axial strain and an associated axial force,

$N$  (Jones 1989). As a result, the load carrying capacity increases beyond the plastic collapse load as will be shown later. To describe this behavior, a yield condition for combined bending moment,  $M$  and axial force,  $N$  needs to be obtained, as presented in the following section.

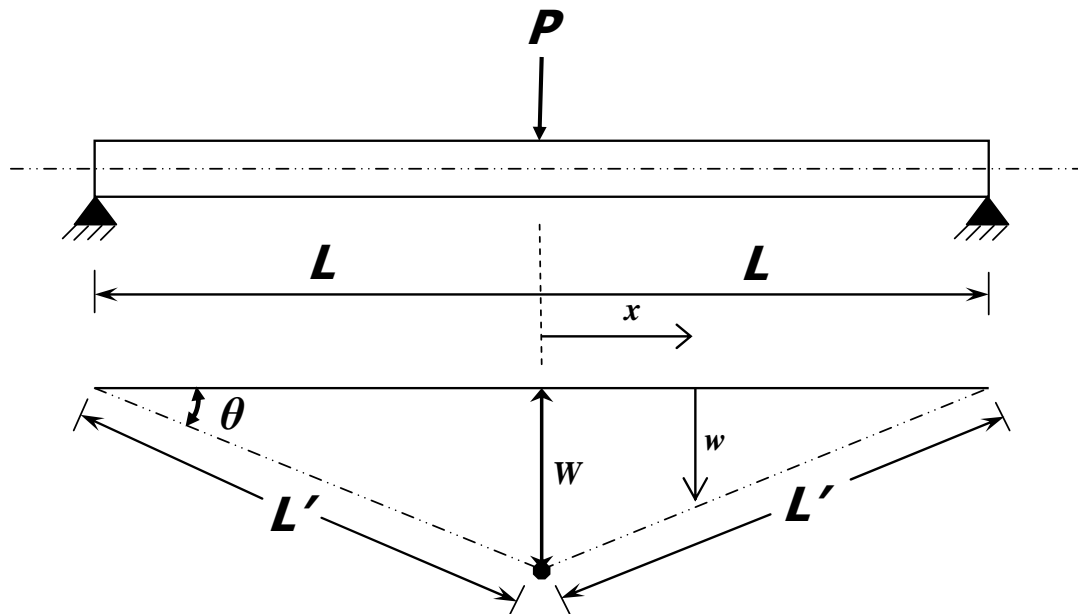


**Figure 2-7** Centrally Loaded Simple Beam under Finite Displacements

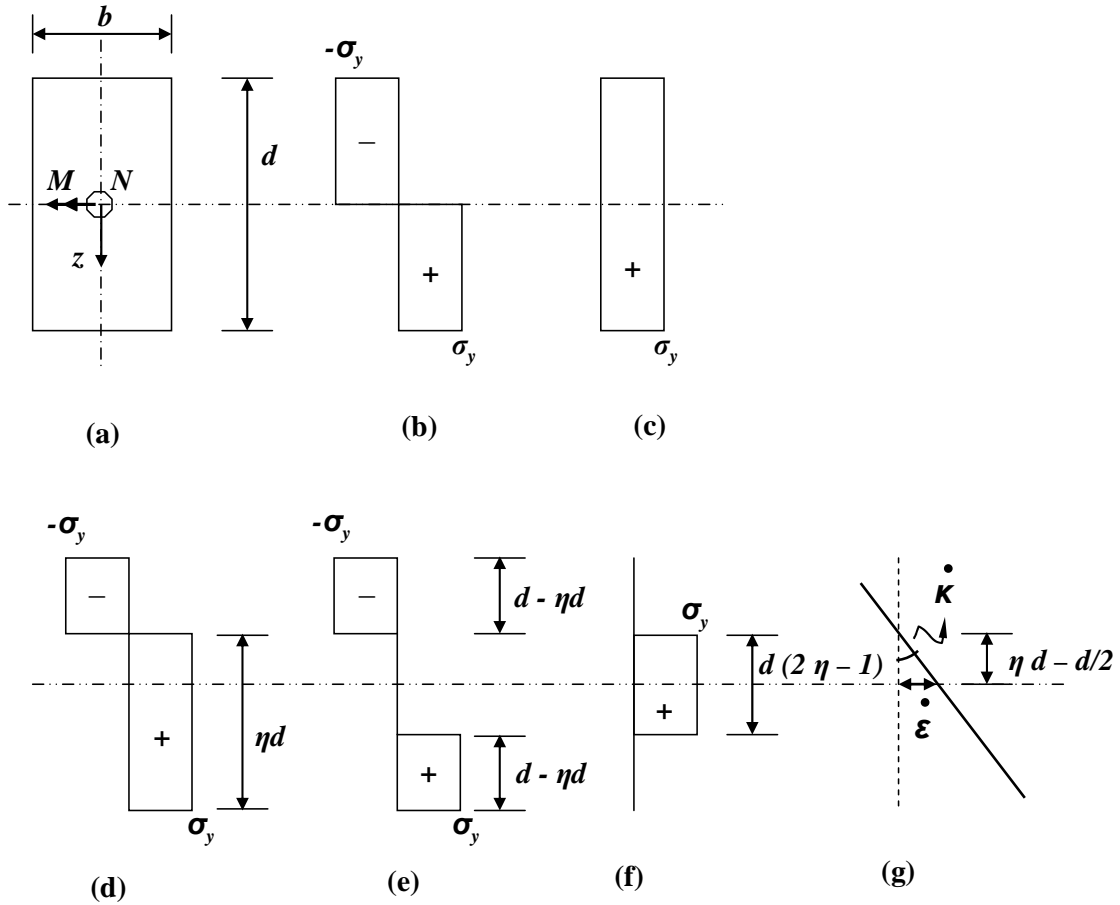
### 2.4.3 $M$ - $N$ Interaction at Cross-Sectional Level

For combined bending moment,  $M$ , and axial force,  $N$  on a rectangular cross-section, with the aid of Figure 2-8, the following  $M$ - $N$  interaction equation that defines the yield condition can be derived:

$$\frac{M}{M_p} + \left[ \frac{N}{N_p} \right]^2 = 1 \quad [2.5]$$

where  $N_p$  is the plastic axial force and  $M_p$  is the plastic bending moment.

A graphical representation of this equation is shown in Figure 2-9.



- (a) Cross-Section
- (b) Stress distribution associated under pure plastic bending moment  $M_p$
- (c) Stress distribution associated under pure plastic axial force  $N_p$
- (d) Stress distribution associated with combined  $M$  and  $N$
- (e)-(f) Stress distribution associated with  $M$  and  $N$  respectively
- (g) Strain distribution across the depth due to the stress distribution in (d)

**Figure 2-8** Combination of Axial force and Moment on a Rigid-Perfectly Plastic Beam with a Rectangular Cross-section (Jones 1989)

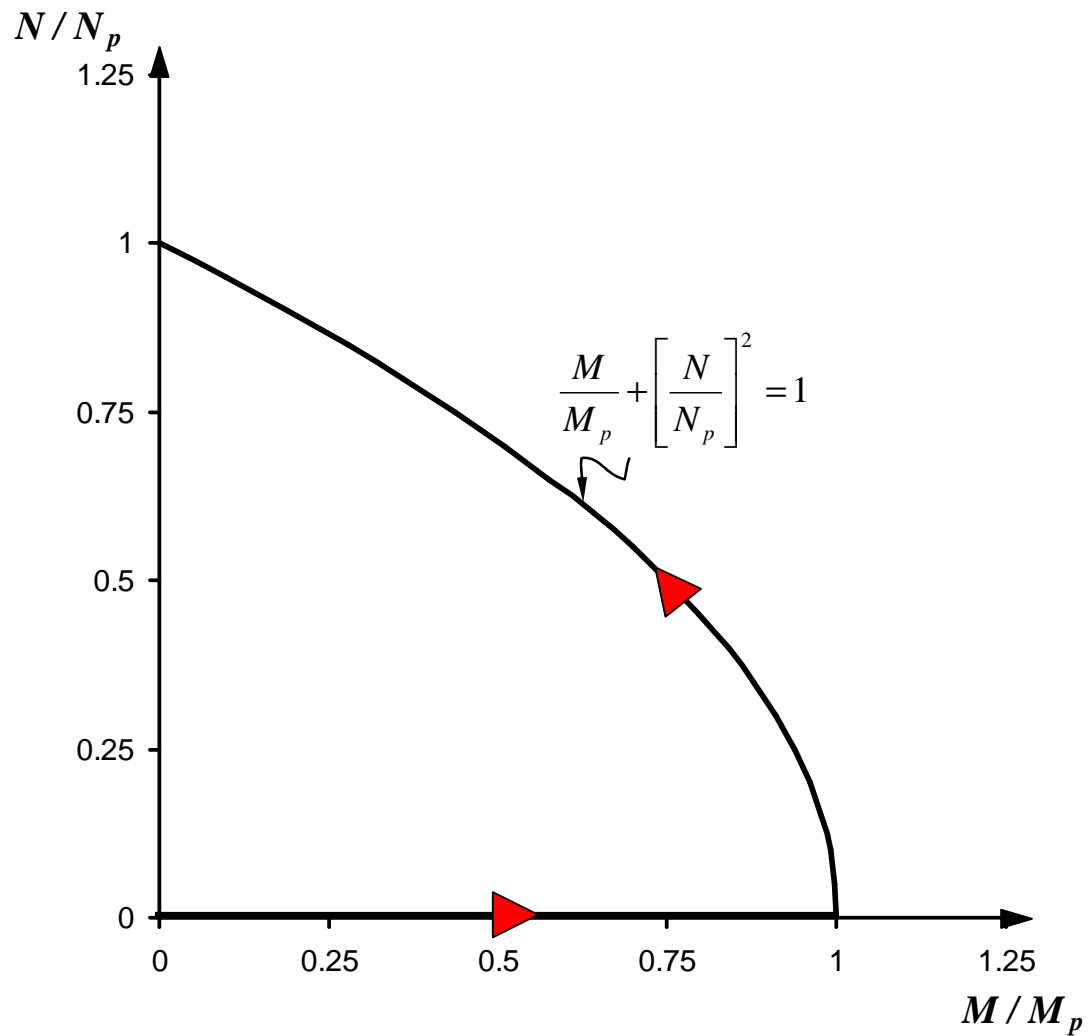


**Figure 2-9** Yield Condition Relating  $M$  and  $N$  required for a Rectangular Cross-Section

When a flexural mechanism forms, transverse deflections result in an axial force,  $N$  and yielding is now controlled by combined  $M$  and  $N$ , as indicated in Figure 2-8. As transverse deflection increases, the plastic neutral axis keeps migrating upwards across the depth and yielding follows the path shown in Figure 2-9 until it is dominated purely by  $N$ .



## 2.4.4 Equilibrium Equations

Under finite displacements, governing equilibrium equations need to be written on the deformed configuration. Jones (1989) illustrates the infinitesimal free body of a beam under generalized transverse loads as shown in Figure 2-10.

Horizontal equilibrium requires:

$$\frac{dN}{dx} = 0 \quad [2.6]$$

which means that membrane force  $N$  is constant throughout the beam

Moment equilibrium requires:

$$\frac{dM}{dx} = Q \quad [2.7]$$

Transverse equilibrium requires:

$$\frac{dQ}{dx} + d(Ndw/dx)/dx + q = 0 \quad [2.8]$$

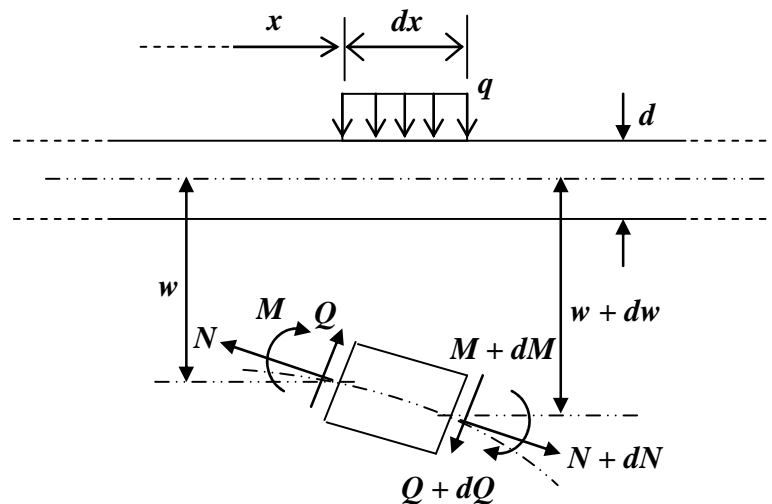


**Figure 2-10** Element of a beam subjected to loads which produce finite transverse displacements (Jones 1989)

By careful inspection, it can be shown the equations above as derived by Jones (1989) assume the following:

- $\sin \theta = 0, \cos \theta = 1$  for horizontal and moment equilibrium
- $\sin \theta = \theta, \cos \theta = 1$  for vertical equilibrium

#### 2.4.5 Deflected Shape Configuration

The deflected shape (Figure 2-7) can be represented as a function of  $x$  using:

$$w = W \left( 1 - \frac{x}{L} \right) \quad [2.9]$$

The change in length in the longitudinal axis of the beam,  $\Delta L$  is given as:

$$\Delta L = 2 \cdot \left[ \left( L^2 + W^2 \right)^{1/2} - L \right] \quad [2.10]$$

The corresponding axial strain,  $\varepsilon$  over a single plastic hinge of length,  $l$  at midspan is given as:

$$\varepsilon = 2L \left[ \left( 1 + \frac{W^2}{L^2} \right)^{1/2} - 1 \right] / l \quad [2.11]$$

Expanding the Equation 2.11 using the binomial theorem and neglecting powers

of  $\left( \frac{W}{L} \right)^2$  greater than two, results in:

$$\varepsilon \cong \left( \frac{W}{L} \right)^2 \left( \frac{L}{l} \right) \quad [2.12]$$

Then, the axial strain rate,  $\dot{\varepsilon}$ , the first derivative of Equation 2.12 with respect to time, is given as:

$$\dot{\varepsilon} = \frac{2W\dot{W}}{L \cdot l} \quad [2.13]$$

Secondly, the change in angle over a midspan plastic hinge length of  $l$ , the associated curvature rate,  $\dot{\kappa}$  is given as:

$$\dot{\kappa} = \frac{2\dot{W}}{L \cdot l} \quad [2.14]$$

From the Equations 2-13 and 2.14 it can be shown that

$$\dot{\varepsilon} / \dot{\kappa} = W \quad [2.15]$$

#### 2.4.6 Load–Deflection

With the use of the previously presented concepts and associated derivations, expressions for internal forces and external load versus deflection of the beam shown in Figure 2-7 can be derived. A stepwise presentation of the procedure and resulting graphical illustration of behavior will also be provided.

Expressions for internal forces ( $M$  and  $N$ ) and then external force ( $P$ ) as a function of transverse deflection,  $W$  will be derived. Once the expressions for  $M$  and  $N$  are obtained, substitution of these equations into the yield condition defined in Equation 2.5 results in normalized load carrying capacity ( $P / P_c$ ) as a function of  $W$ , where  $P_c$  is the plastic collapse load.

- Expressions for axial force,  $N$ :

Axial forces are derived with use of the deflected shape configuration (Figure 2-7) as well as a stress / strain profile illustrated over the depth of rectangular cross-section (Figure 2-8). It is evident from Figure 2-8(f):

$$\frac{N}{N_p} = 2\eta - 1 \quad [2.16]$$

where,

$$N_p = \sigma_y \cdot b \cdot d \quad [2.17]$$

Figure 2-8(g) suggests:

$$\dot{\varepsilon} = \dot{\kappa}(\eta d - d/2) \quad \text{or} \quad \dot{\varepsilon}/\dot{\kappa} = (2\eta - 1)\frac{d}{2} \quad [2.18]$$

where  $\dot{\varepsilon}$ , is the axial strain rate at the centroidal axis and associated  $\dot{\kappa}$  is the curvature rate.

Substituting Equation 2.16 into 2.18 yields:

$$\dot{\varepsilon}/\dot{\kappa} = \left(\frac{d}{2}\right)\left(\frac{N}{N_p}\right) \quad [2.19]$$

which, when combined with Equation 2.15, gives:

$$\frac{N}{N_p} = \frac{2W}{d} \quad \text{for} \quad 0 \leq W \leq \frac{d}{2} \quad [2.20]$$

Equation 2.20 indicates that at zero deflection, the axial force  $N$  is zero. As the beam deflects, plastic flow begins at Point A ( $M=M_p$ ) shown in Figure 2-11 and goes through the yield curve until it reaches to the fully plastic phase where  $N = N_p$  at a deflection of  $W = d/2$  (Point C). Therefore:

$$\frac{N}{N_p} = 1 \quad \text{for} \quad W \geq \frac{d}{2} \quad [2.21]$$

The solid arrows shown in Figure 2-11 represent the generalized strain rate vector which is normal to the yield surface due to the normality requirement of plasticity. At

point C, Equation 2-15 still controls the behavior and the generalized strain vector rotates toward the N-axis as  $W$  increases beyond  $d / 2$  (Jones 1989).

- Expressions for bending Moment,  $M$ :

Bending moment is derived with use of the equilibrium equations presented in Section 2.4.4. The governing equation for the beam shown in Figure 2-7 is obtained by substituting Equation 2.7 into 2.8 with  $q = 0$ :

$$\frac{d^2 M}{dx^2} + \left( \frac{dN}{dx} \right) \cdot \left( \frac{dw}{dx} \right) + N \cdot \frac{d^2 w}{dx^2} = 0 \quad [2.22]$$

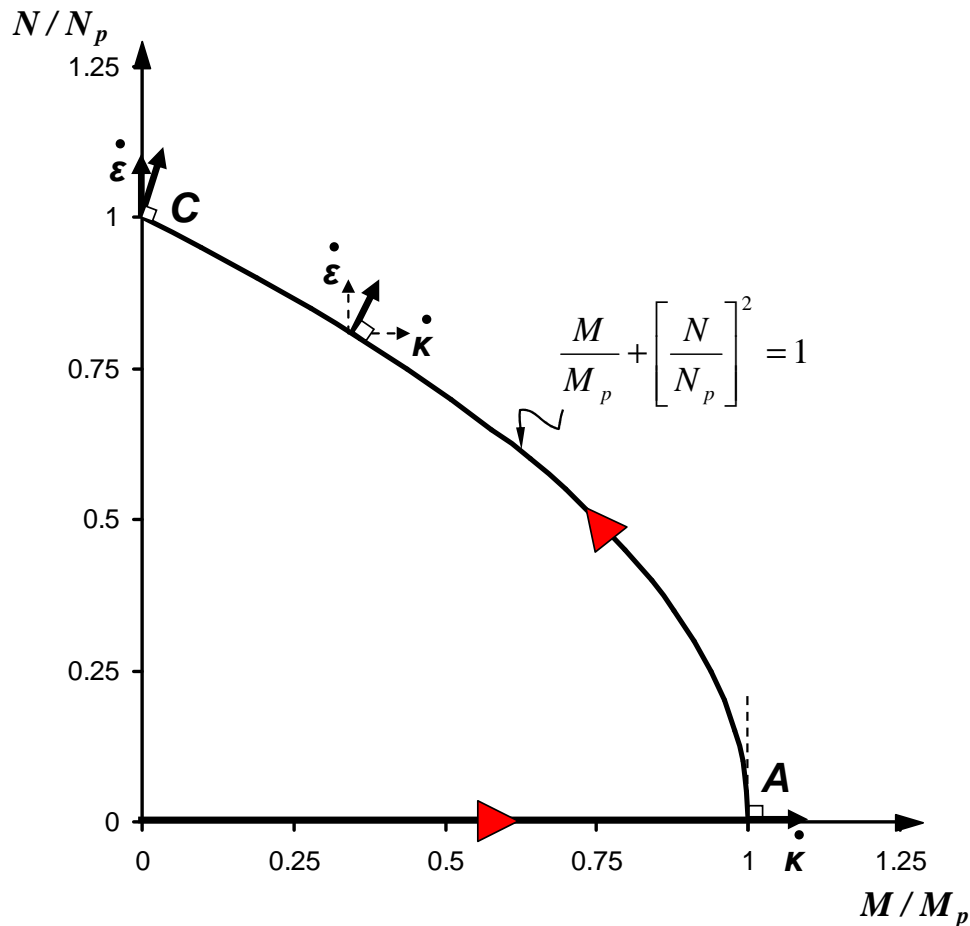


**Figure 2-11** Plastic flow of a rigid-perfectly plastic beam with rectangular cross-

section (Jones 1989)

Recall, Equation 2.9 suggested that the deflected shape expression is a linear function of  $x$ , it follows that the second derivative of  $w$  with respect to  $x$  is zero. In addition, Equation 2.6 suggested that  $N$  is constant along the length. Thus, Equation 2.22 becomes:

$$\frac{d^2 M}{dx^2} = 0 \quad [2.23]$$

By successive integration of Equation 2.23, it follows that:

$$M(x) = Ax + B \quad [2.24]$$

where  $A$  and  $B$  are integration constants. Considering only half of the beam in Figure 2-7 (i.e.  $0 \leq x \leq L$ ) and since  $M = 0$  at the supports, then:

$$M(x) = A \cdot (x - L) \quad [2.25]$$

Now, considering vertical equilibrium at midspan (at  $x = 0$ ), the vertical load  $P$  is resisted by the vertical components of  $N$  and  $Q$ :

$$\frac{P}{2} = -Q \cdot \cos\left(\frac{dw}{dx}\right) - N \cdot \sin\left(\frac{dw}{dx}\right) \quad [2.26]$$

For  $\sin(\theta) = \theta$ ,  $\cos(\theta) = 1$

$$\frac{P}{2} \cong -\frac{dM}{dx} - N \cdot \frac{dw}{dx} \quad [2.27]$$

Equations 2.9 and 2.25 predict that  $\frac{dw}{dx} = \frac{-W}{L}$  and  $\frac{dM}{dx} = A$  respectively, thus:

$$A = \frac{NW}{L} - \frac{P}{2} \quad [2.28]$$

Then, the moment equation becomes:

$$M(x) = \left(\frac{NW}{L} - \frac{P}{2}\right)(x - L) \quad [2.29]$$

At  $x = 0$ ,

$$M = \left(\frac{P}{2} - \frac{NW}{L}\right)L \quad [2.30]$$

Normalizing Equation 2.30 by the plastic moment,  $M_p$ , and eliminating  $N$  with Equation 2.20, gives:

$$\frac{M}{M_p} = \frac{P \cdot L}{2M_p} - \frac{2 \cdot N_p \cdot W^2}{d \cdot M_p} \quad \text{for } 0 \leq W \leq \frac{d}{2} \quad [2.31]$$

▪ External Load,  $P$ :

Under combined bending and axial load, the external load,  $P$  is simply derived with substitution of the previously obtained  $M$  and  $N$  equations as given in Equations 2.20 and 2.31, respectively, into yield condition (Equation 2.5). Thus:

$$\frac{P}{P_c} = 1 + \frac{4W^2}{d^2} \quad \left(0 \leq W \leq \frac{d}{2}\right) \quad [2.32]$$

where  $P_c = \frac{2M_p}{L}$

For transverse deflections  $W$  beyond  $d/2$ , Equation 2.20 suggests that the beam has reached the fully plastic phase ( $N = N_p$ ) and the applied load is resisted by only plastic axial loads as illustrated in Figure 2-12. Therefore, vertical equilibrium  $\sum F_y = 0$  requires:

$$P - 2 \cdot N_p \cdot \sin \theta = 0 \quad [2.33]$$

For  $\sin \theta = \theta = \frac{W}{L}$ , then,

$$P = \frac{2 \cdot N_p \cdot W}{L}. \quad [2.34]$$

Normalizing by  $P_c$  and rearranging yields:

$$\frac{P}{P_c} = \frac{4 \cdot W}{d} \quad (W \geq \frac{d}{2}) \quad [2.35]$$

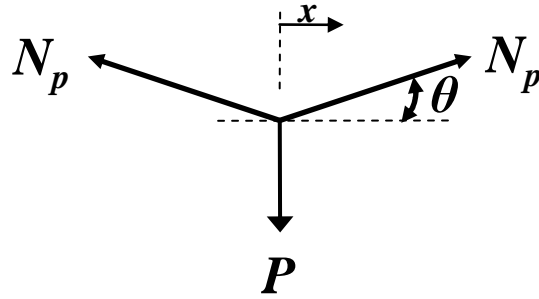


**Figure 2-12** Forces at Midspan ( $x=0$ ) at Fully Plastic Phase

In conclusion, as can be seen in Figure 2-13, the beam reaches the fully plastic axial state at a deflection of one-half of the beam thickness at an external load of twice the plastic collapse load,  $P_c$  (Jones 1989).



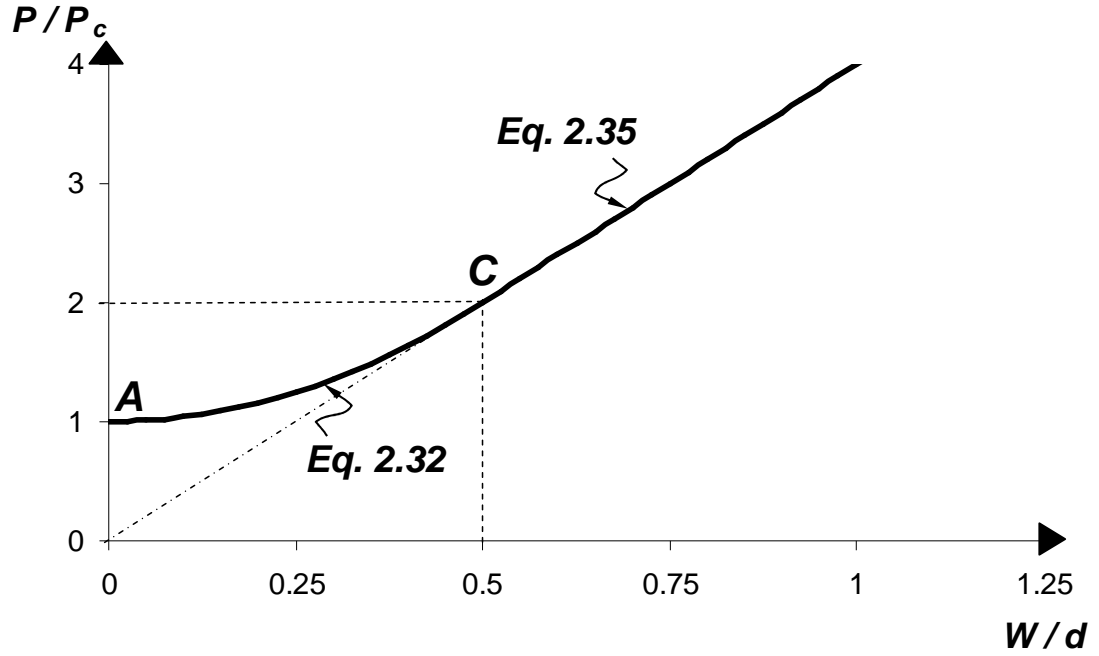


**Figure 2-13** Normalized Load–Deflection curve for simple beam with a rectangular cross-section (Jones 1989)

A similar procedure was conducted for a fully fixed beam subjected to a concentrated load at midspan by Haythornthwaite (1959) and results showed that:

$$\frac{P}{P_c} = 1 + \frac{W^2}{d^2} \quad (0 \leq W \leq d) \quad [2.36]$$

$$\frac{P}{P_c} = \frac{2 \cdot W}{d} \quad (W \geq d) \quad [2.37]$$

where  $P_c = \frac{4M_p}{L}$

## **Chapter 3. THEORETICAL MODELS**

### **3.1 Overview and Scope**

In this chapter, the fundamental behavior of ductile steel beams with idealized boundary conditions due to finite displacements is presented. The ability of a beam to carry loads by transitioning from a flexural mechanism to a cable-like mechanism will be described. Two different theoretical models are developed: rigid-plastic beam model, which is developed in a manner similar to that described by Jones (1989) as reviewed in Section 2.4, and cable analysis, which reflects a special case of resisting the loads only by means of axial forces developed on the member, like a cable.

Two load cases are considered: a concentrated load at midspan and uniformly distributed load along the length. The theories are presented in such a way that load-deflection characteristics of each case are described in a graphical manner, which is obtained with use of a common flow of derivations.

Fully ductile behavior is assumed and stability issues are not considered throughout this section.

### **3.2 Rigid-Plastic Analysis**

Rigid-perfectly plastic behavior of beams was presented in section 2.4 along with other important concepts used in the procedure. Therefore, all assumptions made therein are valid in the development of this section.

Theoretical results for W-shaped beams will be presented. Therefore, an interaction relationship between bending moment,  $M$  and axial force,  $N$  on the cross-sectional level for a W-shape needs to be introduced. A similar procedure to that used for rectangular sections (as presented in Chapter 2) is given. In this case, the  $M$ - $N$  interaction relationship depends upon the plastic neutral axis (PNA) location as illustrated in Figure 3-1 for positive  $M$  and  $N$ . The interaction equations are given as (Horne 1979):

- When the plastic neutral axis is in the web,

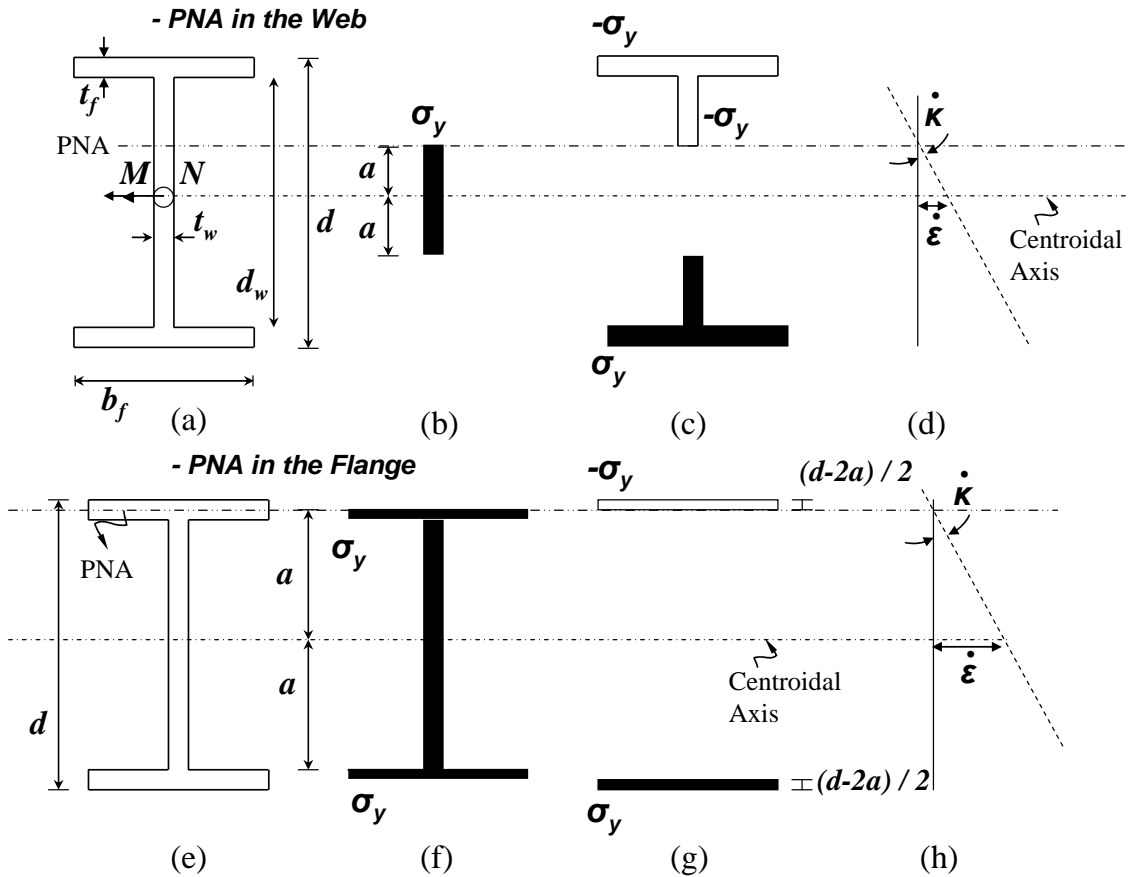
$$\frac{M}{M_p} = 1 - \left[ \frac{N}{N_p} \right]^2 \frac{A^2}{4t_w Z_x} \quad M, N \geq 0 \quad [3.1]$$

- When the plastic neutral axis is in the flange,

$$\frac{M}{M_p} = \left( 1 - \frac{N}{N_p} \right) \cdot \left[ 1 - \left( 1 - \frac{N}{N_p} \right) \frac{A}{2b_f d} \right] \cdot \frac{Ad}{2Z_x} \quad M, N \geq 0 \quad [3.2]$$

where  $M_p$  and  $N_p$  are the plastic moment and plastic axial force, respectively. Other cross-sectional properties can be found in Appendix A.

Equations 3.1 and 3.2 are graphically represented in Figure 3-2 for a W30x124. In this figure,  $M_{pf}$  represents the plastic bending moment calculated using the flanges only (about major axis) and  $N_{pw}$  represents the plastic axial force calculated using the web only. Equation 3.1 is valid between points A and B. Equation 3.2 is valid between points B and C. At Point A, the PNA is at the centroid of the cross-section. At Point B, the PNA is at the interface between web and the flange. At Point C, the PNA can be at or beyond the top of the cross-section.



- (a), (e) Cross-Section (*AISC* notations are used and fillets neglected)
  - (b), (f) Stress distributions associated with  $N$
  - (c), (g) Stress distributions associated with  $M$
  - (d), (h) Strain profile when the neutral axis is in the web and flange respectively
- $\sigma_y$  is the yield stress and  $a$  is the distance between PNA and centroidal axis

**Figure 3-1** Stress distributions in the cross-section based on the location of neutral axis  
(Horne, 1979)

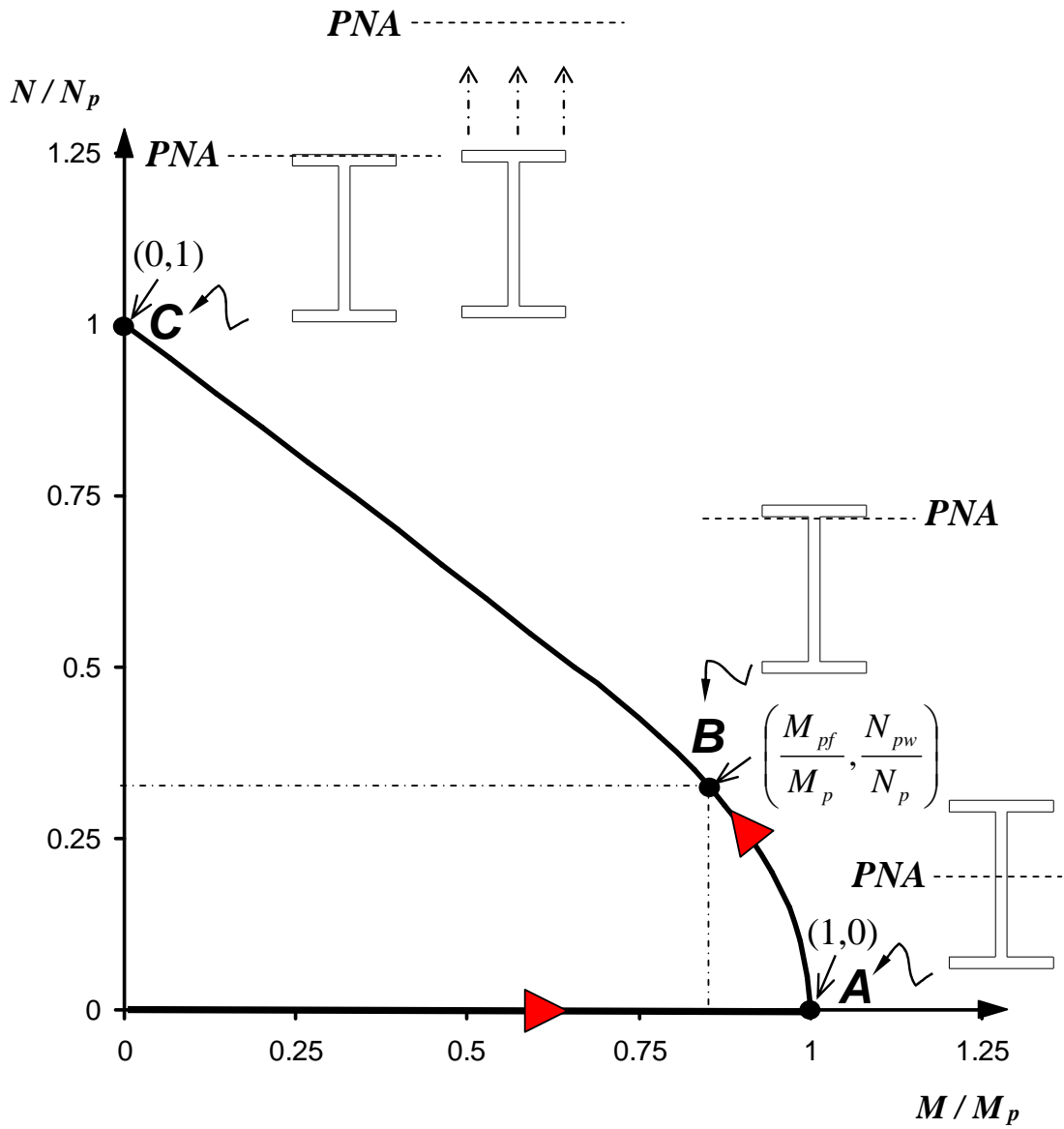


**Figure 3-2**  $M-N$  interaction for W-Shapes (W30x124)

### 3.2.1 Simply Supported Beam with a Concentrated Load at Midspan

The load–deflection characteristics of a rigid–perfectly plastic simple beam with W–shape cross–section (Figure 3-3) can be derived with use of a procedure similar to that described in section 2.4. Expressions for internal forces and external loads throughout the deformation are derived, and then a graphical representation of overall behavior is provided.

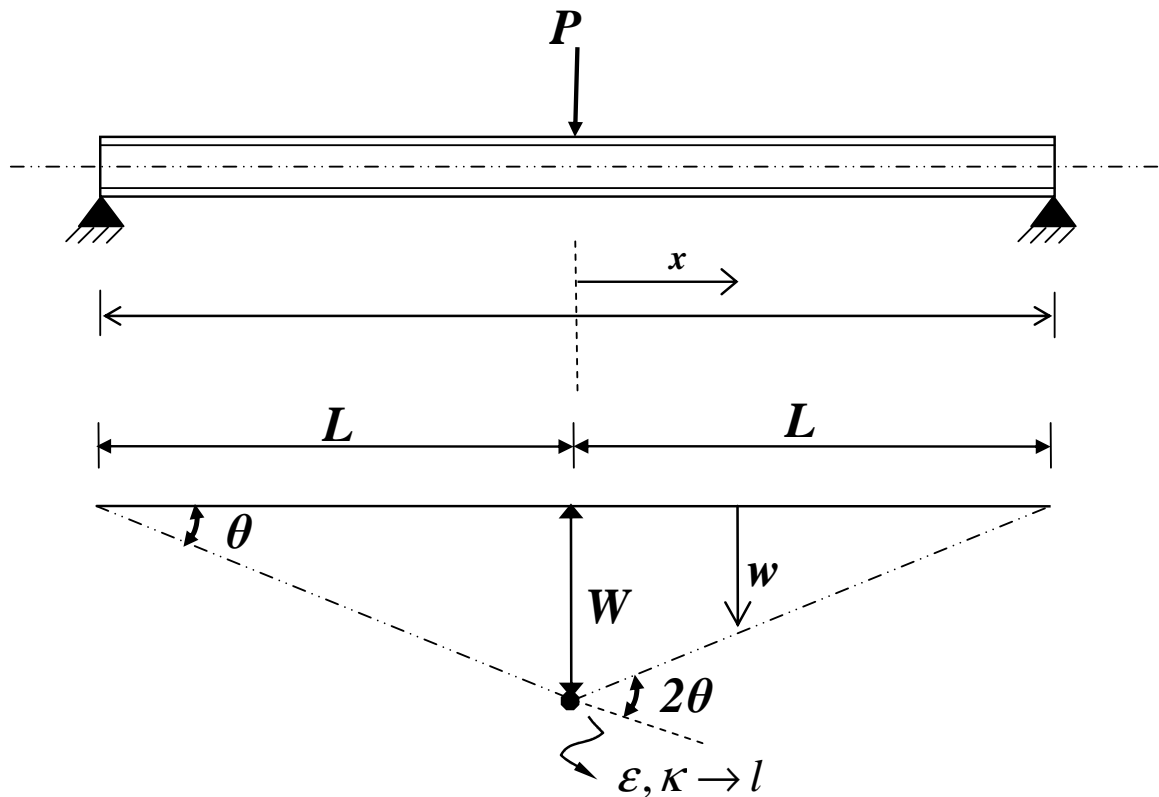


**Figure 3-3** W–Shaped Rigid–Plastic Simple Beam with a Concentrated load at Midspan

- Axial Force,  $N$ :

Once the mechanism condition is reached as shown in Figure 3-3; finite transverse deflection,  $W$  results in development of axial forces,  $N$ . It is evident from

Figure 3-2(d) and (h) that regardless of the PNA location, the ratio of generalized deformation rates is:

$$\dot{\varepsilon} / \dot{\kappa} = a \quad [3.3]$$

When the neutral axis is in the web, it can be seen from Figure 3-2(b) that:

$$N = 2 \cdot a \cdot t_w \cdot \sigma_y \quad [3.4]$$

Thus,

$$\frac{N}{N_p} = \frac{2 \cdot a \cdot t_w}{A} \quad [3.5]$$

where  $N_p = \sigma_y \cdot A$ .

It is noted that the development of the ratio  $\dot{\varepsilon} / \dot{\kappa}$  in Section 2.4 was independent of the cross-section considered. Thus, Equation 2.15 is still valid, therefore Equation 3.3 becomes:

$$a = W \quad [3.6]$$

Substituting  $a$  into Equation 3.5 gives:

$$\frac{N}{N_p} = \frac{2 \cdot W \cdot t_w}{A} \quad [3.7]$$

For the special case when the PNA is at the interface between the web and the flange:

$$N = N_{pw} = \sigma_y \cdot A_w \quad [3.8]$$

Substituting Equation 3.8 into Equation 3.7 and solving for  $W$  gives:

$$W = \frac{A_w}{2 \cdot t_w} = \frac{d_w}{2} \quad [3.9]$$

Equation 3.9 suggests that the PNA moves into the flange for deflections beyond  $\frac{d_w}{2}$ . As

a result, Equation 3.9 is valid for  $0 \leq W \leq \frac{d_w}{2}$ .

When the PNA is in the flange, it can be seen from Figure 3-3(f):

$$N = [A - (d - 2 \cdot a) \cdot b_f] \cdot \sigma_y \quad [3.10]$$

and it follows that:

$$\frac{N}{N_p} = 1 - \frac{[d - 2 \cdot a]}{A} \cdot b_f. \quad [3.11]$$

Substitution of Equation 3.6 into Equation 3.11 gives:

$$\frac{N}{N_p} = 1 - \frac{[d - 2 \cdot W]}{A} \cdot b_f. \quad [3.12]$$

Equation 3.12 suggests that the fully plastic cable state (i.e.,  $N = N_p$ ) is reached

when the second term is zero so that  $W = \frac{d}{2}$ . As a result, Equation 3.12 is valid in the

range of  $\frac{d_w}{2} \leq W \leq \frac{d}{2}$ .

For a pure cable state, Equation 3.12 also suggests that the beam sustains  $N_p$  for deflections beyond  $\frac{d}{2}$ . Thus, the axial force expression can simply be given as:

$$\frac{N}{N_p} = 1 \quad \text{for} \quad \frac{W}{d} \geq \frac{1}{2} \quad [3.13]$$

A plot of  $N/N_p$  versus  $W/d$  is provided in Figure 3-4.

- Bending moment,  $M$ :



Bending moment as a function of transverse deflection,  $W$ , can simply be obtained by substituting the axial force expressions obtained for the two different locations of the PNA indicated earlier into the interaction equations. Thus, when the PNA is in the web, substituting Equation 3.7 into 3.1 gives:

$$\frac{M}{M_p} = 1 - \frac{W^2 \cdot t_w}{Z_x} \quad \text{for} \quad 0 \leq W \leq \frac{d_w}{2} \quad [3.14]$$

and when the PNA is in the flange, substituting Equation 3.12 into 3.2 gives:

$$\frac{M}{M_p} = \frac{(d^2 - 4W^2)}{4Z_x} \cdot b_f \quad \text{for} \quad \frac{d_w}{2} \leq W \leq \frac{d}{2} \quad [3.15]$$

and finally for pure cable state:

$$\frac{M}{M_p} = 0 \quad \text{for} \quad W \geq \frac{d}{2} \quad [3.16]$$

Similarly, a plot of  $M/M_p$  versus  $W/d$  is provided in Figure 3-5.

- External Force,  $P$ :

External load derivation was carried out with substitution of internal forces  $M$  and  $N$  into the corresponding yield condition, as was reviewed in Section 2.4. Bending moment,  $M$  was obtained based on vertical equilibrium at midspan (Equations 2.23 through 2.31). A similar procedure is used to relate bending moment,  $M$  to external load,  $P$  and axial force,  $N$ , to finally obtain the external load,  $P$  as a function of  $W$ . Thus, when the PNA is in the web, substituting Equation 3.7 into Equation 2.29 at  $x=0$  gives:

$$M = \left( \frac{P}{2} - \frac{2 \cdot W^2 \cdot t_w \cdot N_p}{A \cdot L} \right) L \quad [3.17]$$

Now, substituting Equation 3.17 and 3.7 into 3.1, the external load expression is given as:

$$\frac{P}{P_c} = 1 + \frac{W^2 t_w}{Z_x} \quad \text{for} \quad 0 \leq W \leq \frac{d_w}{2} \quad [3.18]$$

where  $P_c = \frac{2 \cdot M_p}{L}$ .

When the PNA is in the flange, substituting Equation 3.12 into Equation 2.30 gives:

$$M = \left( \frac{P \cdot L}{2} - \left[ N_p - \frac{(d - 2W) \cdot b_f \cdot N_p}{A} \right] \cdot W \right) \quad [3.19]$$

Similarly, substituting Equation 3.19 and 3.12 into the yield condition given in Equation 3.2, gives:

$$\frac{P}{P_c} = \frac{1}{Z_x} \left[ \left( \frac{d - 2W}{2} \right)^2 \cdot b_f + AW \right] \quad \text{for} \quad \frac{d_w}{2} \leq W \leq \frac{d}{2} \quad [3.20]$$

where again  $P_c = \frac{2 \cdot M_p}{L}$ .

For the pure cable state, with use of vertical equilibrium of forces shown in Figure 2-12, it can be shown that:

$$\frac{P}{P_c} = \frac{A \cdot W}{Z_x} \quad \text{for} \quad W \geq \frac{d}{2} \quad [3.21]$$

with  $P_c = \frac{2 \cdot M_p}{L}$ .

The theoretical progression of behavior of a simply supported, centrally loaded, rigid-perfectly plastic beam having a W-Shape cross-section is depicted in Figures 3-4 through 3-7. Figure 3-4 displays a plot of normalized axial force versus normalized deflection at midspan. Figures 3-5 shows normalized bending moment with respect to

midspan deflection,  $W$ . Figure 3-6 represents the corresponding  $M$ - $N$  interaction at the midspan section and finally the relationship of the external load,  $P$  with respect to transverse deflection is given in Figure 3-7. Three characteristic points are indicated in the figures: A, B and C. Point A represents the onset of the formation of a flexural mechanism ( $N=0$  and  $M=M_p$  at midspan). As the beam deflects, plastic flow follows the path as shown in Figure 3-6 and the generalized strain vector remains perpendicular to the yield condition. Due to finite displacements, the beam develops axial forces and the PNA starts to migrate upwards away from the centroid as indicated in Figure 3-6. Then, axial force,  $N$ , increases linearly and bending moment,  $M$ , drops quadratically with  $W$  until Point B is reached, which represents the special level of deflection of  $W = d_w / 2$ , as shown in Figures 3-4 and 3-5, respectively. At this point, the PNA is at the interface of the web and the flange as shown in Figure 3-6. Beyond Point B,  $N$  continues to increase linearly whereas  $M$  decreases quadratically with  $W$  at a much faster rate than before Point B. Eventually, the pure cable state is reached (Point C) when the deflection is half as much as the nominal depth of the beam,  $\frac{d}{2}$  ( $N=N_p$  and  $M=0$ ). Beyond this point, external load,  $P$ , is resisted by plastic axial force,  $N_p$ , alone with a cable-like action thus the generalized strain vector rotates towards the  $N$ -axis as the PNA moves away from the cross-section, as shown in Figure 3-6.

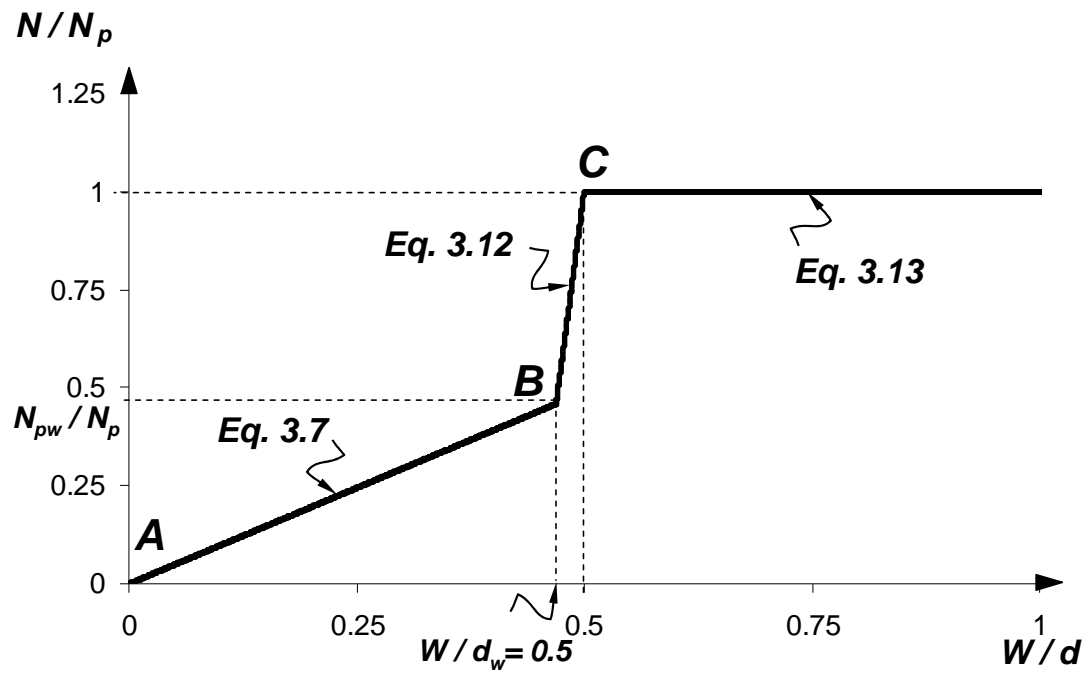


**Figure 3-4** Normalized Axial Force–Deflection Relationship (Midspan)

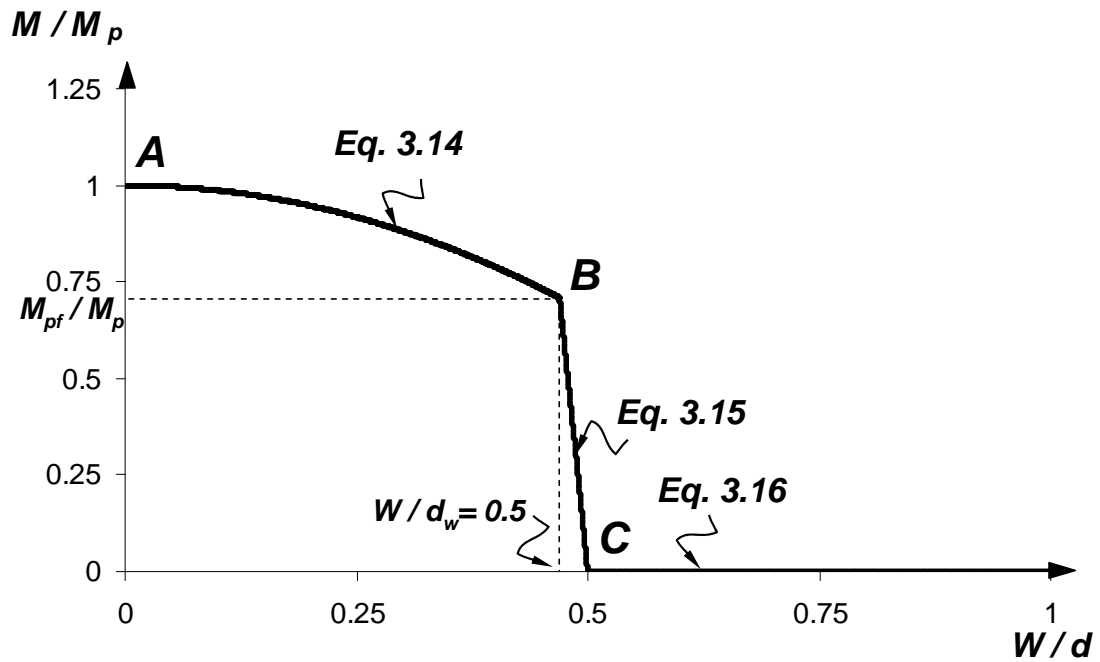


**Figure 3-5** Normalized Moment–Deflection Relationship (Midspan)

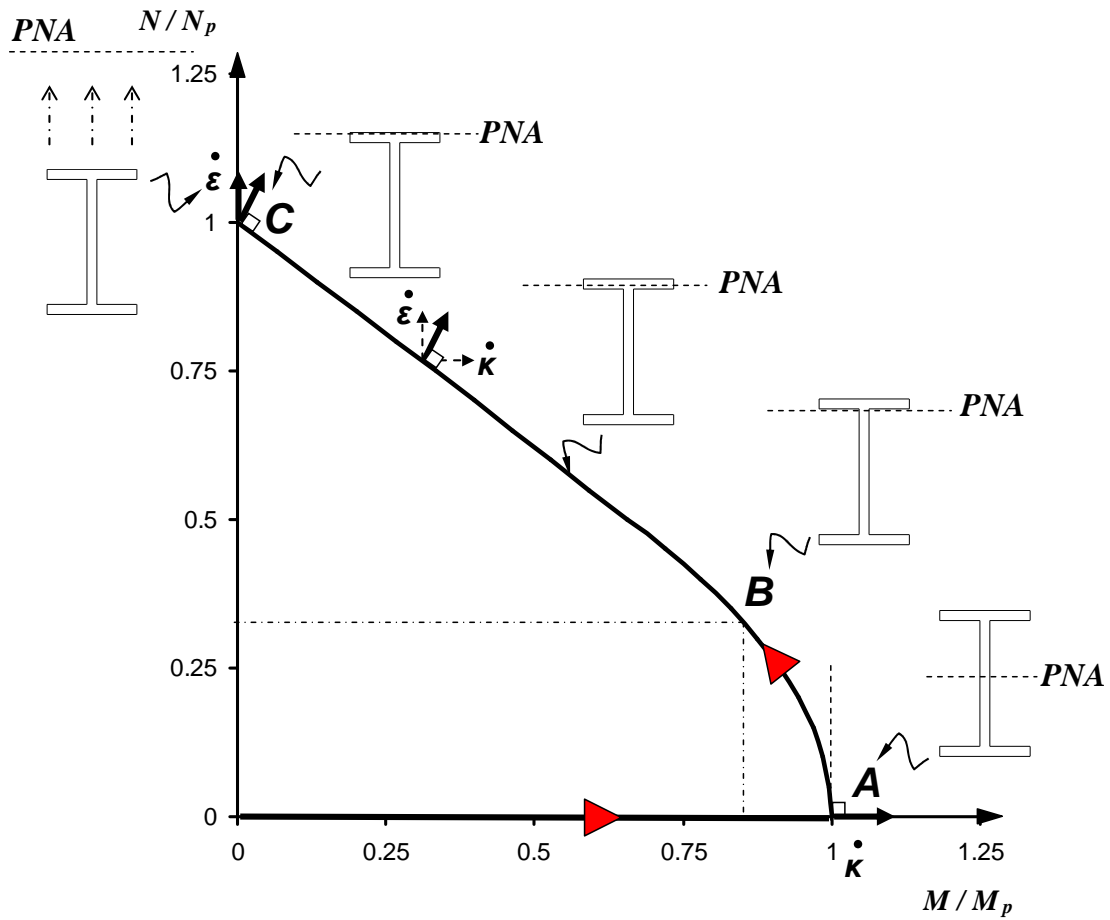


**Figure 3-6** Normalized  $M-N$  interaction for W-Shape cross-section (Midspan)

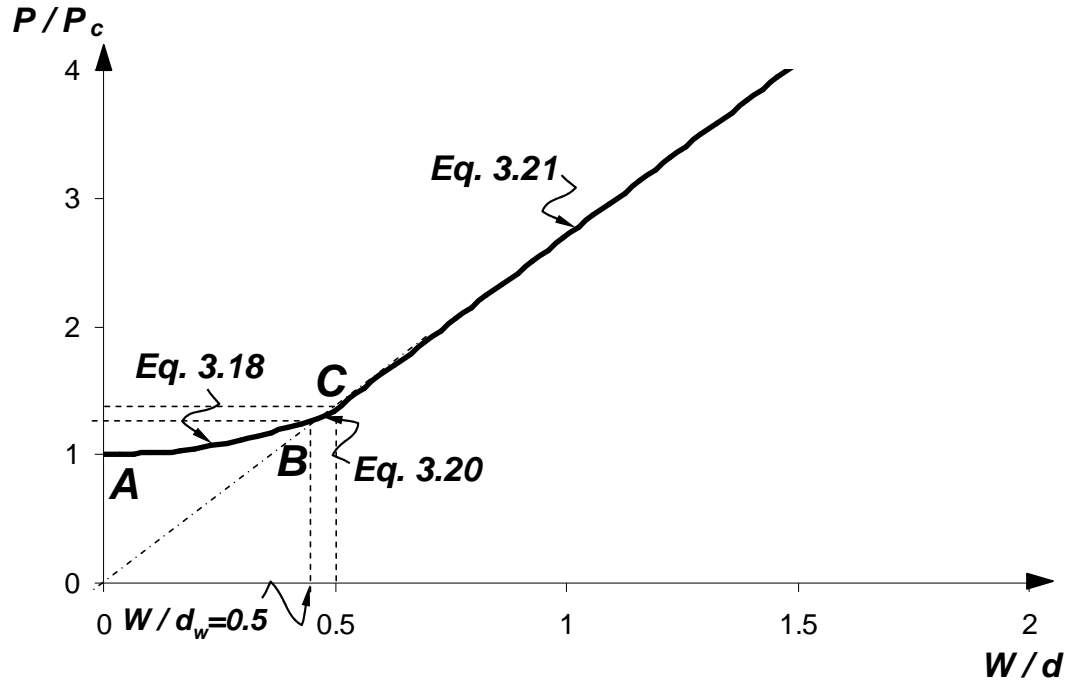


**Figure 3-7** Normalized Load–Deflection Relationship

### 3.2.2 Fully Fixed Beam with a Concentrated Load at Midspan

Similar theoretical steps to those described for a simply supported beam can be carried out for a fully fixed beam (Figure 3-8 (a)) that has a W-Shape cross-section subjected to a concentrated load at midspan. Figure 3-8 (b) illustrates the deflected shape configuration. In this case, three plastic hinges form simultaneously, one at midspan and one at each support once the flexural mechanism condition is reached. As a result, the average strain over midspan plastic hinge length,  $l$ , is given as:

$$\varepsilon = 2L \left[ \left( 1 + \frac{W^2}{L^2} \right)^{1/2} - 1 \right] / 2l \quad [3.22]$$

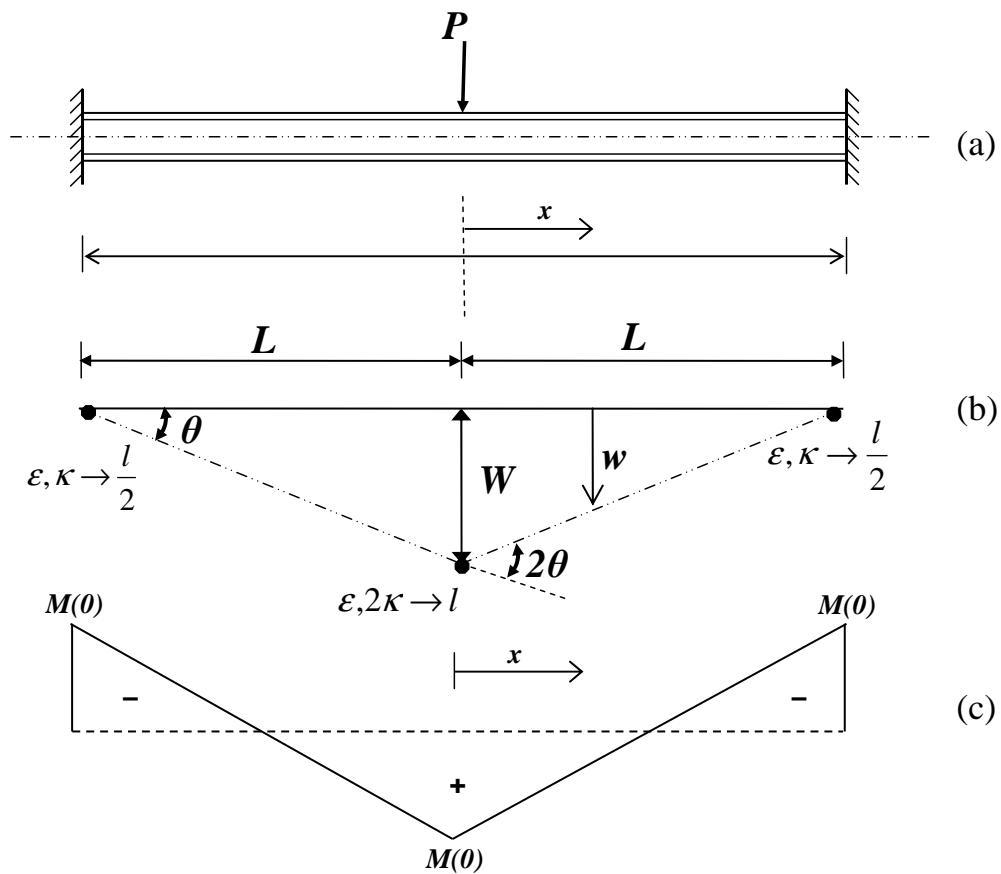
With the aid of binomial series expression, and neglecting powers of  $\left(\frac{W}{L}\right)^2$  greater than

two, gives:

$$\varepsilon \cong \left(\frac{W}{L}\right)^2 \left(\frac{L}{2l}\right) \quad [3.23]$$

Thus, the strain rate becomes:

$$\dot{\varepsilon} = \frac{W\dot{W}}{L \cdot l} \quad [3.24]$$



(a) Beam

(b) Deflected shape configuration

(c) Statically admissible moment diagram

**Figure 3-8** Centrally loaded, fully fixed beam with W-Shape cross-section

On the other hand, the change in angle over the midspan plastic hinge length,  $l$ , gives curvature as:

$$\kappa = \frac{2W}{L \cdot l} \quad [3.25]$$

thus the curvature rate becomes:

$$\dot{\kappa} = \frac{2W \dot{W}}{L \cdot l} \quad [3.26]$$

From Equations 3.24 and 3.26, it follows that:

$$\dot{\varepsilon} / \dot{\kappa} = \frac{W}{2} \quad [3.27]$$

Now, internal load – deflection characteristics can be identified.

- Axial Force,  $N$ :

Equation 3.3 suggests that  $\dot{\varepsilon} / \dot{\kappa} = a = \frac{W}{2}$  regardless of the location of the PNA.

Thus, Equations 3.5 and 3.11 give the following expressions respectively, when the PNA is in the web, and when it is in the flange:

$$\frac{N}{N_p} = \frac{W \cdot t_w}{A} \quad [3.28]$$

$$\frac{N}{N_p} = 1 - \frac{[d - W]}{A} \cdot b_f \quad [3.29]$$

For the special case when the PNA is at the interface between web and the flange:

$$N = N_{pw} = A_w \cdot \sigma_y \quad [3.30]$$



Substituting Equation 3.30 into Equation 3.28 and solving for  $W$  gives:

$$W = d_w$$

Solving Equation 3.29 for  $N = N_p$  (i.e. pure cable state):

$$W = d$$

As a result, Equation 3.28 is valid for  $0 \leq W \leq d_w$ , whereas Equation 3.29 is valid for

$d_w \leq W \leq d$  and suggests that the beam reaches a pure cable state when  $W = d$ .

Eventually at the pure cable state, the beam sustains  $N_p$ , and therefore:

$$\frac{N}{N_p} = 1 \quad \text{for} \quad W \geq d \quad [3.31]$$

- Bending moment,  $M$ :

Moment–deflection equations can be obtained by substitution of axial force expressions into their respective yield condition depending on the location of the PNA.

Thus, when the PNA is in the web, substituting Equation 3.28 into Equation 3.1 gives:

$$\frac{M}{M_p} = 1 - \frac{W^2 \cdot t_w}{4Z_x} \quad \text{for} \quad 0 \leq W \leq d_w \quad [3.32]$$

and when the PNA is in the flange, substituting Equation 3.29 into Equation 3.2 gives:

$$\frac{M}{M_p} = \frac{(d^2 - W^2)}{4Z_x} \cdot b_f \quad \text{for} \quad d_w \leq W \leq d \quad [3.33]$$

For pure cable state:

$$\frac{M}{M_p} = 0 \quad \text{for} \quad W \geq d \quad [3.34]$$

- External Force,  $P$ :

To use the procedure presented in Section 2.4 (Equations 2-23 through 2-31), a bending moment expression is needed to obtain the external force as a function of  $W$ . First, it is evident from Figure 3-8(c) that bending moment can be expressed as (considering one-half of the beam due to symmetry):

$$M(x) = Ax + B. \quad [3.35]$$

Using the boundary values to obtain the constants A and B, at  $x = 0$ :

$$M(0) = B \quad [3.36]$$

and at  $x = L$ :

$$-M(0) = A \cdot L + B \quad [3.37]$$

Solving Equations 3.36 and 3.37 simultaneously, gives:

$$A = \frac{-2M(0)}{L}$$

Thus, the resulting moment expression as a function of  $x$  is given as:

$$M(x) = M(0) \cdot \left[ \frac{-2x}{L} + 1 \right] \quad [3.38]$$

and

$$\frac{dM(x)}{dx} = -\frac{2M(0)}{L}. \quad [3.39]$$

Therefore, the equilibrium Equation 2.27, developed at midspan, becomes:

$$\frac{P}{2} = \frac{2M(0)}{L} + \frac{N \cdot W}{L}. \quad [3.40]$$

Solving for  $M(0)$  gives:

$$M(0) = \frac{P \cdot L}{4} - \frac{N \cdot W}{2}. \quad [3.41]$$

Now, substituting  $M(0)$  into Equation 3.38 gives the moment expression as:

$$M(x) = \left[ \frac{P \cdot L}{4} - \frac{N \cdot W}{2} \right] \cdot \left[ \frac{-2x}{L} + 1 \right]. \quad [3.42]$$

Now, external load expressions can be obtained depending on the location of the PNA as follows:

- When the PNA is in the web, substituting Equation 3.42 (at  $x = 0$ ) and Equation 3.28 into Equation 3.1 gives:

$$\frac{P}{P_c} = 1 + \frac{W^2 \cdot t_w}{4 \cdot Z_x} \quad \text{for } 0 \leq W \leq d_w. \quad [3.43]$$

- When the PNA is in the flange; substituting Equations 3.42 (at  $x = 0$ ) and 3.29 into 3.2 gives:

$$\frac{P}{P_c} = \frac{1}{Z_x} \left[ \left( \frac{d - W}{2} \right)^2 \cdot b_f + \frac{AW}{2} \right] \quad \text{for } d_w \leq W \leq d. \quad [3.44]$$

- For the pure cable state, using the vertical equilibrium of forces shown in Figure 2-12 gives:

$$\frac{P}{P_c} = \frac{A \cdot W}{2Z_x} \quad \text{for } W \geq d \quad [3.45]$$

where  $P_c = \frac{4 \cdot M_p}{L}$  in this case.

We can see that the fixed-fixed case resulted in the same form of equations as the simple beam case. However, twice as much deflection ( $W=d$ ) is needed to form the cable mechanism in this case.

This progression of events throughout the deflection of the beam is indicated in Figures 3-9 through 3-11. Figures 3-9 and 3-10 display, respectively, the plot of

normalized axial force,  $N$ , and bending moment,  $M$ , versus normalized deflection at midspan. Figure 3-11 displays the corresponding plot of normalized external load,  $P$ , versus normalized deflection at midspan. A rigid–perfectly plastic beam starts to deflect once three plastic hinges form at a load of  $P_c$  (indicated as Point A, the onset of formation of a flexural mechanism). When the transverse displacement  $W$  increases, the beam starts to develop axial forces  $N$  and the plastic neutral axis starts to move upwards along the web as depicted in Figure 3-6. As a result,  $M$  starts to drop (Figure 3-10) and yielding is now controlled by combined bending moment and axial force. When the PNA gets into the flange (Point B), moment starts to drop faster (Figure 3-10) and consequently, the axial force increases rapidly (Figure 3-9) until it purely dominates the behavior (Point C). This behavior between points B and C can be attributed to the fact that more area (wide flange) attracts more axial force during the distribution of yielding across the cross–section. Eventually, the beam reaches a cable state (Point C, where  $N = N_p$ ).

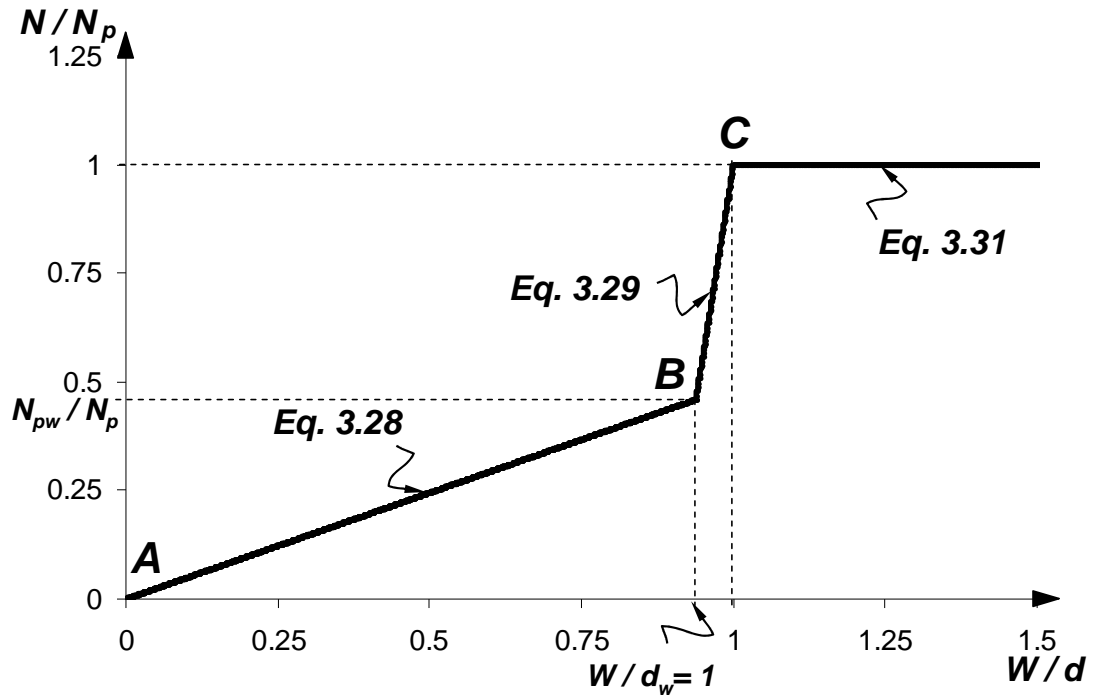


Figure 3-9 Normalized Axial Force-Deflection Relationship (Midspan)

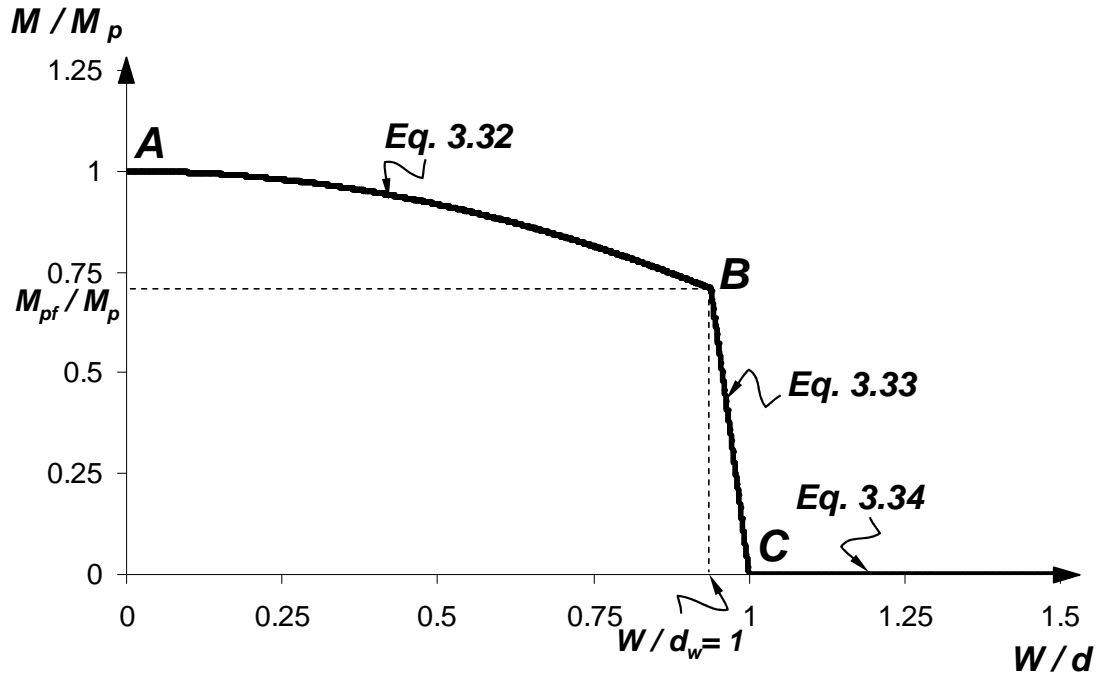
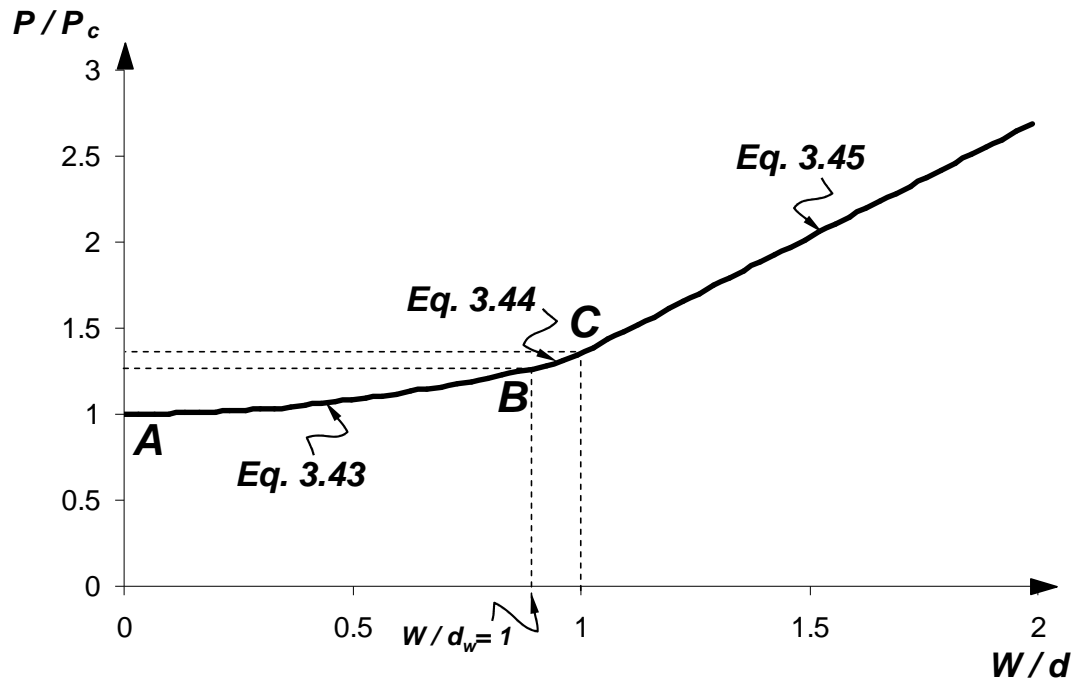


Figure 3-10 Normalized Moment-Deflection Relationship (Midspan)



**Figure 3-11** Normalized Force–Deflection Relationship (Midspan)

### 3.2.3 Fully Fixed Beam with Uniformly Distributed Load along the Length

Rigid–plastic behavior suggests that there is no deflection until the beam reaches a flexural mechanism condition. In this case, plastic hinges (at midspan and end sections) do not form simultaneously. As illustrated in Figure 3-12, it is evident from the theory of plasticity that two plastic hinges form at the supports first (Figure 3-12(a)), and the beam acts like a simple beam. Then, with formation of a midspan plastic hinge, the flexural mechanism condition is reached (Figure 3-12(b)). As the beam deflects further, the deflected shape can be anticipated to transition to a catenary–like shape towards the formation of pure cable action (Figure 3-12(c)).

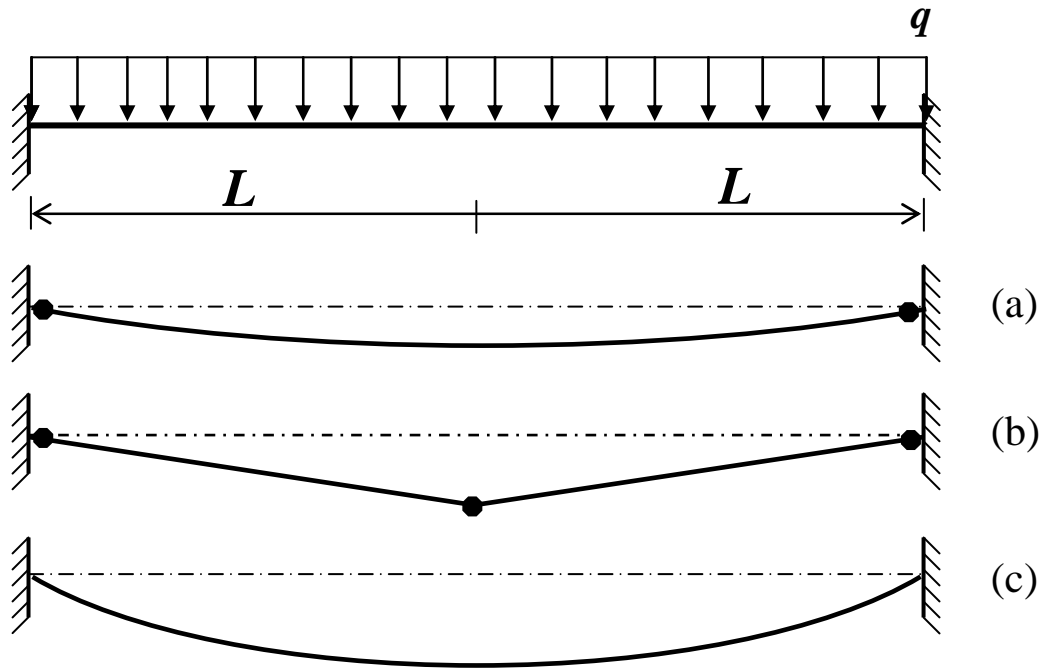


**Figure 3-12** Change in Deflected Shape Configuration Under Uniform Loading

The rigid–plastic analysis procedure presented in this study thus far has assumed a consistent deflected shape throughout the deformation. However, incorporating this deflected shape transition (as shown in Figure (3-12)) in the analysis may not be as straightforward. To implement this phenomenon, two different theories will be presented: Theory I, in which a triangular deflected shape is considered and Theory II, in which a parabolic deflected shape is considered throughout the deformation.

A similar procedure to that used for the concentrated load cases can be carried out. Theories for rectangular and W–Shaped beams are developed and presented next.

### 3.2.3.1 Beam with Rectangular Cross-Section

Using the yield condition provided under combined bending and axial force for rectangular a cross-section, a rigid-plastic analysis procedure is conducted for each theory.

#### 3.2.3.1.1 Theory I

Figure 3-13 illustrates the schematics of Theory I, including the deflected shape configuration and a statically admissible moment diagram.

With the aid of the general equilibrium equations presented in Section 2.4, moment equilibrium in this case is given as:

$$\frac{d^2M}{dx^2} = -q \quad [3.46]$$

which allows us to express moment as follows:

$$M(x) = \frac{-qx^2}{2} + Ax + B \quad [3.47]$$

where A and B are integration constants.

To solve for the constants A and B, boundary values are used:

- At  $x = 0 \Rightarrow M(0) = B$



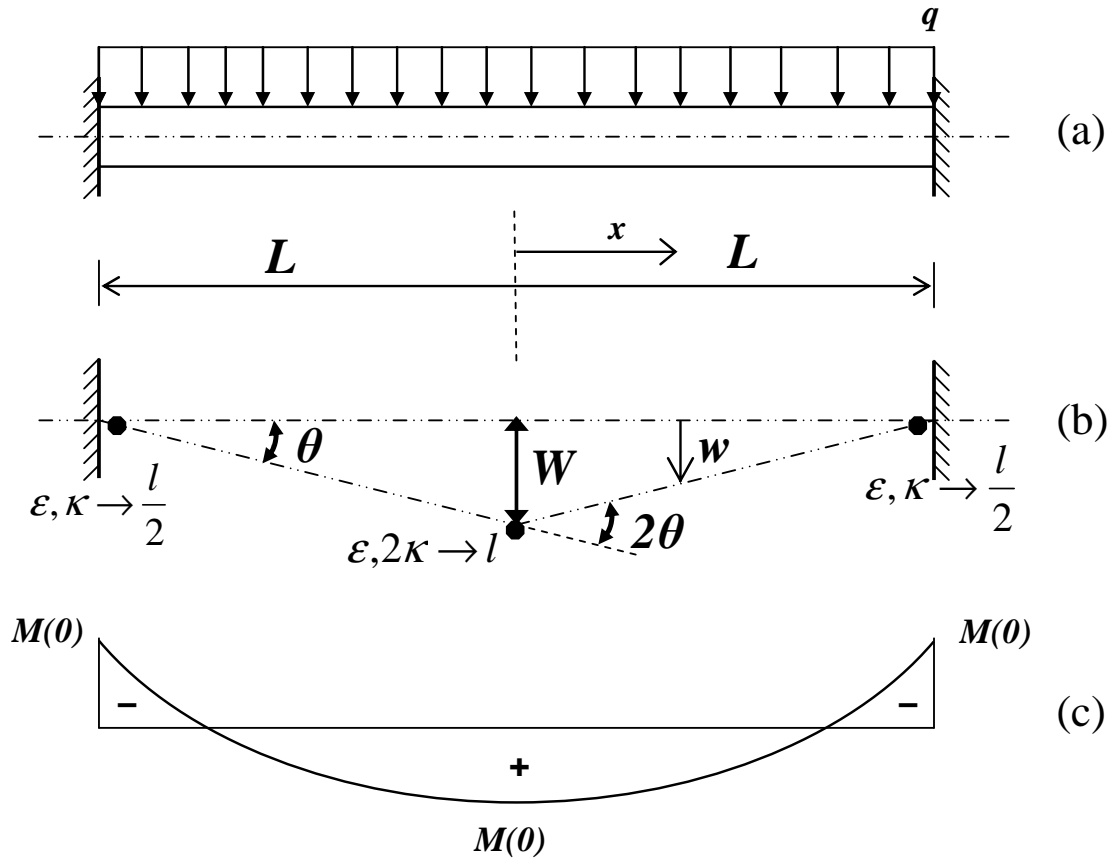


Figure 3-13 Schematics of Theory I

- At  $x = L \Rightarrow -M(0) = \frac{-qL^2}{2} + AL + M(0)$

Thus:

$$A = \frac{qL}{2} - \frac{2M(0)}{L} \quad [3.48]$$

Then, the moment expression is given as:

$$M(x) = \frac{-qx^2}{2} + \left[ \frac{qL}{2} - \frac{2M(0)}{L} \right] x + M(0) \quad [3.49]$$

Now, with use of the expression for vertical equilibrium at midspan given in Equation

2.27 for  $P=0$ , it can be shown that:

$$M(0) = \frac{qL^2}{4} - \frac{NW}{2} \quad [3.50]$$

Having determined the moment expression, the load–deflection characteristics of this case can be derived using the same analysis procedure as before.

- Axial Force,  $N$ :

It can be shown that use of a triangular deflected shape results in the same form of equations as those of the concentrated load case. For example, the ratio of deformation

rates,  $\dot{\varepsilon}/\dot{\kappa}$ , is independent of the cross–section considered. Thus:

$$\dot{\varepsilon}/\dot{\kappa} = \frac{W}{2} \quad [3.51]$$

and:

$$\frac{N}{N_p} = \frac{W}{d} \quad \text{for } W \leq d. \quad [3.52]$$

Equation 3.52 suggests that a pure cable state is reached at a deflection of cross-sectional depth  $d$ . Beyond this deflection, the beam resists the loads with the plastic axial force,  $N_p$ , where the expression is simply given as:

$$\frac{N}{N_p} = 1 \quad \text{for } W \geq d. \quad [3.53]$$

- Bending moment,  $M$ :

Substitution of Equation 3.52 into the yield condition given in Equation 2.5 gives:

$$\frac{M}{M_p} = 1 - \frac{W^2}{d^2} \quad \text{for } W \leq d. \quad [3.54]$$

Equation 3.53 suggests:

$$\frac{M}{M_p} = 0 \quad \text{for } W \geq d \quad [3.55]$$

for a pure cable state.

- External Load,  $q$ :

Having determined internal force equations in Equations 3.50 and 3.52 for  $M$  and  $N$ , respectively, we can substitute them into the yield condition for a rectangular cross-section given in Equation 2.5. Thus, the normalized external load expression is given as:

$$\frac{q}{q_c} = 1 + \frac{W^2}{d^2} \quad \text{for } W \leq d \quad [3.56]$$

where  $q_c = \frac{4M_p}{L^2}$ .

It should be remarked that Theory I predicts an equation that is identical to the form predicted by Haythornthwaite (1959) for beams with a rectangular cross-section under concentrated loading, as given in Equation 2.36.

At the pure cable state, vertical equilibrium of forces in the free body diagram illustrated in Figure 3-14 can be constructed as:

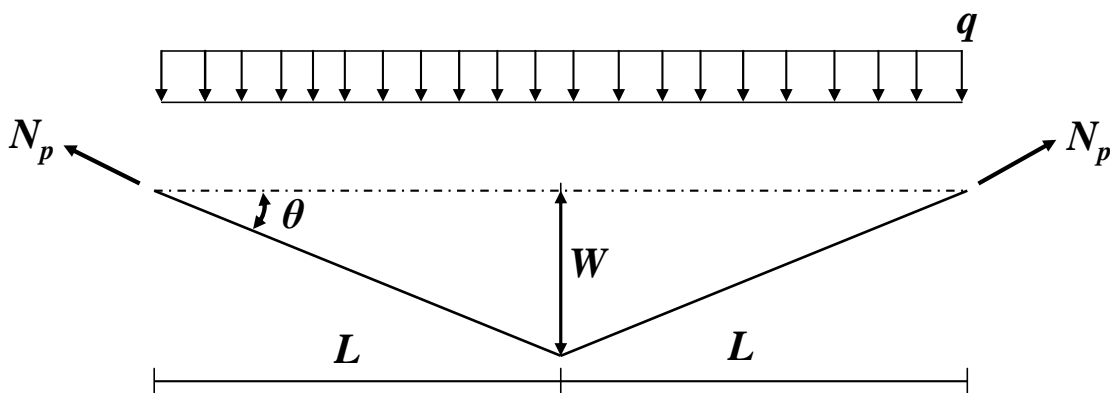


**Figure 3-14** Equilibrium of Forces at Pure Cable State

$\sum F_y = 0 \Rightarrow q \cdot 2L - 2 \cdot N_p \cdot \sin \theta = 0$ , from each it follows that:

$$\frac{q}{q_c} = \frac{W}{d} \quad \text{for } W \geq d \quad [3.57]$$

where again,  $q_c = \frac{4M_p}{L^2}$ .

By inspection, Equations 3.56 and 3.57 do not give the same load at the deflection  $d$ , at which the beam reaches  $N_p$ . This discrepancy will be discussed in the context of Theory II later.

For comparison purposes, the overall load–deflection characteristics of the beam shown in Figure 3-13 associated with Theory I will be graphically illustrated and discussed after the presentation of Theory II in the following section.

### 3.2.3.1.2 Theory II

As illustrated in Figure 3-15(b), a parabolic deflected shape configuration is considered in development of this theory. The deflected shape can be expressed as:

$$w = W \left( 1 - \frac{x^2}{L^2} \right) \quad [3.58]$$

Taking the derivative of Equation 3.58 twice with respect to  $x$  gives:

$$\frac{dw}{dx} = \frac{-2Wx}{L^2} \quad [3.59]$$

$$\frac{d^2w}{dx^2} = \frac{-2W}{L^2} \quad [3.60]$$

Therefore, the governing vertical equilibrium equation presented in Section 2-4 changes with use of this geometry. Substituting Equation 3.60 into Equation 2.8 gives:

$$\frac{d^2 M}{dx^2} + N \cdot \left( \frac{-2W}{L^2} \right) + q = 0 \quad \text{and} \quad [3.61]$$

$$\frac{d^2 M}{dx^2} = \frac{2NW}{L^2} - q. \quad [3.62]$$

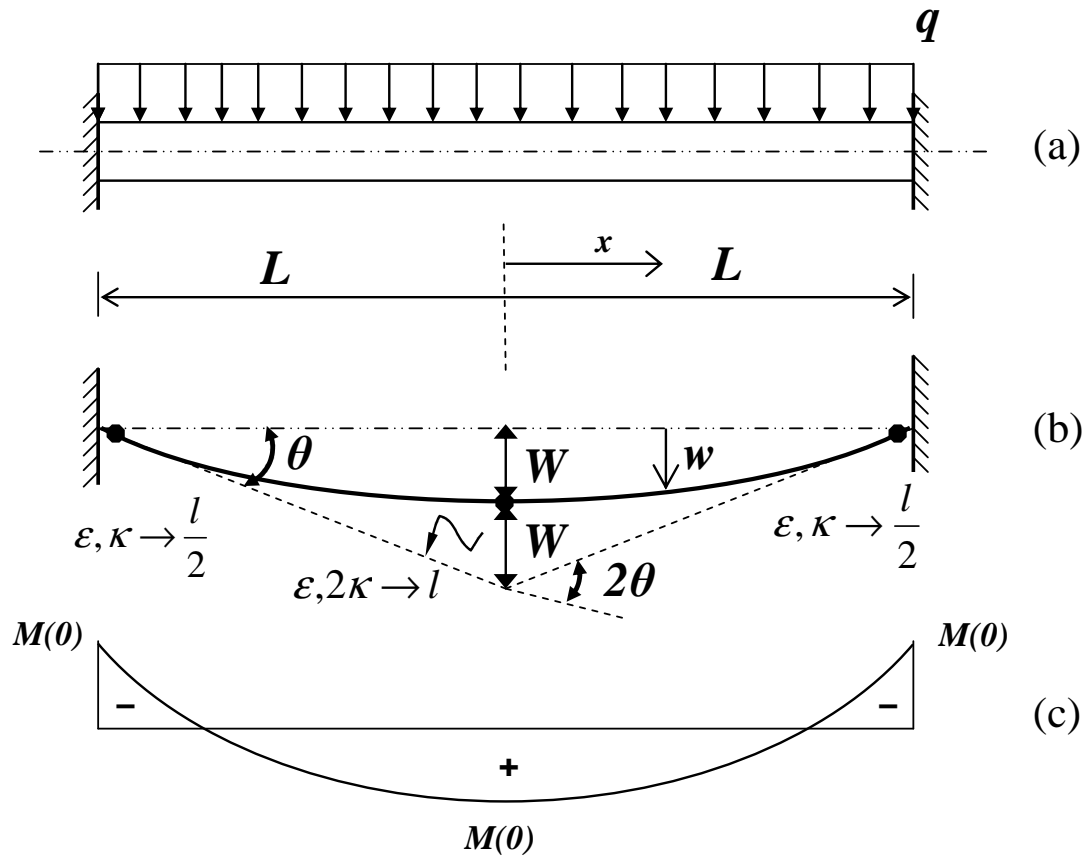


**Figure 3-15** Schematics of Theory II

By integrating Equation 3.62 twice, bending moment as a function of  $x$  becomes:

$$M(x) = \frac{NW}{L^2} x^2 - \frac{q}{2} x^2 + Ax + B. \quad [3.63]$$

Solving for the constants A and B by introducing the boundary values considering the moment diagram presented in Figure 3-15(c):

$$\blacksquare \text{ At } x = -L \Rightarrow M(-L) = -M(0) = NW - \frac{qL^2}{2} - AL + B \quad (\text{I})$$

$$\blacksquare \text{ At } x = L \Rightarrow M(L) = -M(0) = NW - \frac{qL^2}{2} + AL + B \quad (\text{II})$$

Solving (I) and (II) simultaneously yields:

$$A = 0 \quad \text{and} \quad B = \frac{qL^2}{2} - NW - M(0)$$

With aid of the third boundary value,  $M(0)$  at midspan, where  $x=0$ , gives:

$$M(0) = \frac{qL^2}{4} - \frac{NW}{2} \quad [3.64]$$

This deflected shape configuration requires derivation of the change in length of the beam which relates the axial strain and associated axial force definitions. The actual length of the deflected shape shown in Figure 3-15 (b) can be obtained with use of the arc length formulation given as:

$$L' = \int_a^b \sqrt{1 + [f'(x)]^2} dx \quad [3.65]$$

in which  $f'(x)$  is the first derivative of the function of the shape of arc. Due to symmetry, only one-half of the beam is considered. Substitution of Equation 3.59 into Equation 3.65 gives the actual length as:

$$L' = \int_0^L \sqrt{1 + \left[ \frac{-2Wx}{L^2} \right]^2} dx. \quad [3.66]$$

For convenience, let  $\omega = \frac{W}{L}$  and  $\xi = \frac{x}{L}$  then,

$$L' = L \cdot \left[ \int_0^1 \sqrt{1 + 4\omega^2 \xi^2} d\xi \right] \quad [3.67]$$

Evaluation of this integral was performed using Mathcad version 14 (2007) and the solution was obtained to be a sign function of  $\omega$  as follows:

$$L' = L \cdot \left[ \frac{c \operatorname{sgn}(\omega)^2 \sqrt{4\omega^2 + 1}}{2} + \frac{c \operatorname{sgn}(\omega) \cdot \ln(2\omega \cdot c \operatorname{sgn}(\omega) + \sqrt{4\omega^2 + 1})}{4\omega} \right] \quad [3.68]$$

where  $c \operatorname{sgn}(\omega)$  sign function for  $\omega = \frac{W}{L}$ .

By inspection, this complex expression may be approximated using a relatively simple equation in the form:

$$L' = L \cdot (1 + (\alpha \cdot \omega)^2) \quad [3.69]$$

In Figure 3-16, the normalized actual length and the approximation (Equation 3.69) is plotted versus  $\omega$  with  $\alpha = 0.707$ . It can be seen that a good correlation was obtained in representing the actual length of the deflected shape with Equation 3.69.

Since the change in length is:

$$\Delta L = 2L' - 2L \quad [3.70]$$

Then, substituting Equation 3.69 into Equation 3.70, the change in length becomes:

$$\Delta L = 2 \cdot \left[ L \left( 1 + \left[ \alpha \cdot \frac{W}{L} \right]^2 \right) - L \right] \quad [3.71]$$

Setting  $\alpha = 0.707$  Equation 3.71 reduces to:

$$\Delta L = L \cdot \left[ \frac{W}{L} \right]^2 \quad [3.72]$$

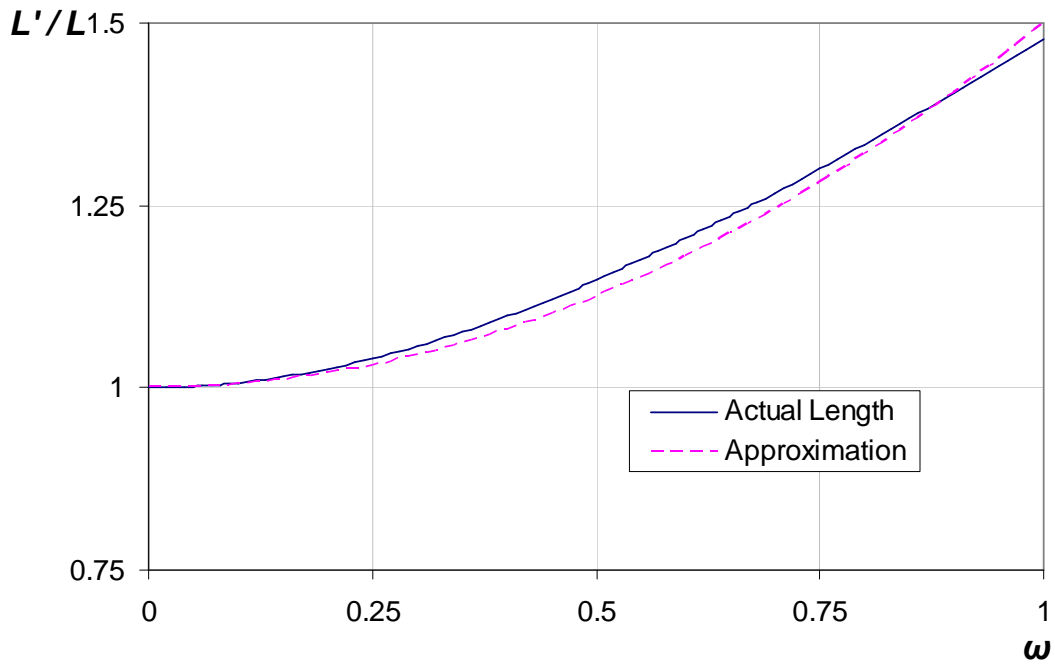


**Figure 3-16** Length of Arc Approximation

Then, the change in length over a total plastic hinge length  $2l$  as shown in Figure 3-15(b) gives an axial strain,  $\varepsilon$ , of:

$$\varepsilon = \frac{\Delta L}{2l} = \frac{L}{2l} \cdot \left[ \frac{W}{L} \right]^2. \quad [3.73]$$

Thus, the axial strain rate,  $\dot{\varepsilon}$ , is given as:

$$\dot{\varepsilon} = \frac{W \cdot \dot{W}}{L \cdot l} \quad [3.74]$$

On the other hand, the total change in angle over the plastic hinge at the end section, which has a length of  $l/2$ , the curvature rate in this case becomes:

$$\dot{\kappa} = \frac{4\dot{W}}{L \cdot l}. \quad [3.75]$$



Thus, the ratio of  $\dot{\varepsilon}/\dot{\kappa}$ , is given as:

$$\dot{\varepsilon}/\dot{\kappa} = \frac{W}{4}. \quad [3.76]$$

Load–deflection characteristics according to this theory can be developed using the rigid–plastic analysis procedure.

▪ Axial Force,  $N$ :

This ratio of  $\dot{\varepsilon}/\dot{\kappa}$  was obtained in Equation 2.19 for a beam of rectangular cross–section. Thus, a combination of this equation with Equation 3.76 gives the axial force expression as:

$$\frac{N}{N_p} = \frac{W}{2d}. \quad [3.77]$$

Equation 3.77 suggests that twice as much deflection,  $2d$  is needed for the beam to reach the pure cable state ( $N = N_p$ ) as in Theory I. Therefore, it is valid for a transverse deflection range of:  $0 \leq W \leq 2d$ .

Then for the pure cable state,

$$\frac{N}{N_p} = 1 \quad \text{for} \quad W \geq 2d. \quad [3.78]$$

▪ Bending moment,  $M$ :

Again, using the yield condition defined for a rectangular cross–section given in Equation 2.5, moment equations can be shown to be:

$$\frac{M}{M_p} = 1 - \frac{W^2}{4d^2} \quad \text{for} \quad W \leq 2d \quad [3.79]$$

and Equation 3.77 suggests that:

$$\frac{M}{M_p} = 0 \quad \text{for } W \geq 2d \quad [3.80]$$

at the pure catenary state

- External Load,  $q$ :

Having determined internal force equations in equations 3.64 and 3.77 for  $M$  and  $N$  respectively, we can substitute them into the yield condition for a rectangular cross-section (Equation 2.5). Thus, the normalized external load expression in this case becomes:

$$\frac{q}{q_c} = 1 + \frac{3W^2}{4d^2} \quad \text{for } W \leq 2d \quad [3.81]$$

where  $q_c = \frac{4M_p}{L^2}$ .

In a similar manner, the derivations can be extended for the deflections beyond  $2d$ . Figure 3-17 illustrates the free body diagram after the beam reaches a pure cable state. Vertical equilibrium requires:

$$\sum F_y = 0 \Rightarrow q \cdot 2L - 2 \cdot N_p \cdot \sin \theta = 0 \quad [3.82]$$

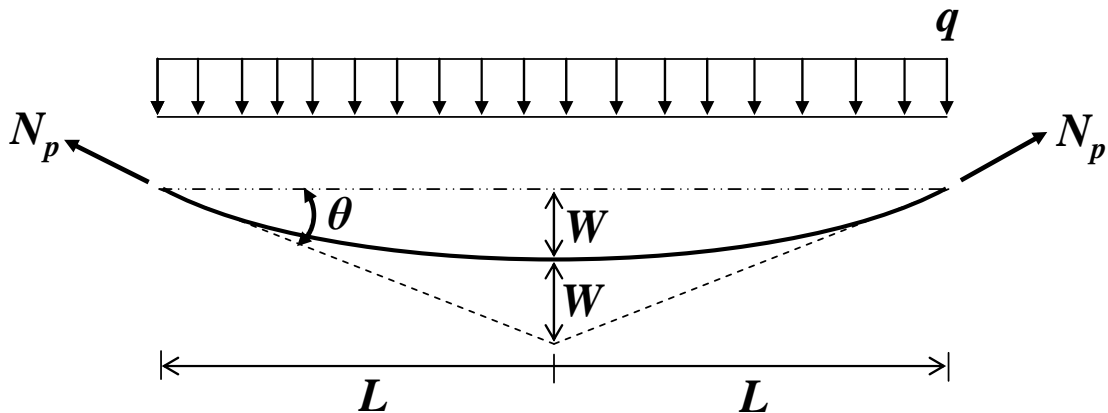


**Figure 3-17** Equilibrium of forces at pure catenary state

For  $\sin \theta = \theta = \frac{2W}{L}$ , it can be shown that:

$$\frac{q}{q_c} = \frac{2W}{d} \quad \text{For } W \geq 2d \quad [3.83]$$

where  $q_c = \frac{4M_p}{L^2}$ .

It is evident that Equations 3.81 and 3.83 result in the same load level at the point of a pure cable state ( $W = 2d$ ).

Figures 3.18 through 3.20 illustrate the overall load–deflection characteristics of fully clamped, rectangular shaped beams under uniform loading as predicted by Theory I and II. Characteristic points A and C represent the point of mechanism condition formation and point of pure cable state, respectively. The subscripts I and II refer to Theory I and II, respectively.

Since Theory I did not accurately predict the behavior upon formation of the pure cable state, it is not represented in Figures 3-18, 3-19, and 3-20 beyond point  $C_I$ . However, it should be noted that the extension line of Theory I (Figure 3-18) that passes through the origin coincides with point  $C_{II}$ , which represents the point of pure cable state predicted by Theory II. This agreement can be attributed to the transition in deflected shape configuration presented in Figure 3-12.

As a concluding remark, different theories based on different deflected shape considerations provide boundaries to the real behavior, which is discussed in the context of the finite element analyses presented in Chapter 4.

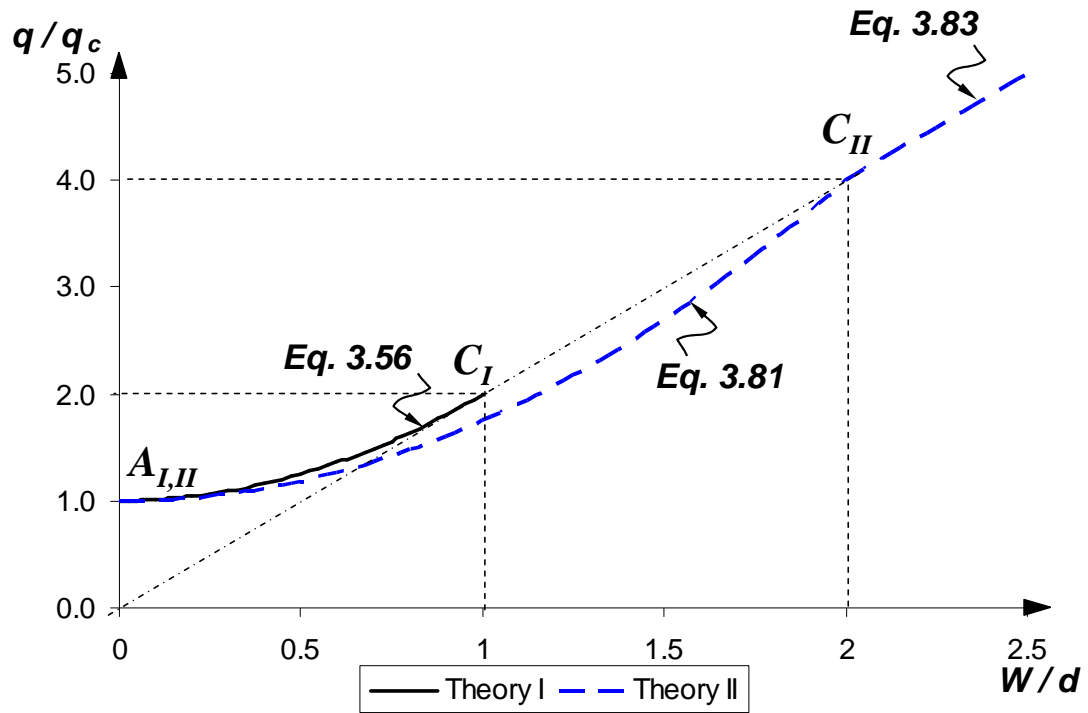


Figure 3-18 Normalized Load-Deflection relationship

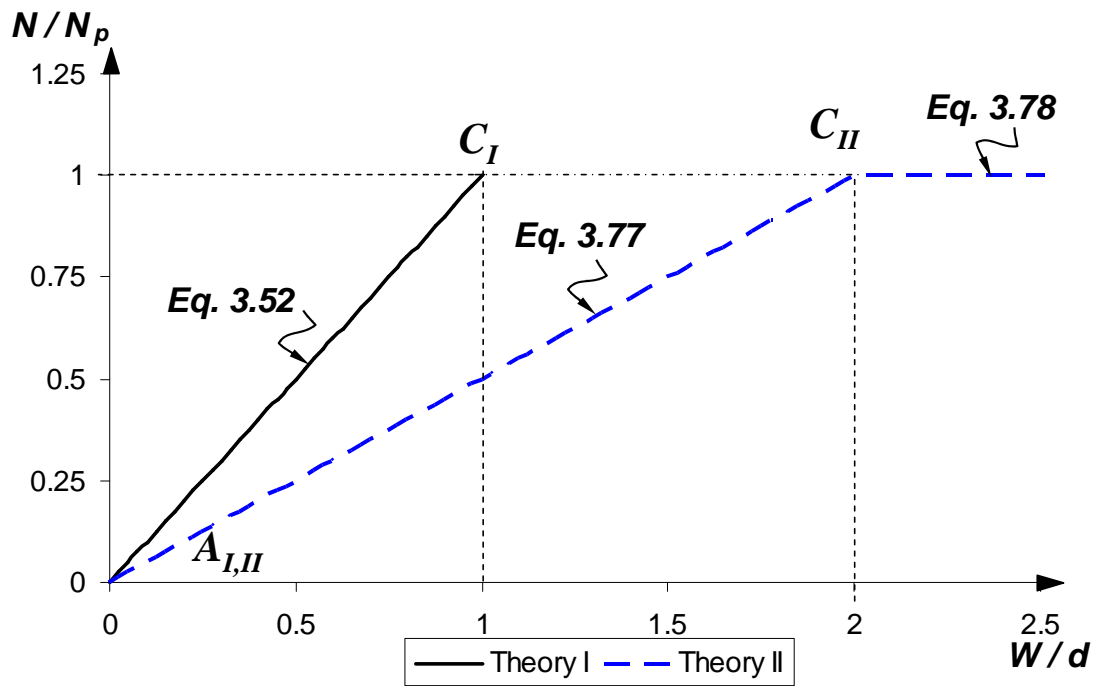
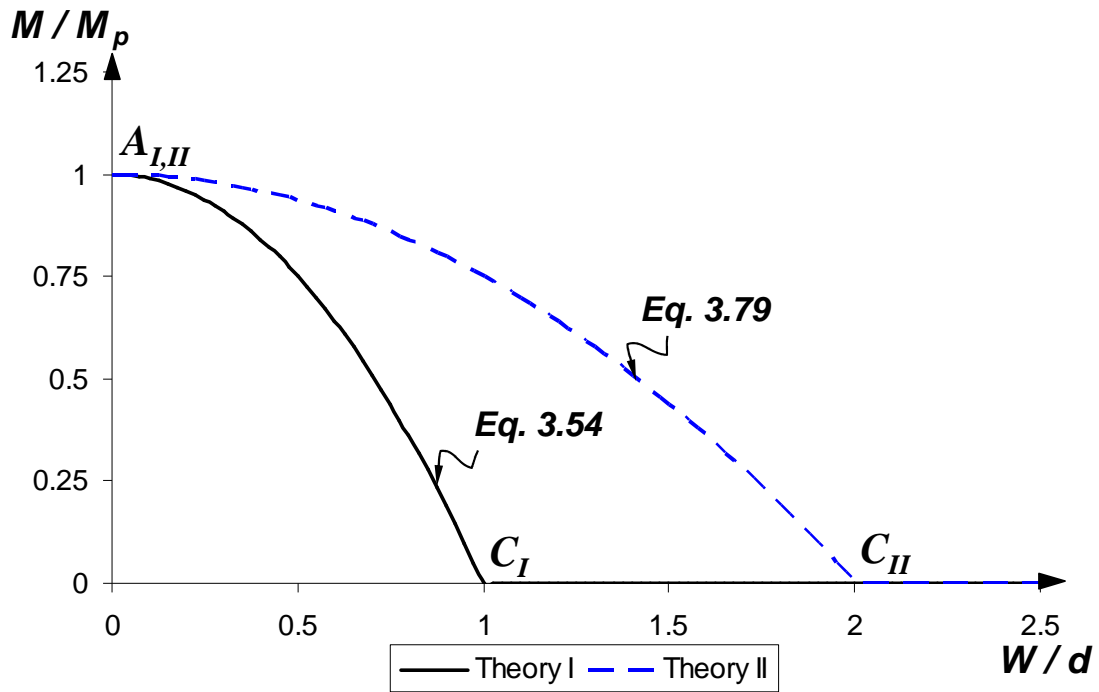


Figure 3-19 Normalized Axial Force-Deflection relationship



**Figure 3-20** Normalized Moment – Deflection Relationship

### 3.2.3.2 Beam with W-Shaped Cross-Section

Two theories based on triangular and parabolic deflected shapes can be developed for beams with W-Shapes. Characteristics, such as the mechanism condition and statically admissible moment diagram for each theory as presented in Figure 3-13 and Figure 3-15, respectively, are independent of the cross-section. The difference here is the dependency of the yield condition on the location of the PNA across the beam depth, as given in Equations 3-1 and 3-2. Load-deflection characteristics of W-Shaped beams predicted by each theory can be obtained in a similar manner as before.

#### 3.2.3.2.1 Theory I

It was observed that results using Theory I predicted the identical form of equation given by Haythornthwaite (1959) for the beam with a rectangular cross-section under concentrated load case. Therefore, with similar anticipation, the rigid-plastic analysis procedure was conducted, and the results were shown to be analogous to the load-deflection characteristics given for W-Shaped beams under concentrated loading as presented in Section 3.2.2. Depending on the location of the PNA, predictions of Theory I are given as follows:

- When the PNA is in the web, where  $0 \leq W \leq d_w$

$$\frac{N}{N_p} = \frac{W \cdot t_w}{A}, \quad [3.84]$$

$$\frac{M}{M_p} = 1 - \frac{W^2 \cdot t_w}{4 \cdot Z_x}, \text{ and} \quad [3.85]$$

$$\frac{q}{q_c} = 1 + \frac{W^2 \cdot t_w}{4 \cdot Z_x}, \quad [3.86]$$

Where  $q_c = \frac{4M_p}{L^2}$ .

- When the PNA is in the flange, where  $d_w \leq W \leq d$

$$\frac{N}{N_p} = 1 - \frac{[d - W]}{A} \cdot b_f, \quad [3.87]$$

$$\frac{M}{M_p} = \frac{(d^2 - W^2) \cdot b_f}{4 \cdot Z_x}, \text{ and} \quad [3.88]$$

$$\frac{q}{q_c} = \frac{1}{Z_x} \left[ \left( \frac{d - W}{2} \right)^2 \cdot b_f + \frac{AW}{2} \right], \quad [3.89]$$

where  $q_c = \frac{4M_p}{L^2}$ .

As shown in the procedure presented for beams with rectangular cross-section, Theory I did not accurately predict the behavior beyond pure cable formation (i.e. for  $W \geq d$ ) with use of the vertical equilibrium presented in Figure 3-14. Thus, equations predicted by Theory I beyond the pure cable state are not presented. In similar manner, for comparison purposes, graphical representation of results given herein will be presented after presentation of Theory II results.

### 3.2.3.2.2 Theory II

Schematics of Theory II were given in Figure 3-15 earlier. A similar rigid-plastic analysis procedure as that presented in Section 3.2.3.1.2 was implemented for W-Shaped beams with introduction of corresponding yield condition. Therefore, load-deflection characteristics of the behavior predicted by Theory II can be obtained as follows:

- Axial Force,  $N$ :
  - When the PNA is in the web:

Coupling Equation 3.3 with Equation 3.76, then substituting the result into Equation 3.5, the normal force expression yields:

$$\frac{N}{N_p} = \frac{W \cdot t_w}{2A} \quad [3.90]$$

Applicability of Equation 3.90 can similarly be investigated for the special case where the PNA is at the interface between web and flange. Solving for  $W$  at

$N = N_{pw}$  gives:

$$W = 2d_w \quad [3.91]$$

Thus, Equation 3.90 is valid for the range of  $0 \leq W \leq 2d_w$ .

- When the PNA is in the flange:

Coupling equations 3.3 and 3.76, then substituting the result into Equation 3.11, the normal force expression is given as:

$$\frac{N}{N_p} = 1 - \frac{\left[ d - \frac{W}{2} \right] \cdot b_f}{A}. \quad [3.92]$$

Equation 3.92 suggests that the beam reaches a pure cable state at a deflection of twice the beam depth  $2d$ . Thus it is valid in a range of  $2d_w \leq W \leq 2d$ .

- Beyond the pure cable state:

$$\frac{N}{N_p} = 1 \quad \text{for } W \geq 2d. \quad [3.93]$$

- Bending moment,  $M$ :

Substitution of the previously defined normal force equations into their corresponding yield condition gives:

- When the PNA is in the web:

$$\frac{M}{M_p} = 1 - \frac{W^2 \cdot t_w}{16 \cdot Z_x} \quad 0 \leq W \leq 2d_w. \quad [3.94]$$

- When the PNA is in the flange:

$$\frac{M}{M_p} = \left[ d^2 - \left( \frac{W}{2} \right)^2 \right] \cdot \frac{b_f}{4Z_x} \quad \text{for } 2d_w \leq W \leq 2d. \quad [3.95]$$

- Beyond the pure cable state:



$$\frac{M}{M_p} = 0 \quad \text{for } W \geq 2d. \quad [3.96]$$

- External Load,  $q$ :

Substituting the axial force equations for each location of the PNA, along with the moment equation derived from equilibrium equations (given in Equation 3.64), into the respective yield condition, gives:

- When the PNA is in the web:

$$\frac{q}{q_c} = 1 + \frac{3W^2 t_w}{16Z_x} \quad \text{For } 0 \leq W \leq 2d_w \quad [3.97]$$

where  $q_c = \frac{4M_p}{L^2}$ .

- When the PNA is in the flange:

$$\frac{q}{q_c} = \frac{1}{4Z_x} \left[ \left( d - \frac{W}{2} \right) \cdot \left( d - \frac{3W}{2} \right) b_f + 2AW \right]. \quad [3.98]$$

- Beyond the pure cable state:

With use of vertical equilibrium of forces in the free body diagram as given in Figure 3-17, it can be shown that:

$$\frac{q}{q_c} = \frac{AW}{2 \cdot Z_x} \quad \text{for } W \geq 2d \quad [3.99]$$

where  $q_c = \frac{4M_p}{L^2}$ .

Finally, progression of events in a graphical manner is indicated in the Figures 3-21, 3-22 and 3-23. Load–deflection characteristics predicted by the two theories for a W–Shaped beam under uniform loading are presented. Figure 3-21 displays a plot of

normalized external load versus normalized deflection,  $W$ , at midspan. Figures 3-22 shows the normalized axial force,  $N$ , with respect to normalized midspan deflection,  $W$ , and finally the relationship of the bending moment,  $M$  with respect to transverse deflection is given in Figure 3-23. In these figures, characteristic points A, B and C are again indicated with respective subscripts representing each theory presented herein. It can be seen that the overall progression of events are common for the two theories except they occur at a different level of transverse deflection for each theory. Theory I is again presented with a dashed line beyond the pure cable state ( $C_I$ ), as it was shown that it does not accurately represent the behavior in this region.

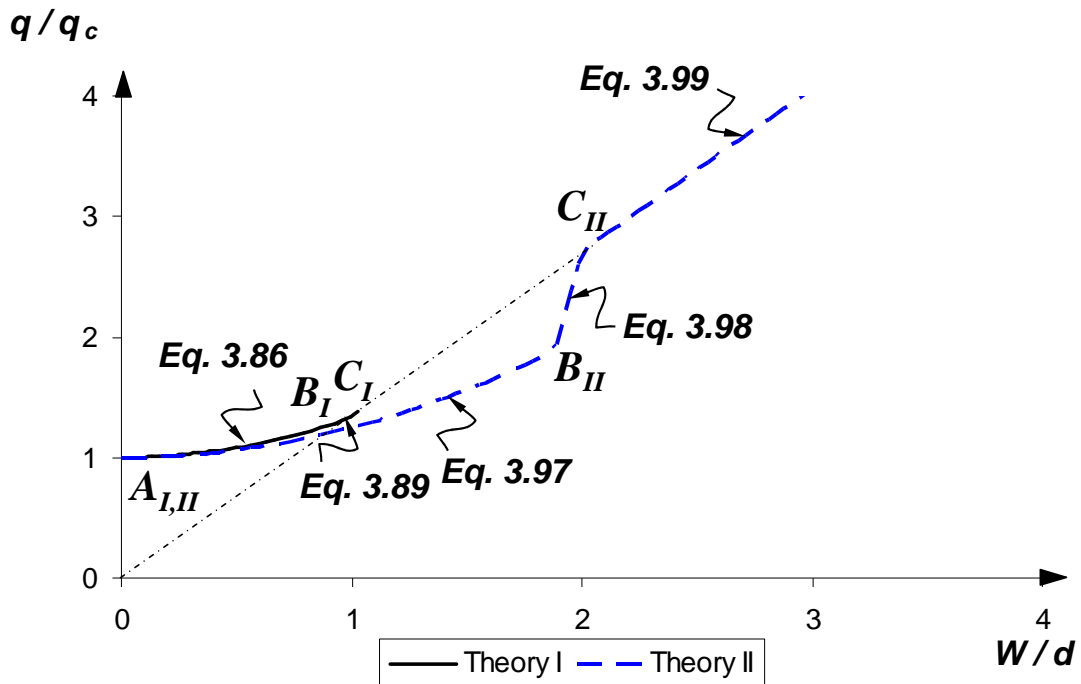


**Figure 3-21** Normalized Load–Deflection relationship

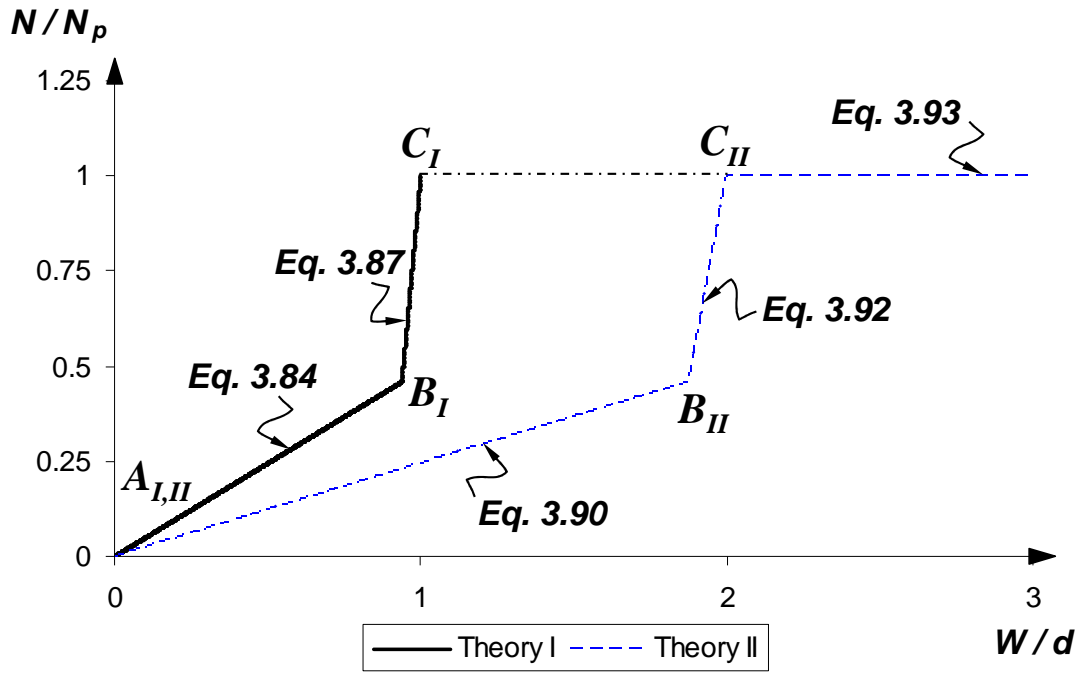


Figure 3-22 Normalized Axial Force–Deflection relationship

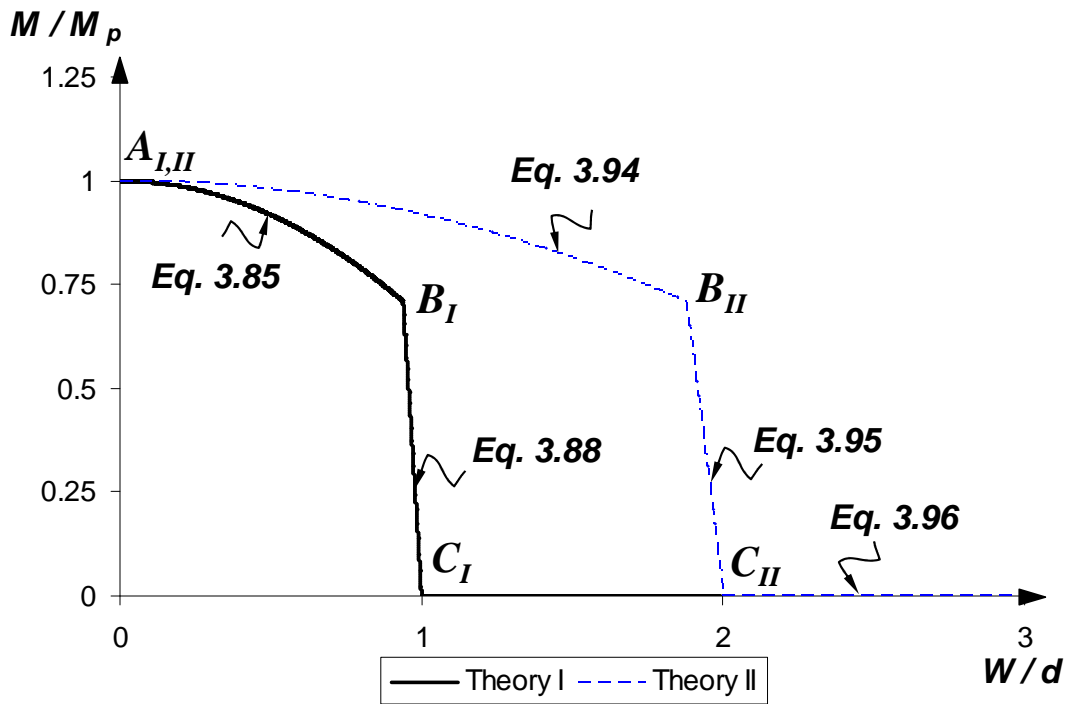
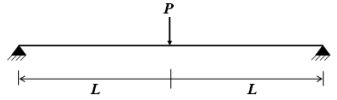
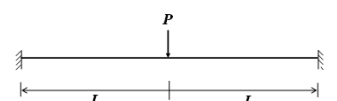
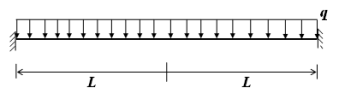


Figure 3-23 Normalized Moment–Deflection relationship

### 3.2.4 Summary

The rigid-plastic behavior of ductile steel beams with idealized boundary conditions was presented. Load-deflection characteristics for each loading, boundary conditions and cross-section types were described throughout the deformation of the beam. Results showed that the load-deflection characteristics for each cross-section type are predominantly affected by the corresponding yield condition under combined bending and axial forces. It was also seen that a similar form of equations for normalized load, axial force and bending moment as a function of transverse deflection  $W$  and cross-sectional properties, described the behavior at each case. The amount of transverse deflection at the onset of pure cable behavior, defined as  $W_{cat}$ , was predicted in order of nominal depth,  $d$  of the cross-section independent of the cross-section type. Table 3-1 summarizes the  $W_{cat}$  predictions using the rigid-plastic theory for each case presented herein.

**Table 3-1**  $W_{cat}$  predicted by Rigid-Plastic Theory

Case	$W_{cat}$
	$d/2$
	$d$
	Theory I : $d$ Theory II : $2d$

### 3.3 Cable Analysis

In this section, a theoretical analysis procedure is developed for a special type of behavior, commonly referred to as “cable action”. It is assumed that the member has no resistance to bending; therefore, external loads are resisted only by means of axial forces that develop in the member as it deflects. With use of the elastic–perfectly plastic material idealization shown in Figure 3-24, deformations remain elastic until the plastic axial force,  $N_p$ , is reached (Point C). Beyond this point, the beam member sustains  $N_p$  and yielding occurs along the length. Theoretically, this type of “pure cable” behavior can be anticipated from infinitely long beams as discussed later in Chapter 4.

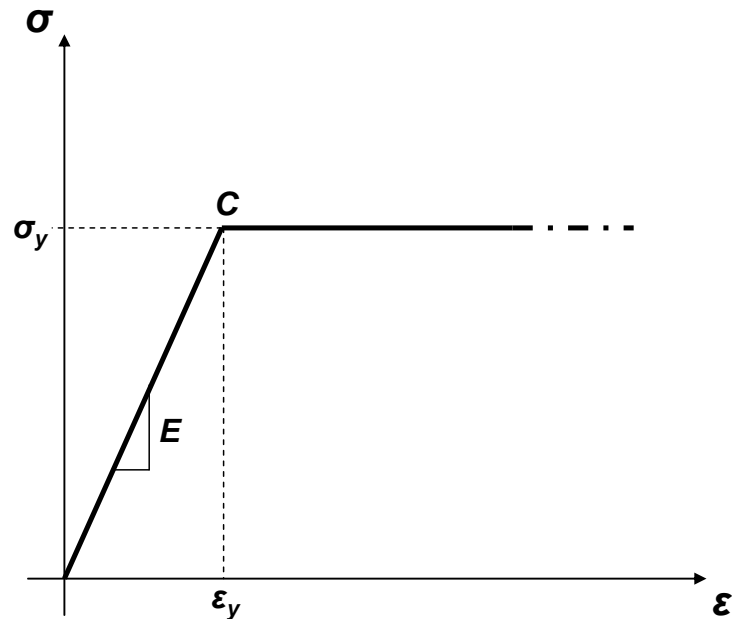


**Figure 3-24** Material idealization used in Cable analysis

It can be anticipated that the load–deflection characteristics of this type of behavior are independent of the boundary conditions associated with the rotational degree

of freedom at the supports, since there is no resistance to bending. Therefore, assuming full axial fixity at the supports, an analysis procedure was developed to describe the load–deflection characteristics under a midspan concentrated load, and under a uniformly distributed load is presented next.

### 3.3.1 Concentrated Load Case

An analysis procedure is presented to derive internal and external loads as a function of midspan deflection,  $W$  for a beam under a concentrated load at midspan.

- Axial Force,  $N$ :

Axial strain associated with axial forces can be determined by deriving the change in length of the beam as shown in Figure 3-25.

$$\Delta L = L' - L = \sqrt{L^2 + W^2} - L \quad [3.100]$$

and

$$\varepsilon = \frac{\Delta L}{L}. \quad [3.101]$$

Substituting Equation 3-100 into Equation 3-101 gives:

$$\varepsilon = \left(1 + \frac{W^2}{L^2}\right)^{1/2} - 1 \quad [3.102]$$

For small  $\frac{W}{L}$ , with the aid of a binomial expression, Equation 3.102 can be reduced to the

form:

$$\varepsilon = \frac{1}{2} \cdot \left[\frac{W}{L}\right]^2. \quad [3.103]$$

Thus, the associated axial force can be determined as:

$$N = \sigma \cdot A = E \cdot \varepsilon \cdot A. \quad [3.104]$$

Substituting Equation 3.103 into Equation 3.104 yields:

$$N = \frac{E \cdot A}{2} \cdot \left[ \frac{W}{L} \right]^2. \quad [3.105]$$

Thus, Equation 3.105 predicts that the axial force,  $N$ , is a quadratic function of transverse deflection,  $W$ .

In the special case when the beam reaches the pure plastic cable state (i.e.  $N = N_p = \sigma_y \cdot A$ ), Equation 3.105 gives:

$$\frac{W_{cat}}{L} = \sqrt{\frac{2 \cdot \sigma_y}{E}}. \quad [3.106]$$

It can be seen that, Equation 3.106 is independent of the cross-section of the beam.

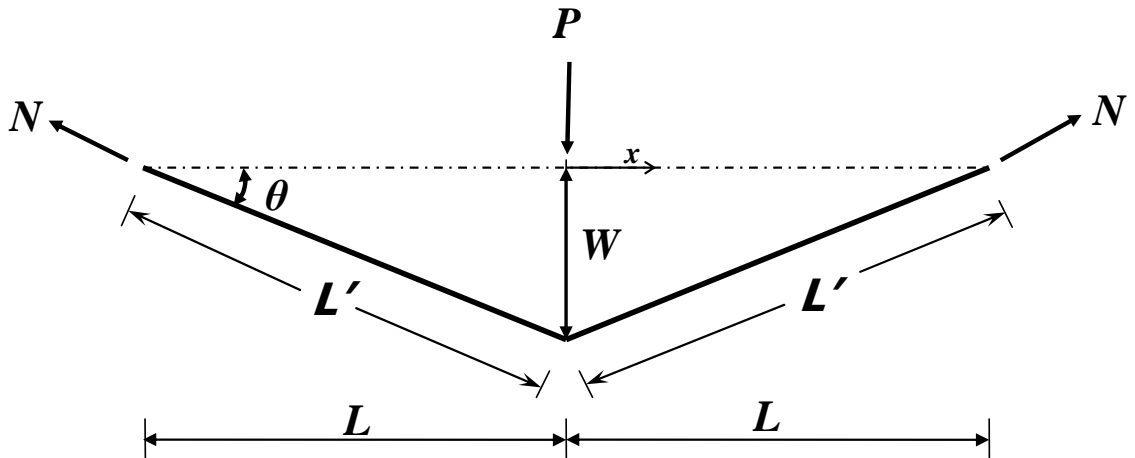


**Figure 3-25** Free body diagram under concentrated load

- External Load,  $P$ :

Considering vertical equilibrium of the forces given in Figure 3.25:

$$\sum F_y = 0 \Rightarrow P - 2 \cdot N \cdot \sin \theta = 0$$

and assuming that  $\sin \theta = \theta = \frac{W}{L}$ , it follows that:

$$P = \frac{2 \cdot N \cdot W}{L}. \quad [3.107]$$

Substituting Equation 3.105 into Equation 3.107, gives:

$$P = E \cdot A \cdot \left[ \frac{W}{L} \right]^3. \quad [3.108]$$

Thus, Equation 3.108 gives the external load,  $P$ , as a cubic function of transverse deflection,  $W$ .

### 3.3.2 Uniformly Distributed Load Case

The deflected shape associated with this load case is represented with a parabolic configuration as illustrated in Figure 3-26. The rigid-plastic analysis procedure presented previously indicated that this configuration appropriately represents the behavior at the pure cable state.

To obtain load-deflection characteristics of this case, a similar procedure is carried out to that for the concentrated load case presented earlier.

- Axial Force,  $N$ :

The axial strain based on a parabolic configuration was derived in the context of rigid-plastic analysis. Recall, considering one-half of the beam that the actual length was approximated in terms of a parameter,  $\alpha$ . For convenience, derivations herein will be given as a function of  $\alpha$  and then, an acceptable value used to represent the actual length



in the deflected shape associated with this type of behavior is provided. Therefore, with use of Equation 3.71, change in length is given as:

$$\Delta L = 2L \cdot \alpha^2 \cdot \left[ \frac{W}{L} \right]^2 \quad [3.109]$$

Thus axial the strain over the length of the beam member:

$$\varepsilon = \frac{\Delta L}{2L} = \alpha^2 \cdot \left[ \frac{W}{L} \right]^2 \quad [3.110]$$

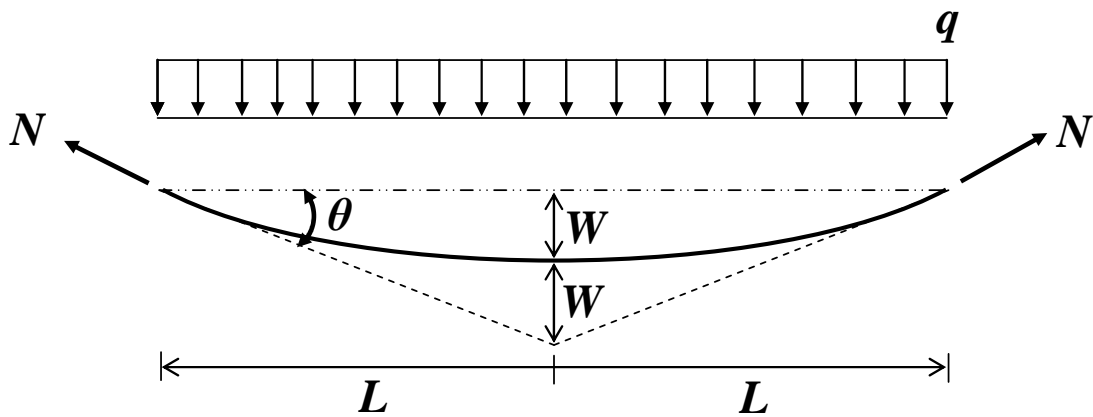


**Figure 3-26** Free body diagram under uniform loading

Substituting 3.110 into Equation 3.104, gives:

$$N = \alpha^2 \cdot E \cdot A \cdot \left[ \frac{W}{L} \right]^2 \quad [3.111]$$

Equation 3.111 predicts that the axial force,  $N$ , is a quadratic function of transverse deflection,  $W$ .

For the special case, when the beam reaches the pure plastic cable state (i.e.  $N = N_p = \sigma_y \cdot A$ ) it can be deduced from Equation 3.111 that:

$$\frac{W_{cat}}{L} = \frac{1}{\alpha} \cdot \sqrt{\frac{\sigma_y}{E}} \quad [3.112]$$

It can be seen that Equation 3.112 is also independent of the cross-section.

- External Load,  $q$ :

Considering vertical equilibrium of forces given in Figure 3.26:

$$\sum F_y = 0 \Rightarrow q \cdot 2L - 2 \cdot N \cdot \sin \theta = 0. \quad [3.113]$$

It follows that:

$$q = \frac{2NW}{L^2}. \quad [3.114]$$

Substituting Equation 3.111 into Equation 3.114 gives:

$$q = \frac{2\alpha^2 EA}{L} \cdot \left[ \frac{W}{L} \right]^3. \quad [3.115]$$

Thus, Equation 3.115 gives external load,  $q$ , as a cubic function of transverse deflection,  $W$ .

To represent the actual length of the deflected shape shown in Figure 3-26, the arc length approximation given in Equation 3.69 is utilized. In similar manner, an infinitely

long beam assumption will predict an infinitely small  $\frac{W}{L}$ . In Figure 3-27, the  $\alpha$

parameter (determined according to Equation 3.69) is plotted versus  $\omega = \frac{W}{L}$ . By

inspection, it is found that  $\alpha$  approaches 0.816 when  $\omega$  goes to zero. As a result, under uniform loading, the deflected shape associated with this special case of “cable action” can be approximated by Equation 3.69 with  $\alpha = 0.816$ .

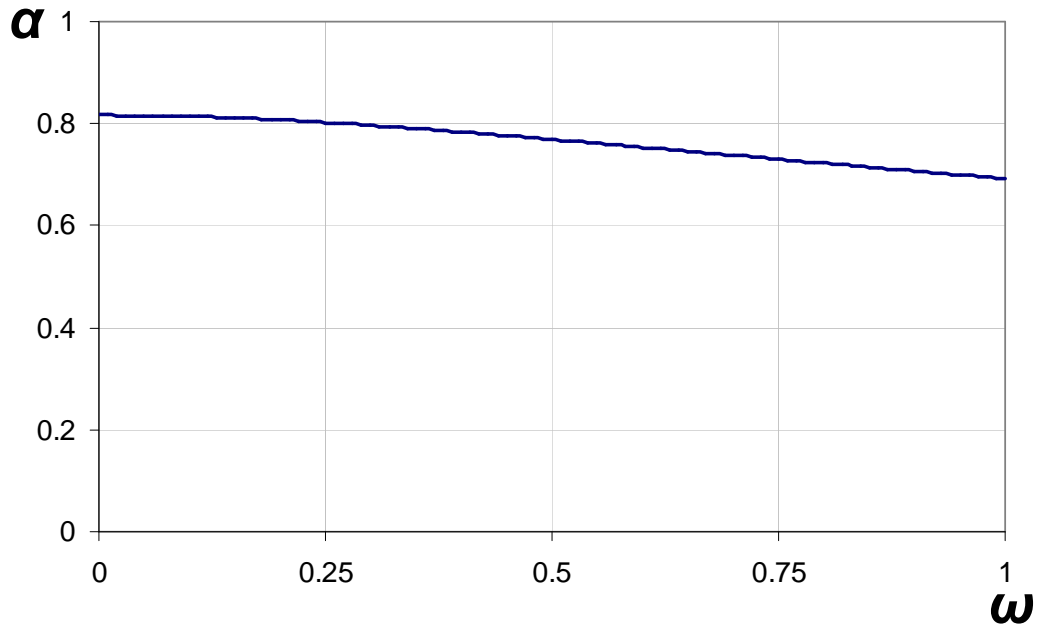


**Figure 3-27**  $\alpha - \omega$  relationship

### 3.3.3 Summary

Load–deflection characteristics of ductile steel beams under different load conditions predicted by cable behavior were presented. It was seen that the procedure is predominantly affected by the deflected shape configuration and is independent of cross–section used. In fact, the deflection at the onset of pure cable behavior,  $W_{cat}$  was shown to be a function of material properties and span length. By rearranging Equations 3.106 and 3.112,  $W_{cat}$  predictions by cable theory can be given as:

- $W_{cat} = \sqrt{\frac{2 \cdot \sigma_y}{E}} \cdot L$  for a concentrated midspan loading, and
- $W_{cat} = \frac{1}{\alpha} \cdot \sqrt{\frac{\sigma_y}{E}} \cdot L$  for uniformly distributed loading,

where  $\alpha$  is a parameter used to determine the actual length of the parabolic deflected shape, and can be taken as 0.816. As remarked earlier, these predictions are independent of the boundary conditions, therefore, they can be used for simple beams as well as for beams fixed at both ends.

### 3.4 Conclusion and Expected Behavior

In this chapter, ductile behavior of steel beams under finite displacements was described using two different theories; rigid–plastic and cable. It can be recognized that each of these models represents special cases of beam behavior. Therefore, a conclusion can be driven with regards to how each theory relates to the actual, elastic–perfectly plastic behavior which is commonly used in practice. As illustrated in Figure 3-28, which graphically describe the overall behavior on  $M$ – $N$  interaction at a cross–sectional level, rigid–plastic and cable theories can be regarded as theoretical lower and upper bounds of the actual behavior, respectively. The paths on the figure represent the behavior depicted by each case throughout the deformation of the beam. Brief descriptions of these paths are given as follows:

- Path OAC: Represents rigid–plastic behavior. No deflection occurs until the mechanism condition is reached ( $M = M_p$  at all possible plastic hinge locations). Once the condition is satisfied (Point A), the beam starts to deflect, and develops axial forces,  $N$ . From then on, yielding occurs with a combination of  $M$  and  $N$  and follows the path shown until the beam reaches the pure cable state (Point C).

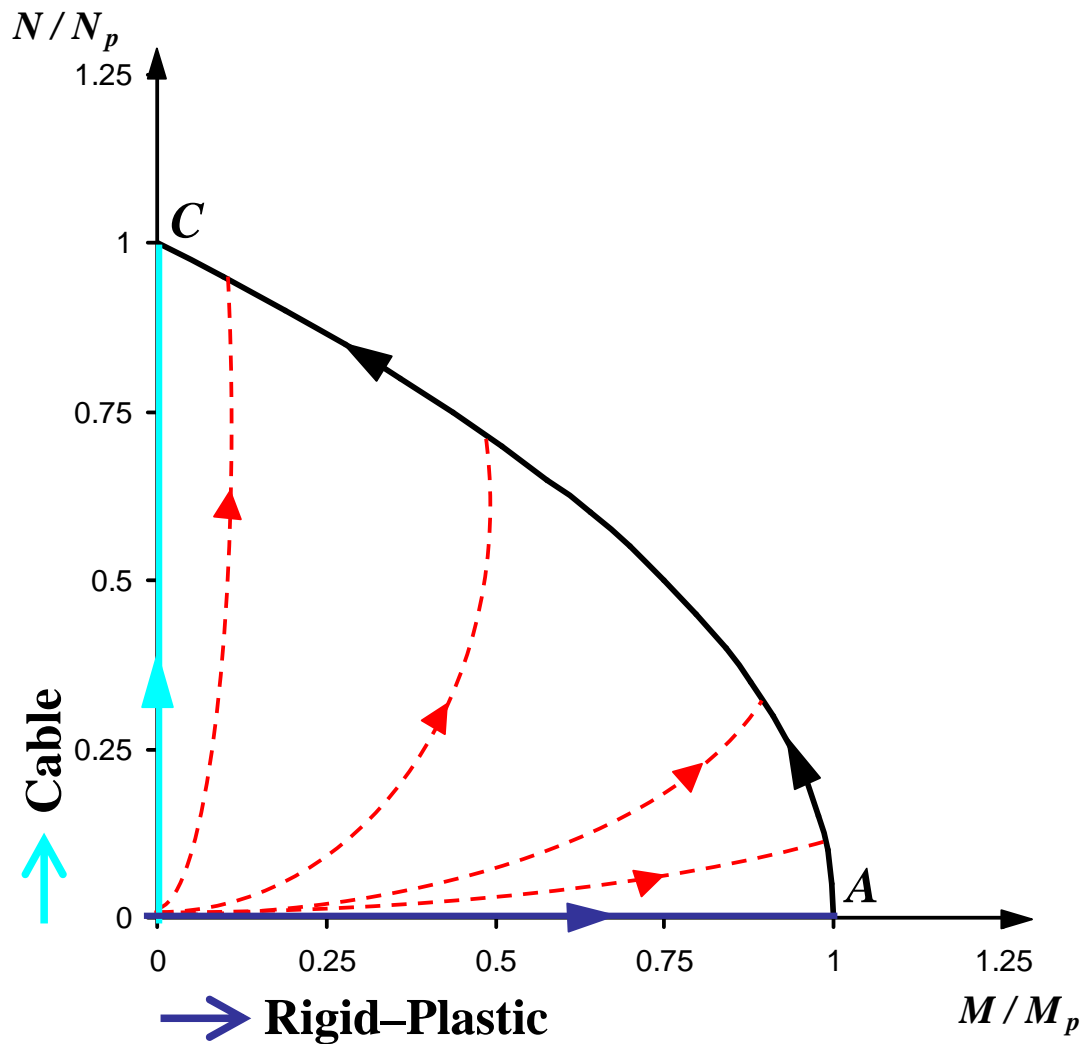


**Figure 3-28** Expected behavior representation on  $M-N$  interaction

- Path O-dashed lines-C: Represents the actual behavior, depending upon the flexibility of the elastic-plastic beam member. For very flexible, i.e. long beams, the behavior may be represented with steeper dashed lines and approaches cable theory. For very short, relatively rigid beams, the behavior is represented with shallower dashed lines, approaching rigid-plastic theory. In the case of the dashed lines, the beam may encounter finite displacements in the elastic regime and develop axial forces. When

the axial forces become large enough, plastic hinges form under a combination of  $M$  and  $N$  (before reaching full  $M_p$ ).

- Path OC: Represents the cable behavior. The beam has no bending resistance and carries the loads only by means of axial force throughout the deflection until reaching a pure cable state (i.e.  $N=N_p$ ). As noted earlier, infinitely long beams may exhibit this special upper bound behavior.

To summarize, the actual behavior of ductile steel beams will fall somewhere in between the bounding theories developed in this chapter. Ensuing efforts presented in the following chapters will focus on how to represent the characteristics of actual behavior with use of these unique theories.

## **Chapter 4. ANALYTICAL MODELS**

### **4.1 Introduction**

In this chapter, Finite Element (FE) analyses of steel beams with idealized boundary conditions, including the effect of geometric and material nonlinearity, are described. First, a set of preliminary FE analyses were executed for comparison with the theoretical findings presented in Chapter 3. Then, a parametric study was conducted to identify the main geometric factors affecting the actual behavior.

Both loading and cross-sectional cases considered for steel beams, as presented in Chapter 3 were studied, focusing on beams with fixed ends. FE models were developed and analyzed using *Open System for Earthquake Engineering Simulations* (OpenSees) software (McKenna et al. 2000).

### **4.2 Modeling Concepts**

Modeling tools available in OpenSees (McKenna et al. 2000) are presented next and were used in this study.

#### **4.2.1 Fiber Section Discretization**

In order to keep track of the propagation of yielding through the cross-section, the fiber section modeling object available in OpenSees was used.

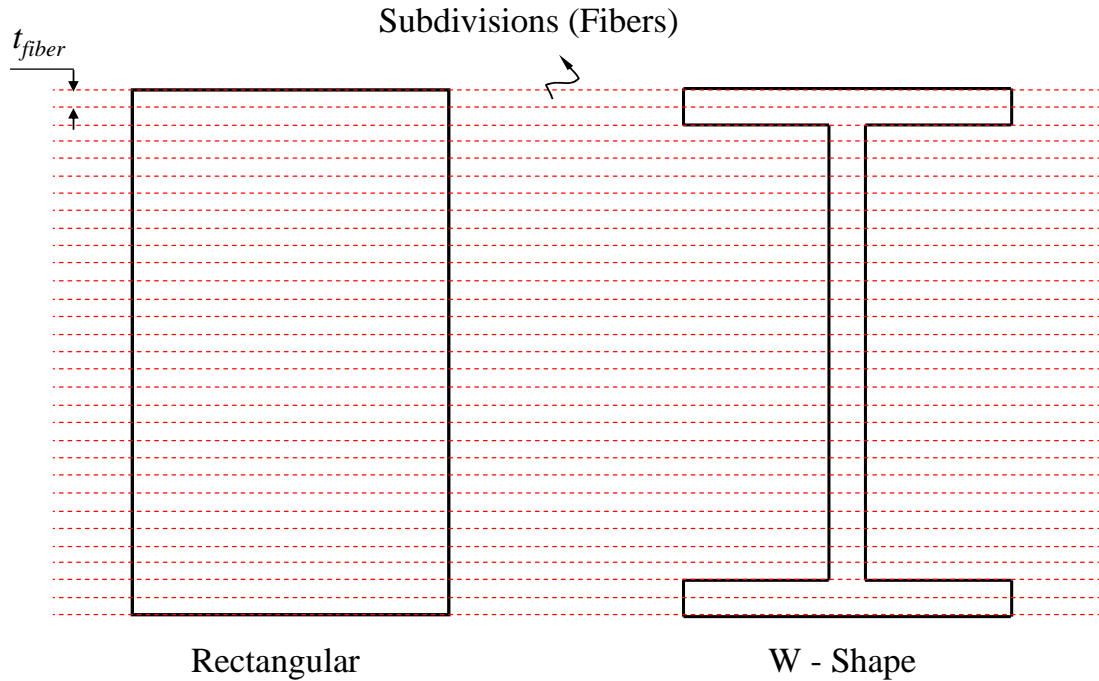


**Figure 4-1** Schematic of Fiber Section Discretization of Cross-Sections

As illustrated in Figure 4-1, sections considered in this study were subdivided into smaller regions (fibers) for which the material stress-strain response is integrated to give the resultant behavior.

Thickness of the fibers,  $t_{fiber}$  was consistently taken as  $5 \times 10^{-3}$  inches for all the FE models presented herein. For W-Shapes, fillets are neglected and the required number of fibers was calculated, and then assigned to the web and the flange.

#### 4.2.2 Corotational Transformation

In order to account for geometric nonlinearity, the geometric transformation object that is available in OpenSees, the so-called “corotational transformation” was used. In this procedure, the beam element stiffness and internal forces are transformed from the basic (reference) system to a global coordinate system. According to De Sousa



(2000), geometrically nonlinear systems can be analyzed using this formulation in which rigid–body displacements are set apart from element deformations by attaching a reference coordinate system that rotates and translates with the element throughout the deformation.

### **4.2.3 Selection of Beam Element**

Among the variety of element types available in the OpenSees library, a force-based “Nonlinear Beam–Column Element” was selected for use in this study. This element, which was proposed by Neuenhofer and Filippou (1998) utilizes force interpolation functions for varying internal forces due to transverse displacements and explicitly satisfies equilibrium in the deformed shape. The spread of plasticity is considered along the length of the element. Considering both geometric and material nonlinearity in the problem, the use of this element type, in conjunction with fiber section and corotational transformation objects in OpenSees, has been proposed by Scott et al (2008).

The number of elements along the length of the beam models was consistently taken as one hundred (100) throughout the FE analyses presented herein.

### **4.2.4 Material**

A uniaxial elastic–perfectly plastic material model, as shown in Figure 4-2 was used for all the FE models.

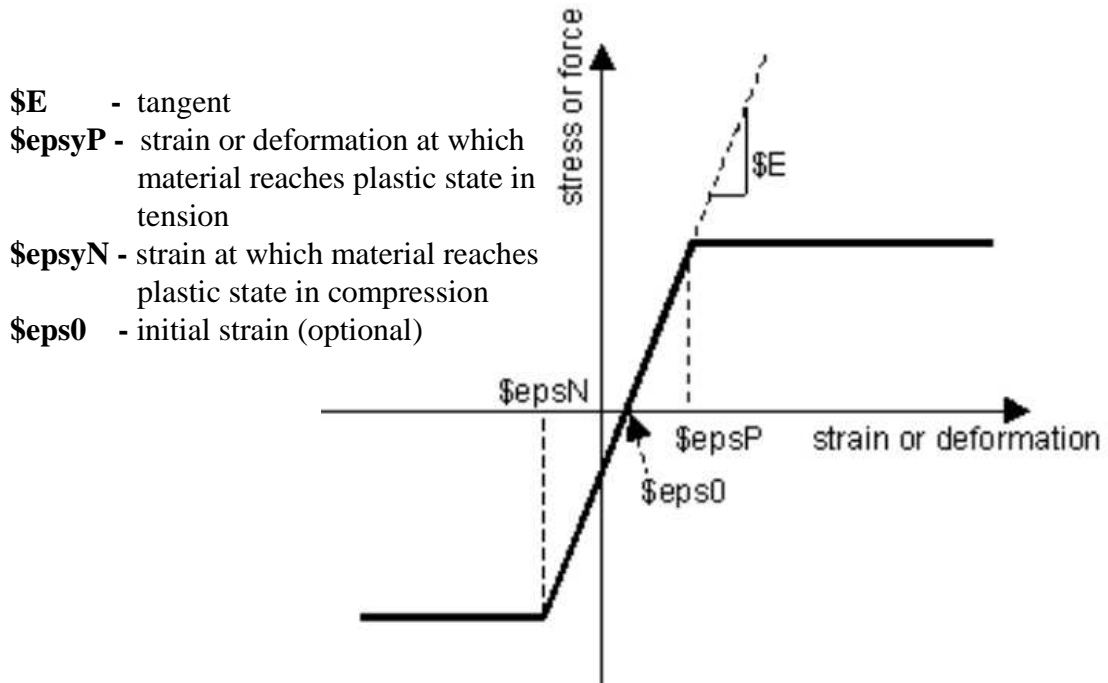


**Figure 4-2** Uniaxial Elastic–perfectly plastic material

(<http://opensees.berkeley.edu/OpenSees/manuals/usermanual/index.html>)

#### 4.2.5 Loading and Analysis

The static “Displacement Control” analysis object available in OpenSees was used throughout the FE analyses presented herein. In this type of analysis, an appropriate midspan transverse displacement increment is given as an input. The applied external load is also inputted as the corresponding plastic collapse load for each load case considered ( $P_c$  or  $q_c$ ). For the standard case considered here (fully fixed beams spanning  $2L$ ), these plastic collapse loads are calculated with use of the theory of plasticity and given as:

- $P_c = \frac{4M_p}{L}$  for beams with a concentrated load at midspan

- $q_c = \frac{4M_p}{L^2}$  for beams with a uniformly distributed load along the length.

where  $M_p$  was calculated neglecting the fillets.

As a result, at each step, using a given displacement increment, OpenSees provides the external load as a fraction of the corresponding plastic collapse load inputted

$$\left(\frac{P}{P_c} \text{ or } \frac{q}{q_c}\right).$$

Typical OpenSees input files for the concentrated load case and the distributed load case are provided in Appendices B1 and B2, respectively.

### 4.3 Preliminary FE Analyses

The theoretical fundamentals of rigid–plastic and cable behavior for ductile steel beams with idealized boundary conditions were presented in Chapter 3. Here in Chapter 4, a set of preliminary nonlinear FE analyses on steel beams with similar load and geometric configuration is described, with an emphasis on the fixed-fixed beams. The primary objectives of this section are as follows:

- Verify the theoretical behavior predicted by each theory.
- Generate FE analysis results using elastic-perfectly plastic material properties and compare to theoretical results.

#### 4.3.1 Approach

The approach taken to accomplish the objectives of this section is given next.

- Comparison with Rigid–plastic Theory:

In order to enable a direct comparison of FE analysis results with the rigid-plastic theory, a simple approach that involves the use of various values of Young's Modulus of Elasticity,  $E$ , was used, with a value of 29,000 ksi for steel as the benchmark case.

- Comparison with Cable Theory:

As noted earlier, theoretically pure cable behavior may be anticipated for infinitely long beams. In order to enable a comparison of FE analysis results with the cable theory, rather large span lengths were assigned.

- Presentation of results:

The preliminary FE analysis results are presented graphically in comparison with theoretical results. For comparison with the rigid-plastic theory, the following plots are

shown: normalized external load,  $P/P_c$  (or  $q/q_c$ ), versus normalized deflection,  $W/d$ ,

normalized axial force,  $N/N_p$ , versus normalized deflection,  $W/d$ , normalized moment,

$M/M_p$ , versus normalized deflection,  $W/d$ , and normalized  $M-N$  interaction

( $N/N_p$  versus  $M/M_p$ ). For comparison with cable theory, the following plots are shown:

external load,  $P$  (or  $q$ ) versus normalized deflection,  $W/L$ , normalized axial force, ,

versus normalized deflection,  $W/L$  and normalized  $M-N$  interaction ( $N/N_p$  versus

$M/M_p$ ).  $M$  and  $N$  are typically given at midspan, unless noted otherwise.

### 4.3.2 Description of Preliminary FE Models

Figure 4-3 shows a schematic of the beam models considered in the preliminary FE analyses. The beam which is fixed at its ends is modeled with 100 nonlinear beam-column elements along the length.

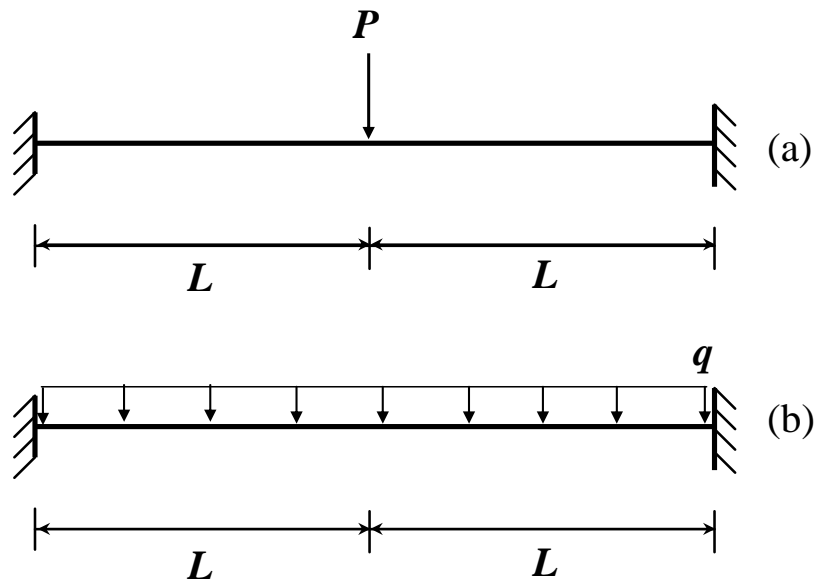


**Figure 4-3** Schematic of preliminary FE beam models

The cross-section of the beam was chosen as either W-Shaped or rectangular. When a W-Shaped cross-section was used, a first floor W30x124 beam section was used as typical (Khandelwal and El-Tawil 2007), whereas a rectangular cross-section was selected in such a way that it gave approximately the same plastic section modulus,  $Z_x$ , as a W30x124. As a result, the rectangular section chosen had a unit width of 1 inch and a nominal depth,  $d$ , of 40 inches. In addition, a W24x192 was used in some distributed load cases as noted in the relevant sections. Cross-sections were discretized as fiber sections as illustrated in Figure 4-1 with a typical fiber thickness,  $t_{fiber}$ , of  $5 \times 10^{-3}$  inches.

As noted earlier, a uniaxial elastic–perfectly plastic steel material model was used in all cases. The various material yield stresses,  $\sigma_y$ , and span length,  $2L$ , of the beams used in this study are given in Table 4-1. In addition, the elastic moduli used in the FE analyses for comparison with the rigid–plastic theory are given in Table 4-2. In these tables, N/A implies that results for the case given are not available.

**Table 4-1** Summary of Model Parameters in Preliminary FE Models

Models For Comparison with Rigid - Plastic Theory							
Section	Length, $2L$ (in)	$\sigma_y$ (ksi)	$N_p$ (kips)	$M_p$ (k-in)	$P_c$ (k)	$q_c$ (k/in)	
REC ( <i>bx</i> d)	1x40	700	58	2320	23200	265.1	0.758
W Shape	W30x124	700	58	2094	23390	267.3	N/A
	W24x192	720	50	2810	27976	N/A	0.863

Models For Comparison with Cable Theory					
Section	A (in <sup>2</sup> )	Length, $2L$ (in)	$\sigma_y$ (ksi)	$N_p$ (kips)	
REC ( <i>bx</i> d)	1x40	40.0	$7.2 \times 10^6$	50	2000
W Shape	W30x124	36.1	$7.2 \times 10^6$	50	1805

**Table 4-2** Elasticity Modulus

Modulus of Elasticity, E	Concentrated Loading	Uniformly Distributed Loading
E*	√	√
Ex20	√	N/A
Ex50	√	N/A
Ex100	√	√
Ex200	N/A	√

\*E=29000 ksi (Benchmark Case)

### 4.3.3 Comparison of Results with Rigid–Plastic Theory

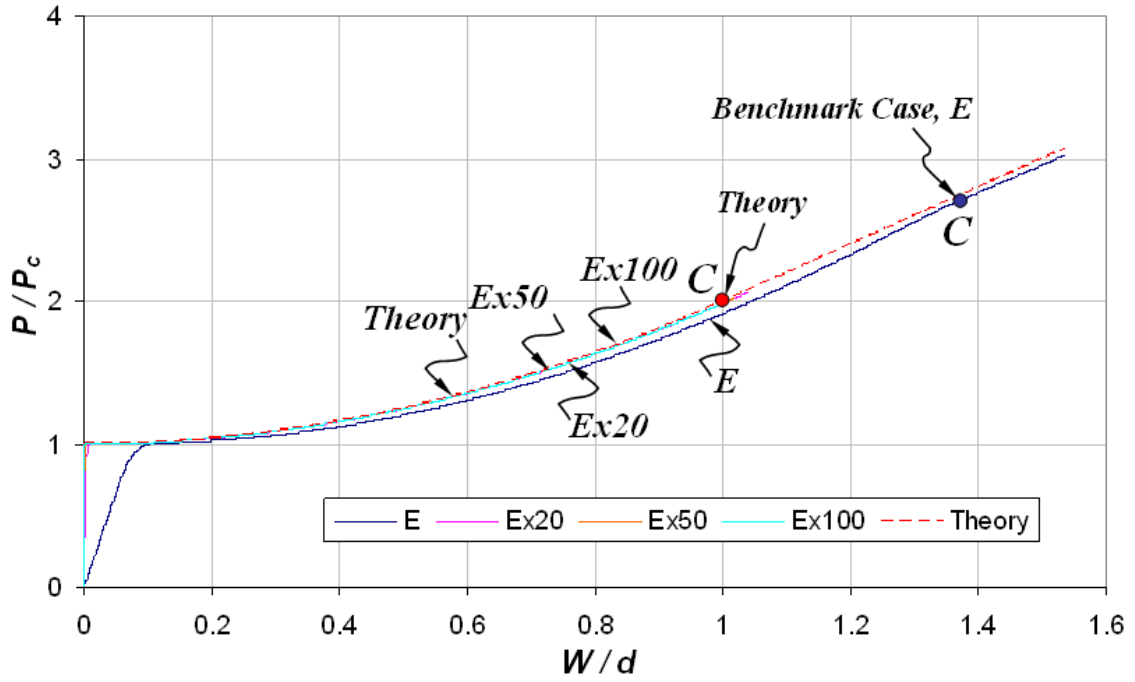
The beam shown in Figure 4-3 was modeled and analyzed in OpenSees with the parameters given in Table 4-1 for different elastic moduli as specified in Table 4-2. The presentation of results is broken into the two load cases considered with rectangular and W–Shapes.

### 4.3.3.1 Concentrated Load Case

Analysis results for the beam shown in Figure 4-3(a) are given in comparison with rigid-plastic theoretical results for each cross-section considered.

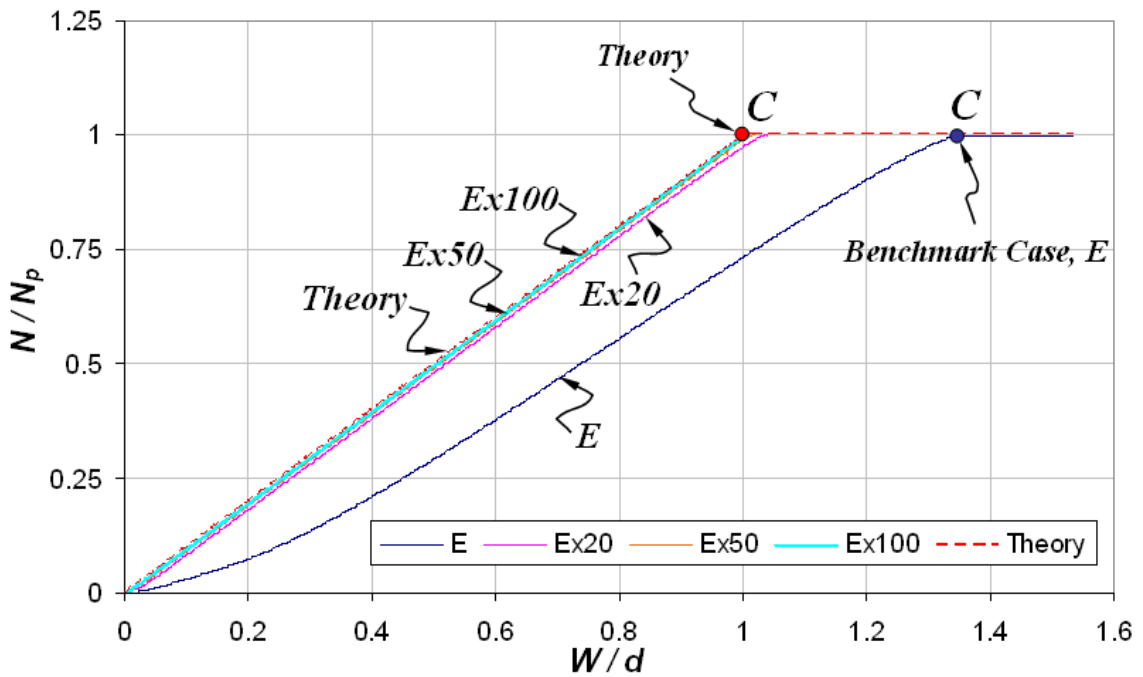
#### 4.3.3.1.1 Beam with Rectangular Cross-Section

FE analysis results for the beam shown in Figure 4-3(a) with a rectangular cross-section are presented in comparison with theoretical results in Figures 4-4, 4-5 and 4-6. The onset of pure cable behavior is referred to in these figures as Point “C” for the benchmark case and the theoretical cases. Figures 4-4 through 4-6 show that there is a significant difference between theory and FE analysis in predicting the onset of pure cable behavior. According to rigid-plastic theory, pure cable behavior is reached when  $W=d$ , whereas the FE analysis results for the benchmark case predict that pure cable behavior is reached when  $W=1.34 d$ . When large values of  $E$  are used, it can be seen that the point of pure cable behavior approaches that predicted by theory.



Note: C is the onset of point of pure cable behavior

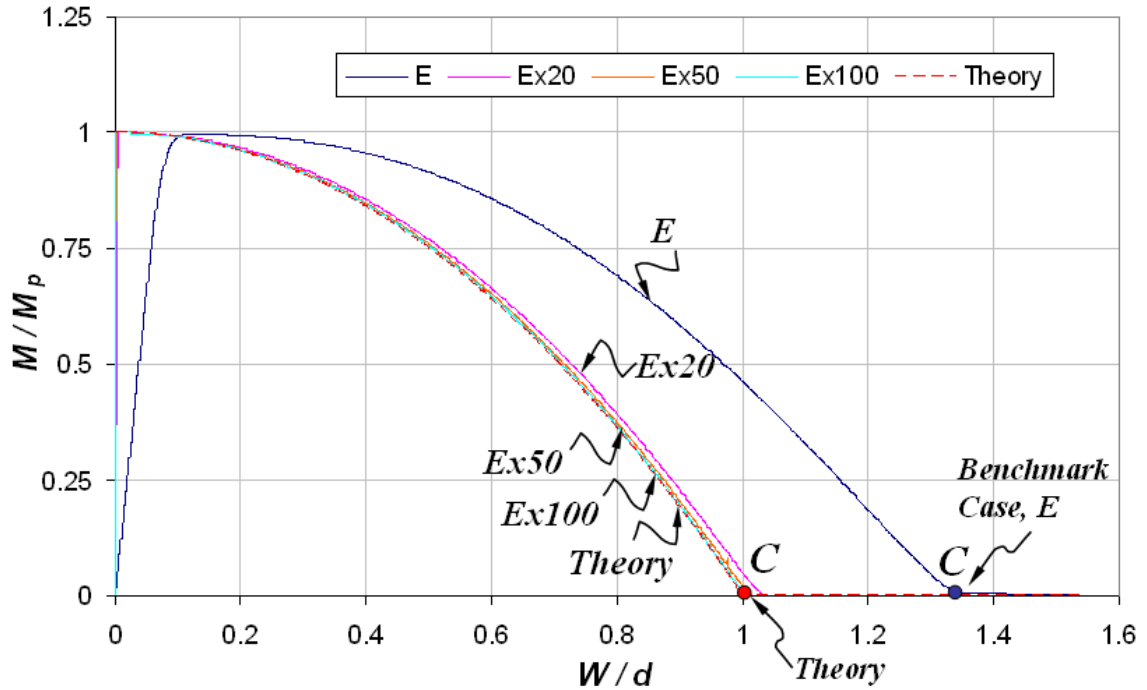
**Figure 4-4** Normalized Load-Deflection Plot



Note: C is the onset of point of pure cable behavior

**Figure 4-5** Normalized Axial Force-Deflection Plot (Midspan)





Note: *C* is the onset of point of pure cable behavior

**Figure 4-6** Normalized Moment–Deflection Plot (Midspan)

Another comparison can be made on the normalized  $M$ – $N$  interaction plot shown in Figure 4-7. The theoretical point for the onset of the flexural mechanism condition is indicated as Point “A” whereas Point “C” represents the point of pure cable behavior. It can be seen that the beam models with large  $E$  almost follow the path predicted by the rigid–plastic theory. On the other hand, the benchmark case,  $E$  reaches Point A before developing full  $M_p$ . The reason is that the axial force developed in the elastic regime causes a plastic hinge under combined  $M$  and  $N$ . As a result, the benchmark case representing the actual behavior reaches pure cable behavior at a significantly larger transverse deflection than predicted by the rigid-plastic theory.

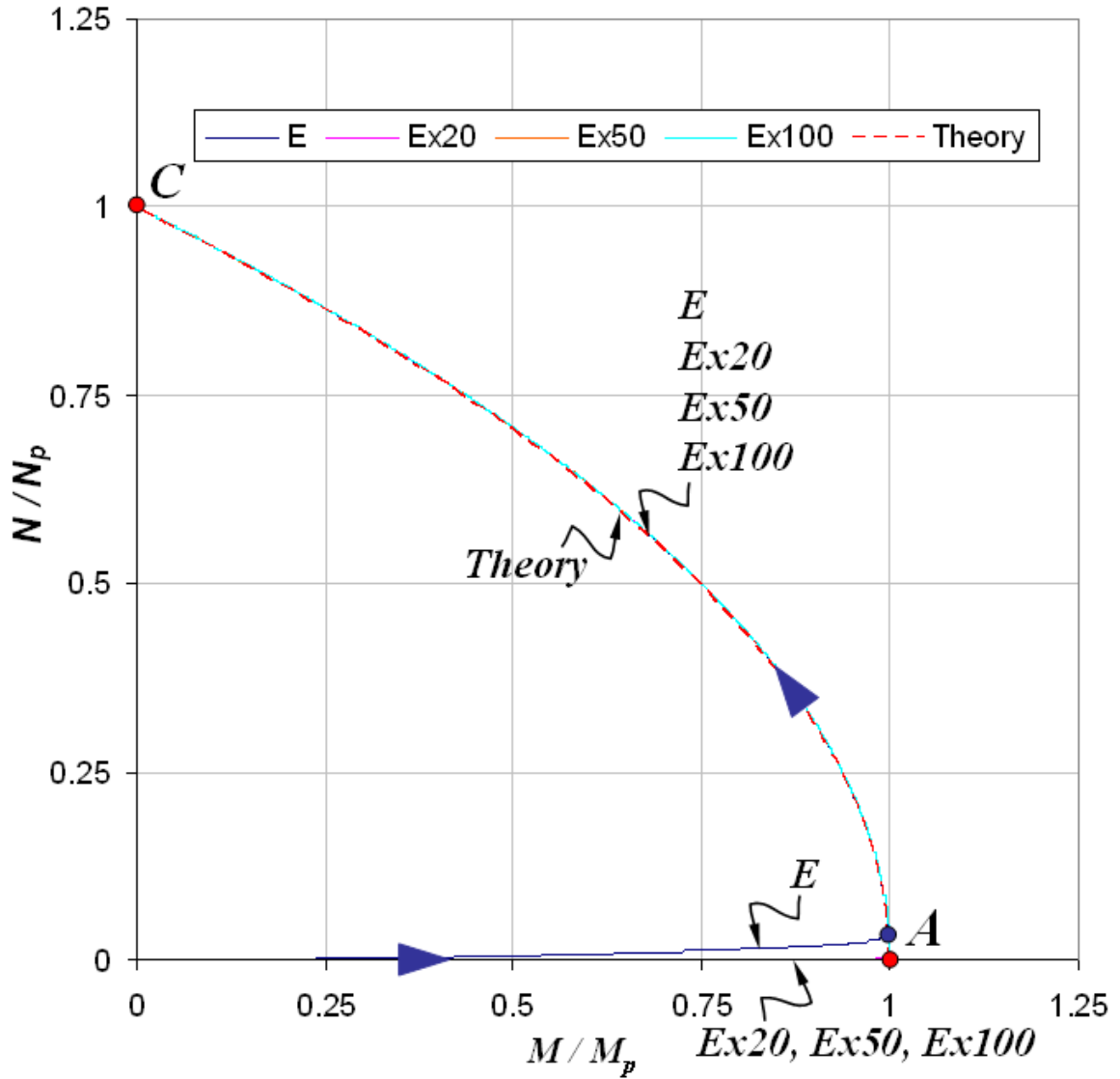
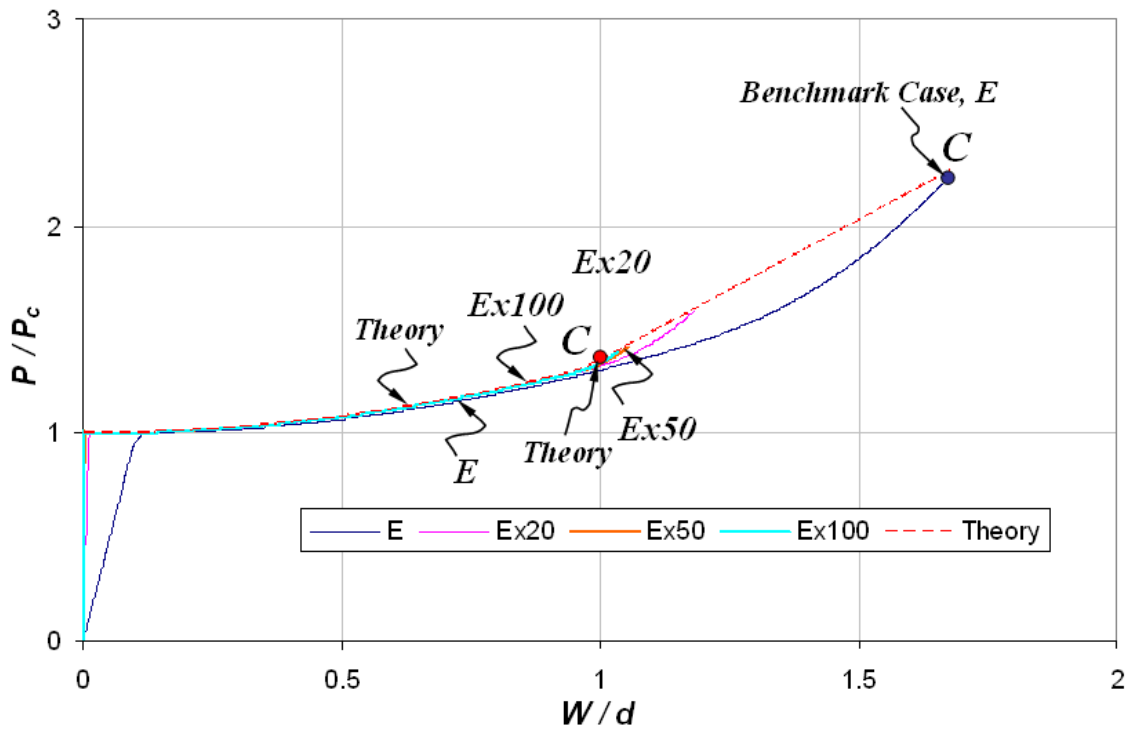


Figure 4-7 Normalized  $M-N$  interaction Plot (Midspan)

#### 4.3.3.1.2 Beam with W-Shape Cross-Section

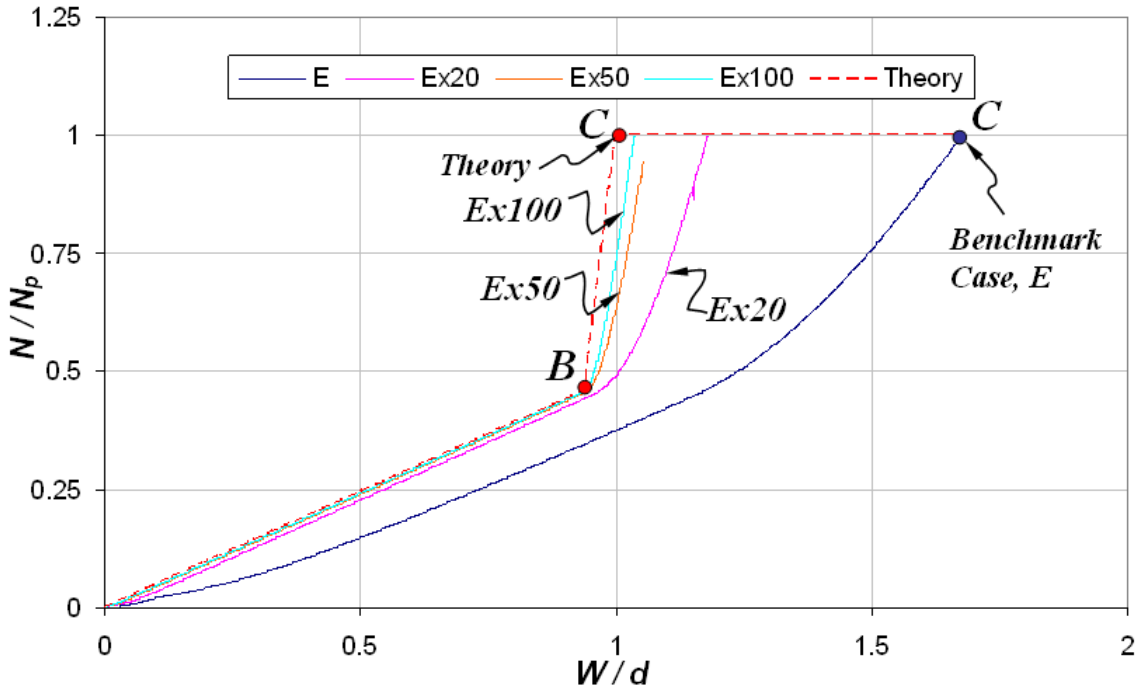
FE analysis results for the beam shown in Figure 4-3(a) with a W30x124 cross-section are presented in Figures 4-8 through 4-11. The point of pure cable behavior is referred to in these figures as Point “C”. In addition, the theoretical Point B where the PNA is at the interface between the web and flange is also shown in the normalized axial force versus the normalized deflection and normalized moment versus normalized

deflection plots shown in Figures 4-9 and 4-10, respectively. In general, similar comparison statements can be made as for the rectangular cross-section results. As can be seen in these figures, the primary difference between the theoretical and benchmark cases is that  $E$  is again observed to greatly affect the prediction of the point of pure cable state (Point C). According to theory, pure cable behavior is reached when  $W=d$  for W-Shapes, whereas the FE analysis results for the benchmark case predict that pure cable behavior is reached when  $W=1.68 d$ . When large values of  $E$  are used though, it can be seen that the point of pure cable behavior predicted by the FE models approaches that predicted by theory.



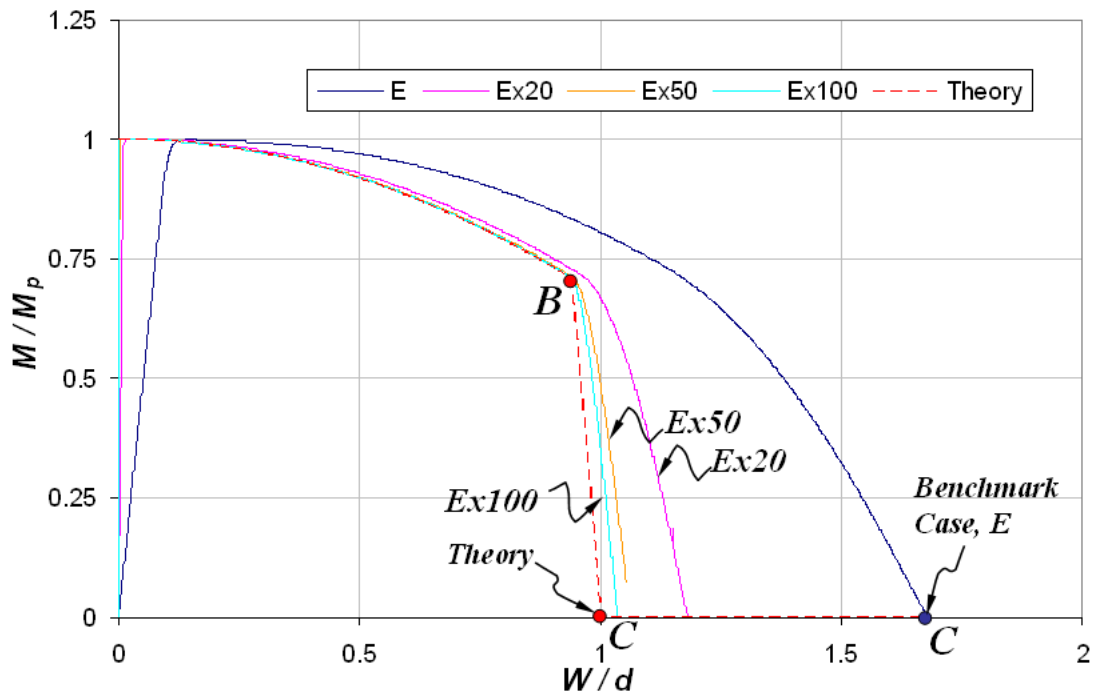
Note: C is the onset of point of pure cable behavior

**Figure 4-8** Normalized Load-Deflection Plot



Note: C is the onset of point of pure cable behavior

**Figure 4-9** Normalized Axial Force–Deflection Plot (Midspan)



Note: C is the onset of point of pure cable behavior

**Figure 4-10** Normalized Moment–Deflection Plot (Midspan)

In addition, it is evident from the  $M-N$  interaction relationship at midspan shown in Figure 4-11 that all cases eventually fall on the yield curve and follow the same path. For the benchmark case, in which  $E=29,000$  ksi, the beam again exhibits substantial transverse deflections in elastic regime and develops axial forces. Thus, the mechanism condition forms under combined  $M$  and  $N$ , as opposed to the prediction by the rigid-plastic theory, where for Point A,  $M=M_p$ .

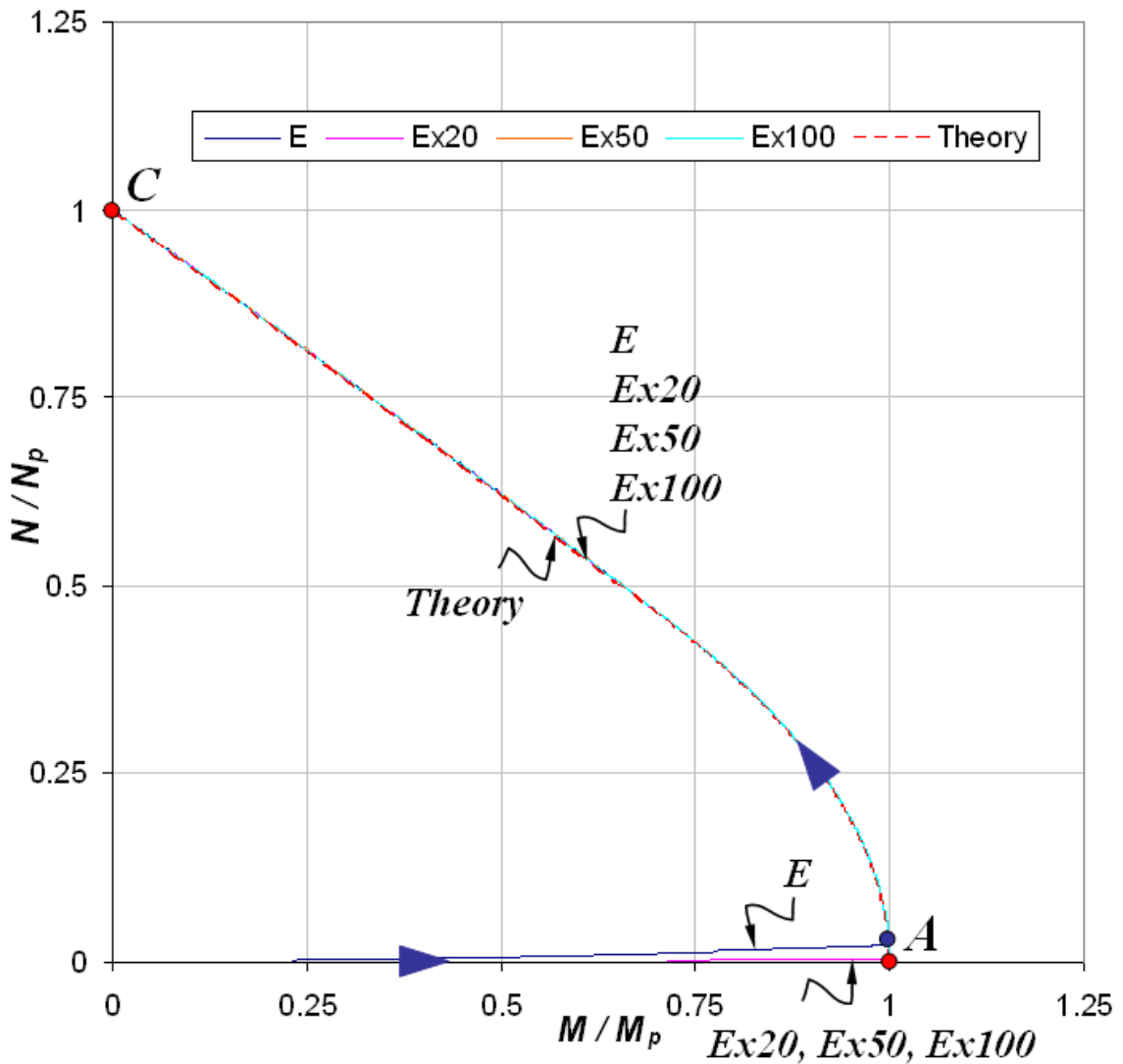


**Figure 4-11** Normalized  $M-N$  interaction Plot (Midspan)

### 4.3.3.2 Distributed Load Case

Preliminary FE analysis results for the beam shown in Figure 4-3(b) are compared to results obtained using the rigid-plastic theory for each of the cross-sections and elastic moduli as given in Tables 4-1 and 4-2, respectively.

#### 4.3.3.2.1 Beam with Rectangular Cross-Section

FE analysis results for the beam shown in Figure 4-3(b) are presented in comparison with result obtained using rigid-plastic theory in Figures 4-12, 4-13 and 4-14. The onset of pure cable behavior is indicated in these figures as points  $C_I$  and  $C_{II}$ , for Theory I and Theory II, respectively, as presented in Chapter 3. According to Theory I, pure cable behavior is reached when  $W=d$ , whereas according to Theory II, pure cable behavior is reached when  $W=2d$ . The FE analysis results for the benchmark case predict that pure cable behavior is reached when  $W=2.32 d$ . For cases when large E values are used, it can be seen that the point of pure cable behavior prediction approaches that predicted by Theory II.

Moreover, Figures 4-13 and 4-14 show that the behavior exhibited by *Ex100* and *Ex200* is in general bounded by the Theory I and Theory II predictions. In particular, it can be noted that Theory I at low  $W/d$  values is tangent to the FE analysis results, which gradually converge to Theory II towards the point of pure cable behavior ( $C_{II}$ ). This can be attributed to the deflected shape transitioning from a triangular shape to a parabolic configuration as discussed in Section 3.2.3. Indeed, Theory I, which was developed based on a triangular deflected shape predicts the behavior well in the early stages, whereas

Theory II which was developed based on a parabolic deflected shape, predicts the behavior well near the point of a pure cable state ( $C_{II}$ ).

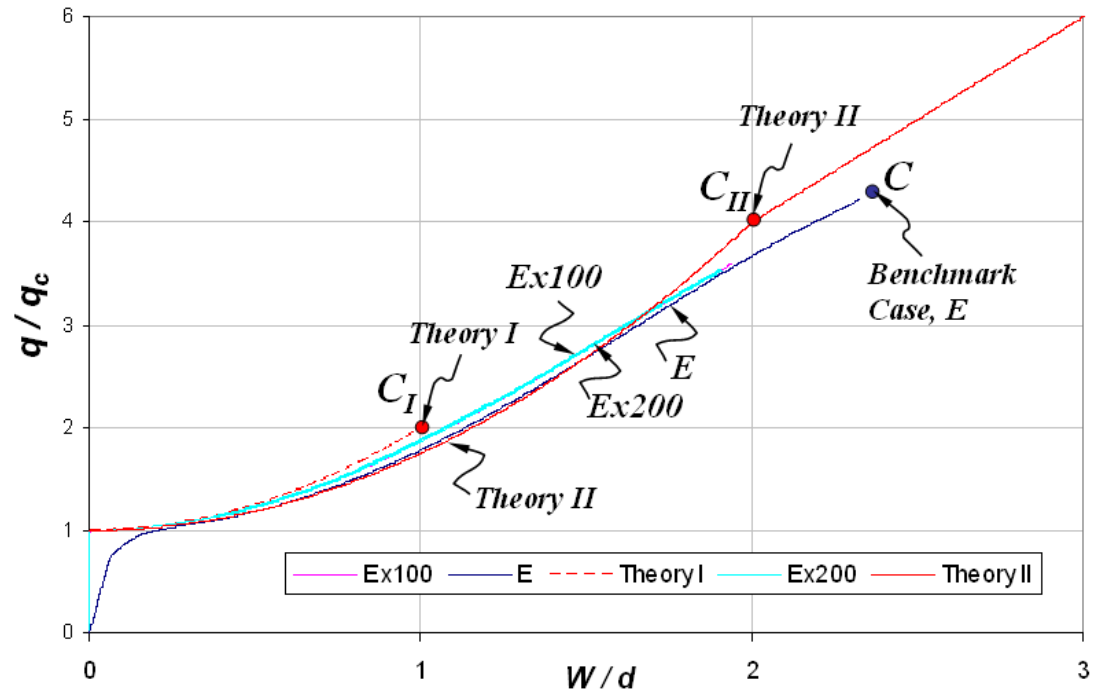


**Figure 4-12** Normalized Load–Deflection Plot

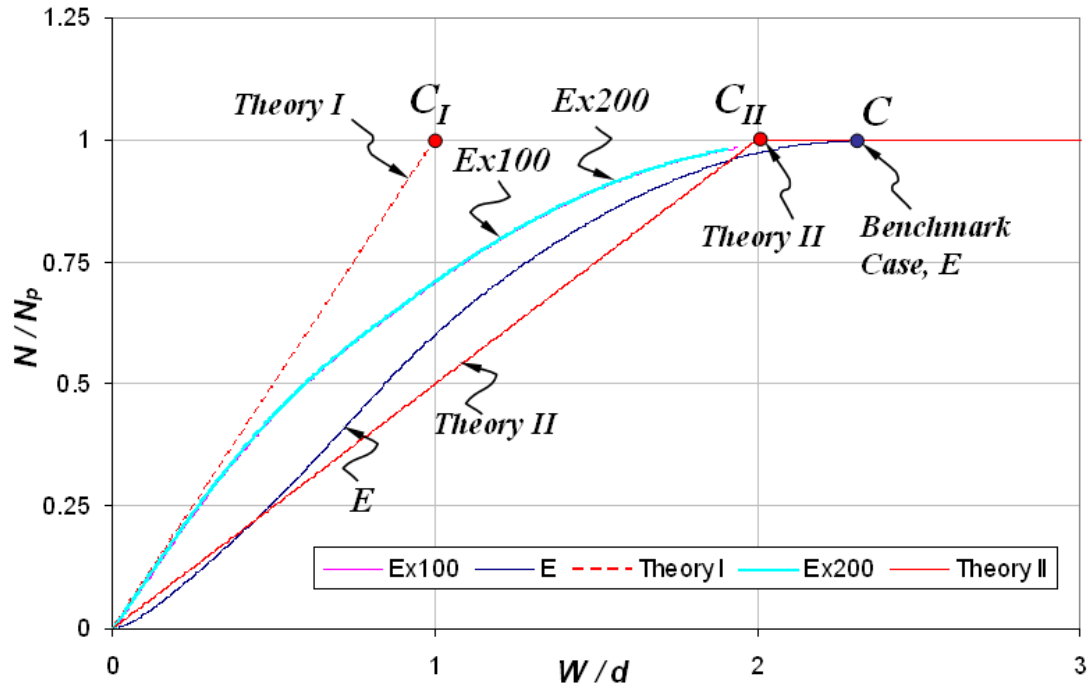


**Figure 4-13** Normalized Axial Force–Deflection Plot (End)

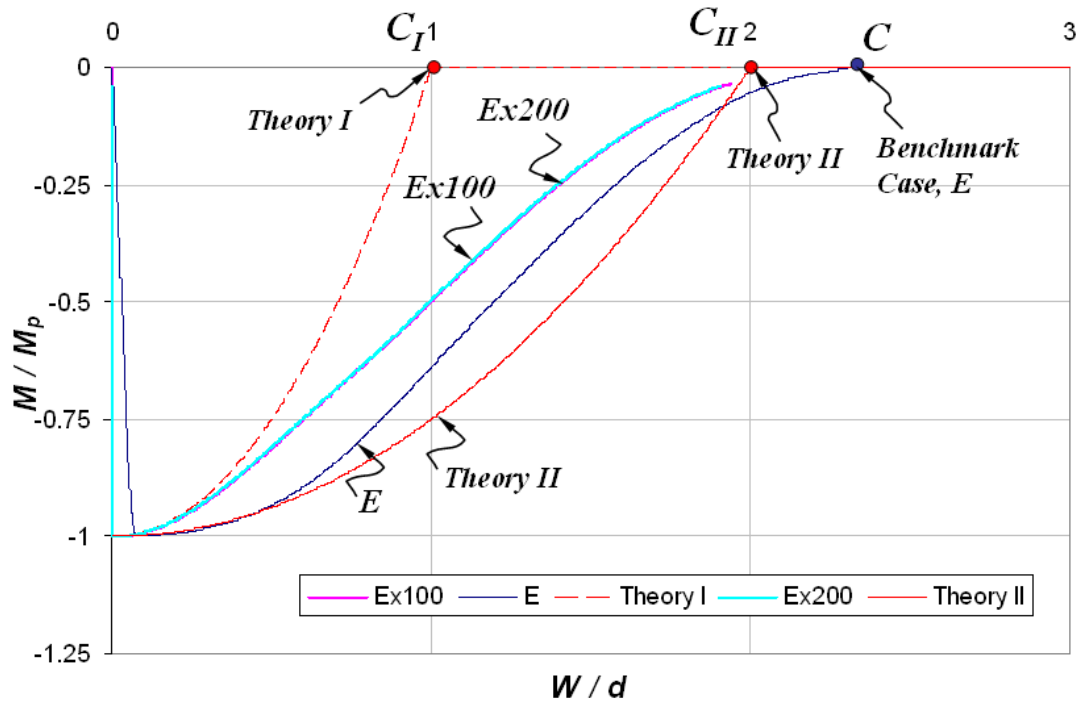


**Figure 4-14** Normalized Moment–Deflection Plot (End)



Normalized  $M-N$  interaction curves are given in Figures 4-15 and 4-16 for an end section and for midspan, respectively. As seen in Figure 4-15, all FE models perfectly follow the yield curve once they reach a flexural mechanism condition (Point A). On the other hand, it is evident from Figure 4-16 that the midspan section indeed develops a plastic hinge once it reaches the mechanism condition (Point A), but does not necessarily follow the yield curve later on.

Recall that, besides the different deflected shape considered, both theories under uniform loading predicted that a midspan plastic hinge is sustained throughout the deformation of the beam. Therefore, neither of theories perfectly represents the actual rigid-plastic behavior predicted by stiffer FE models throughout the deformation.

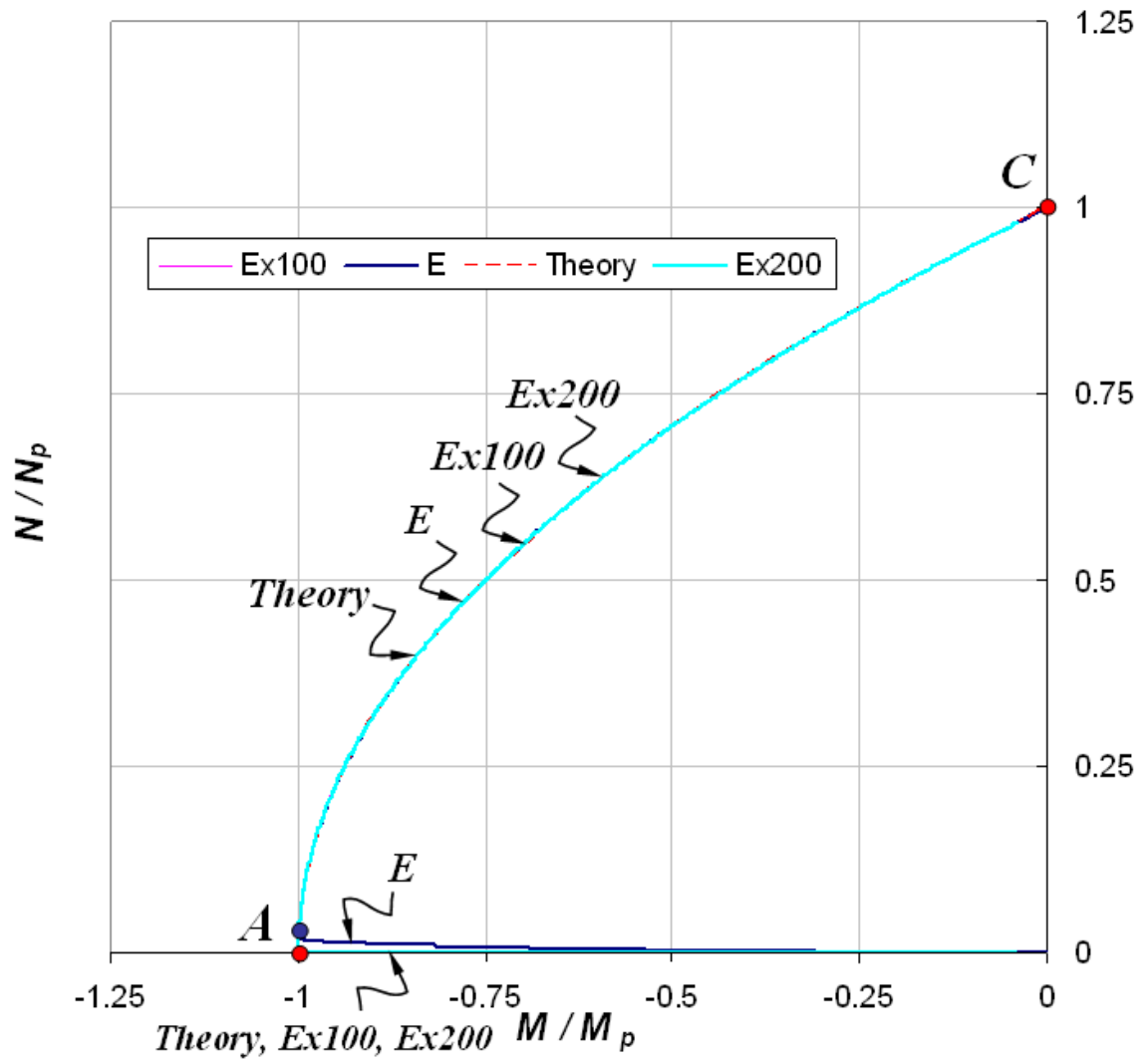
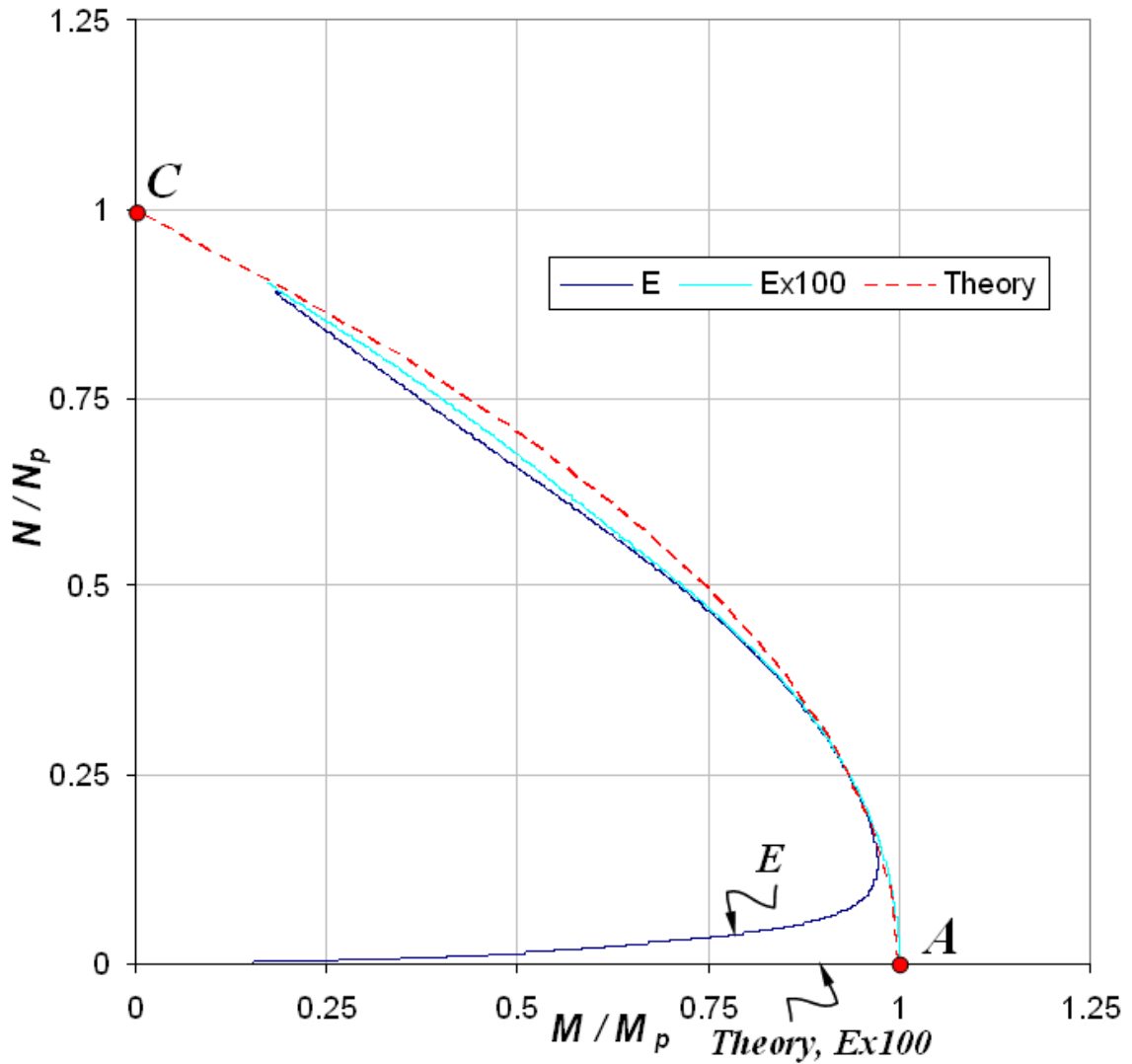


Figure 4-15 Normalized  $M-N$  interaction (End)



**Figure 4-16** Normalized  $M-N$  interaction (Midspan)

#### 4.3.3.2.2 Beam with W-Shape Cross-Section

Under uniform loading, preliminary FE analysis results presented for a beam with rectangular cross-section provided a great deal of understanding as to how the FE models compare with theoretical results. FE analysis results for the beam shown in Figure 4-3(b) with a W24x192 cross-section are presented in Figures 4-17 through 4-21. The point of pure cable behavior is indicated in these figures as Points  $C_I$  and  $C_{II}$  for Theory I and

Theory II, respectively. In addition, the theoretical Point B where the PNA is at the interface between the web and flange, is also shown in the normalized axial force versus normalized deflection and normalized moment versus normalized deflection plots shown in Figures 4-18 and 4-19, respectively. It can be seen in these figures that the difference between theoretical results and those for benchmark case, in which  $E=29,000$  ksi, is again observed to play a significant role in predicting the onset of a pure cable state (Point C). According to Theory I, pure cable behavior is reached when  $W=d$  for W-Shapes, whereas according to Theory II, pure cable behavior is reached when  $W=2d$ . On the other hand, FE analysis results for the benchmark case predict that pure cable behavior is reached when  $W=2.74 d$ . When large values of  $E$  are used, it can be seen that the point of pure cable behavior prediction by FE models somewhat approach that predicted by Theory II.

In addition, as can be seen in Figures 4-18 and 4-19, theoretical prediction of behavior can be considered as the boundaries to the FE models for the *Ex100* and *Ex200* cases. In fact, it can be noted that the results obtained by Theory I at low values of  $W/d$  are tangent to the FE analysis results, which converge to Theory II towards the point of pure cable behavior ( $C_{II}$ ). This result is similar to that described in the discussion of comparison of FE results with theoretical results for rectangular sections in Section 4.3.3.2.1.

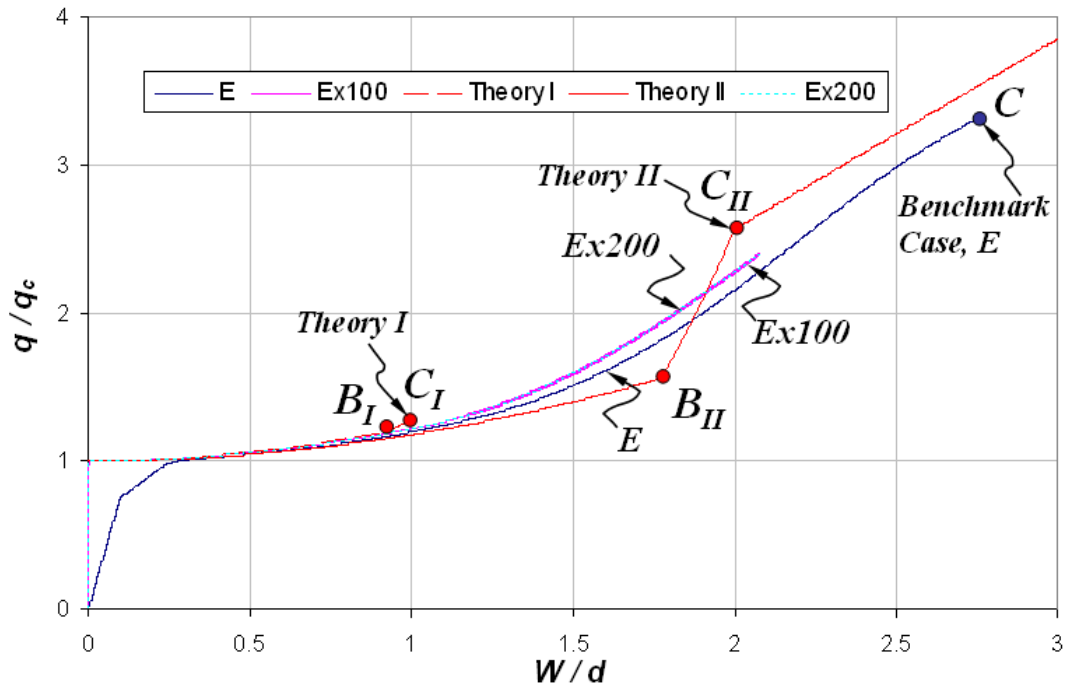


**Figure 4-17** Normalized Load–Deflection Plot

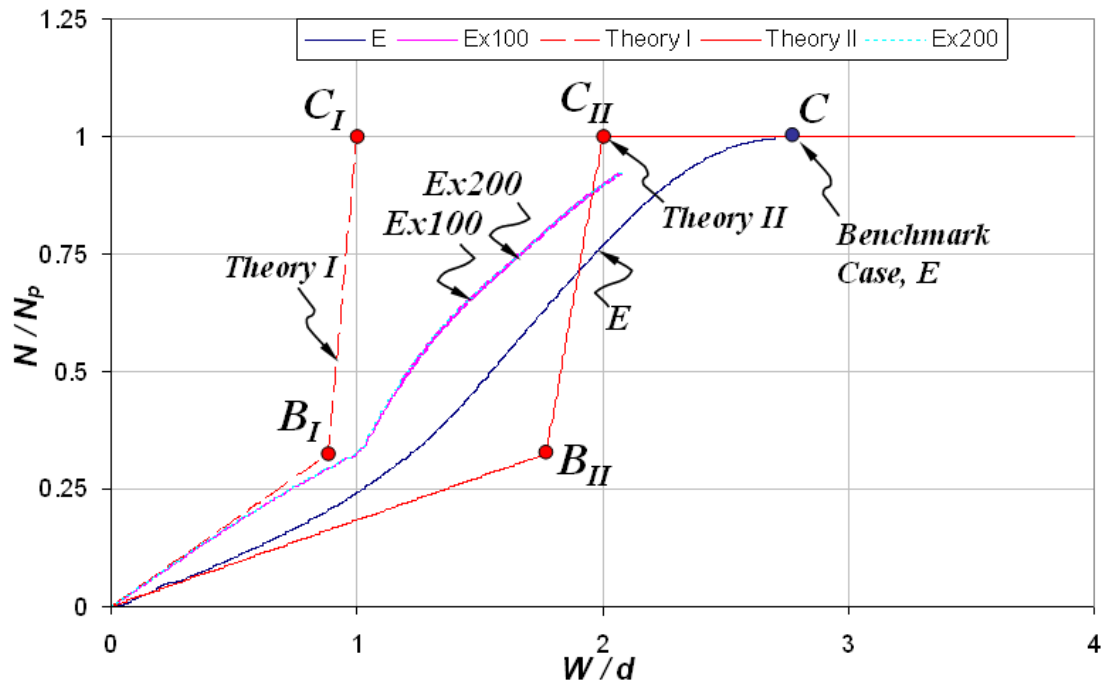


**Figure 4-18** Normalized Axial Force–Deflection Plot (End)

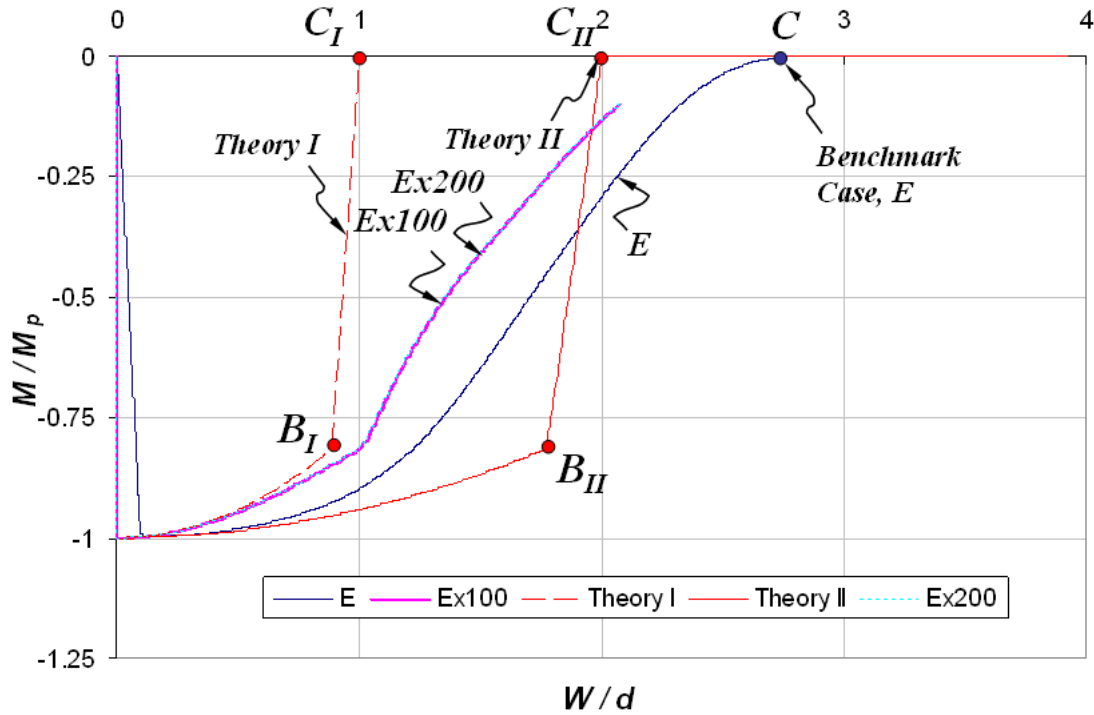


**Figure 4-19** Normalized Moment–Deflection Plot (End)

Normalized  $M$ – $N$  interaction curves are given in Figures 4-20 and 4-21 for an end section and at midspan, respectively. As can be seen in Figure 4-20, all FE models perfectly follow the yield curve once they reach the mechanism condition (Point A), whereas the midspan section indeed develops a plastic hinge once it reaches the mechanism condition (Point A), but does not necessarily follow the yield curve later on, as seen in Figure 4-21.

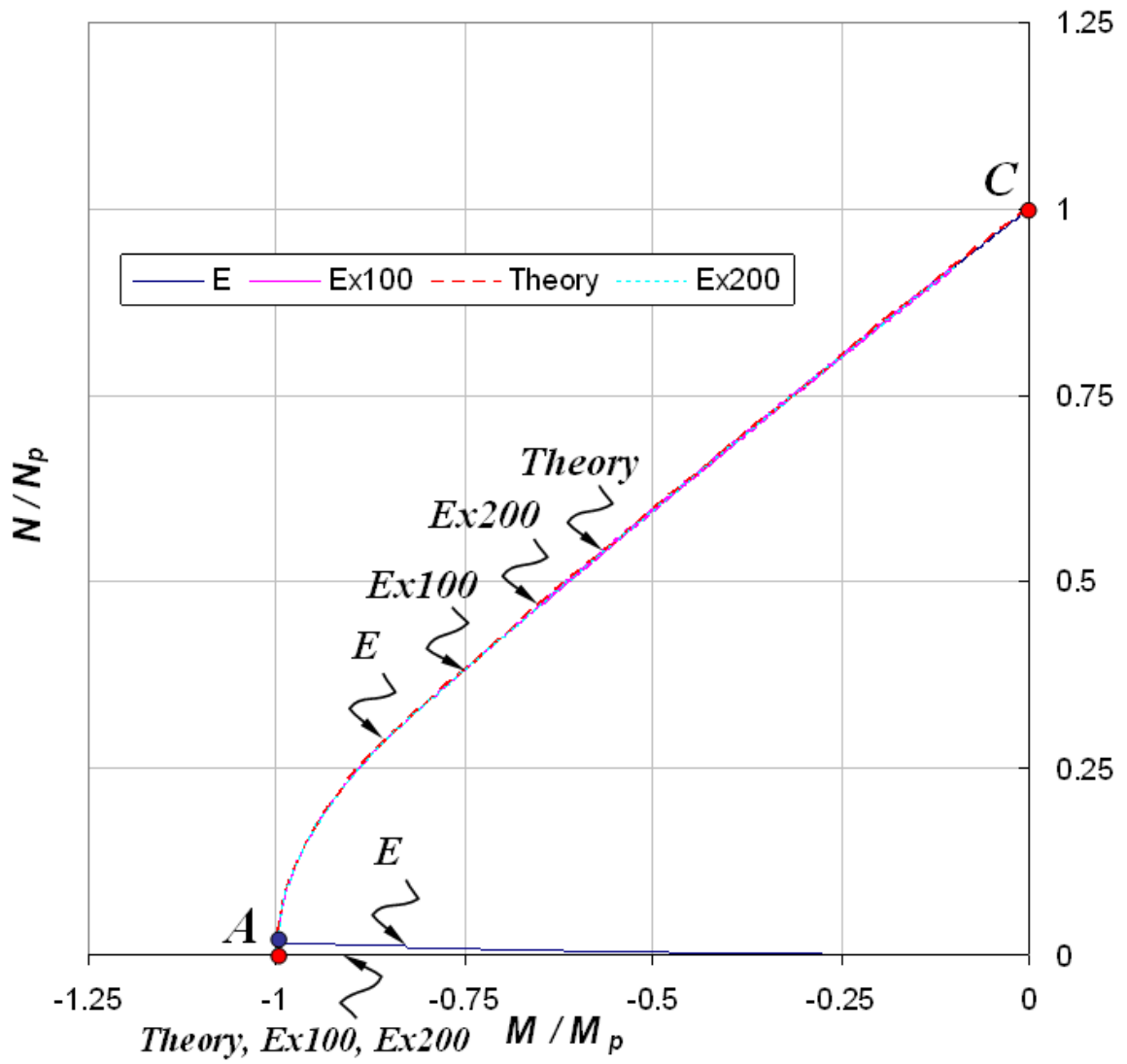
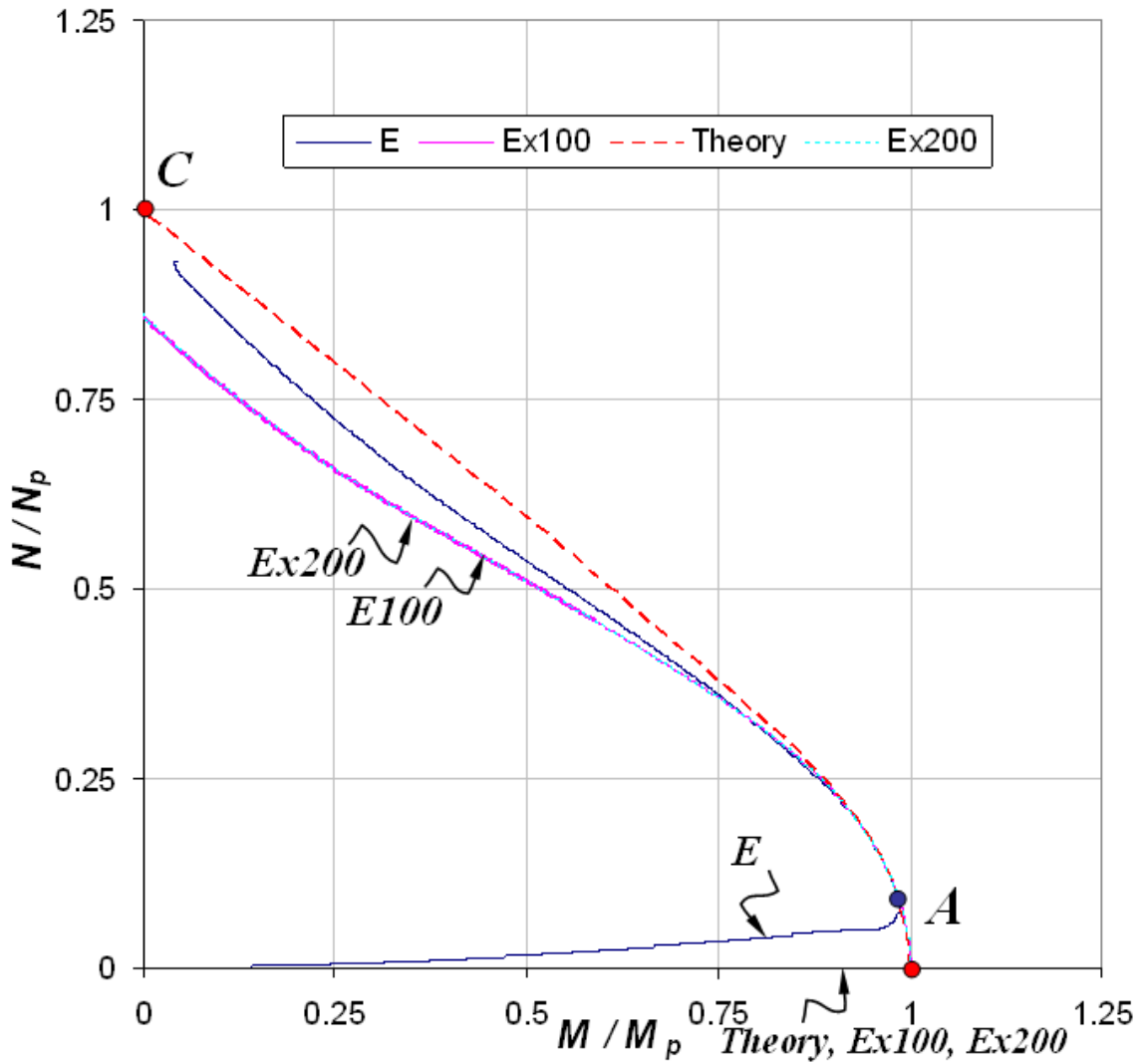


Figure 4-20 Normalized  $M-N$  interaction (End)



**Figure 4-21** Normalized  $M-N$  interaction (Midspan)

#### 4.3.4 Comparison of Results with Cable Theory

The beam shown in Figure 4-3 was modeled and analyzed in OpenSees using the rather large span lengths given in Table 4-1. Results are presented in comparison with theoretical results for the two load cases considered separately. Even though cable theory predicts that the load–deflection characteristics, as well as the midspan deflection at the



onset of pure cable state ( $W_{cat}$ ) are independent of cross-section, FE results for rectangular and W-Shaped cross-sections given in Table 4-1 are considered.

#### 4.3.4.1 Concentrated Load Case

It can be seen from the external load-deflection plot given in Figure 4-22 that the theoretical results are in excellent agreement with FE model results for both cross-section types, in spite of the existence of a small flexural resistance as recognized from the  $M-N$  interaction curves shown in Figures 4-24 and 4-25 for the midspan section of a rectangular beam and a W-Shaped beam, respectively. In fact, the point of pure cable behavior (C) occurs at the exact same deflection as suggested by the theoretical results given by Equation 3-106.

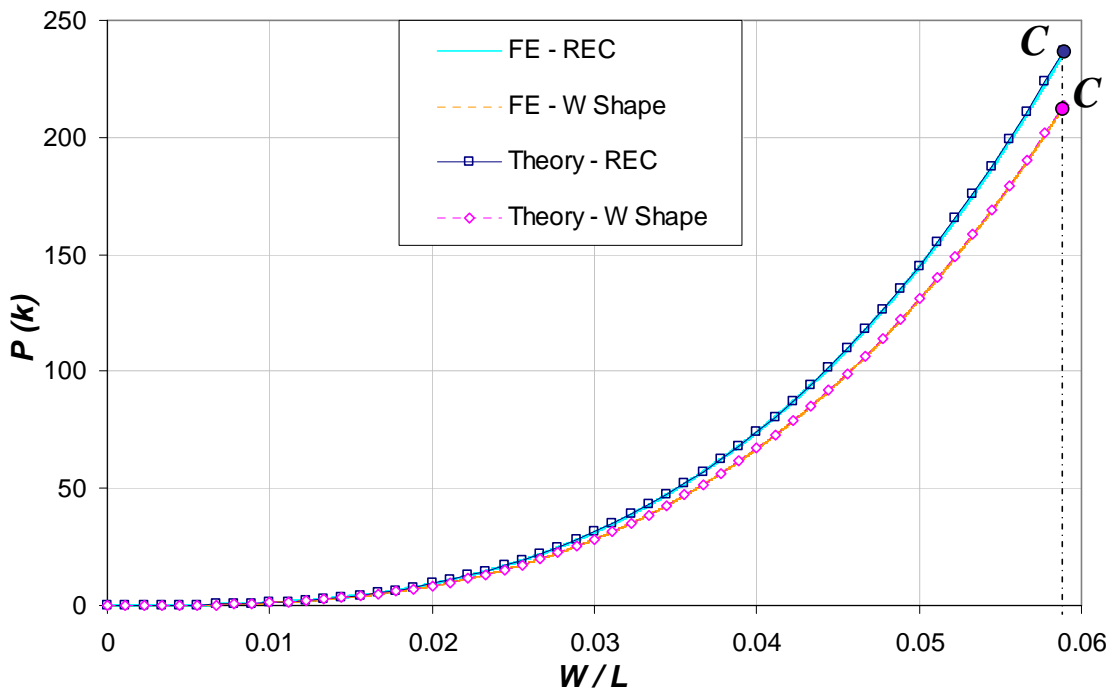


**Figure 4-22** External Load – Normalized Deflection Plot

It should be noted that the slight difference in the load–deflection curves shown in Figure 4-22 for the different cross–section types is due to the difference in cross–sectional area of the beam models as given in Table 4-1. Recall, an area term exists in Equation 3-108 which relates external load  $P$  to normalized transverse deflection,  $W/L$ . On the other hand, all of the curves resulting from FE models and from theory are in a perfect agreement once the axial force,  $N$  is normalized by  $N_p$ , as suggested by Equation 3-105 (Figure 4-23)

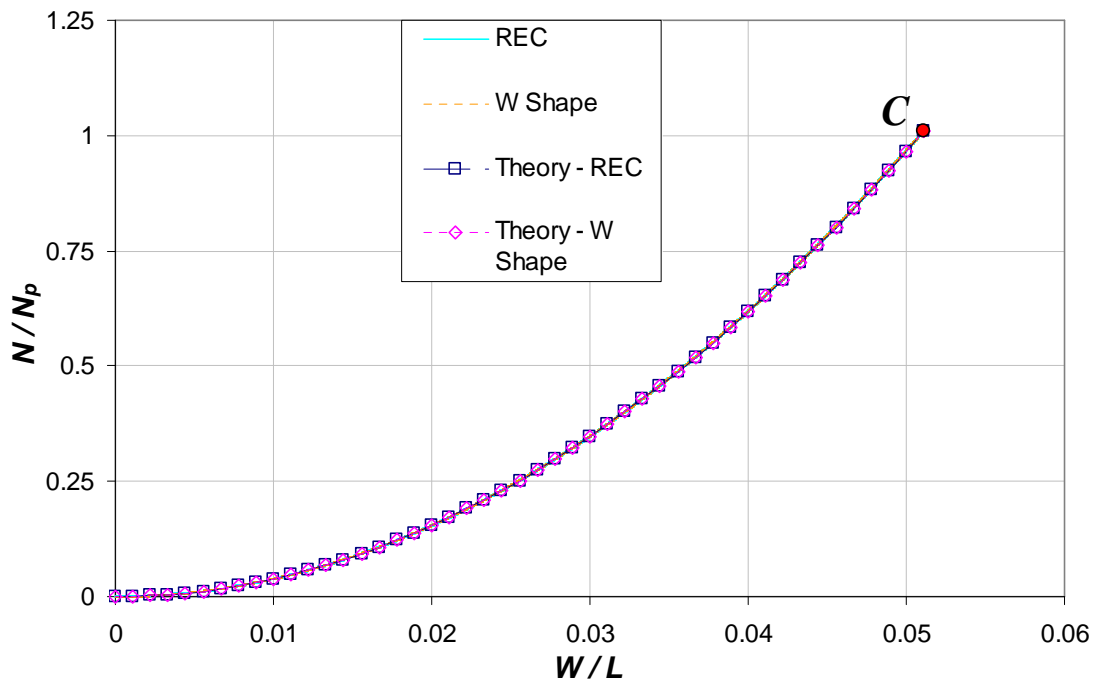


**Figure 4-23** Normalized Axial Force – Deflection Plot (Midspan)

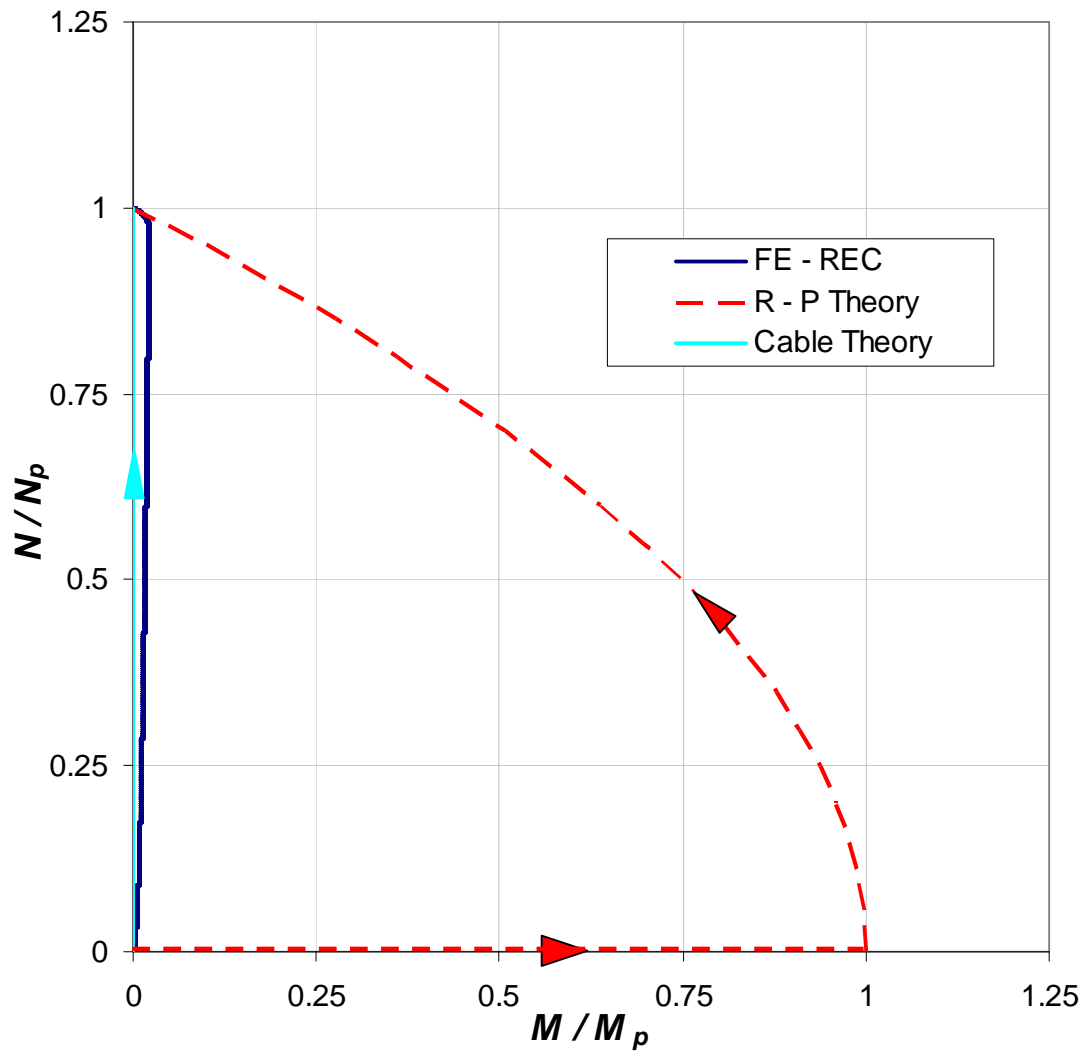


**Figure 4-24** Normalized  $M-N$  interaction (REC Section, Midspan)

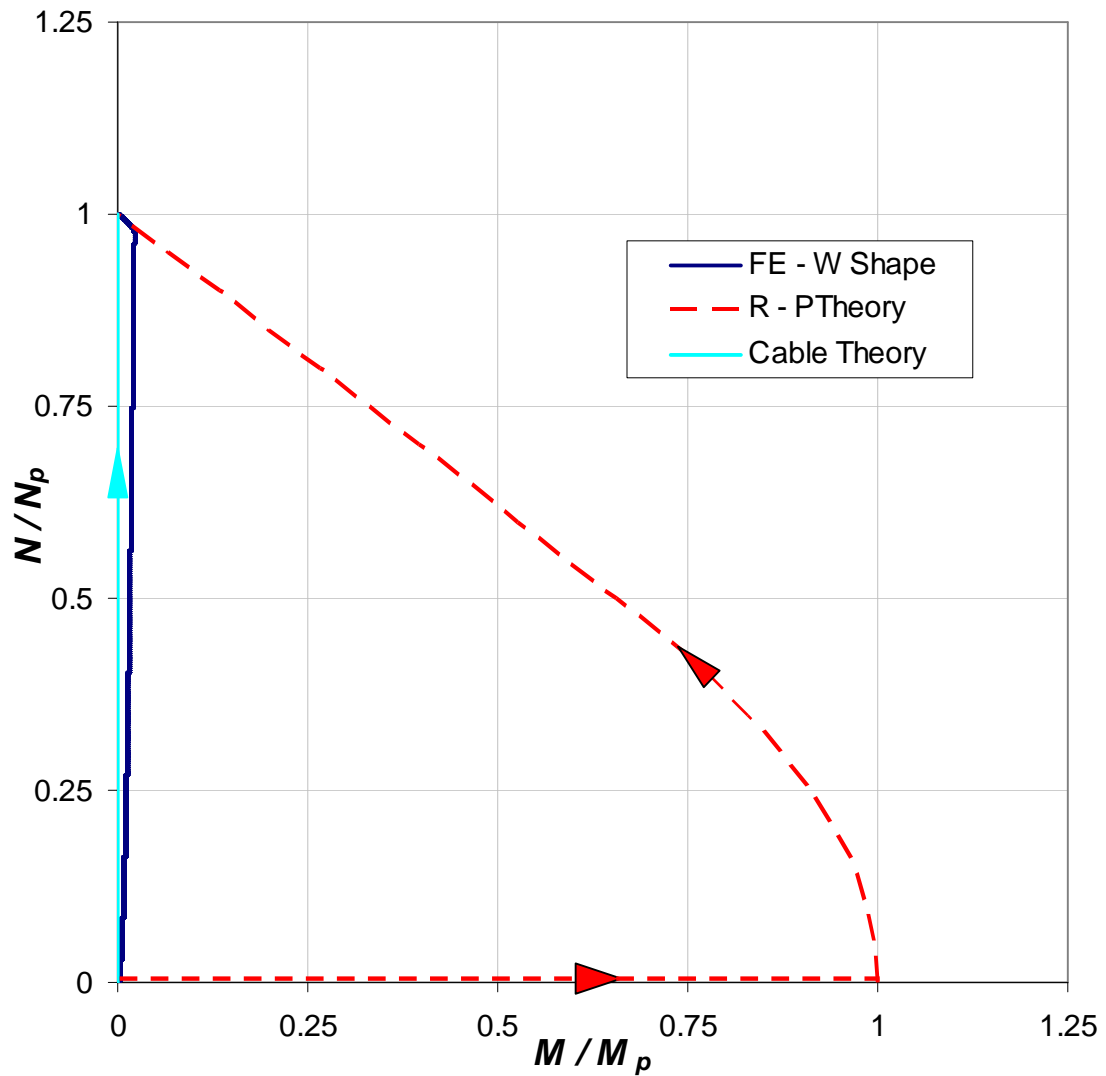


**Figure 4-25** Normalized  $M$ - $N$  interaction (W-Shape, Midspan)

#### 4.3.4.2 Distributed Load Case

Similar to the concentrated load case, FE results were found to be in excellent agreement with the theoretical results. Independence of the onset point of a pure cable state with cross-sectional properties was suggested for this case by Equation 3-112.

Indeed, FE results for Point C perfectly coincide with theoretical results for both beam models as shown in Figures 4-26 and 4-27. It should be noted that the theoretical curves

are based on the proposed value of  $\alpha = 0.816$  to represent the deflected shape configuration in this case, as given in Equation 3-116. Similar to results for concentrated load, a slight difference in cross-sectional area gives two different load–deflection curves corresponding to the different cross-section shapes, as seen in Figure 4-26, whereas normalized load–deflection plot again compares perfectly with theory, as shown in Figure 4-27.

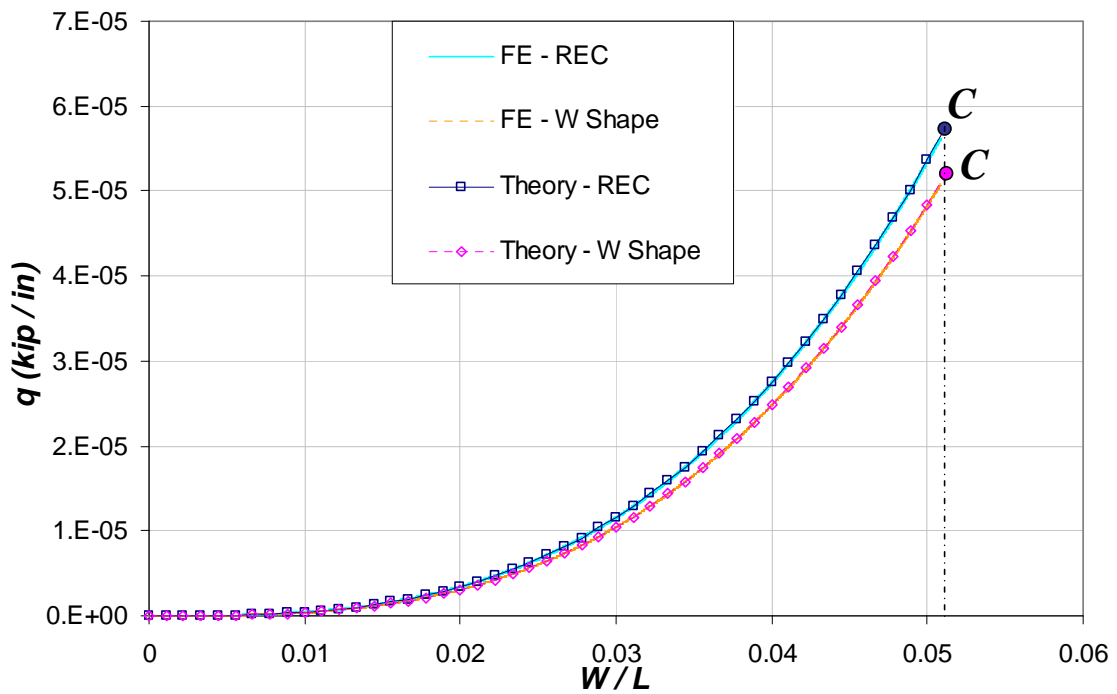


**Figure 4-26** Normalized Load–Deflection Plot

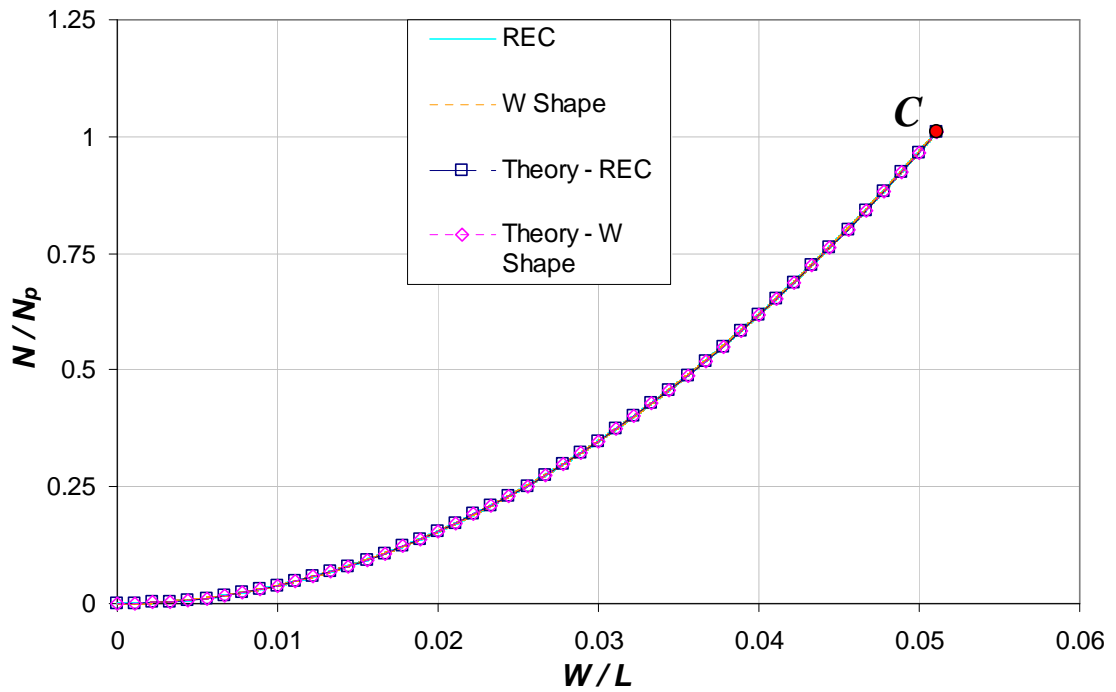


**Figure 4-27** Normalized Axial Force–Deflection Plot

Normalized  $M$ – $N$  interaction curves for rectangular and W–Shaped beams, shown in Figure 4-28 and 4-29, respectively, predict a slight resistance in bending as they hit the yield curve under predominantly axial load, and a slight nonzero bending moment before reaching the pure cable state.

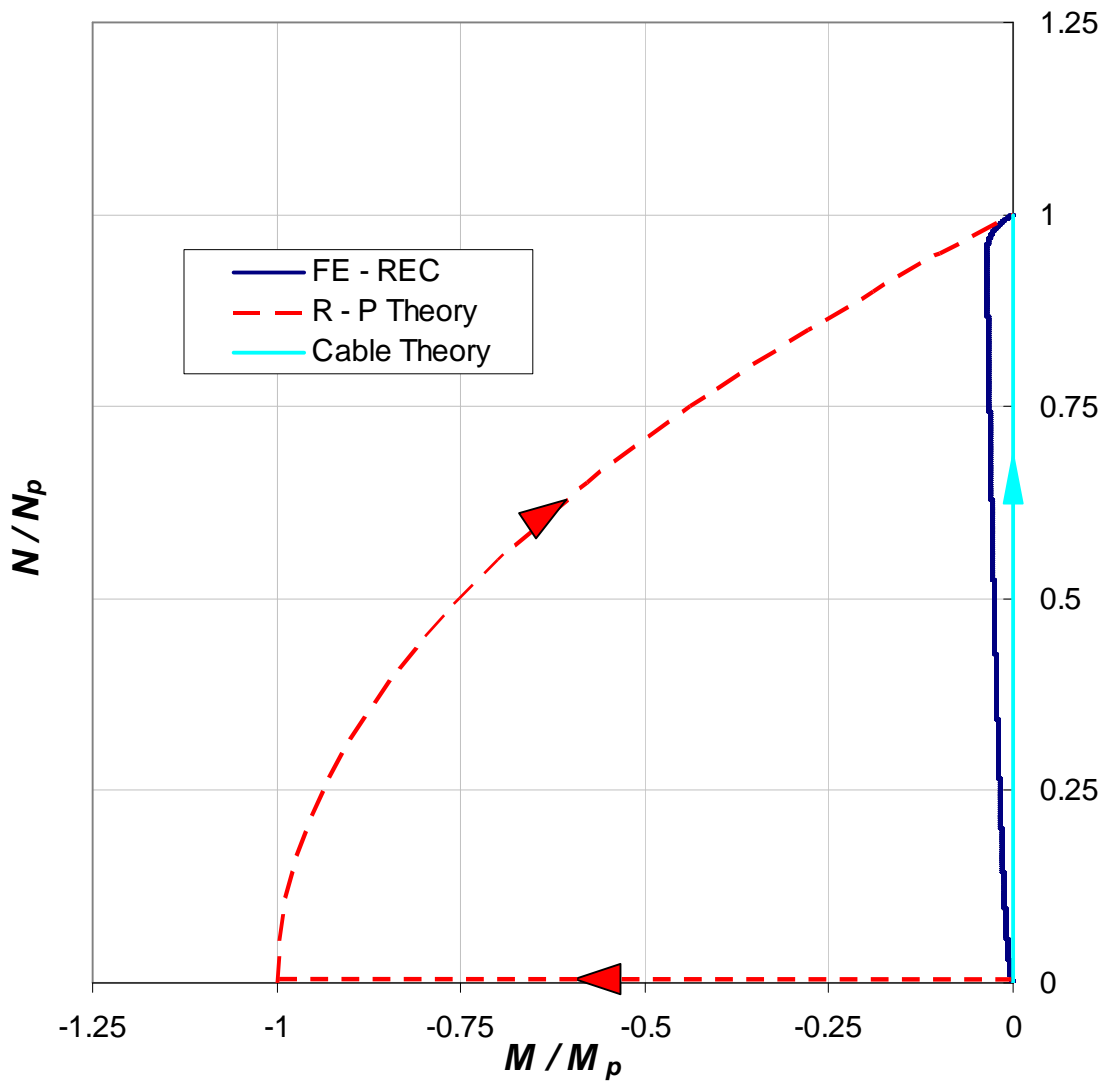


**Figure 4-28** Normalized  $M-N$  interaction (REC Section, End)

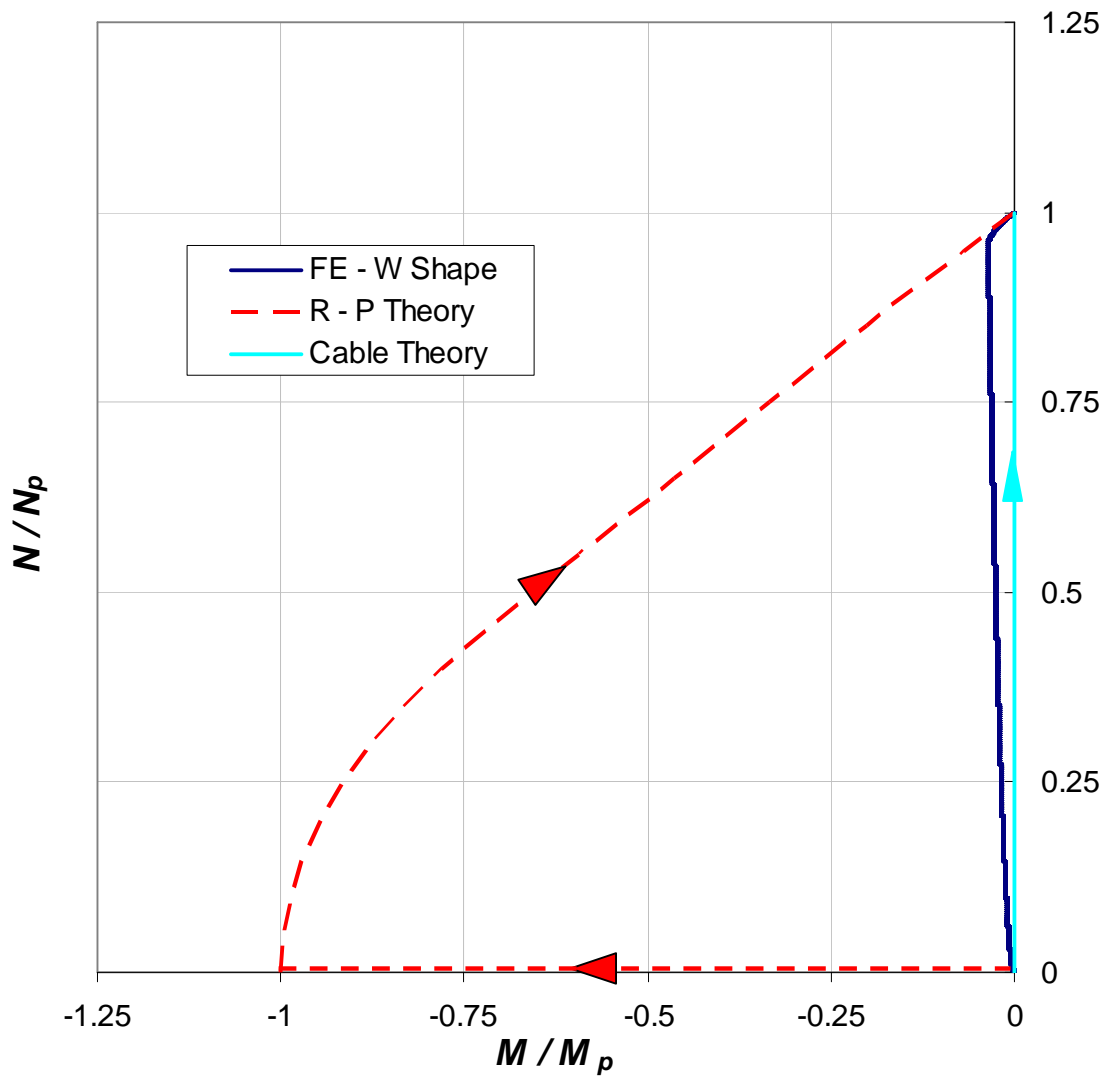


**Figure 4-29** Normalized  $M$ - $N$  interaction (W-Shape, End)

#### 4.3.5 Summary and Conclusion

FE models of rectangular and W-Shaped steel beams, fixed at both ends, were developed and analyzed in OpenSees and the results were compared and discussed with the results from rigid-plastic and cable theories. In general, the results showed that both rigid-plastic and cable theories can be replicated numerically with appropriate FE



modeling. In particular, the transverse deflection at the onset point of pure cable behavior,  $W_{cat}$  predicted by each theory was discussed. Following additional conclusions are made for this study:

- For the concentrated load case, both rigid–plastic and cable theory predictions were explicitly verified using FE modeling. Therefore, the theoretical prediction for the onset point of pure cable behavior presented in Chapter 3 can be used.
- For the distributed load case, FE analysis results showed that Theory I and Theory II set boundaries for the actual behavior, but neither one represents the behavior throughout the deformation. Nevertheless, the point of interest,  $W_{cat}$  suggested by Theory II was verified to be appropriate. FE and theoretical results in regard to the cable theory were in excellent agreement; thus, the theoretical prediction for the onset point of pure cable behavior given in Chapter 3 can also be used.
- Benchmark FE models representing the actual elastic–perfectly plastic beam behavior revealed the substantial effect of elastic deformations with regard to the onset point of pure cable behavior. It was observed that the elastic deformations caused a delay in forming pure cable action compared to rigid–plastic theory prediction.

#### **4.4 Parametric Study**

Preliminary FE analysis results proved the adequacy of the theoretical models developed in Chapter 3. It was seen that the actual elastic–perfectly plastic beam behavior was generally in closer agreement with rigid–plastic behavior. In fact, the effect of elastic deformations was to cause a delay in formation of a pure cable state beyond the one predicted by rigid–plastic theory. Based on this important observation, a parametric study

was conducted with FE analyses in order to identify and study the parameters affecting the formation of pure cable behavior for elastic–perfectly plastic beams.

A beam fixed at both ends was analyzed for the cross-sections and loading conditions considered in Chapter 3.

#### 4.4.1 Approach

Based on the results of the preliminary FE analyses, the onset point of pure cable behavior for elastic– perfectly plastic beams seemed to be predominantly affected by the elastic deformations of the member. In particular, transverse deflections that a beam exhibits in the elastic range result in a lag in  $W_{cat}$  beyond that predicted by rigid–plastic theory.

Rigid–plastic behavior assumes that no deformations take place until the flexural mechanism condition is reached. An elastic–perfectly plastic beam however, deflects prior to reaching a mechanism. As illustrated in Figure 4-30, a beam with full end fixity reaches a flexural mechanism at Point A. Deflection at the plastic collapse load ( $P_c$  or  $q_c$ ) may be associated with the following well known maximum elastic midspan deflection equations for fixed-fixed beams spanning  $2L$ :

$$\delta_{\max} = \frac{P \cdot L^3}{24 \cdot E \cdot I_x} \quad \text{under central concentrated load} \quad [4.1]$$

$$\delta_{\max} = \frac{q \cdot L^4}{24 \cdot E \cdot I_x} \quad \text{under uniform loading along the length} \quad [4.2]$$

For simplicity, the load-deflection relationship for the distributed load case is idealized as illustrated by the dotted line in Figure 4-30(b). Therefore, substituting the plastic collapse

loads,  $P_c = \frac{4M_p}{L}$  and  $q_c = \frac{4M_p}{L^2}$  for concentrated and uniform loading into Equations 4.1

and 4.2, respectively, gives the same expression for  $\delta_p$  as:

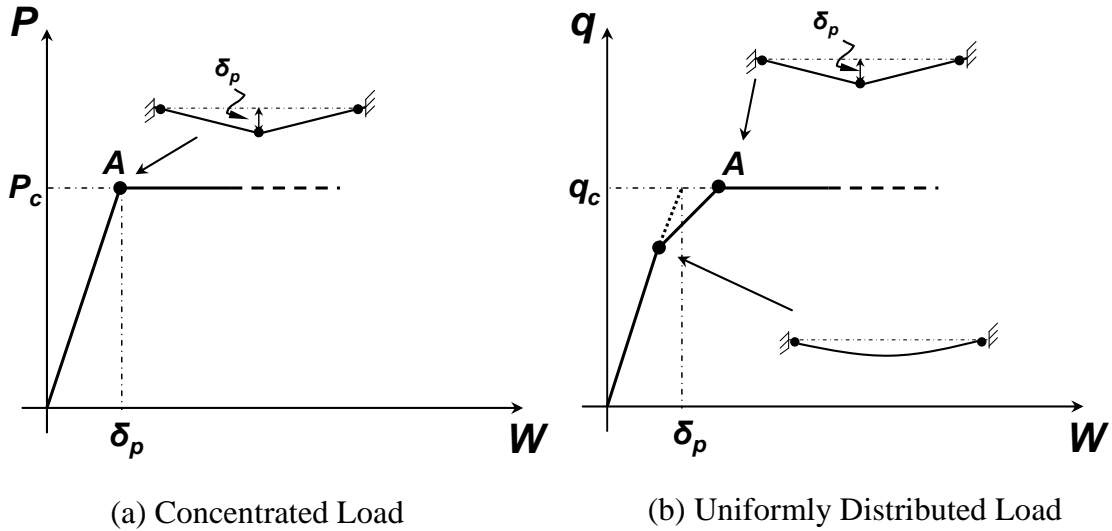


**Figure 4-30**  $\delta_p$  Definition

$$\delta_p = \frac{M_p \cdot L^2}{6EI_x} \quad \text{or} \quad \delta_p = \frac{\sigma_y Z_x L^2}{6EI_x} \quad [4.3]$$

where  $M_p = \sigma_y \cdot Z_x$ .

Equation 4-3 suggests that the effect of elastic deformations consists of geometric and material properties.

The following parameters are considered in the parametric FE analyses:  $\delta_p$ ,  $\delta_p / d$ ,  $\delta_p / 2L$  and  $L / d$ . The effect of these parameters on the behavior is described next.

#### 4.4.2 Description of Beam Models

The beams are modeled and analyzed using OpenSees with the concepts presented in Section 4-2. A description of the beam models considered in this section is given below. The other parameters are given for each case separately.

- Elastic – perfectly plastic steel material with  $\sigma_y = 50\text{ksi}$  and  $E = 29000\text{ ksi}$  is used in all cases.
- The cross-sections are discretized using fiber sections with a constant fiber thickness,  $t_{fiber} = 5 \times 10^{-3}\text{ inches}$
- The number of elements along the length of the beam members is constantly taken as 100.

#### 4.4.3 Concentrated Load Case

##### 4.4.3.1 Constant $\delta_p$

Several beam geometries with W-Shaped cross sections were modeled and analyzed in OpenSees. First, a 60 ft ( $2L$ ) beam with W30x124 cross-section was selected and the corresponding  $\delta_p$  was calculated using Equation 4.3. The other beam sections were chosen among different W-Shape groups listed in the *AISC Steel Construction Manual* (2005) in such a way that they produce same  $\delta_p$  as that for a W30x124 by changing the span length. Table 4-3 lists the beam cross-sections considered with other parameters of interest, and the resultant deflection at the onset of pure cable behavior.

**Table 4-3** Beam Models Considered with constant  $\delta_p$

Beam No	Section	$d$ (in)	$L$ (in)	$N_p$ (kips)	$M_p$ (k-in)	$P_c$ (kips)	$\delta_p$ (in)	$\delta_p / d$	$W_{cat}$ (in)	$W_{cat} / d$
1	W30x124	30.2	360	1805	20164	224	2.83	0.094	49.7	1.65
2	W27x129	27.6	345	1910	19494	226	2.83	0.103	46.5	1.68
3	W24x131	24.5	327	1784	18432	225	2.83	0.116	43.0	1.76
4	W21x122	21.7	308	1921	15279	198	2.83	0.131	39.4	1.81
5	W18x130	19.3	289	1875	14555	201	2.83	0.147	35.9	1.86

It can be seen from Table 4-3 that for deeper members, a larger deflection is required to reach the pure cable state. However, when  $W_{cat}$  is normalized by nominal depth,  $d$ , an opposite trend is observed in the  $W_{cat} / d$  parameter.

Figures 4-31, 4-32 and 4-33 give normalized load deflection relationships. It can be seen from these figures that when  $\delta_p$  is constant, the point of pure cable state (C) is close for different cross-sections. In particular,  $W_{cat} / d$  varies from 1.65 to 1.86, which is a difference, approximately of 13% with respect to the smallest value of  $W_{cat} / d$ .

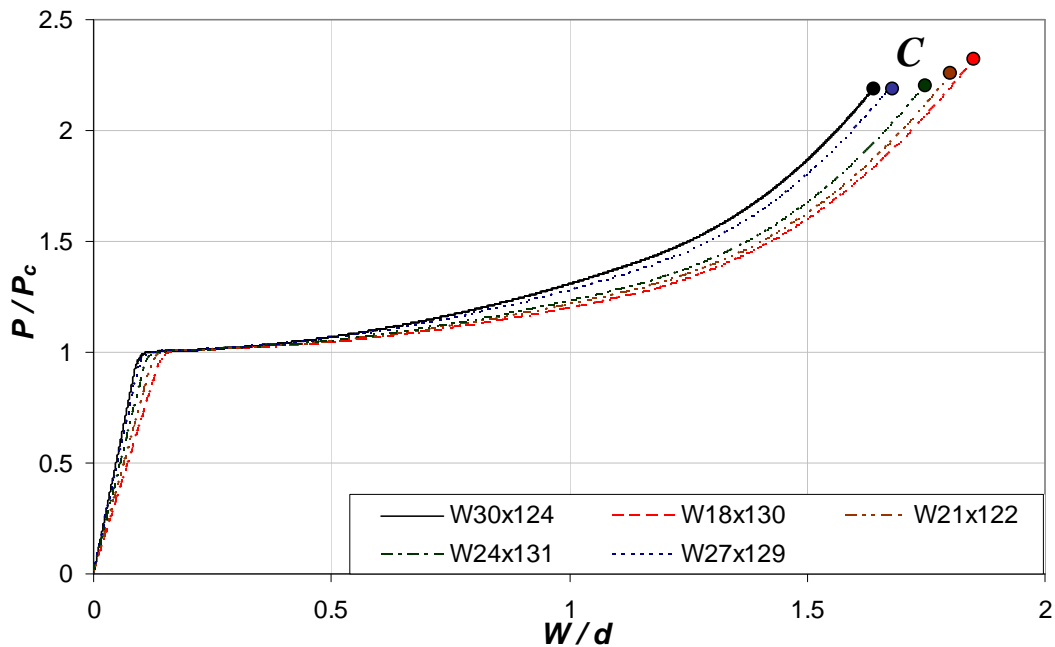


**Figure 4-31** Normalized Load–Deflection Plot for Constant  $\delta_p$

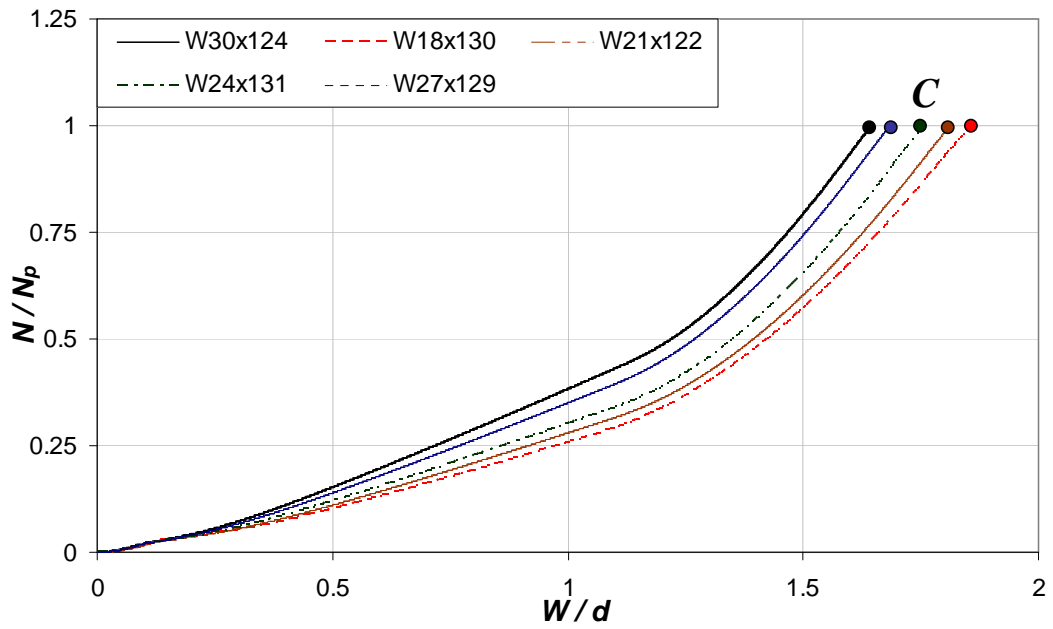


**Figure 4-32** Normalized Axial Force–Deflection Plot for Constant  $\delta_p$  (Midspan)

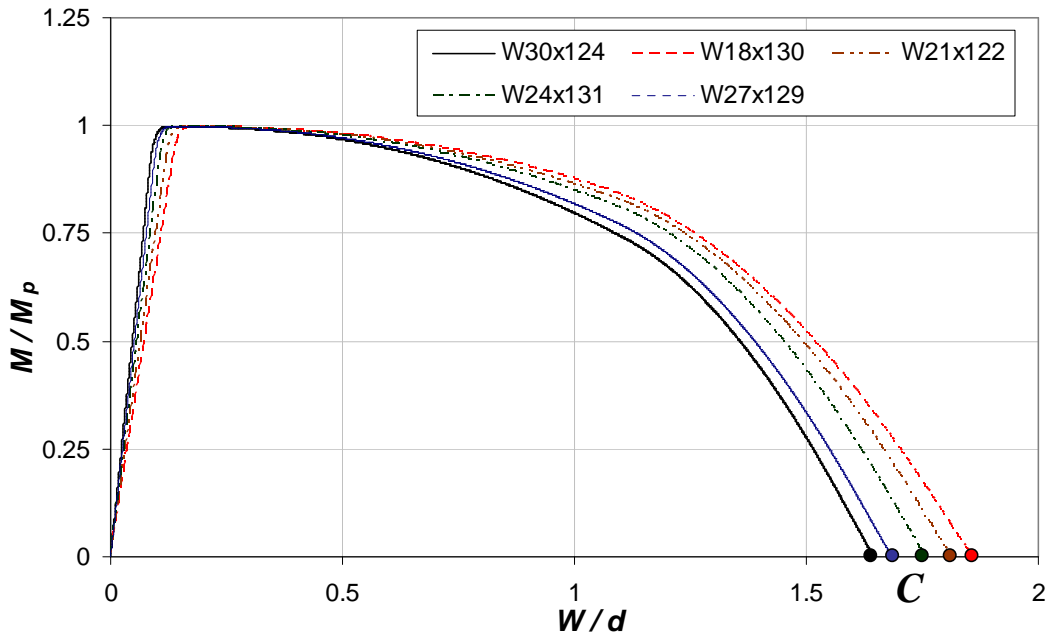


**Figure 4-33** Normalized Moment–Deflection Plot for Constant  $\delta_p$

To summarize, the results showed that the onset point of pure cable behavior,  $W_{cat}$  is not only sensitive to  $\delta_p$ . In similar manner, with the idea of eliminating the nominal depth,  $d$ , from the problem, FE analyses for different beam geometries with constant  $\delta_p/d$  were conducted and are presented next.

#### 4.4.3.2 Constant $\delta_p/d$

In this section, eight groups of beam models with constant  $\delta_p/d$  were analyzed, each including three beams with varying nominal depth,  $d$ . W-Shaped cross-sections within each group were chosen from the *AISC Steel Construction Manual* (2005) to cover a wide range of  $d$ . From the cross-sectional properties, the required length ( $2L$ ) for  $\delta_p/d$  is obtained using Equation 4.3 and was assigned to each beam model. Rectangular cross-sections were chosen to have approximately the same nominal depth and cross-sectional area as the corresponding W-Shapes.  $\delta_p/d$  varied between groups, from 0.01 to 2.00 to cover a wide range of behavior.

All cases were analyzed using OpenSees and  $W_{cat}$  was determined by inspection of the output transverse deflection at midspan at the point when  $N/N_p \cong 1.0$  is reached. However, unlike the W-Shape results, rectangular cross-section cases typically exhibit a plateau at  $\frac{N}{N_p} \cong 1.0$ . This can be seen in Figure 4-34 which shows a typical normalized axial force-deflection plot for rectangular shape cases that is used in this process.  $W_{cat}$  was determined as the deflection level at the onset of the apparent plateau which consistently corresponded to  $\frac{N}{N_p} \geq 0.99$ . Having observed such a trend from FE analysis

results prompted the idea that the beam models reach the pure cable state and sustain  $N_p$  as predicted by the theory.

The parameters used and the results obtained are given in Tables 4-4 and 4-5 for the beams with rectangular and W-shaped cross-sections, respectively. The tables also provide the resultant  $W_{cat}$  in its normalized forms with respect to  $d$ ,  $\delta_p$  and  $2L$ .

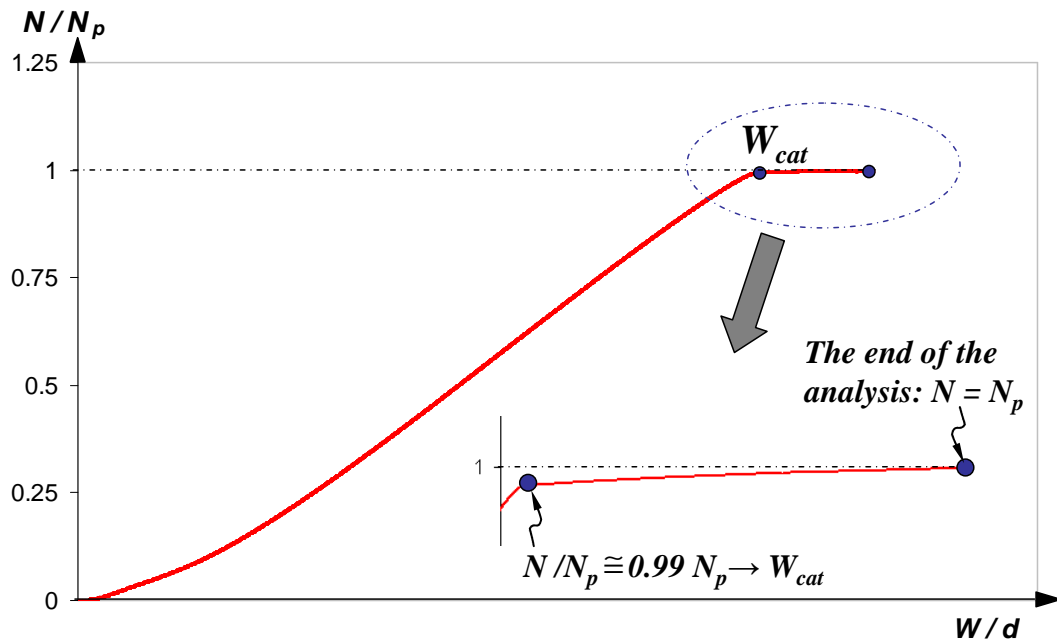


**Figure 4-34** Typical Normalized Axial Force–Deflection plot used to determine  $W_{cat}$  for

Rectangular Shape Cases



**Table 4-4** FE Models with Rectangular Shapes (Constant  $\delta_p/d$ )

Group	b (in)	d (in)	L (in)	L/d	$\delta_p$ (in)	$\delta_p/d$	$W_{cat}$ (in)	$W_{cat}/d$	$W_{cat}/\delta_p$	$\delta_p/2L$	$W_{cat}/2L$
1	1.90	36	122.6	3.4	0.36	0.01	37.53	1.04	104.2	0.0015	0.153
	4.50	15	51.1	3.4	0.15	0.01	15.63	1.04	104.2	0.0015	0.153
	2.50	26	88.6	3.4	0.26	0.01	27.12	1.04	104.3	0.0015	0.153
2	2.40	40	304.6	7.6	2.00	0.05	49.87	1.25	24.9	0.0033	0.082
	2.20	25	190.4	7.6	1.25	0.05	31.17	1.25	24.9	0.0033	0.082
	1.40	10	76.2	7.6	0.50	0.05	12.48	1.25	25.0	0.0033	0.082
3	2.20	39	420.0	10.8	3.90	0.10	55.48	1.42	14.2	0.0046	0.066
	1.20	24	258.5	10.8	2.40	0.10	34.00	1.42	14.2	0.0046	0.066
	2.00	9	96.9	10.8	0.90	0.10	12.78	1.42	14.2	0.0046	0.066
4	1.70	36	474.9	13.2	5.40	0.15	56.09	1.56	10.4	0.0057	0.059
	0.95	6	79.1	13.2	0.90	0.15	9.34	1.56	10.4	0.0057	0.059
	3.60	21	277.0	13.2	3.15	0.15	32.76	1.56	10.4	0.0057	0.059
5	1.70	40	609.3	15.2	8.00	0.20	67.28	1.68	8.4	0.0066	0.055
	2.50	26	396.0	15.2	5.20	0.20	43.74	1.68	8.4	0.0066	0.055
	1.50	12	182.8	15.2	2.40	0.20	20.20	1.68	8.4	0.0066	0.055
6	2.00	40	746.2	18.7	12.00	0.30	75.82	1.90	6.3	0.0080	0.051
	1.00	8	149.2	18.7	2.40	0.30	15.16	1.90	6.3	0.0080	0.051
	1.25	24	447.7	18.7	7.20	0.30	45.48	1.90	6.3	0.0080	0.051
7	1.60	43	1035.6	24.1	21.50	0.50	96.14	2.24	4.5	0.0104	0.046
	2.70	11	264.9	24.1	5.50	0.50	24.60	2.24	4.5	0.0104	0.046
	1.10	27	650.2	24.1	13.50	0.50	60.38	2.24	4.5	0.0104	0.046
8	1.90	36	1734.0	48.2	72.00	2.00	134.48	3.74	1.9	0.0208	0.039
	4.50	15	722.5	48.2	30.00	2.00	56.12	3.74	1.9	0.0208	0.039
	2.50	26	1252.3	48.2	52.00	2.00	97.34	3.74	1.9	0.0208	0.039

**Table 4-5** FE Models with W-Shapes (Constant  $\delta_p/d$ )

Group	Section	d (in)	L (in)	L/d	$\delta_p$ (in)	$\delta_p/d$	$W_{cat}$ (in)	$W_{cat}/d$	$W_{cat}/\delta_p$	$\delta_p/2L$	$W_{cat}/2L$
1	W36x231	36.50	143.4	3.9	0.37	0.01	42.31	1.16	115.9	0.0013	0.148
	W12x230	15.10	57.4	3.8	0.15	0.01	16.57	1.10	109.7	0.0013	0.144
	W24x229	26.00	101.3	3.9	0.26	0.01	29.55	1.14	113.6	0.0013	0.146
2	W40x327	40.8	350.0	8.6	2.03	0.05	58.04	1.42	28.6	0.0029	0.083
	W24x192	25.5	218.5	8.6	1.27	0.05	37.12	1.46	29.3	0.0029	0.085
	W10x49	10	88.2	8.8	0.50	0.05	14.92	1.49	30.1	0.0028	0.085
3	W40x297	39.8	491.5	12.3	3.98	0.10	66.86	1.68	16.8	0.0040	0.068
	W8x58	8.75	107.7	12.3	0.88	0.10	14.76	1.69	16.9	0.0041	0.068
	W24x103	24.5	302.2	12.3	2.45	0.10	41.06	1.68	16.8	0.0041	0.068
4	W36x210	36.7	551.0	15.0	5.51	0.15	67.24	1.83	12.2	0.0050	0.061
	W6x20	6.38	95.9	15.0	0.96	0.15	11.84	1.86	12.4	0.0050	0.062
	W18x258	21.5	318.1	14.8	3.23	0.15	39.38	1.83	12.2	0.0051	0.062
5	W40x235	39.7	845.0	21.3	11.91	0.30	88.86	2.24	7.5	0.0070	0.053
	W12x65	12.1	263.7	21.8	3.63	0.30	28.30	2.34	7.8	0.0069	0.054
	W24x229	26	554.6	21.3	7.80	0.30	58.97	2.27	7.6	0.0070	0.053
6	W40x278	40.2	981.8	24.4	16.08	0.40	99.36	2.47	6.2	0.0082	0.051
	W8x40	8.25	205.3	24.9	3.30	0.40	20.88	2.53	6.3	0.0080	0.051
	W24x103	24.5	604.5	24.7	9.80	0.40	61.46	2.51	6.3	0.0081	0.051
7	W44x230	42.9	1188.1	27.7	21.45	0.50	115.98	2.70	5.4	0.0090	0.049
	W10x100	11.1	304.2	27.4	5.55	0.50	31.36	2.82	5.6	0.0091	0.052
	W27x102	27.1	748.1	27.6	13.55	0.50	72.40	2.67	5.3	0.0091	0.048
8	W36x231	36.50	2028.6	55.6	73.00	2.00	160.00	4.38	2.2	0.0180	0.039
	W12x230	15.10	811.7	53.8	30.20	2.00	63.84	4.23	2.1	0.0186	0.039
	W24x229	26.00	1432.1	55.1	52.00	2.00	113.70	4.37	2.2	0.0182	0.040

The following are observations from Tables 4-4 and 4-5:

- For each group, constant  $\delta_p / d$  resulted in identical  $L / d$  and  $\delta_p / 2L$  values for rectangular section cases (Table 4-4) but a slight difference in those values for W-Shaped beams (Table 4-5). This can be explained as follows. If the moment of inertia about the major axis,  $I_x = S_x \cdot \frac{d}{2}$  is substituted into Equation 4.3, it follows that:

$$\delta_p = \frac{\sigma_y \cdot Z_x \cdot L^2}{3 \cdot E \cdot S_x \cdot d} \quad [4.4]$$

Introducing the shape factor,  $f$ , which is defined as:

$$f = \frac{Z_x}{S_x} \quad [4.5]$$

into Equation 4.4, gives:

$$\frac{\delta_p}{d} = \frac{\sigma_y \cdot f}{3 \cdot E} \cdot \left[ \frac{L}{d} \right]^2 \quad [4.6]$$

The shape factor is constant ( $f = 1.5$ ) for rectangular cross-sections. Therefore, for a constant  $\delta_p / d$ ,  $L / d$  must also be the same within each group in Table 4-4. The slight difference in shape factor among W-Shapes ( $f \cong 1.15$ ) results in the slight difference in  $L / d$  within each group in Table 4-5.

In a similar manner, re-writing Equation 4.6 as follows shows why  $\delta_p / 2L$  also follows the same trend as  $L / d$ :

$$\frac{\delta_p}{2L} = \frac{\sigma_y \cdot f}{6 \cdot E} \cdot \left[ \frac{L}{d} \right] \quad [4.7]$$

- Rigid-plastic theory suggests that regardless of the cross-section, centrally loaded, fully fixed beam reaches the onset point of pure cable state when the deflection equals

- the depth of the beam (i.e.,  $W_{cat} / d = 1.0$ ). Indeed, as can be seen from both tables,  $W_{cat} / d$  approaches 1.0 as  $\delta_p / d$  approaches zero (relatively rigid cases).
- The output parameters  $W_{cat} / d$ ,  $W_{cat} / \delta_p$  and  $W_{cat} / 2L$  are almost identical within each group for rectangular shape cases (Table 4-4) but there exists slight difference for the W-Shape cases (Table 4-5), especially in relatively more rigid groups.

A graphical presentation of the relationships between these variables that seem to follow a pattern is provided next. The output variables:  $W_{cat} / \delta_p$ ,  $W_{cat} / d$  and  $W_{cat} / 2L$  are plotted versus the input variables:  $\delta_p / d$ ,  $\delta_p / 2L$  and  $L / d$ , respectively. Therefore, in total, nine plots will be shown. In these plots, each point represents one beam model.

Plots of  $W_{cat} / \delta_p$  versus  $\delta_p / d$ ,  $\delta_p / 2L$  and  $L / d$ , are given in Figures 4-35, 4-36 and 4-37 respectively. It can be seen that the points representing the rectangular beams within each group are coincident. However, the points for W-Shaped beams within each group do not necessarily coincide. In particular, Figure 4-35 shows that the points for the W-Shapes within each group do nearly coincide except for the very rigid cases. Figure 4-35 is the only figure in that group of three figures that uses an independent variable of  $\delta_p / d$  which happens to be constant with each group of three beams. The reason for these observations will be explored in detail in Chapter 5. The figures also show that agreement for each group of beams with the same cross-section type has the tendency to improve as  $\delta_p / d$  increases, or as beam flexibility increases. In addition, the figures show that  $W_{cat} / \delta_p$  decays with increasing  $\delta_p / d$ ,  $\delta_p / 2L$  and  $L / d$ .

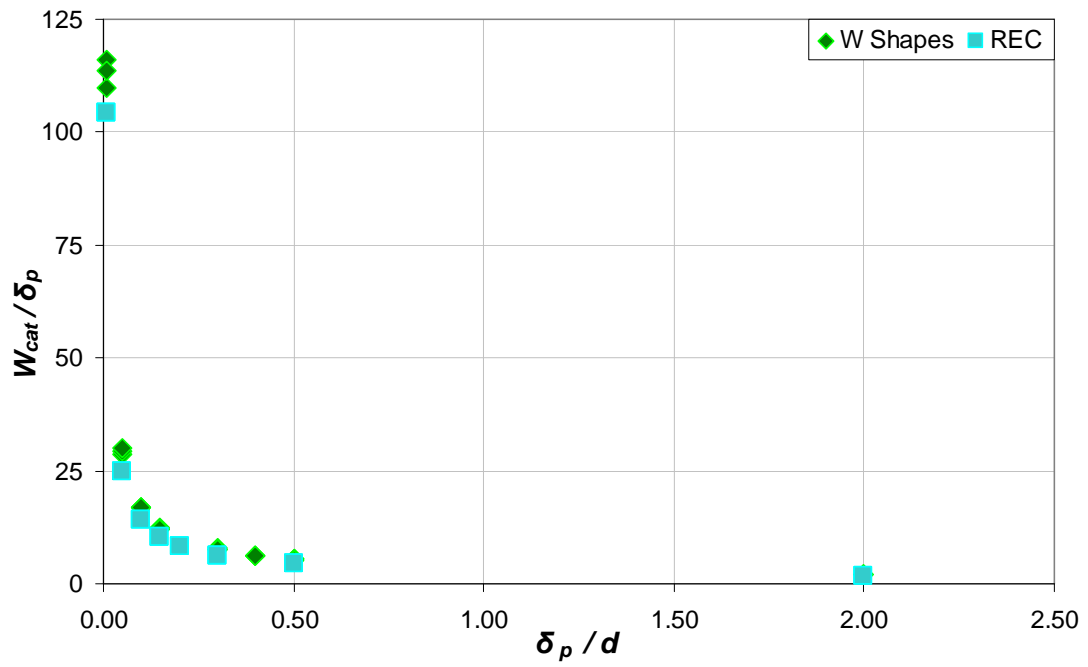


**Figure 4-35**  $W_{cat} / \delta_p - \delta_p / d$  Relationship (Constant  $\delta_p / d$  within each group)

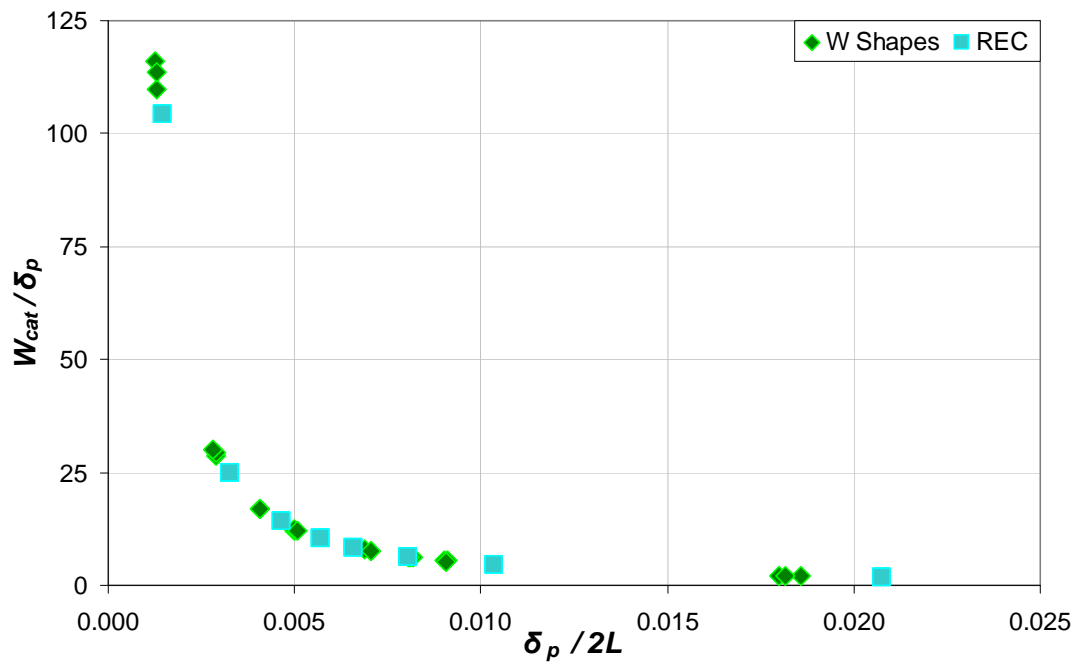


**Figure 4-36**  $W_{cat} / \delta_p - \delta_p / 2L$  Relationship (Constant  $\delta_p / d$  within each group)

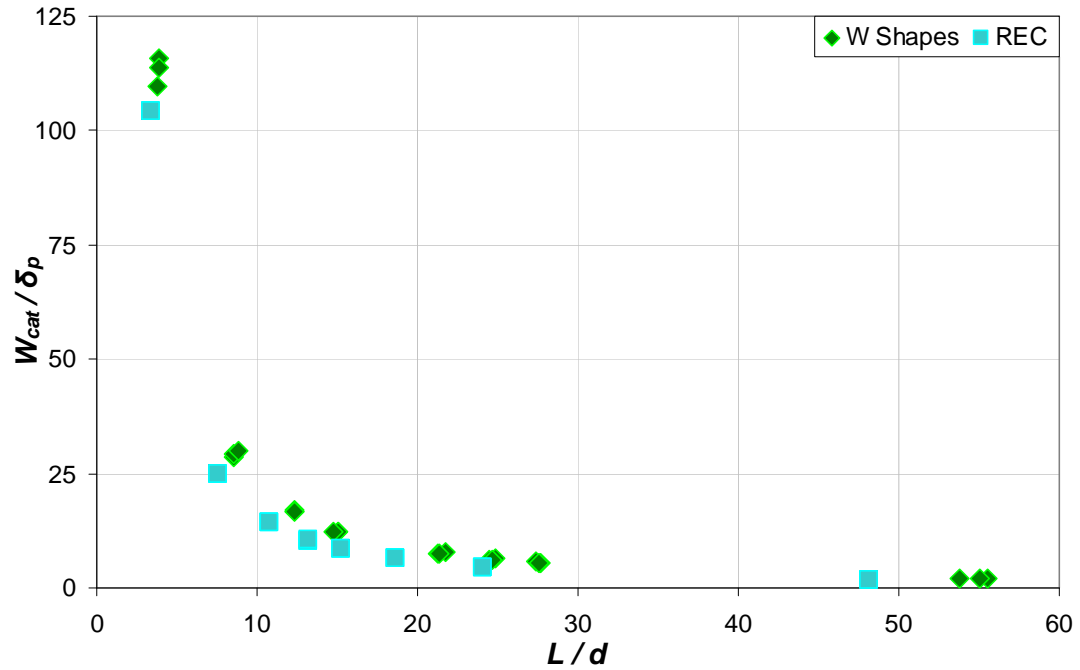


**Figure 4-37**  $W_{cat}/\delta_p - L/d$  relationship (Constant  $\delta_p/d$  within each group)

Plots of  $W_{cat}/d$  versus  $\delta_p/d$ ,  $\delta_p/2L$  and  $L/d$  are given in Figures 4-38, 4-39 and 4-40, respectively. Again, it can be seen that the points representing the rectangular cross-section cases within each group are coincident, but the points for the W-Shapes within each group do not necessarily coincide. The agreement for the W-Shapes is best in Figure 4-38, which is the only figure in that group of figures that uses an independent variable of  $\delta_p/d$ . The figures also show that  $W_{cat}/d$  increases with increasing  $\delta_p/d$ ,  $\delta_p/2L$  and  $L/d$ .

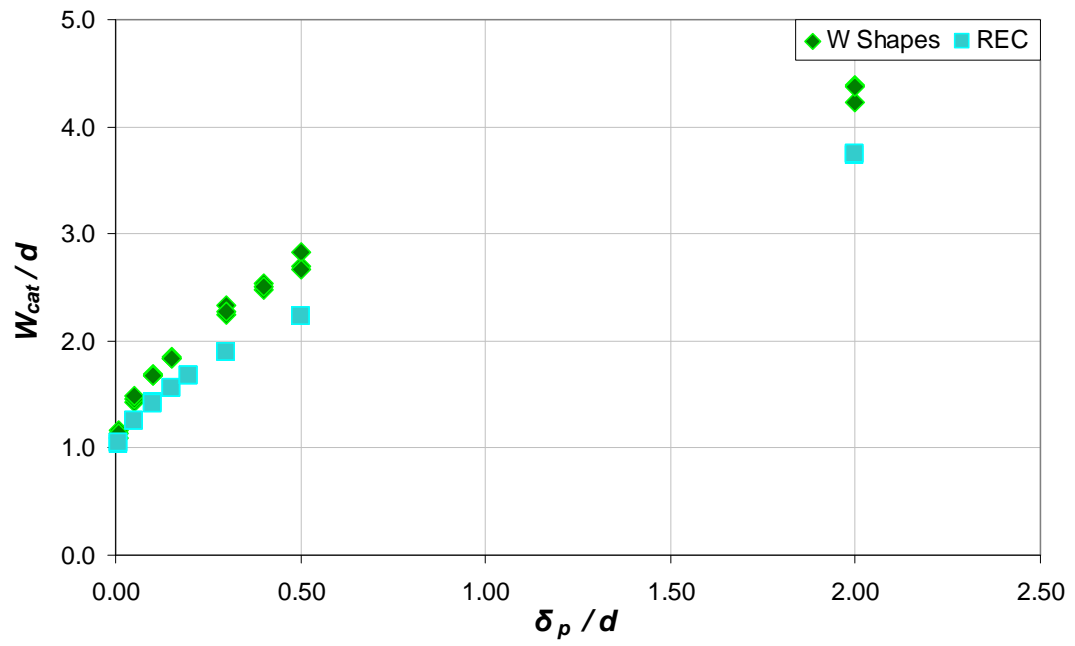


**Figure 4-38**  $W_{cat} / d$  -  $\delta_p / d$  Relationship (Constant  $\delta_p / d$  within each group)

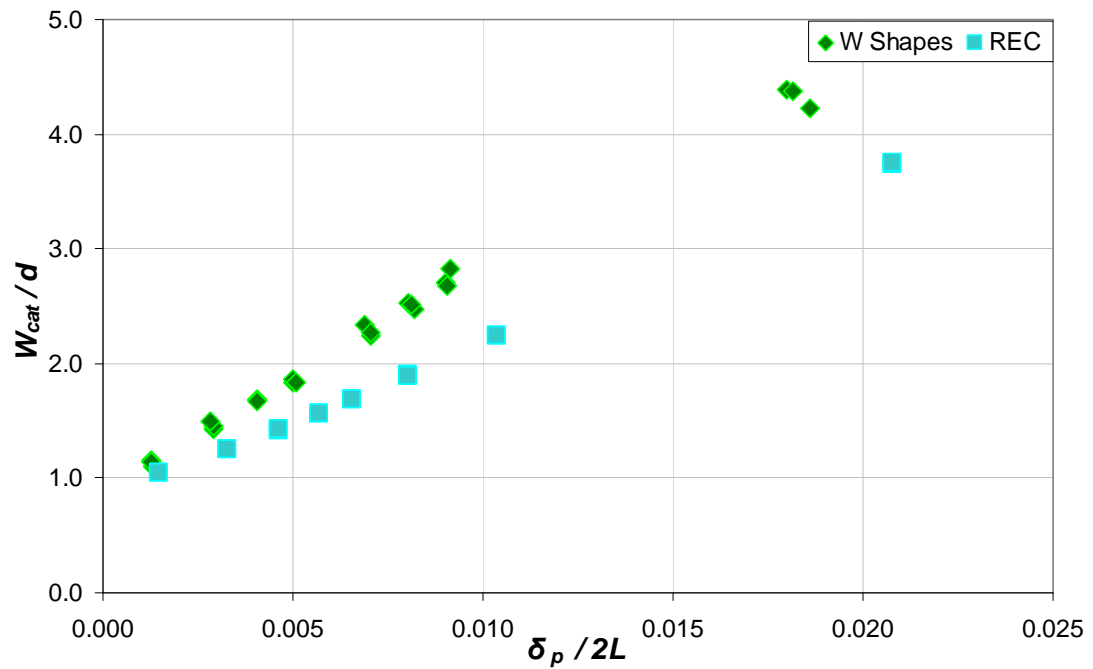


**Figure 4-39**  $W_{cat} / d$  -  $\delta_p / 2L$  Relationship (Constant  $\delta_p / d$  within each group)

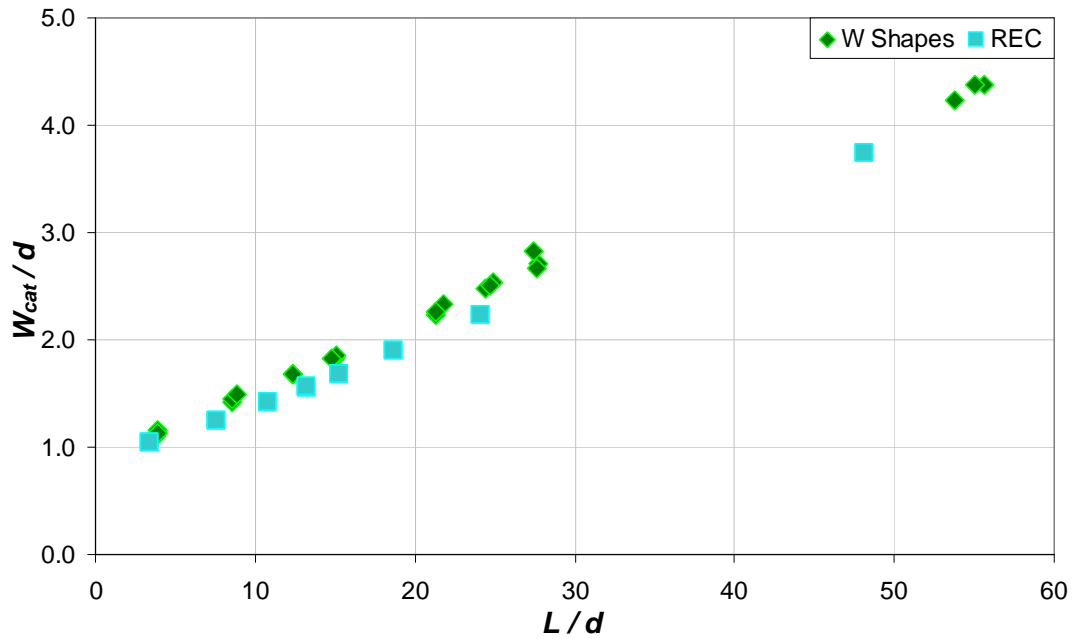


**Figure 4-40**  $W_{cat}/d - L/d$  Relationship (Constant  $\delta_p/d$  within each group)

Plots of  $W_{cat}/2L$  versus  $\delta_p/d$ ,  $\delta_p/2L$  and  $L/d$  are given in Figures 4-41, 4-42 and 4-43, respectively. Similar observations as before can be made. The points for the rectangular cross-section cases within each group are coincident, but the points for the W-Shapes within each group do not necessarily coincide. The agreement for the W-Shapes is best in Figure 4-41, which is the only figure that uses an independent variable of  $\delta_p/d$ . The figures also show that  $W_{cat}/2L$  decreases with increasing  $\delta_p/d$ ,  $\delta_p/2L$  and  $L/d$ .

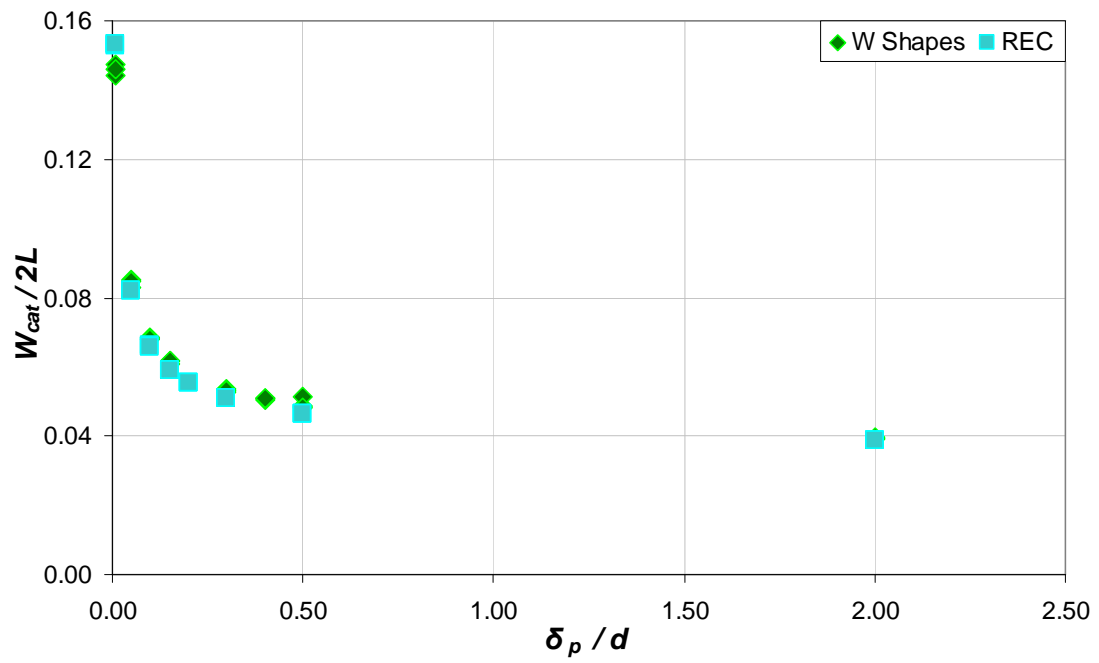


**Figure 4-41**  $W_{cat} / 2L - \delta_p / d$  Relationship (Constant  $\delta_p / d$  within each group)

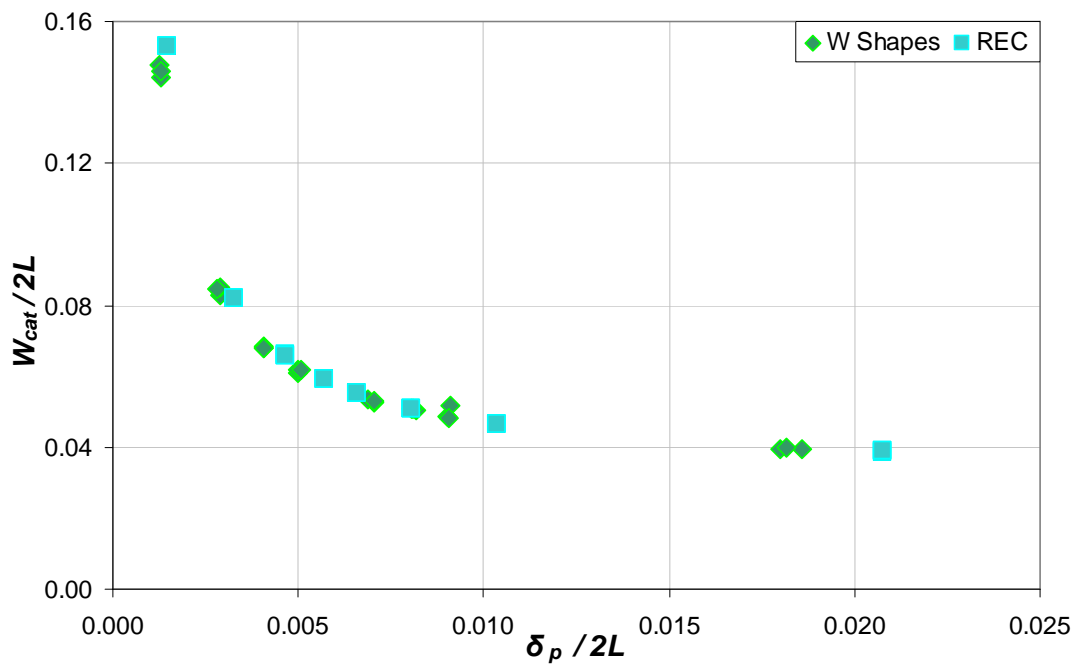


**Figure 4-42**  $W_{cat} / 2L - \delta_p / 2L$  Relationship (Constant  $\delta_p / d$  within each group)



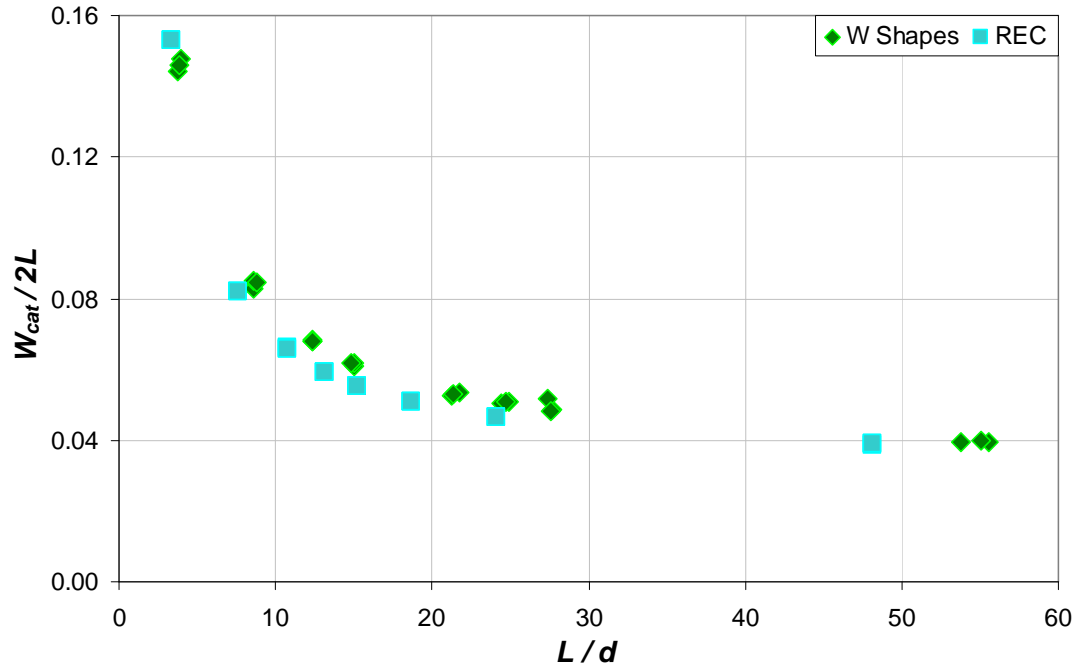


**Figure 4-43**  $W_{cat} / 2L - L / d$  Relationship (Constant  $\delta_p / d$  within each group)

#### 4.4.3.3 Constant $\delta_p / 2L$

A similar procedure as before is used. For beams with rectangular cross sections, the results are the same as shown previously in Table 4-4. This table is rearranged and presented as Table 4-6. For beams with W-Shapes, the eight groups indicated in Table 4-5 were re-analyzed. The required span length for each beam model and associated  $\delta_p / 2L$  values were determined using Equation 4-7.

**Table 4-6** FE Models with Rectangular Shapes (Constant  $\delta_p / 2L$ )

Group	b (in)	d (in)	L (in)	L / d	$\delta_p$ (in)	$\delta_p / d$	$W_{cat}$ (in)	$W_{cat} / d$	$W_{cat} / \delta_p$	$\delta_p / 2L$	$W_{cat} / 2L$
1	1.90	36	122.6	3.4	0.36	0.01	37.53	1.04	104.2	0.0015	0.153
	4.50	15	51.1	3.4	0.15	0.01	15.63	1.04	104.2	0.0015	0.153
	2.50	26	88.6	3.4	0.26	0.01	27.12	1.04	104.3	0.0015	0.153
2	2.40	40	304.6	7.6	2.00	0.05	49.87	1.25	24.9	0.0033	0.082
	2.20	25	190.4	7.6	1.25	0.05	31.17	1.25	24.9	0.0033	0.082
	1.40	10	76.2	7.6	0.50	0.05	12.48	1.25	25.0	0.0033	0.082
3	2.20	39	420.0	10.8	3.90	0.10	55.48	1.42	14.2	0.0046	0.066
	1.20	24	258.5	10.8	2.40	0.10	34.00	1.42	14.2	0.0046	0.066
	2.00	9	96.9	10.8	0.90	0.10	12.78	1.42	14.2	0.0046	0.066
4	1.70	36	474.9	13.2	5.40	0.15	56.09	1.56	10.4	0.0057	0.059
	0.95	6	79.1	13.2	0.90	0.15	9.34	1.56	10.4	0.0057	0.059
	3.60	21	277.0	13.2	3.15	0.15	32.76	1.56	10.4	0.0057	0.059
5	1.70	40	609.3	15.2	8.00	0.20	67.28	1.68	8.4	0.0066	0.055
	2.50	26	396.0	15.2	5.20	0.20	43.74	1.68	8.4	0.0066	0.055
	1.50	12	182.8	15.2	2.40	0.20	20.20	1.68	8.4	0.0066	0.055
6	2.00	40	746.2	18.7	12.00	0.30	75.82	1.90	6.3	0.0080	0.051
	1.00	8	149.2	18.7	2.40	0.30	15.16	1.90	6.3	0.0080	0.051
	1.25	24	447.7	18.7	7.20	0.30	45.48	1.90	6.3	0.0080	0.051
7	1.60	43	1035.6	24.1	21.50	0.50	96.14	2.24	4.5	0.0104	0.046
	2.70	11	264.9	24.1	5.50	0.50	24.60	2.24	4.5	0.0104	0.046
	1.10	27	650.2	24.1	13.50	0.50	60.38	2.24	4.5	0.0104	0.046
8	1.90	36	1734.0	48.2	72.00	2.00	134.48	3.74	1.9	0.0208	0.039
	4.50	15	722.5	48.2	30.00	2.00	56.12	3.74	1.9	0.0208	0.039
	2.50	26	1252.3	48.2	52.00	2.00	97.34	3.74	1.9	0.0208	0.039

**Table 4-7** FE Models with W-Shapes (Constant  $\delta_p / 2L$ )

Group	Section	d (in)	L (in)	L / d	$\delta_p$ (in)	$\delta_p / d$	$W_{cat}$ (in)	$W_{cat} / d$	$W_{cat} / \delta_p$	$\delta_p / 2L$	$W_{cat} / 2L$
1	W36x231	36.50	165.5	4.5	0.49	0.01	43.82	1.20	90.2	0.0015	0.132
	W12x230	15.10	64.1	4.2	0.19	0.01	17.00	1.13	90.4	0.0015	0.133
	W24x229	26.00	115.8	4.5	0.34	0.01	30.54	1.17	89.8	0.0015	0.132
2	W40x327	40.80	397.0	9.7	2.61	0.06	60.94	1.49	23.4	0.0033	0.077
	W24x192	25.50	255.9	10.0	1.68	0.07	39.28	1.54	23.4	0.0033	0.077
	W10x49	10.00	102.9	10.3	0.68	0.07	15.84	1.58	23.4	0.0033	0.077
3	W40x297	39.80	563.6	14.2	5.23	0.13	71.42	1.79	13.6	0.0046	0.063
	W8x58	8.75	123.2	14.1	1.14	0.13	15.77	1.80	13.8	0.0046	0.064
	W24x103	24.50	346.2	14.1	3.21	0.13	43.84	1.79	13.6	0.0046	0.063
4	W36x210	36.70	627.1	17.1	7.13	0.19	72.12	1.97	10.1	0.0057	0.058
	W6x20	6.38	109.2	17.1	1.24	0.19	12.66	1.98	10.2	0.0057	0.058
	W18x258	21.50	356.9	16.6	4.06	0.19	41.52	1.93	10.2	0.0057	0.058
5	W40x235	39.70	787.2	19.8	10.34	0.26	85.12	2.14	8.2	0.0066	0.054
	W12x65	12.10	251.6	20.8	3.30	0.27	27.50	2.27	8.3	0.0066	0.055
	W24x229	26.00	517.9	19.9	6.80	0.26	56.35	2.17	8.3	0.0066	0.054
6	W40x278	40.20	964.1	24.0	15.50	0.39	98.20	2.44	6.3	0.0080	0.051
	W8x40	8.25	205.3	24.9	3.30	0.40	20.87	2.53	6.3	0.0080	0.051
	W24x103	24.50	599.6	24.5	9.64	0.39	60.20	2.46	6.2	0.0080	0.050
7	W44x230	42.90	1366.2	31.8	28.36	0.66	125.98	2.94	4.4	0.0104	0.046
	W10x100	11.10	346.2	31.2	7.19	0.65	32.39	2.92	4.5	0.0104	0.047
	W27x102	27.10	857.5	31.6	17.80	0.66	79.06	2.92	4.4	0.0104	0.046
8	W36x231	36.50	2340.8	64.1	97.20	2.66	179.84	4.93	1.9	0.0208	0.038
	W12x230	15.10	905.9	60.0	37.62	2.49	71.14	4.71	1.9	0.0208	0.039
	W24x229	26.00	1637.7	63.0	68.00	2.62	127.80	4.92	1.9	0.0208	0.039

Plots of  $W_{cat} / \delta_p$  versus  $\delta_p / d$ ,  $\delta_p / 2L$  and  $L / d$  are given in Figures 4-44, 4-45 and 4-46, respectively. Plots of  $W_{cat} / d$  versus  $\delta_p / d$ ,  $\delta_p / 2L$  and  $L / d$  are given in Figures 4-47, 4-48 and 4-49, respectively. Plots of  $W_{cat} / 2L$  versus  $\delta_p / d$ ,  $\delta_p / 2L$  and  $L / d$ , are given in Figures 4-50, 4-51 and 4-52, respectively.

Very similar observations as before can be made by comparing Figures 4-44 through 4-52 with Figures 4-35 and 4-43. However, there is one exception. In the current case, the points for the W-Shapes within each group show the best agreement for cases that use an independent variable of  $\delta_p / 2L$ , which happens to be constant for each group of three beams. This can be seen in Figures 4-45, 4-48 and 4-51.

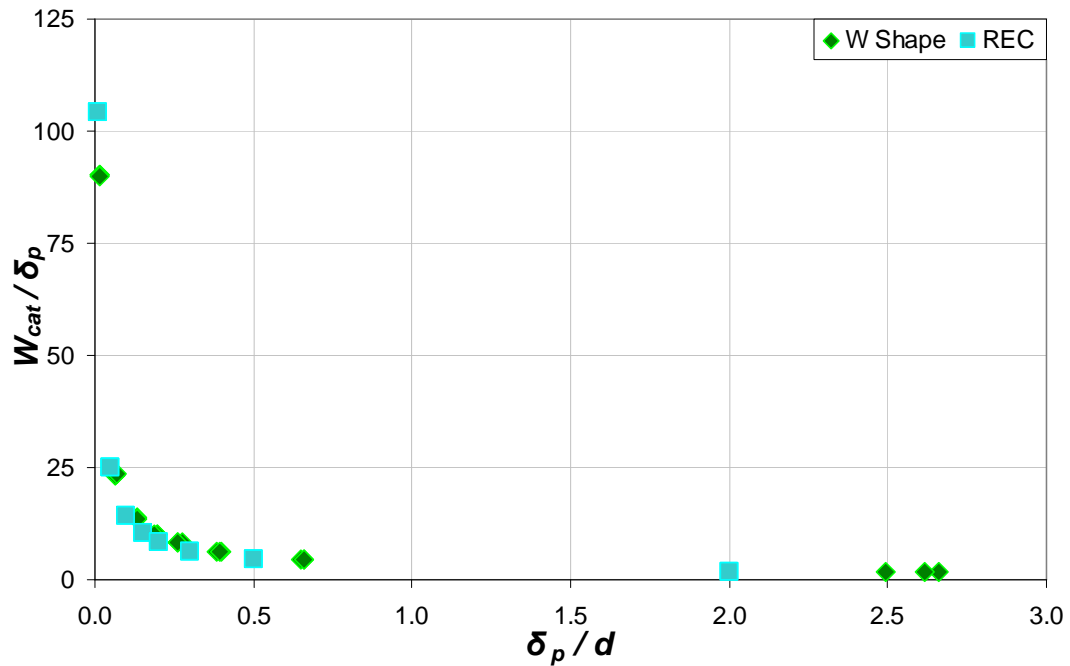


**Figure 4-44**  $W_{cat} / \delta_p - \delta_p / d$  Relationship (Constant  $\delta_p / 2L$  within each group)

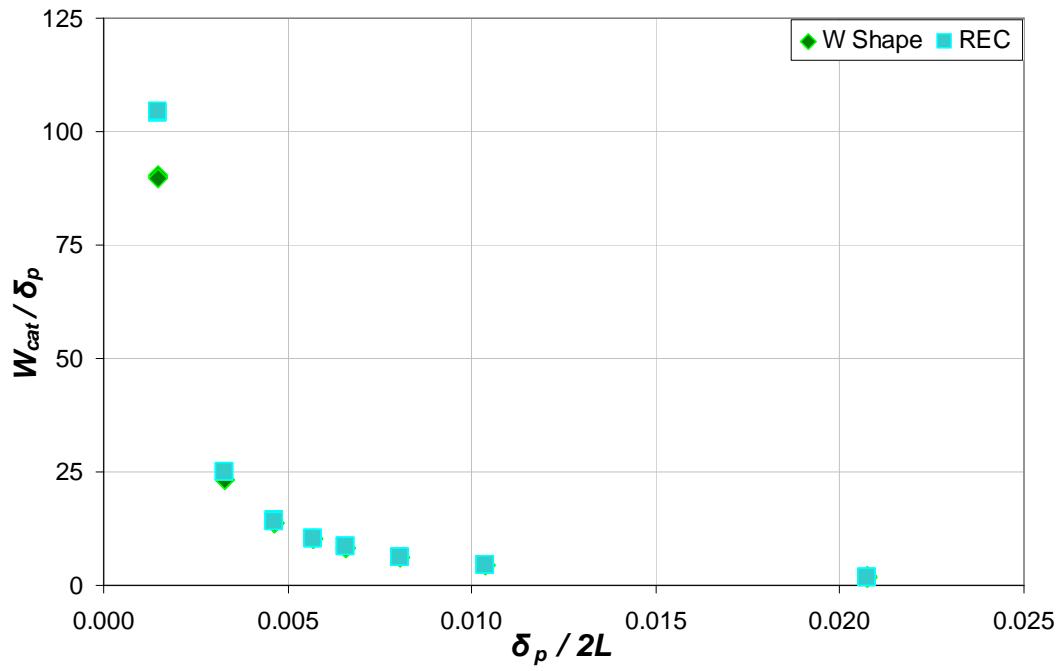


**Figure 4-45**  $W_{cat} / \delta_p - \delta_p / 2L$  Relationship (Constant  $\delta_p / 2L$  within each group)

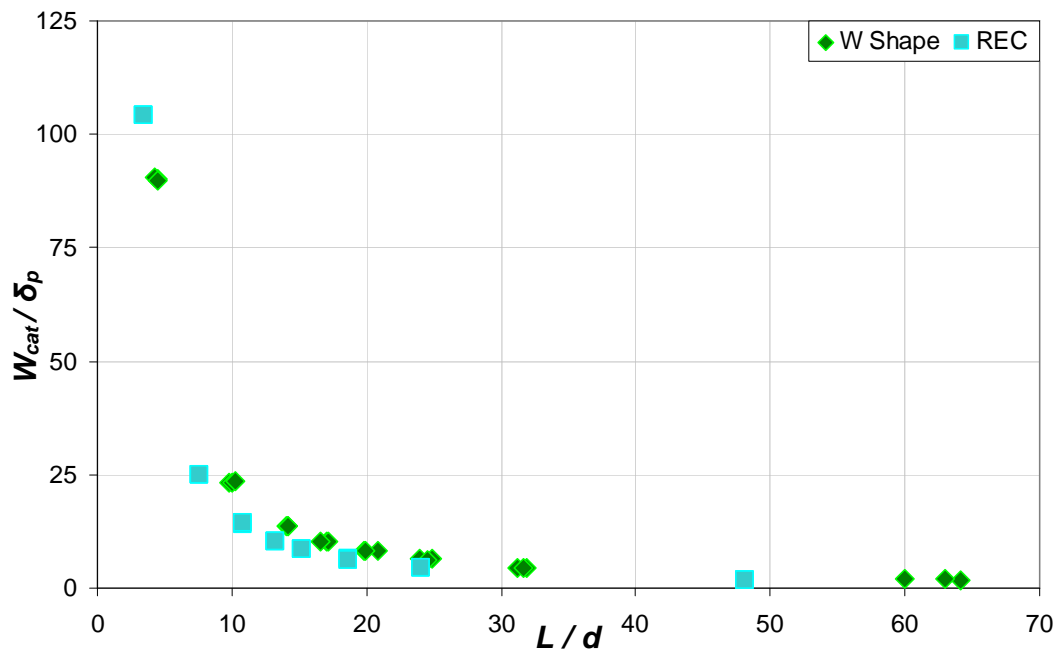


**Figure 4-46**  $W_{cat} / \delta_p - L / d$  Relationship (Constant  $\delta_p / 2L$  within each group)

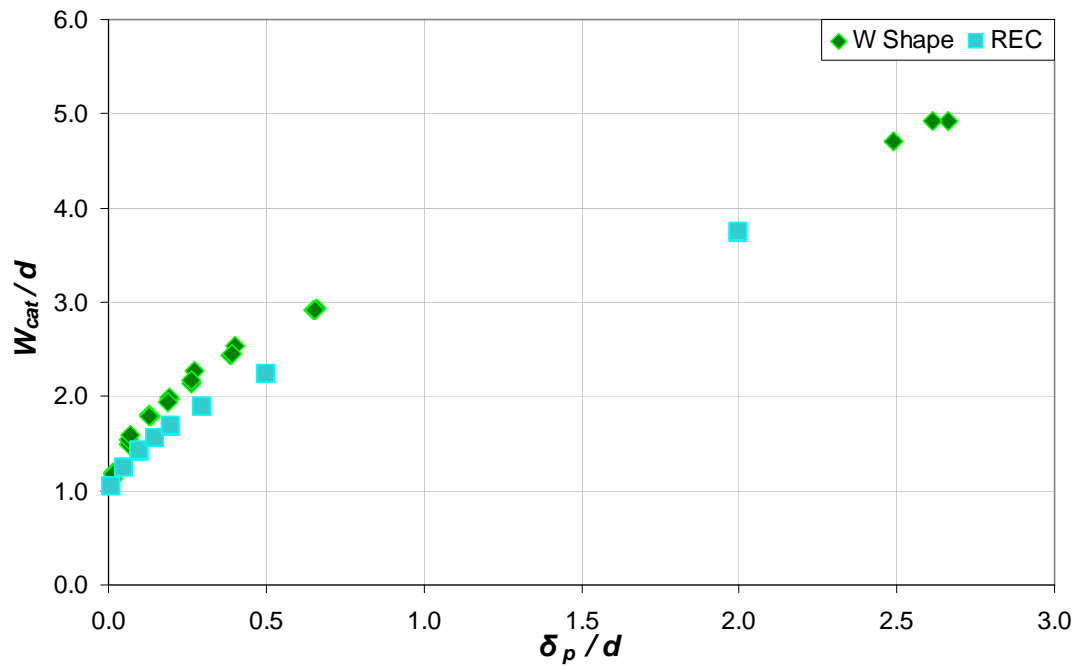


**Figure 4-47**  $W_{cat}/d - \delta_p/d$  Relationship (Constant  $\delta_p/2L$  within each group)

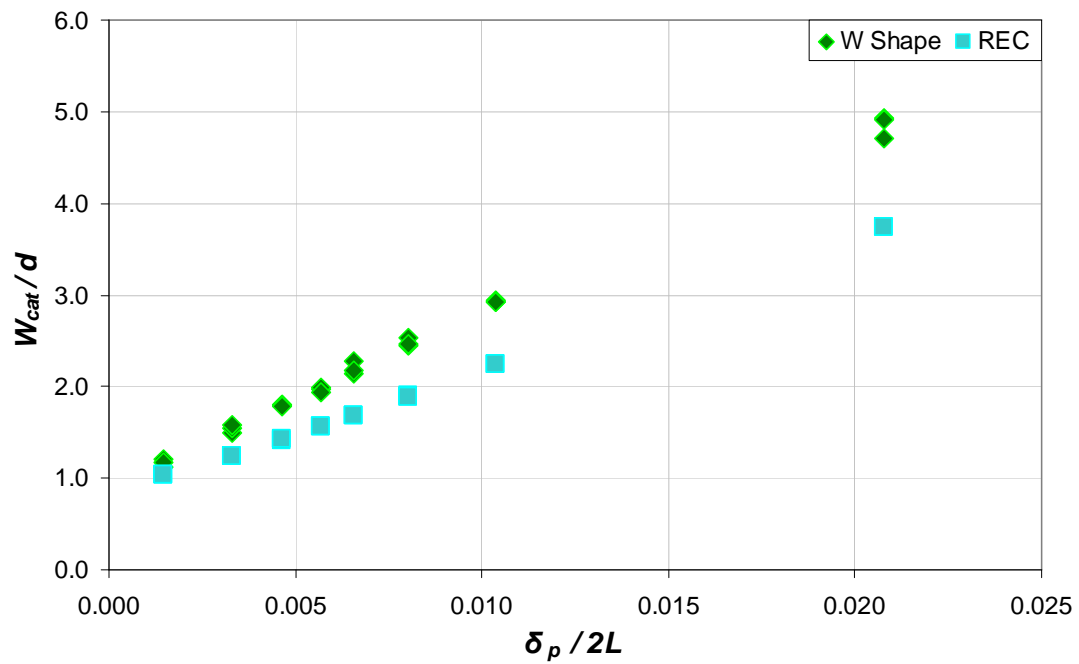


**Figure 4-48**  $W_{cat}/d - \delta_p/2L$  Relationship (Constant  $\delta_p/2L$  within each group)

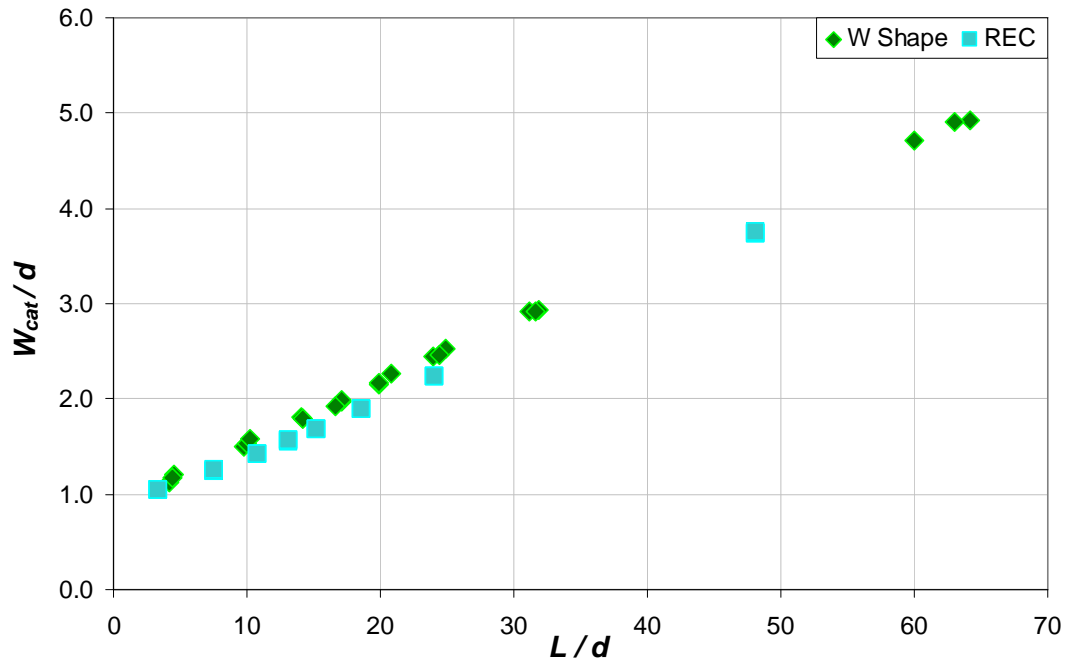


Figure 4-49  $W_{cat}/d - L/d$  Relationship (Constant  $\delta_p/2L$  within each group)

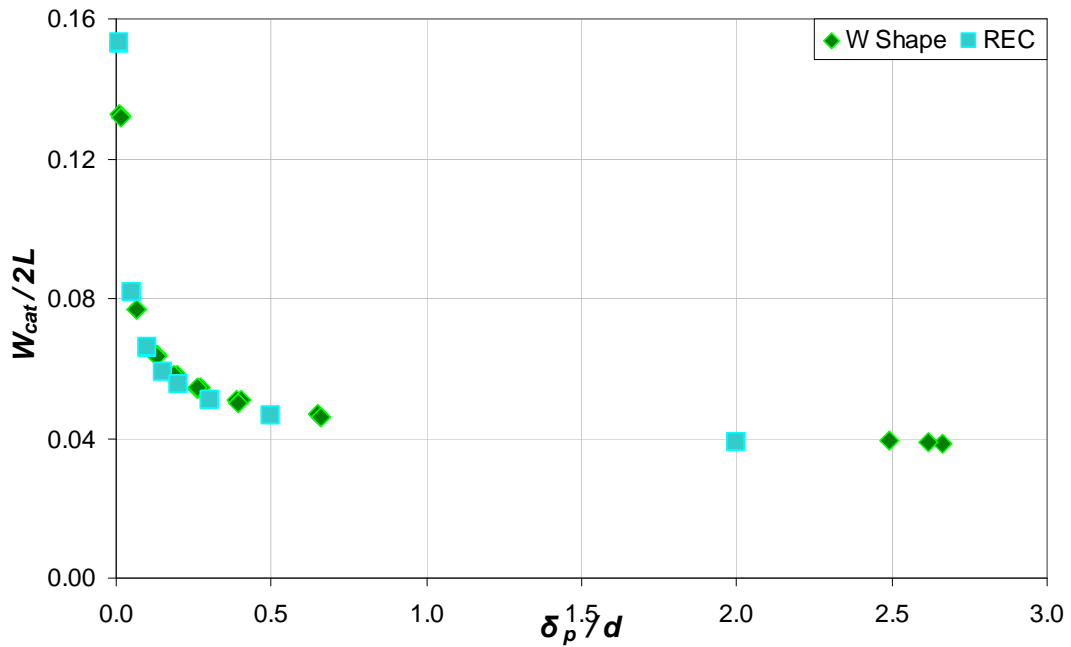
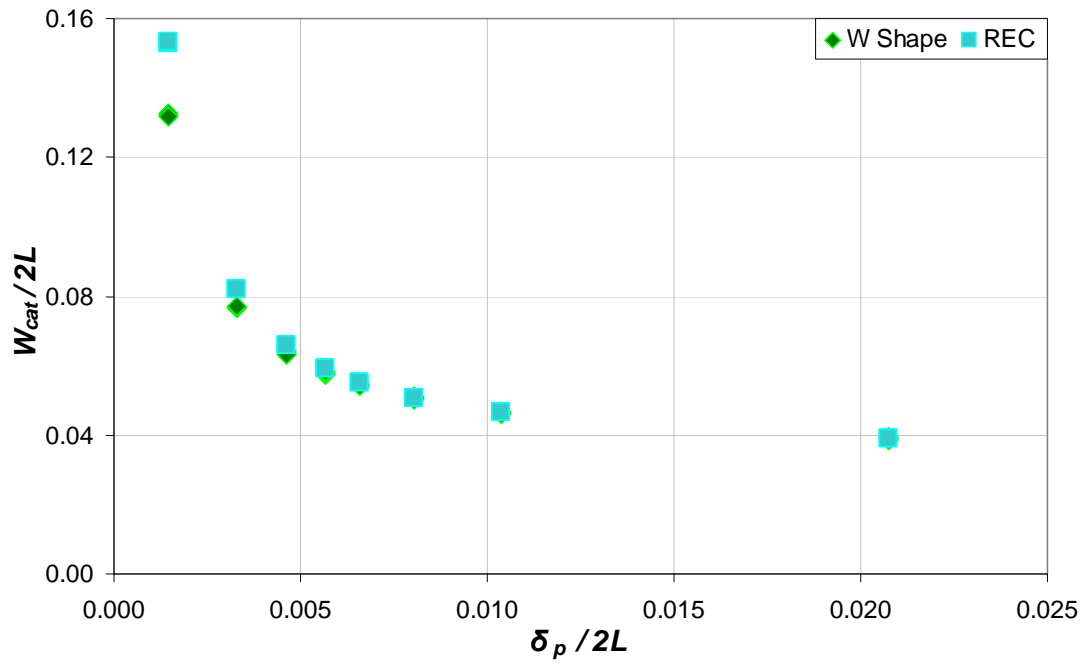
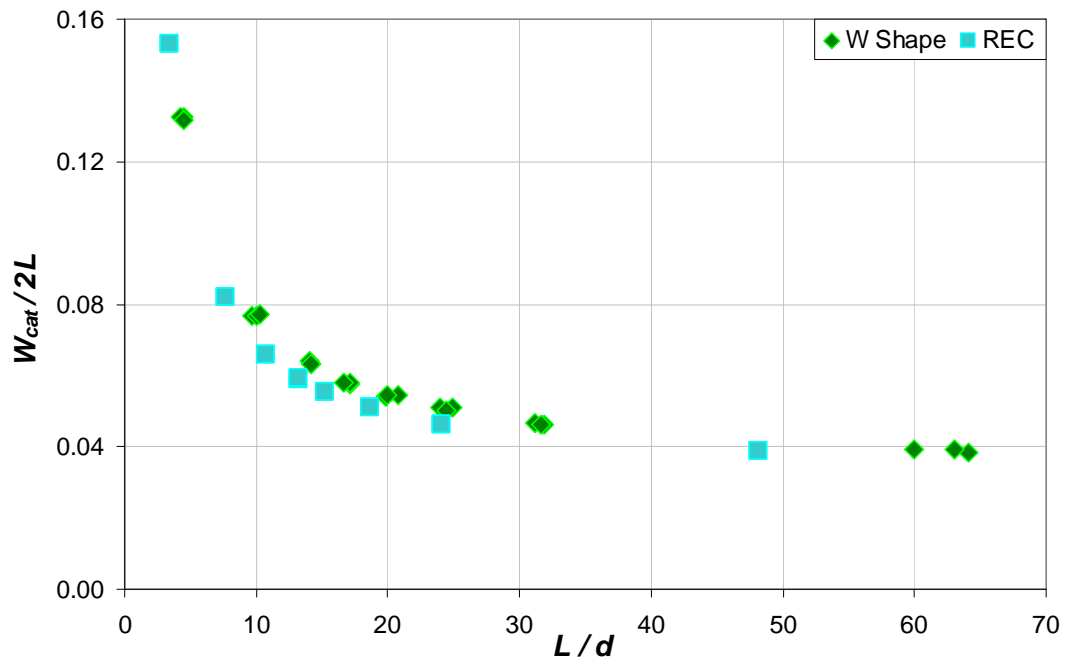


Figure 4-50  $W_{cat}/2L - \delta_p/d$  Relationship (Constant  $\delta_p/2L$  within each group)



**Figure 4-51**  $W_{cat}/2L - \delta_p/2L$  Relationship (Constant  $\delta_p/2L$  within each group)



**Figure 4-52**  $W_{cat}/2L - L/d$  Relationship (Constant  $\delta_p/2L$  within each group)

#### 4.4.3.4 Constant $L/d$

Again, a similar procedure as before is used. For beams with rectangular cross sections, the results are the same as those shown in Table 4-4. This table is rearranged and is presented in Table 4-8. For the beams with W-Shapes, the required span length for each beam model and associated span-to-depth ratio,  $L/d$ , was determined using Equation 4-7. The parameters used and results obtained for beams with W-shapes are given in Table 4-9.

**Table 4-8** FE Models with Rectangular Shapes (Constant  $L/d$  case)

Group	$b$ (in)	$d$ (in)	$L$ (in)	$L/d$	$\delta_p$ (in)	$\delta_p/d$	$W_{cat}$ (in)	$W_{cat}/d$	$W_{cat}/\delta_p$	$\delta_p/2L$	$W_{cat}/2L$
1	1.90	36.0	122.6	3.4	0.36	0.01	37.53	1.04	104.2	0.0015	0.153
	4.50	15.0	51.1	3.4	0.15	0.01	15.63	1.04	104.2	0.0015	0.153
	2.50	26.0	88.6	3.4	0.26	0.01	27.12	1.04	104.3	0.0015	0.153
2	2.40	40.0	304.6	7.6	2.00	0.05	49.87	1.25	24.9	0.0033	0.082
	2.20	25.0	190.4	7.6	1.25	0.05	31.17	1.25	24.9	0.0033	0.082
	1.40	10.0	76.2	7.6	0.50	0.05	12.48	1.25	25.0	0.0033	0.082
3	2.20	39.0	420.0	10.8	3.90	0.10	55.48	1.42	14.2	0.0046	0.066
	1.20	24.0	258.5	10.8	2.40	0.10	34.00	1.42	14.2	0.0046	0.066
	2.00	9.0	96.9	10.8	0.90	0.10	12.78	1.42	14.2	0.0046	0.066
4	1.70	36.0	474.9	13.2	5.40	0.15	56.09	1.56	10.4	0.0057	0.059
	0.95	6.0	79.1	13.2	0.90	0.15	9.34	1.56	10.4	0.0057	0.059
	3.60	21.0	277.0	13.2	3.15	0.15	32.76	1.56	10.4	0.0057	0.059
5	1.70	40.0	609.3	15.2	8.00	0.20	67.28	1.68	8.4	0.0066	0.055
	2.50	26.0	396.0	15.2	5.20	0.20	43.74	1.68	8.4	0.0066	0.055
	1.50	12.0	182.8	15.2	2.40	0.20	20.20	1.68	8.4	0.0066	0.055
6	2.00	40.0	746.2	18.7	12.00	0.30	75.82	1.90	6.3	0.0080	0.051
	1.00	8.0	149.2	18.7	2.40	0.30	15.16	1.90	6.3	0.0080	0.051
	1.25	24.0	447.7	18.7	7.20	0.30	45.48	1.90	6.3	0.0080	0.051
7	1.60	43.0	1035.6	24.1	21.50	0.50	96.14	2.24	4.5	0.0104	0.046
	2.70	11.0	264.9	24.1	5.50	0.50	24.60	2.24	4.5	0.0104	0.046
	1.10	27.0	650.2	24.1	13.50	0.50	60.38	2.24	4.5	0.0104	0.046
8	1.90	36.0	1734.0	48.2	72.00	2.00	134.48	3.74	1.9	0.0208	0.039
	4.50	15.0	722.5	48.2	30.00	2.00	56.12	3.74	1.9	0.0208	0.039
	2.50	26.0	1252.3	48.2	52.00	2.00	97.34	3.74	1.9	0.0208	0.039



**Table 4-9** FE Models with W-Shapes (Constant  $L/d$  case)

Group	Section	$d$ (in)	$L$ (in)	$L/d$	$\delta_p$ (in)	$\delta_p/d$	$W_{cat}$ (in)	$W_{cat}/d$	$W_{cat}/\delta_p$	$\delta_p/2L$	$W_{cat}/2L$
1	W36x231	36.50	124.3	3.4	0.27	0.01	40.89	1.12	149.2	0.0011	0.164
	W12x230	15.10	51.4	3.4	0.12	0.01	16.16	1.07	133.3	0.0012	0.157
	W24x229	26.00	88.6	3.4	0.20	0.01	28.61	1.10	143.9	0.0011	0.162
2	W40x327	40.80	310.7	7.6	1.60	0.04	55.72	1.37	34.9	0.0026	0.090
	W24x192	25.50	194.2	7.6	0.97	0.04	35.38	1.39	36.6	0.0025	0.091
	W10x49	10.00	76.2	7.6	0.37	0.04	14.10	1.41	38.1	0.0024	0.093
3	W40x297	39.80	428.7	10.8	3.03	0.08	62.94	1.58	20.8	0.0035	0.073
	W8x58	8.75	94.2	10.8	0.67	0.08	13.87	1.59	20.7	0.0036	0.074
	W24x103	24.50	263.9	10.8	1.87	0.08	38.68	1.58	20.7	0.0035	0.073
4	W36x210	36.70	484.1	13.2	4.25	0.12	63.06	1.72	14.8	0.0044	0.065
	W6x20	6.38	84.2	13.2	0.74	0.12	11.11	1.74	15.1	0.0044	0.066
	W18x258	21.50	283.6	13.2	2.56	0.12	36.77	1.71	14.3	0.0045	0.065
5	W40x235	39.70	604.7	15.2	6.10	0.15	73.36	1.85	12.0	0.0050	0.061
	W12x65	12.10	184.3	15.2	1.77	0.15	23.08	1.91	13.0	0.0048	0.063
	W24x229	26.00	396.0	15.2	3.98	0.15	48.43	1.86	12.2	0.0050	0.061
6	W40x278	40.20	749.9	18.7	9.38	0.23	82.70	2.06	8.8	0.0063	0.055
	W8x40	8.25	153.9	18.7	1.86	0.22	17.48	2.12	9.4	0.0060	0.057
	W24x103	24.50	457.0	18.7	5.60	0.23	50.92	2.08	9.1	0.0061	0.056
7	W44x230	42.90	1033.2	24.1	16.22	0.38	104.46	2.43	6.4	0.0079	0.051
	W10x100	11.10	267.3	24.1	4.28	0.39	27.27	2.46	6.4	0.0080	0.051
	W27x102	27.10	652.7	24.1	10.31	0.38	65.82	2.43	6.4	0.0079	0.050
8	W36x231	36.50	1758.1	48.2	54.83	1.50	144.13	3.95	2.6	0.0156	0.041
	W12x230	15.10	727.3	48.2	24.25	1.61	59.02	3.91	2.4	0.0167	0.041
	W24x229	26.00	1252.3	48.2	39.76	1.53	102.58	3.95	2.6	0.0159	0.041

Plots of  $W_{cat}/\delta_p$  versus  $\delta_p/d$ ,  $\delta_p/2L$  and  $L/d$  are given in Figures 4-53, 4-54 and 4-55, respectively. Plots of  $W_{cat}/d$  versus  $\delta_p/d$ ,  $\delta_p/2L$  and  $L/d$  are given in Figures 4-56, 4-57 and 4-58, respectively. Plots of  $W_{cat}/2L$  versus  $\delta_p/d$ ,  $\delta_p/2L$  and  $L/d$  are given in Figures 4-59, 4-60 and 4-61, respectively.

Very similar observations as before can be made by comparing Figures 4-53 through 4-61 with Figures 4-35 through 4-43, respectively, for the constant  $\delta_p/d$  case, and with Figures 4-44 through 4-52, respectively, for the constant  $\delta_p/2L$  case. However, there is one exception. In the current case, the points for the W-Shapes within each group show the best agreement for cases that use an independent variable of  $L/d$ , which

happens to be constant for each group of three beams. This can be seen in Figures 4-55, 4-58, and 4-61.

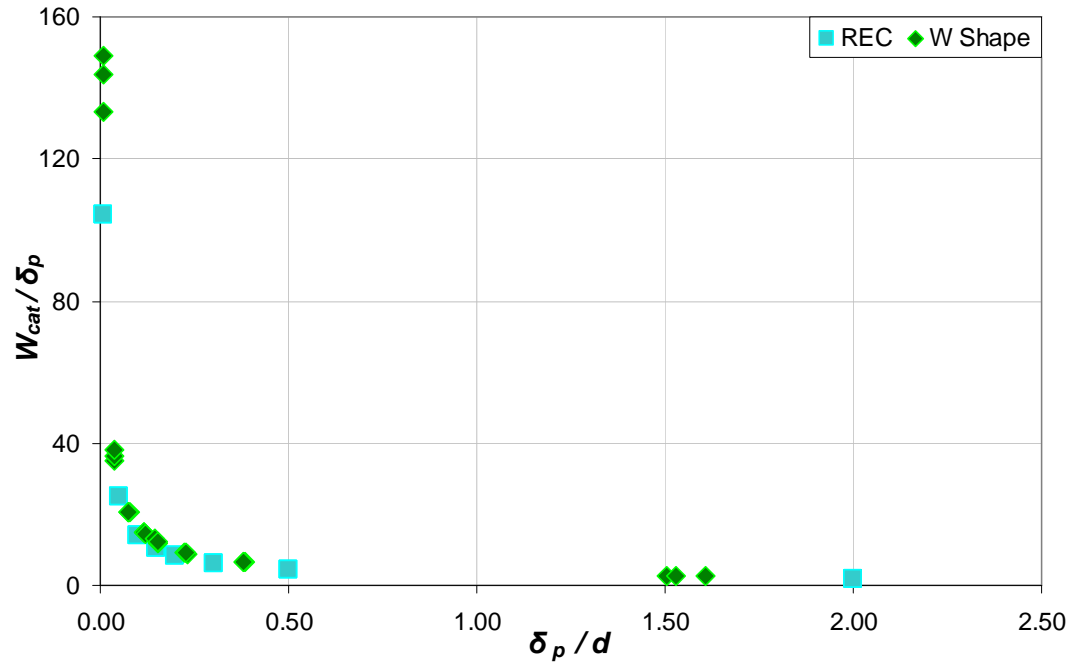


**Figure 4-53**  $W_{cat} / \delta_p - \delta_p / d$  Relationship (Constant  $L / d$  within each group)

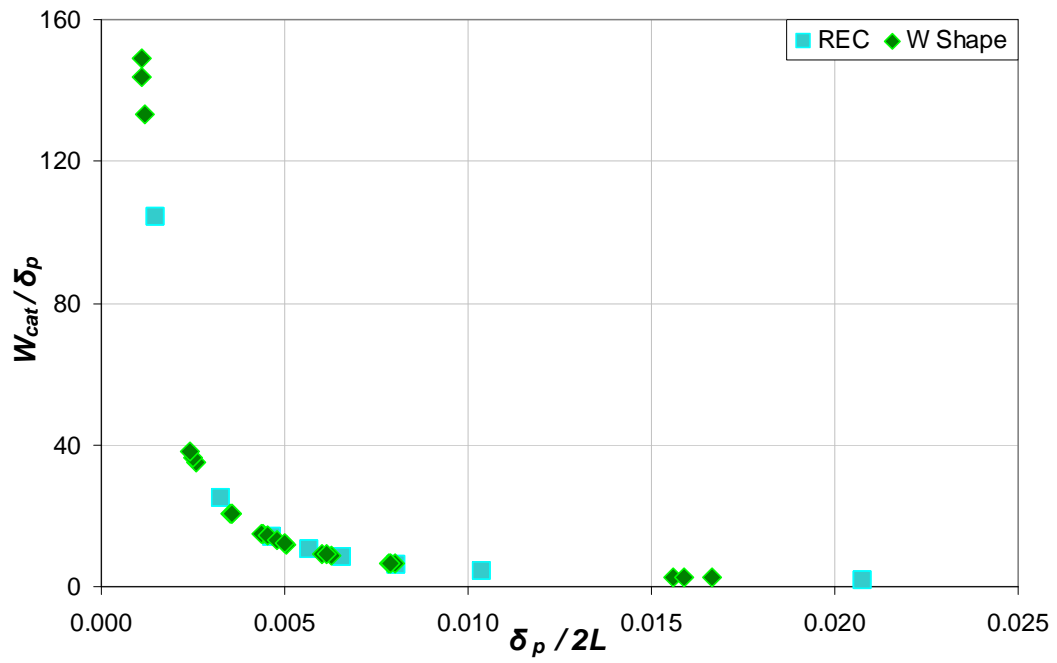


**Figure 4-54**  $W_{cat} / \delta_p - \delta_p / 2L$  Relationship (Constant  $L / d$  within each group)

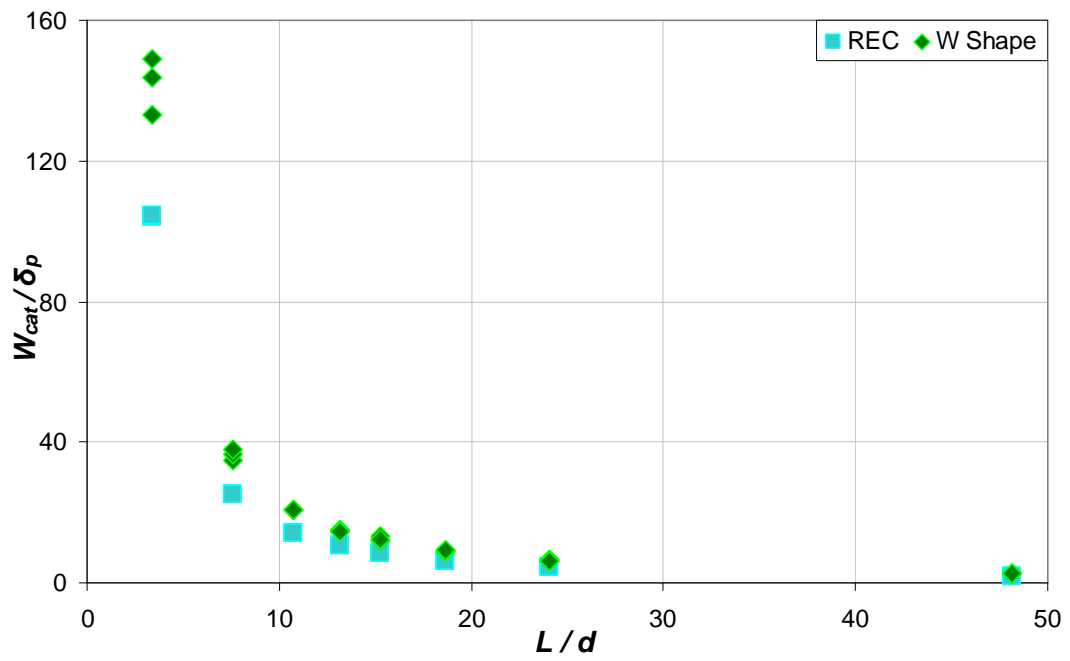


**Figure 4-55**  $W_{cat} / \delta_p - L / d$  Relationship (Constant  $L / d$  within each group)

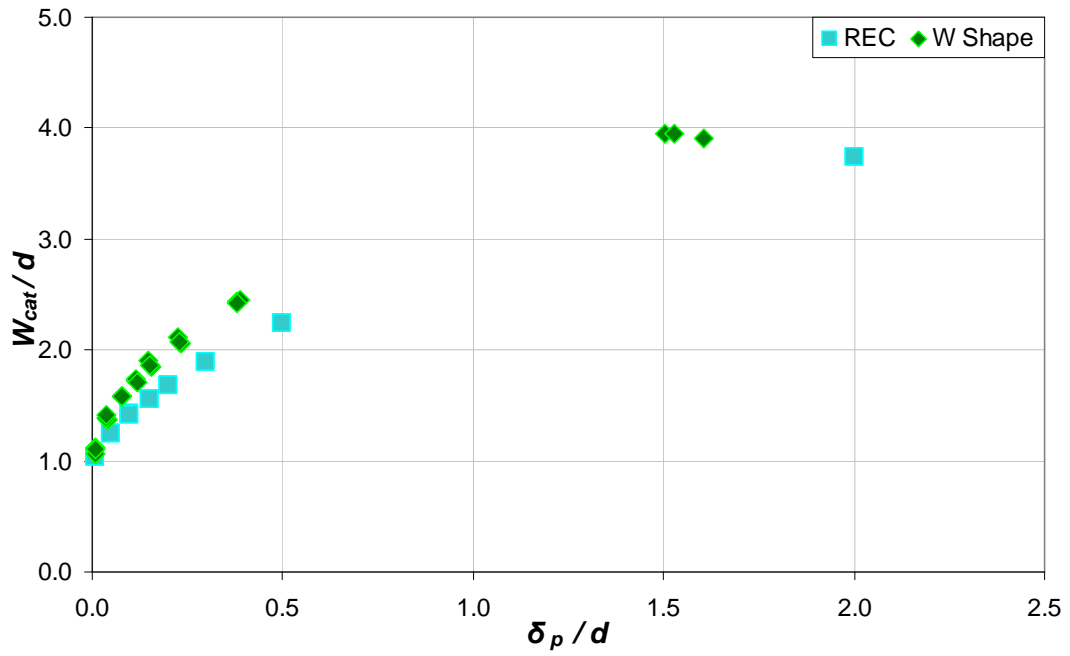


**Figure 4-56**  $W_{cat} / d - \delta_p / d$  Relationship (Constant  $L / d$  within each group)

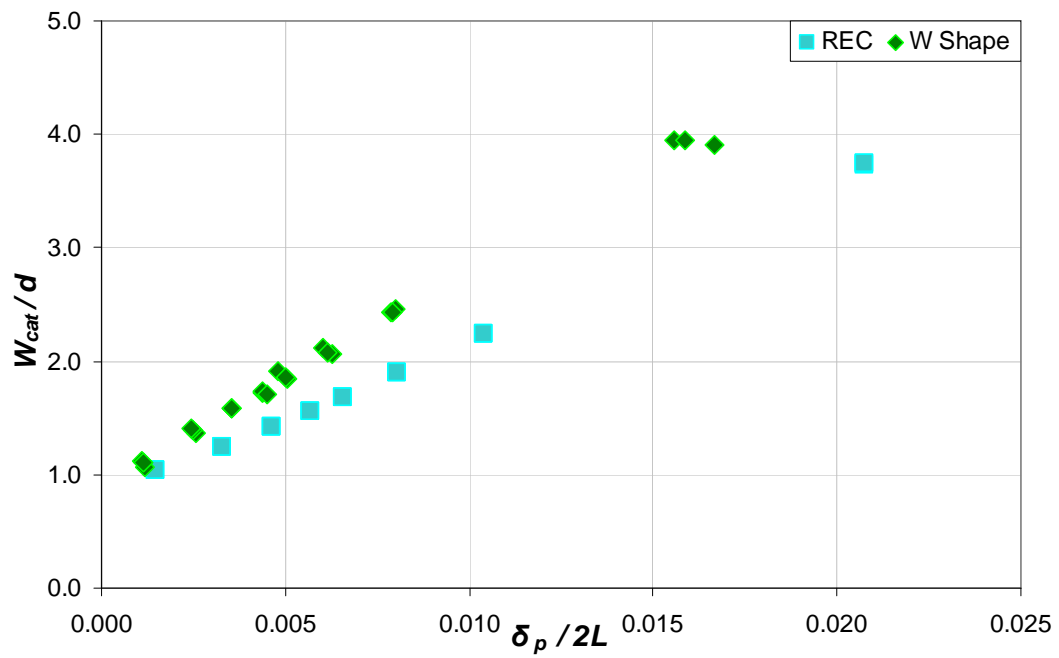


**Figure 4-57**  $W_{cat} / d - \delta_p / 2L$  Relationship (Constant  $L / d$  within each group)

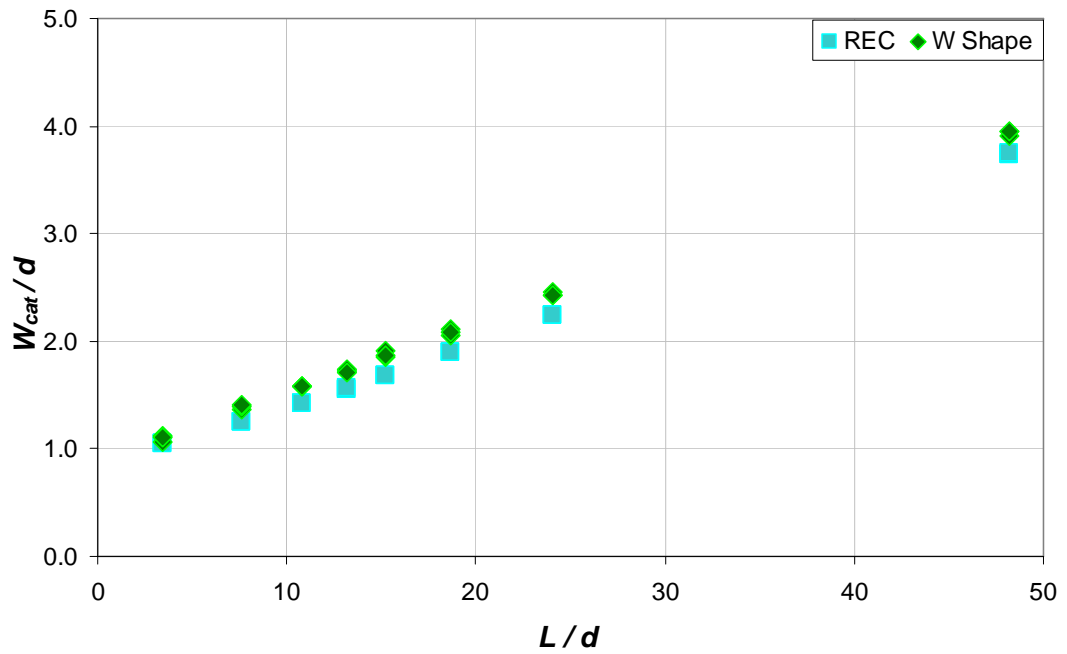


**Figure 4-58**  $W_{cat}/d - L/d$  Relationship (Constant  $L/d$  within each group)

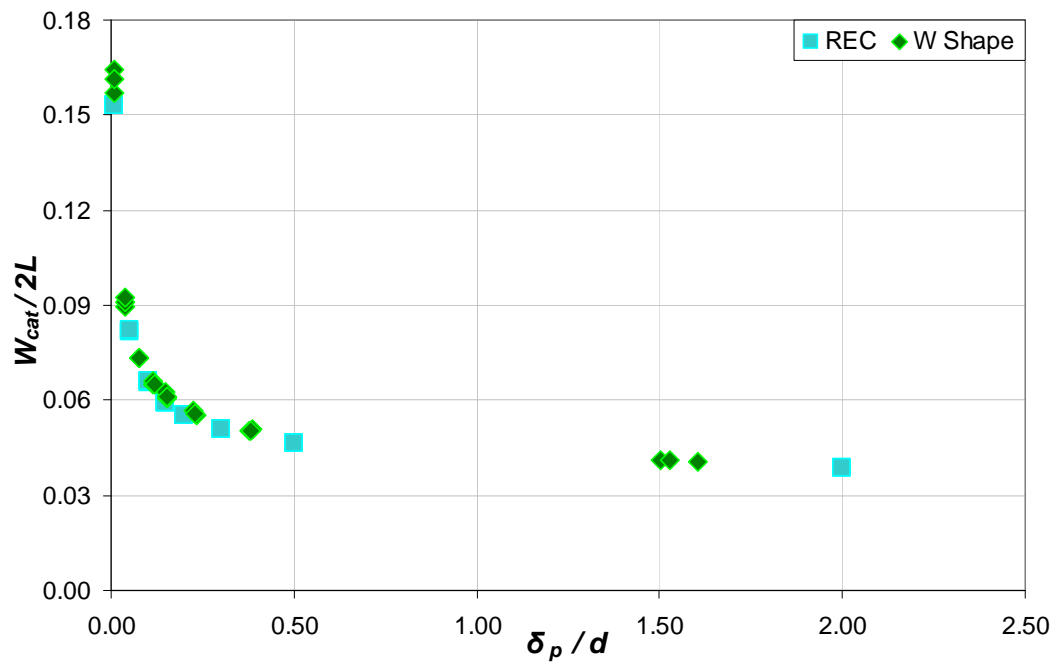


**Figure 4-59**  $W_{cat}/2L - \delta_p/d$  Relationship (Constant  $L/d$  within each group)

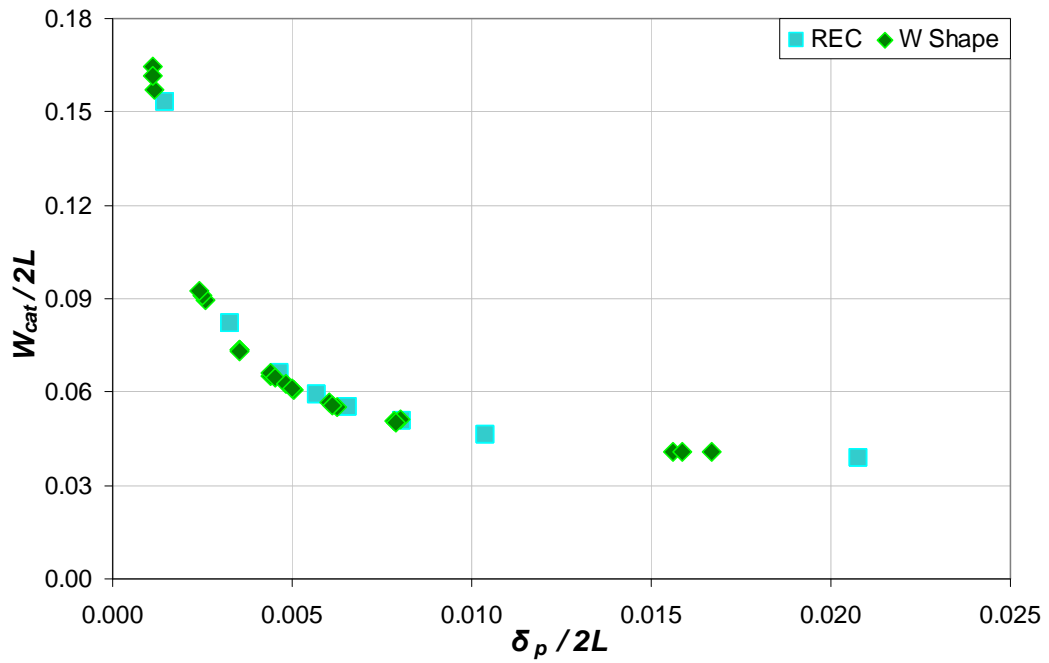


**Figure 4-60**  $W_{cat}/2L - \delta_p/2L$  Relationship (Constant  $L/d$  within each group)

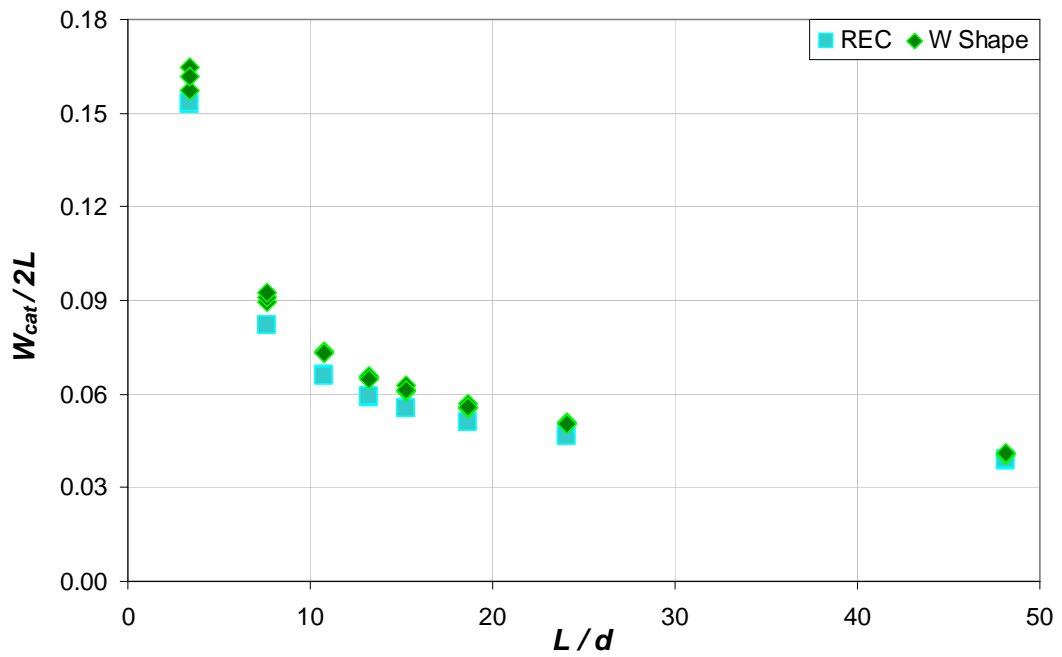


**Figure 4-61**  $W_{cat}/2L - L/d$  Relationship (Constant  $L/d$  within each group)

#### 4.4.4 Distributed Load Case

A similar study was conducted for fully fixed beams under uniform loading, as shown in Figure 4-3(b).

Only the case of constant  $L/d$  is presented herein. Similar observations as for fully fixed beams under a concentrated load at midspan were made. The parameters used and results obtained are given in Tables 4-10 and 4-11 for beams with rectangular and W-Shapes, respectively.

**Table 4-10** FE Models with Rectangular Sections (Uniform Loading)

Group	$b$ (in)	$d$ (in)	$L$ (in)	$L/d$	$\delta_p$ (in)	$\delta_p/d$	$W_{cat}$ (in)	$W_{cat}/d$	$W_{cat}/\delta_p$	$\delta_p/2L$	$W_{cat}/2L$
1	1.90	36.00	122.6	3.4	0.36	0.01	67.74	1.88	188.2	0.0015	0.276
	4.50	15.00	51.1	3.4	0.15	0.01	28.23	1.88	188.2	0.0015	0.276
	2.50	26.00	88.6	3.4	0.26	0.01	48.93	1.88	188.2	0.0015	0.276
2	2.40	40.00	304.6	7.6	2.00	0.05	89.63	2.24	44.8	0.0033	0.147
	2.20	25.00	190.4	7.6	1.25	0.05	56.03	2.24	44.8	0.0033	0.147
	1.40	10.00	76.2	7.6	0.50	0.05	22.41	2.24	44.8	0.0033	0.147
3	2.20	39.00	420.0	10.8	3.90	0.10	93.07	2.39	23.9	0.0046	0.111
	1.20	24.00	258.5	10.8	2.40	0.10	57.27	2.39	23.9	0.0046	0.111
	2.00	9.00	96.9	10.8	0.90	0.10	21.48	2.39	23.9	0.0046	0.111
4	1.70	36.00	474.9	13.2	5.40	0.15	89.58	2.49	16.6	0.0057	0.094
	0.95	6.00	79.1	13.2	0.90	0.15	14.93	2.49	16.6	0.0057	0.094
	3.60	21.00	277.0	13.2	3.15	0.15	52.27	2.49	16.6	0.0057	0.094
5	1.70	40.00	609.3	15.2	8.00	0.20	102.96	2.57	12.9	0.0066	0.084
	2.50	26.00	396.0	15.2	5.20	0.20	66.92	2.57	12.9	0.0066	0.084
	1.50	12.00	182.8	15.2	2.40	0.20	30.90	2.58	12.9	0.0066	0.085
6	2.00	40.00	746.2	18.7	12.00	0.30	108.84	2.72	9.1	0.0080	0.073
	1.00	8.00	149.2	18.7	2.40	0.30	21.85	2.73	9.1	0.0080	0.073
	1.25	24.00	447.7	18.7	7.20	0.30	65.32	2.72	9.1	0.0080	0.073
7	1.60	43.00	1035.6	24.1	21.50	0.50	126.58	2.94	5.9	0.0104	0.061
	2.70	11.00	264.9	24.1	5.50	0.50	32.38	2.94	5.9	0.0104	0.061
	1.10	27.00	650.2	24.1	13.50	0.50	79.48	2.94	5.9	0.0104	0.061
8	1.90	36.00	1734.0	48.2	72.00	2.00	143.38	3.98	2.0	0.0208	0.041
	4.50	15.00	722.5	48.2	30.00	2.00	59.72	3.98	2.0	0.0208	0.041
	2.50	26.00	1252.3	48.2	52.00	2.00	103.56	3.98	2.0	0.0208	0.041

**Table 4-11** FE Models with W-Shapes (Uniform Loading)

Group	Section	$d$ (in)	$L$ (in)	$L/d$	$\delta_p$ (in)	$\delta_p/d$	$W_{cat}$ (in)	$W_{cat}/d$	$W_{cat}/\delta_p$	$\delta_p/2L$	$W_{cat}/2L$
1	W36x231	36.50	124.3	3.4	0.27	0.01	64.47	1.77	235.2	0.0011	0.259
	W12x230	15.10	51.4	3.4	0.12	0.01	27.50	1.82	226.8	0.0012	0.267
	W24x229	26.00	88.6	3.4	0.20	0.01	51.48	1.98	258.9	0.0011	0.291
2	W40x327	40.80	310.7	7.6	1.60	0.04	87.88	2.15	55.0	0.0026	0.141
	W24x192	25.50	194.2	7.6	0.97	0.04	55.44	2.17	57.3	0.0025	0.143
	W10x49	10.00	76.2	7.6	0.37	0.04	21.12	2.11	57.1	0.0024	0.139
3	W40x297	39.80	428.7	10.8	3.03	0.08	95.58	2.40	31.6	0.0035	0.111
	W8x58	8.75	94.2	10.8	0.67	0.08	22.77	2.60	34.0	0.0036	0.121
	W24x103	24.50	263.9	10.8	1.87	0.08	57.94	2.36	31.0	0.0035	0.110
4	W36x210	36.70	484.1	13.2	4.25	0.12	98.58	2.69	23.2	0.0044	0.102
	W6x20	6.38	84.2	13.2	0.74	0.12	16.25	2.55	22.0	0.0044	0.097
	W18x258	21.50	283.6	13.2	2.56	0.12	57.43	2.67	22.4	0.0045	0.101
5	W40x235	39.70	604.7	15.2	6.10	0.15	110.64	2.79	18.1	0.0050	0.091
	W12x65	12.10	184.3	15.2	1.77	0.15	34.24	2.83	19.3	0.0048	0.093
	W24x229	26.00	396.0	15.2	3.98	0.15	72.86	2.80	18.3	0.0050	0.092
6	W40x278	40.20	749.9	18.7	9.38	0.23	117.02	2.91	12.5	0.0063	0.078
	W8x40	8.25	153.9	18.7	1.86	0.22	24.22	2.94	13.1	0.0060	0.079
	W24x103	24.50	457.0	18.7	5.60	0.23	71.06	2.90	12.7	0.0061	0.078
7	W44x230	42.90	1033.2	24.1	16.22	0.38	136.05	3.17	8.4	0.0079	0.066
	W10x100	11.10	267.3	24.1	4.28	0.39	34.23	3.08	8.0	0.0080	0.064
	W27x102	27.10	652.7	24.1	10.31	0.38	85.72	3.16	8.3	0.0079	0.066
8	W36x231	36.50	1758.1	48.2	54.83	1.50	154.70	4.24	2.8	0.0156	0.044
	W12x230	15.10	727.3	48.2	24.25	1.61	62.76	4.16	2.6	0.0167	0.043
	W24x229	26.00	1252.3	48.2	39.76	1.53	109.48	4.21	2.8	0.0159	0.044

Plots of  $W_{cat}/\delta_p$  versus  $\delta_p/d$ ,  $\delta_p/2L$  and  $L/d$  are given in Figures 4-62, 4-63 and 4-64, respectively. Plots of  $W_{cat}/d$  versus  $\delta_p/d$ ,  $\delta_p/2L$  and  $L/d$  are given in Figures 4-65, 4-66 and 4-67, respectively. Plots of  $W_{cat}/2L$  versus  $\delta_p/d$ ,  $\delta_p/2L$  and  $L/d$  are given in Figures 4-68, 4-69 and 4-70, respectively.



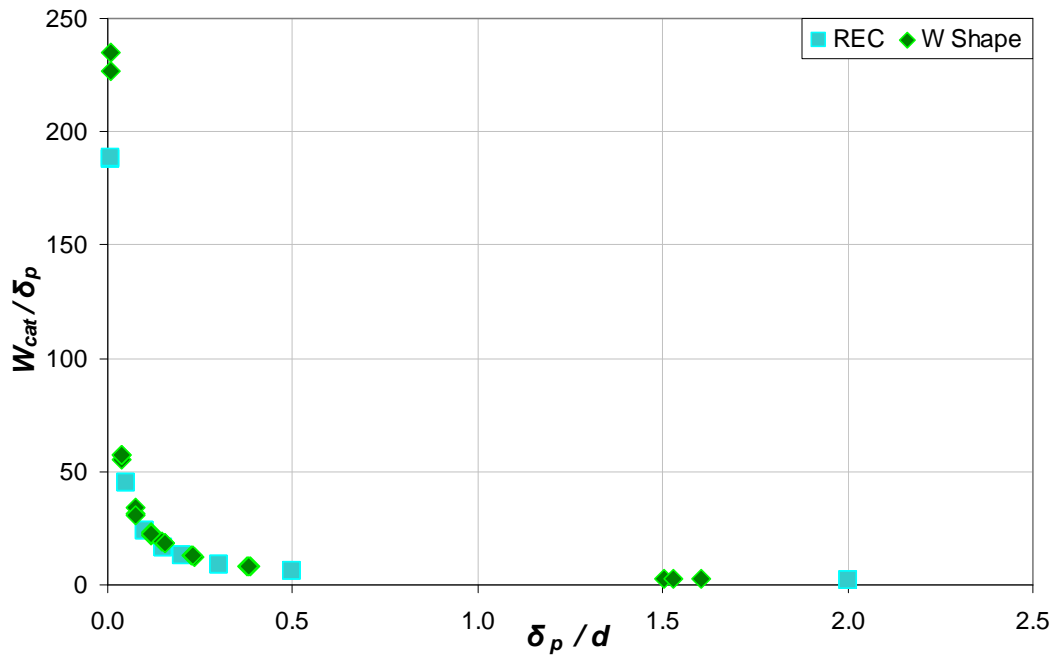


**Figure 4-62**  $W_{cat} / \delta_p - \delta_p / d$  Relationship (Constant  $L / d$  within each group)

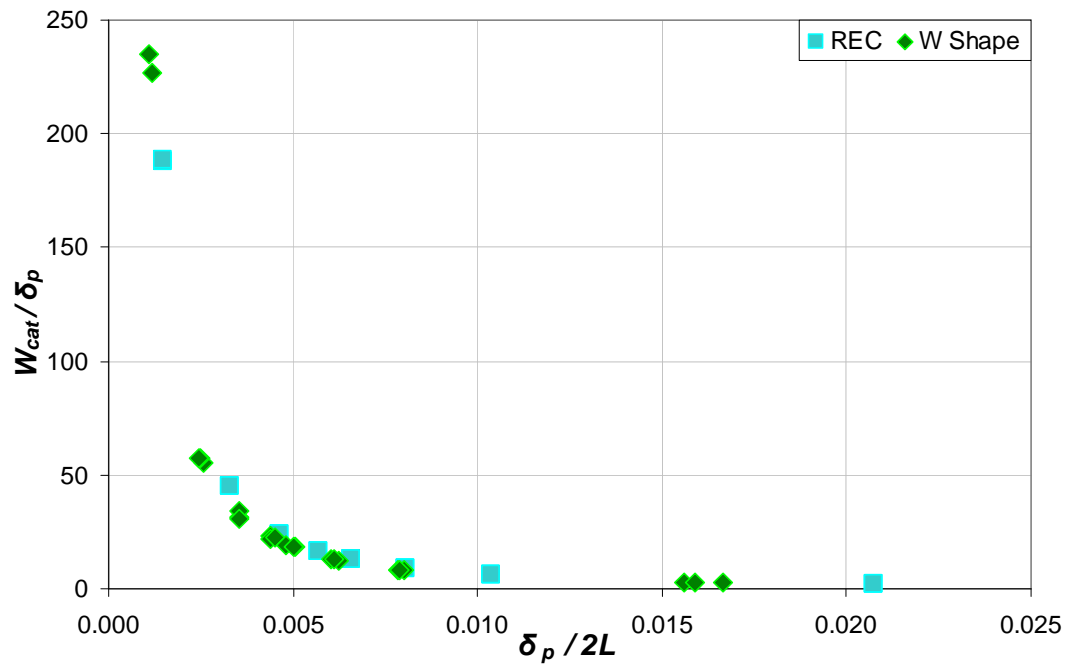


**Figure 4-63**  $W_{cat} / \delta_p - \delta_p / 2L$  Relationship (Constant  $L / d$  within each group)

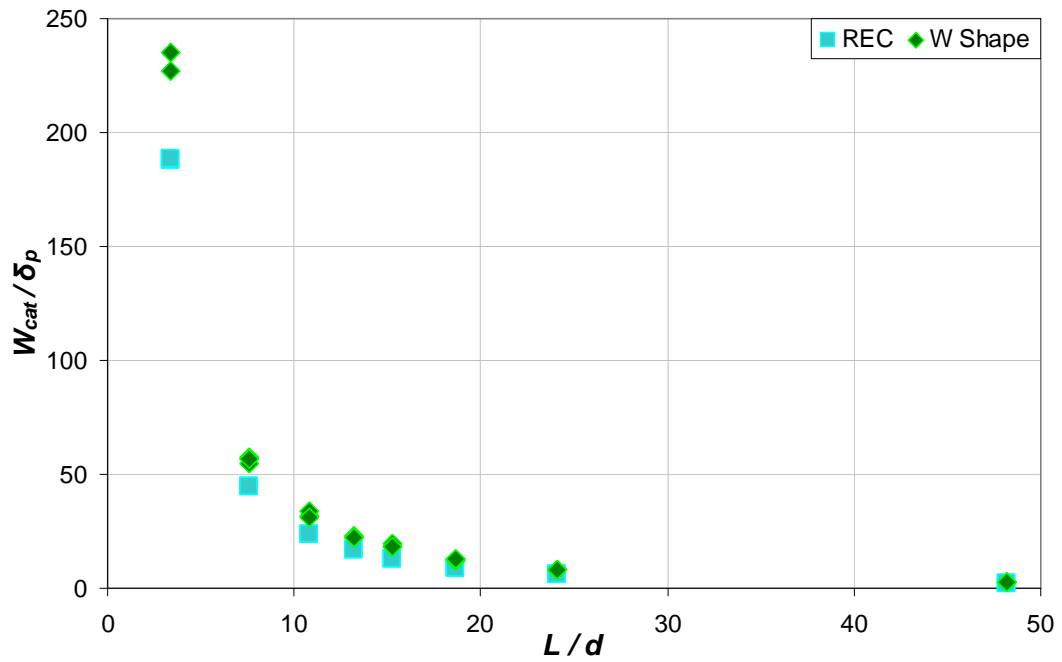


**Figure 4-64**  $W_{cat} / \delta_p - L/d$  Relationship (Constant  $L/d$  within each group)

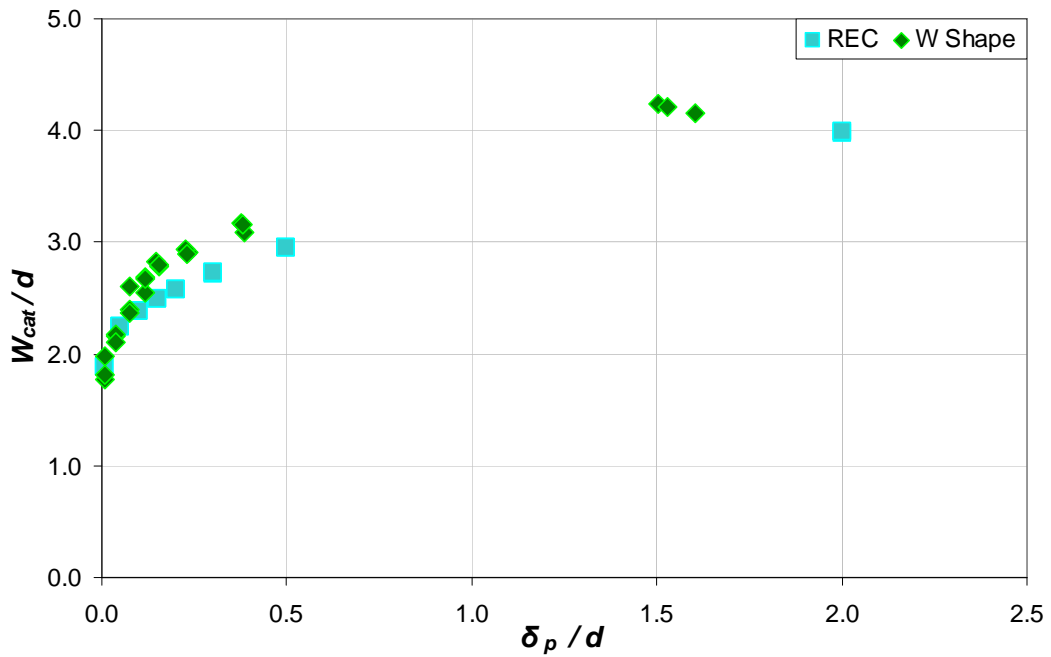


**Figure 4-65**  $W_{cat} / d - \delta_p / d$  Relationship (Constant  $L/d$  within each group)

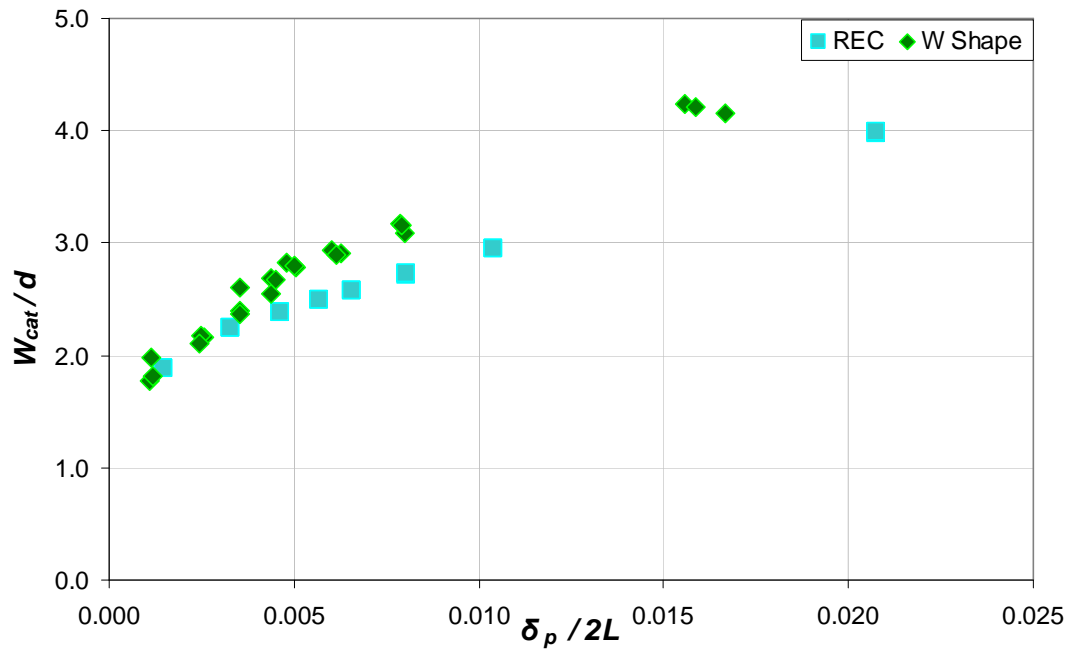


**Figure 4-66**  $W_{cat}/d - \delta_p/2L$  Relationship (Constant  $L/d$  within each group)

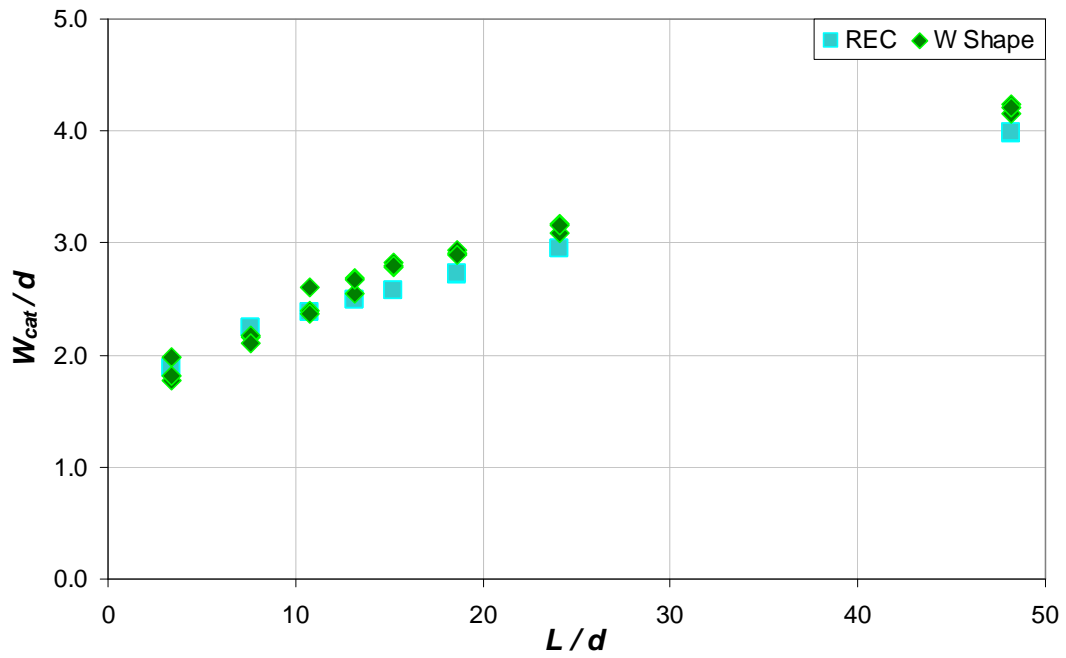


**Figure 4-67**  $W_{cat}/d - L/d$  Relationship (Constant  $L/d$  within each group)

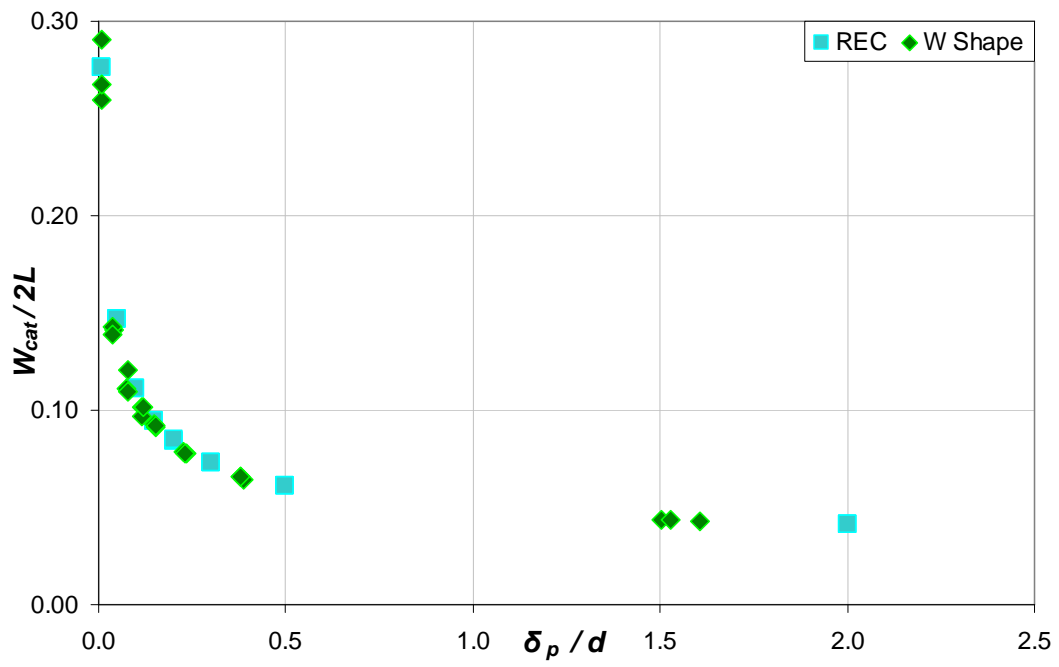


**Figure 4-68**  $W_{cat}/2L - \delta_p/d$  Relationship (Constant  $L/d$  within each group)

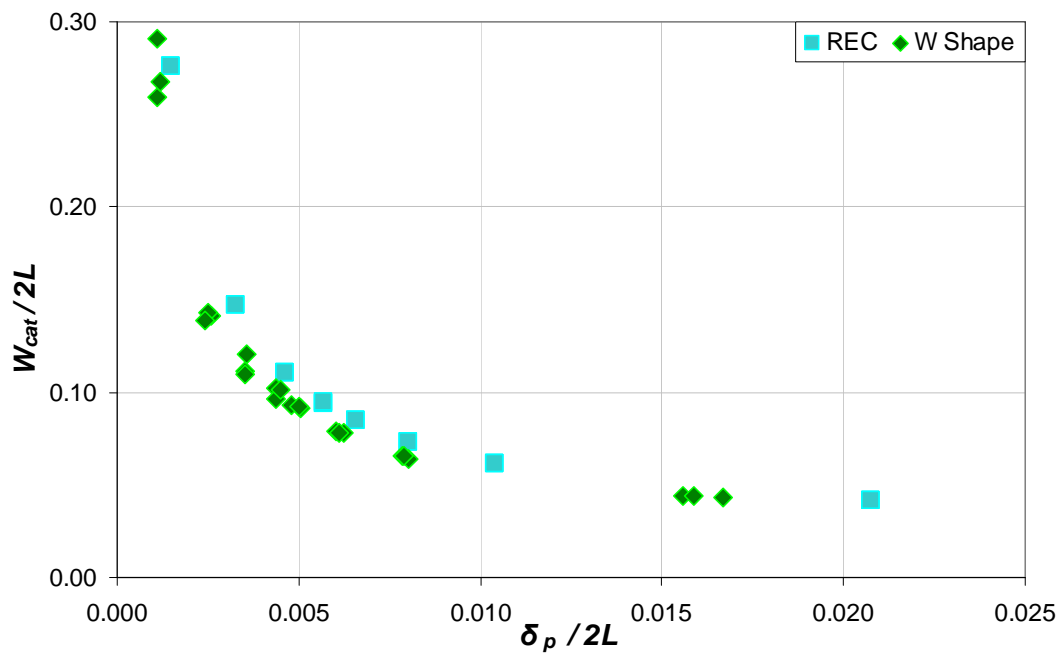


**Figure 4-69**  $W_{cat}/2L - \delta_p/2L$  Relationship (Constant  $L/d$  within each group)

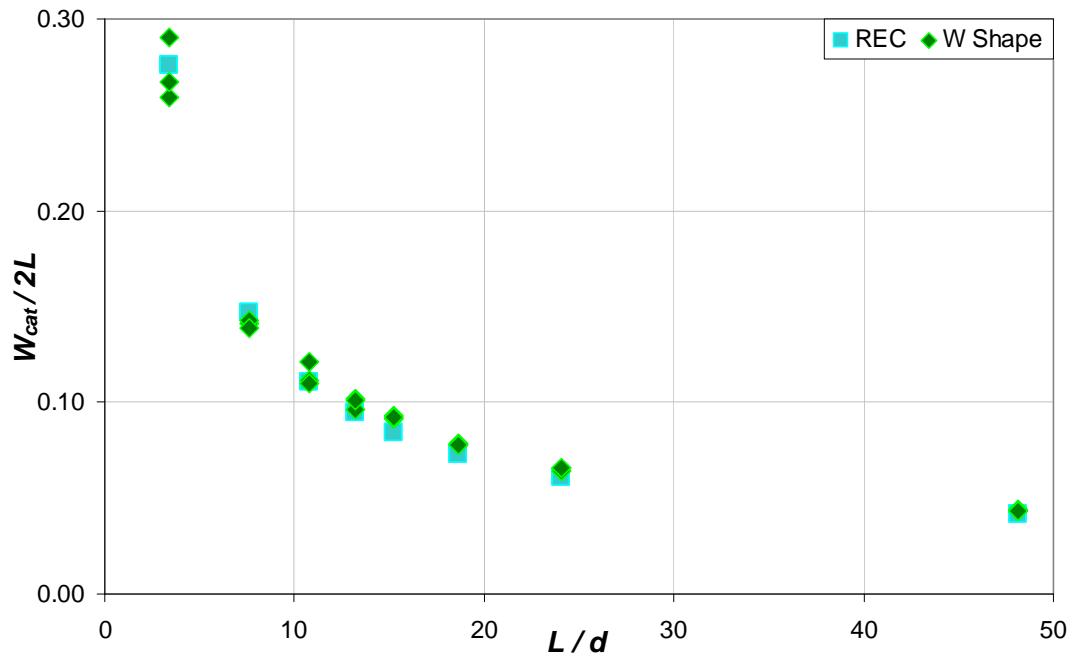


**Figure 4-70**  $W_{cat}/2L - L/d$  Relationship (Constant  $L/d$  within each group)

#### 4.4.5 Summary and Conclusions

A parametric FE analysis study of elastic–perfectly plastic steel beams with full end fixity was conducted. Through preliminary FE analysis results, geometric parameters that had an influence on the onset of pure cable state,  $W_{cat}$  were identified and studied using beam models for rectangular and W–Shaped cross–sections.

A cursory study revealed that the midspan displacement at the onset of pure cable behavior,  $W_{cat}$ , is not only influenced by  $\delta_p$ ; even for the same  $\delta_p$ , it was observed that  $W_{cat}$  varied significantly with the cross-section used. However, further investigations revealed that the point of pure cable behavior is reached at approximately the same ratio of midspan displacement to depth,  $W_{cat}/d$ , regardless of the cross section used. This

initial study led to another parametric study with a wider scope. In particular, the effect of  $\delta_p / d$ ,  $\delta_p / 2L$  and  $L / d$  on  $W_{cat} / \delta_p$ ,  $W_{cat} / d$  and  $W_{cat} / 2L$  was investigated.

## Chapter 5. EQUATIONS FOR THE ONSET OF PURE CABLE BEHAVIOR

### 5.1 Overview

Rigid–plastic and cable theories for fully fixed beams with rectangular and W–Shaped cross-sections were developed in Chapter 3. Preliminary FE analysis results presented in Chapter 4 showed that results from both theories can be simulated numerically. However, they represent an ideal beam behavior. FE parametric studies as presented in Chapter 4 showed that the elastic–perfectly plastic response can be neither represented precisely by rigid–plastic nor cable theory, but is expected to fall in between the two. The studies focused on finding the midspan deflection level at the onset of pure cable behavior,  $W_{cat}$ . The observed trends for  $W_{cat}$ , with respect to the geometric parameters studied, prompted an investigation into the possibility of developing an equation that would predict the onset point of pure cable behavior in terms of the theoretical predictions presented in Chapter 3.

Trends for  $W_{cat}$  can be expressed in several ways, such as those discussed in Chapter 4. The following three forms of relationships were selected:

- $W_{cat} / \delta_p$  versus  $\delta_p / 2L$  (Formulation I)
- $W_{cat} / d$  versus  $L / d$  (Formulation II)
- $W_{cat} / 2L$  versus  $L / d$  (Formulation III)

Theoretical expressions for  $W_{cat}$  in these forms were developed using both rigid-plastic and cable theories, and were compared to FE analysis results for the concentrated and uniformly distributed load cases from Chapter 4.

## 5.2 Concentrated Load Case

### 5.2.1 Formulation I

- Rigid-plastic theory:

The onset point of pure cable behavior for a fully fixed beam is independent of the cross-section and occurs when the deflection equals the nominal depth of the section,  $d$  (i.e.  $W_{cat} = d$ ). Therefore:

$$\frac{W_{cat}}{\delta_p} = \frac{d}{\delta_p} \quad [5.1]$$

which can be written as:

$$\frac{W_{cat}}{\delta_p} = \frac{1}{2} \cdot \frac{1}{\left[\frac{L}{d}\right]} \frac{1}{\left[\frac{\delta_p}{2L}\right]}. \quad [5.2]$$

Substituting  $L/d$  from Equation 4.7 into Equation 5.2 yields:

$$\frac{W_{cat}}{\delta_p} = \frac{1}{12} \cdot \frac{\sigma_y \cdot f}{E} \frac{1}{\left[\frac{\delta_p}{2L}\right]^2} \quad [5.3]$$

- Cable Theory

It has been shown in Section 3.3.1 that the onset point of pure cable behavior is independent of cross-section type and can be written in the form:



$$\frac{W_{cat}}{L} = \sqrt{\frac{2\sigma_y}{E}} \quad [5.4]$$

which can be rewritten as:

$$\frac{W_{cat}}{\delta_p} = \sqrt{\frac{2\sigma_y}{E}} \cdot \frac{1}{2 \cdot \left[ \frac{\delta_p}{2L} \right]} \quad [5.5]$$

or

$$\frac{W_{cat}}{\delta_p} = \sqrt{\frac{\sigma_y}{2E}} \cdot \frac{1}{\left[ \frac{\delta_p}{2L} \right]} \quad [5.6]$$

Plots of  $W_{cat}/\delta_p$  versus  $\delta_p/2L$  as suggested by each theory are given in Figures 5-1 through 5-4 in comparison with FE analysis results presented in Chapter 4. Since  $W_{cat}$  according to the rigid-plastic theory is affected by the shape factor ( $f$ ) (Equation 5-3), the plots are presented for beams with rectangular and W-Shaped cross-sections independently. Figure 5-1 shows the comparison with FE analysis results for rectangular shaped beams. Figure 5-2, 5-3, and 5-4 show the comparison with FE results for W-Shaped beams with constant  $\delta_p/d$ ,  $\delta_p/2L$ , and  $L/d$ , respectively. The shape factor,  $f$ , in Equation 5.3 was taken as an average value of 1.15 for all W-Shapes considered.

For beams with rectangular cross-section, it can be seen from Figure 5-1 that the FE analysis results tend to approach those for the rigid-plastic theory for relatively stiff beams and approach cable theory results for relatively flexible beams. Similar observations can be made for beams with W-Shapes as shown in Figures 5-2, 5-3 and 5-4. With the purpose of representing the behavior over the entire range, a new curve is introduced which was obtained by linear superposition of Equations 5.3 and 5.6:

$$\frac{W_{cat}}{\delta_p} = \frac{1}{12} \cdot \frac{\sigma_y \cdot f}{E} \frac{1}{\left[\frac{\delta_p}{2L}\right]^2} + \sqrt{\frac{\sigma_y}{2E}} \cdot \frac{1}{\left[\frac{\delta_p}{2L}\right]} \quad [5.7]$$

Equation 5.7 is represented by the solid curve in Figures 5-1 through 5-4.

Equation 5.7 approaches the rigid-plastic theory for relatively stiff beams and cable theory for relatively flexible beams.

It can be seen that Equation 5.7 is in excellent agreement with the FE results for W-Shapes (Figures 5-2 through 5-4) and in good agreement with the FE results for rectangular shapes (Figure 5-1). Minor discrepancies that can be seen in the figures will be discussed in Section 5.4.

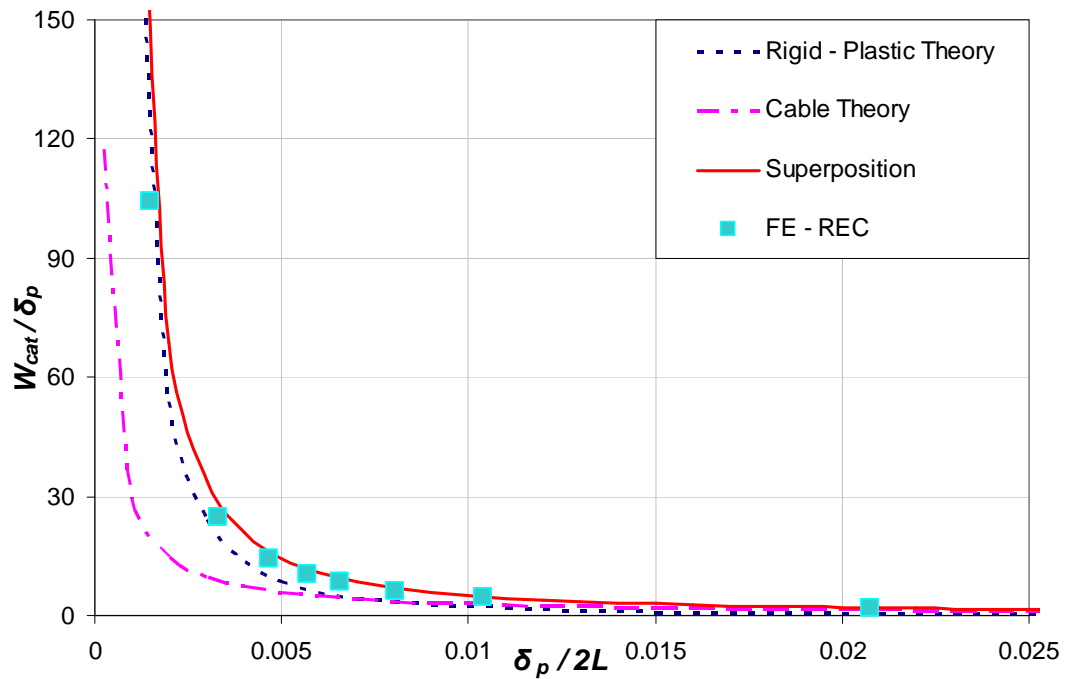


**Figure 5-1** Comparison with FE results (REC Shapes)

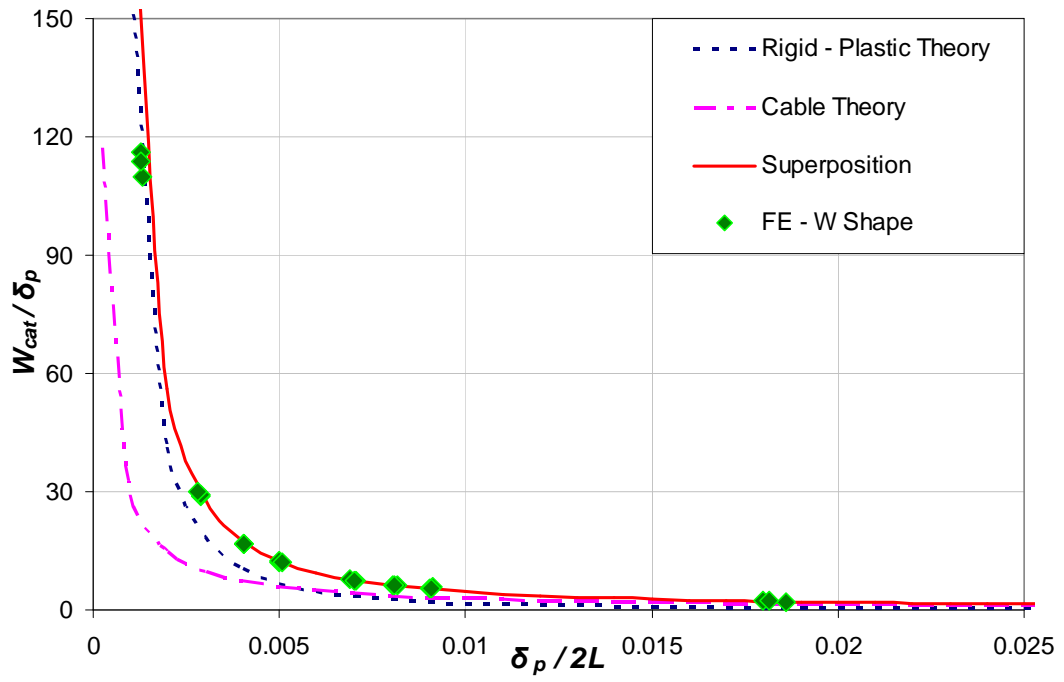


**Figure 5-2** Comparison with FE results (W-Shapes: Constant  $\delta_p/d$  case)

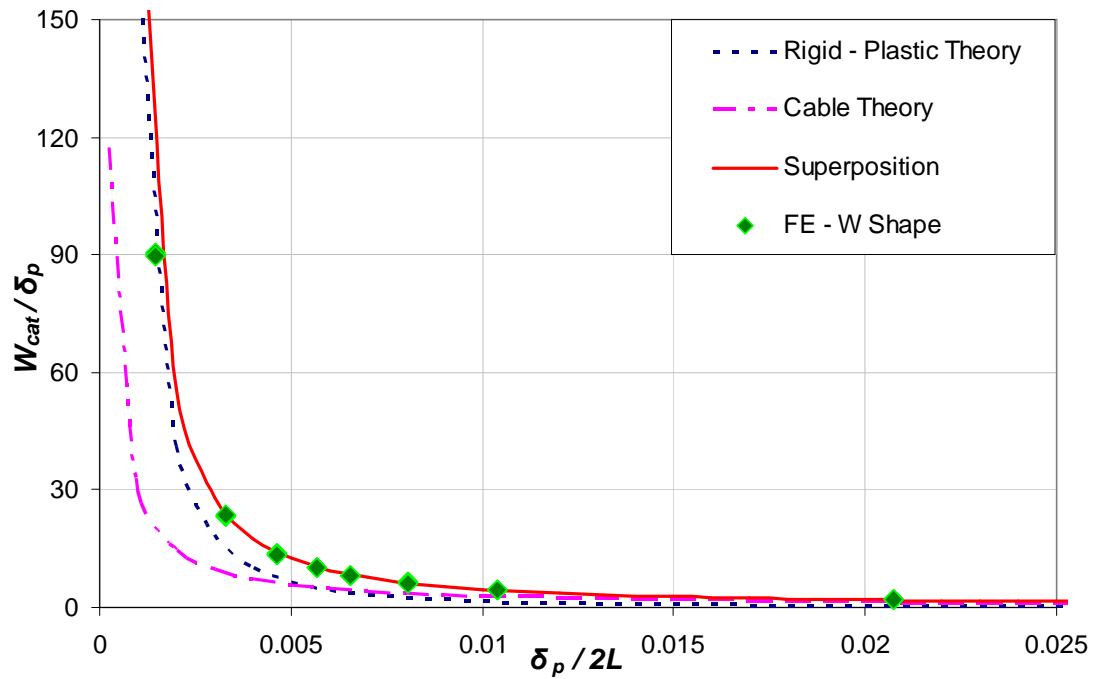


**Figure 5-3** Comparison with FE results (W-Shapes: Constant  $\delta_p/2L$  case)

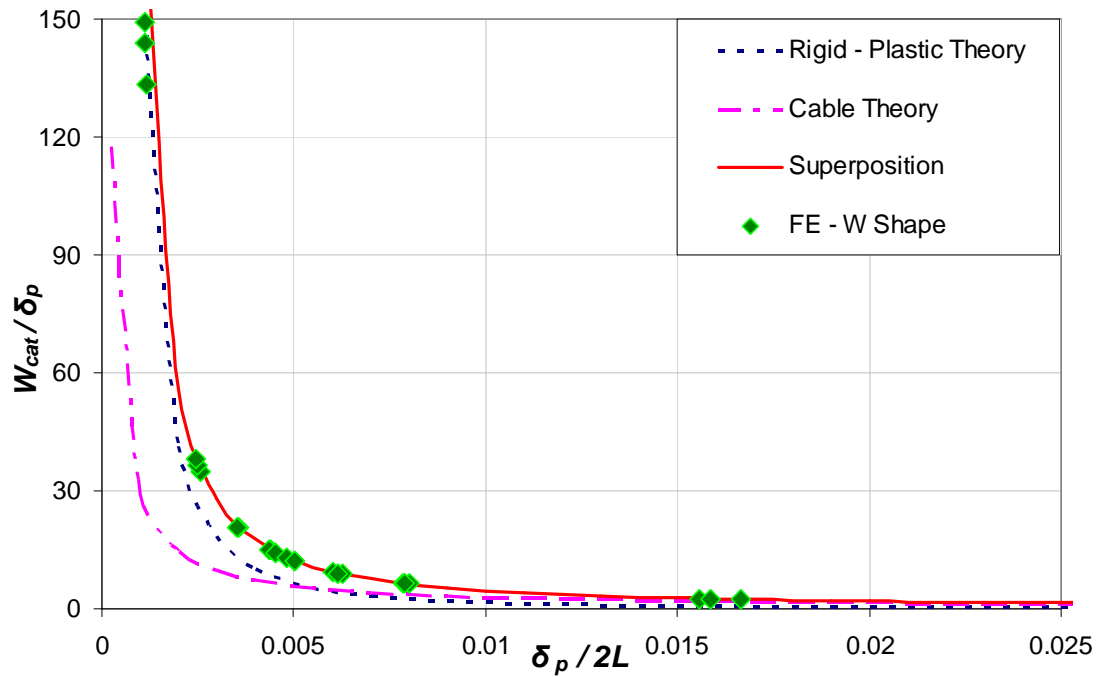


**Figure 5-4** Comparison with FE results (W-Shapes: Constant  $L/d$  case)

### 5.2.2 Formulation II

- Rigid-plastic theory:

The onset point of pure cable behavior for a fully fixed beam is independent of the cross-section and occurs when the deflection equals the nominal depth of the section,  $d$  (i.e.  $W_{cat} = d$ ). Therefore:

$$\frac{W_{cat}}{d} = 1. \quad [5.8]$$

- Cable theory:

It has been shown in Section 3.3.1 that the onset point of pure cable behavior is independent of cross-section type and can be written in the form:

$$\frac{W_{cat}}{L} = \sqrt{\frac{2\sigma_y}{E}} \quad [5.9]$$

which can be rearranged to give:

$$\frac{W_{cat}}{d} = \sqrt{\frac{2\sigma_y}{E}} \cdot \left[ \frac{L}{d} \right]. \quad [5.10]$$

FE analysis results compared with the results from Formulation I shown previously demonstrated that the linear superposition of the theoretical predictions appropriately represented the behavior. Accordingly, the superposition equation for Formulation II is given as:

$$\frac{W_{cat}}{d} = 1 + \sqrt{\frac{2\sigma_y}{E}} \cdot \left[ \frac{L}{d} \right]. \quad [5.11]$$

As can be seen, this formulation is independent of the shape factor. Thus, the comparison can be presented for both cross-section types together.

Figure 5-5, 5-6, and 5-7 show the comparison of theoretical predictions with FE results for rectangular and W-Shaped beams with constant  $\delta_p / d$ ,  $\delta_p / 2L$ , and  $L / d$ , respectively. Again, it can be seen that FE analysis results are in excellent agreement with Equation 5.11.

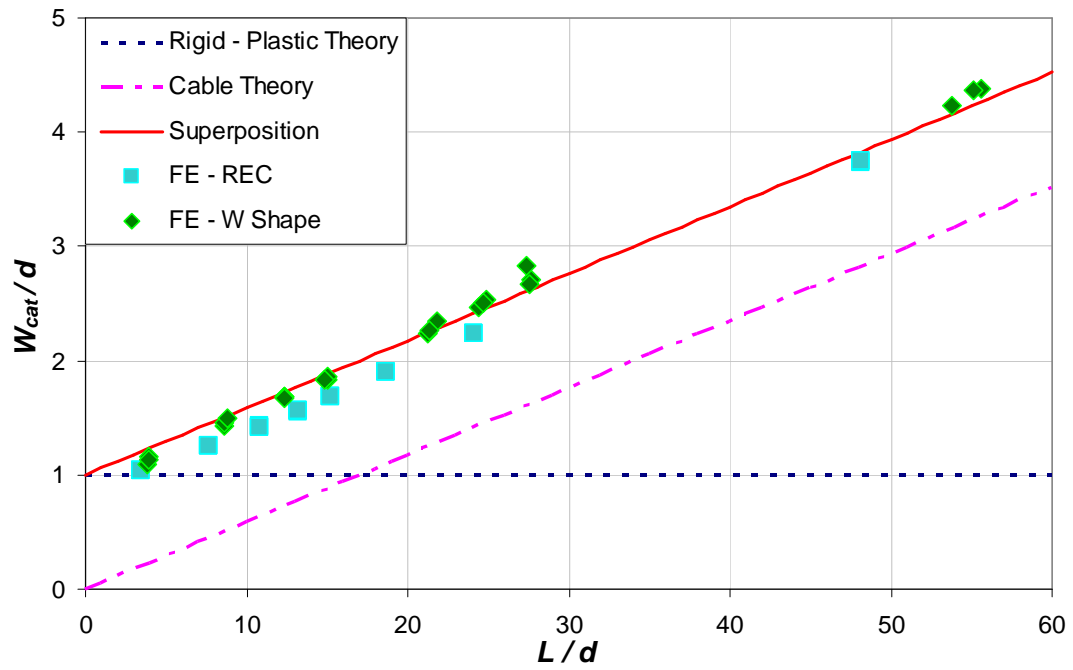


Figure 5-5 Comparison with FE results (Constant  $\delta_p/d$  case)

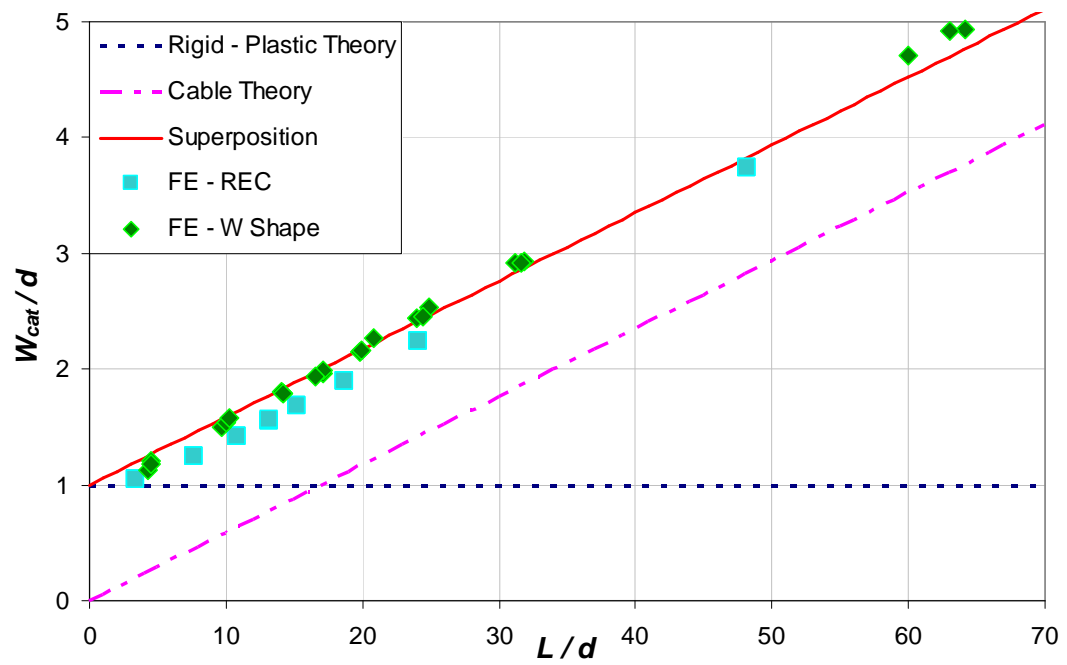
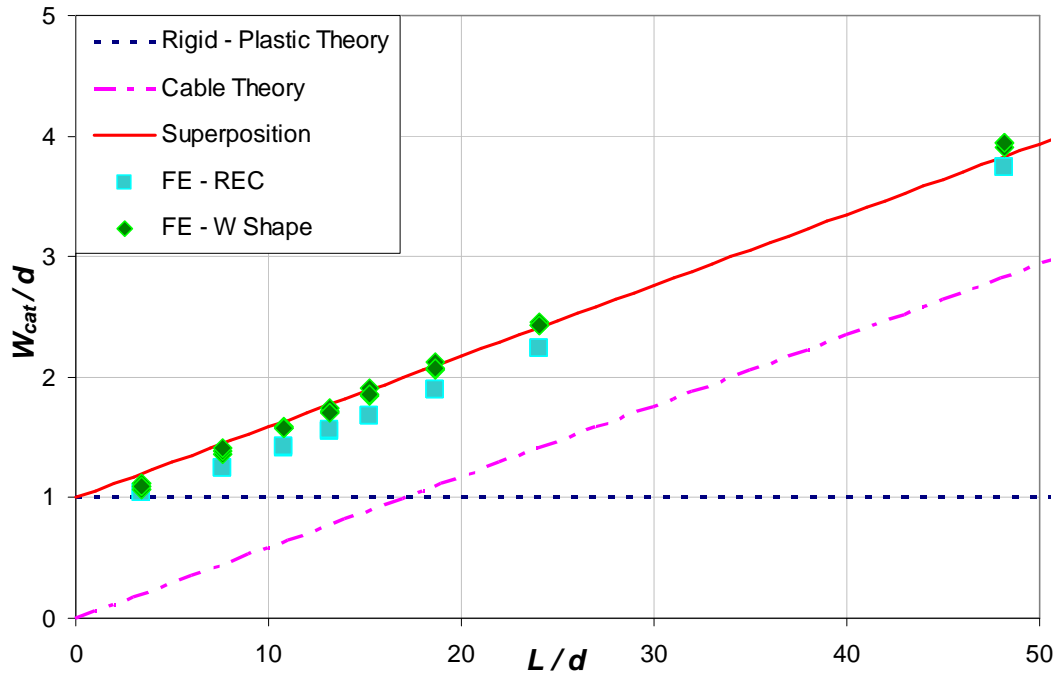


Figure 5-6 Comparison with FE results (Constant  $\delta_p/2L$  case)



**Figure 5-7** Comparison with FE results (Constant  $L/d$  case)

### 5.2.3 Formulation III

- Rigid-plastic theory:

The onset point of pure cable behavior for fully fixed beam was predicted to be equal to the nominal depth,  $d$ , regardless of the cross-section type (i.e.  $W_{cat} = d$ ).

Therefore:

$$\frac{W_{cat}}{2L} = \frac{d}{2L} \quad [5.12]$$

which can be written as:

$$\frac{W_{cat}}{2L} = \frac{1}{2 \cdot \left[ \frac{L}{d} \right]} \quad [5.13]$$

- Cable theory:

It has been shown in Section 3.3.1 that the onset point of pure cable behavior is independent of cross-section type and can be written in the form:

$$\frac{W_{cat}}{2L} = \sqrt{\frac{\sigma_y}{2E}}. \quad [5.14]$$

Similarly, the superposition equation in this case becomes:

$$\frac{W_{cat}}{2L} = \frac{1}{2 \cdot \left[ \frac{L}{d} \right]} + \sqrt{\frac{\sigma_y}{2E}}. \quad [5.15]$$

Similar to the second formulation, this representation is also independent of the shape factor ( $f$ ). Therefore the comparisons with FE analysis results are presented together for rectangular and W-Shaped beams.

The following figures (5-8 through 5-10) give the plots of  $W_{cat}/2L$  versus  $L/d$  predicted by each theory, along with the representation with superposition equation (Equation 5.15) in comparison with FE results for each case considered in the parametric study in Chapter 4. As can be seen in these figures, the superposition equation as given in Equation 5.15 indicates excellent agreement with FE results. In particular, W-Shapes are again in excellent agreement with results from the superposition curve given in Equation 5-15. Typically, rectangular shaped beams always fall below the curve, which will also be discussed in Section 5.4.



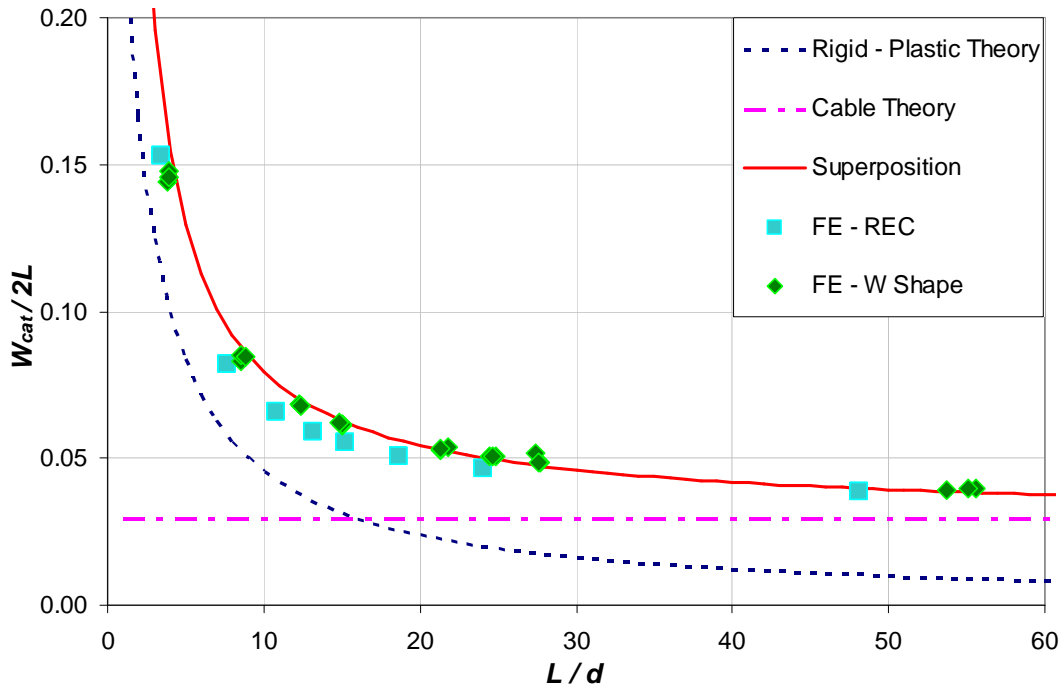


Figure 5-8 Comparison with FE results (Constant  $\delta_p/d$  case)

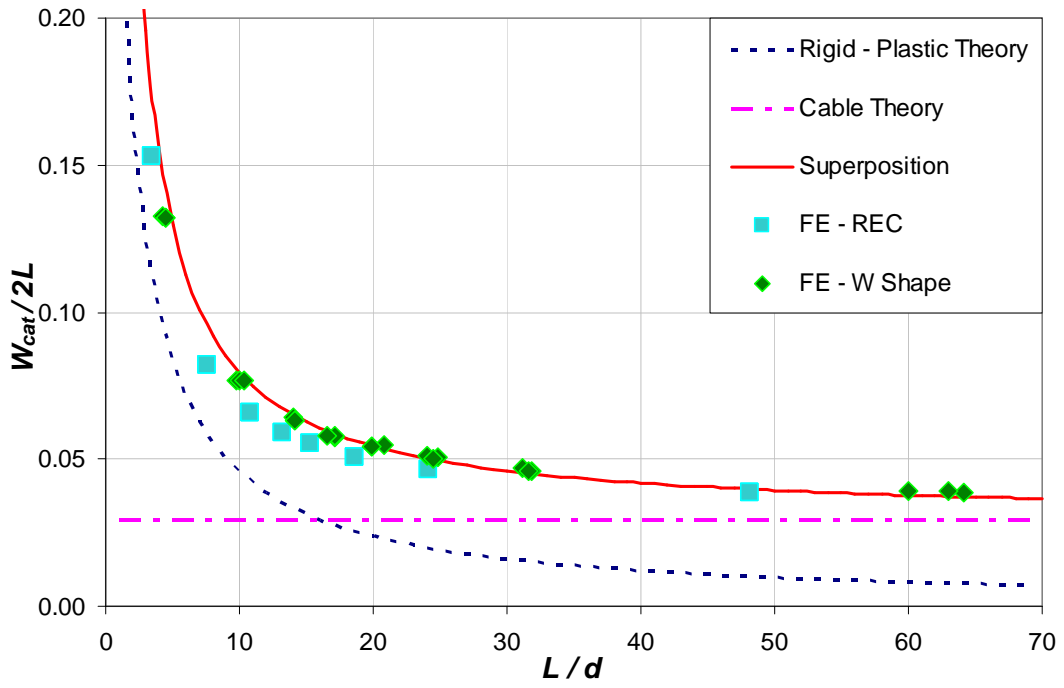
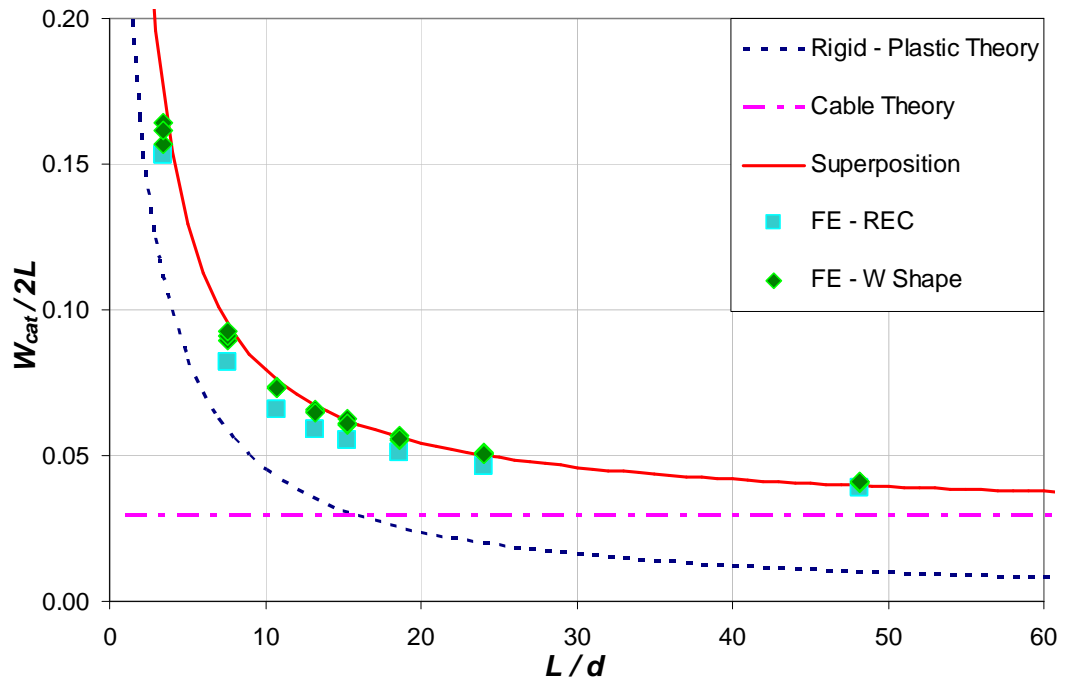


Figure 5-9 Comparison with FE results (Constant  $\delta_p/2L$  case)



**Figure 5-10** Comparison with FE results (Constant  $L/d$  case)

### 5.3 Distributed Load Case

A similar procedure for the beams with uniformly distributed load along the length was implemented.

Theoretical expressions for  $W_{cat}$  in these forms were developed using both rigid-plastic and cable theories, and were compared to FE analysis results for the concentrated and uniformly distributed load cases. Since the preliminary FE analysis results as presented in Section 4.3.3.2 showed that Theory II predicted the deflection at the onset of pure cable behavior somewhat accurately, Theory II will be used herein.

#### 5.3.1 Formulation I

- Rigid-plastic theory:

The onset point of pure cable behavior for a fully fixed beam is independent of the cross-section and occurs when the deflection equals twice the nominal depth of the section,  $2d$  (i.e.  $W_{cat} = 2d$ ). Therefore:

$$\frac{W_{cat}}{\delta_p} = \frac{2d}{\delta_p} \quad [5.16]$$

which can be arranged as:

$$\frac{W_{cat}}{\delta_p} = \frac{1}{\left[\frac{L}{d}\right]} \frac{1}{\left[\frac{\delta_p}{2L}\right]} \quad [5.17]$$

Now, substitution of  $L/d$  from Equation 4.7 into Equation 5.17 yields:

$$\frac{W_{cat}}{\delta_p} = \frac{1}{6} \cdot \frac{\sigma_y \cdot f}{E} \frac{1}{\left[\frac{\delta_p}{2L}\right]^2} \quad [5.18]$$

- Cable Theory:

It has been shown in Section 3.3.2 that the onset point of pure cable behavior independent of cross-section type and can be written in the form:

$$\frac{W_{cat}}{2L} = \frac{1}{2\alpha} \cdot \sqrt{\frac{\sigma_y}{E}} \quad [5.19]$$

where  $\alpha$  was verified to be 0.816. Re-arranging Equation 5.19 as follows and using  $\alpha = 0.816$ , Equation 5.19 becomes:

$$\frac{W_{cat}}{\delta_p} = 0.6127 \cdot \sqrt{\frac{\sigma_y}{E}} \cdot \frac{1}{\left[\frac{\delta_p}{2L}\right]} \quad [5.20]$$

Finally, the superposition equation for this case becomes:

$$\frac{W_{cat}}{\delta_p} = \frac{1}{6} \cdot \frac{\sigma_y \cdot f}{E} \frac{1}{\left[\frac{\delta_p}{2L}\right]^2} + 0.6127 \cdot \sqrt{\frac{\sigma_y}{E}} \cdot \frac{1}{\left[\frac{\delta_p}{2L}\right]} \quad [5.21]$$

In Figures 5-11 and 5-12,  $W_{cat} / \delta_p$  is plotted versus  $\delta_p / 2L$ , including the predictions given in Equations 5.18, 5.20 and 5.21, in comparison with FE analysis results from the parametric study in Section 4.4.4. Since the rigid-plastic theory prediction given in Equation 5.18 involves the shape factor term, comparison is made for each of the cross section types independently. As in the concentrated load case, an average shape factor is used for W-Shapes ( $f = 1.15$ ) to produce the theoretical prediction shown in Figure 5-12. As can be seen in these figures, FE results are in good agreement with the rigid-plastic theory for small  $\delta_p / 2L$  values, whereas cable theory produces better agreement for relatively large values of  $\delta_p / 2L$  (i.e. for the flexible regime). The superposition equation given in Equation 5.21 is again in excellent agreement with the FE results over the entire range.

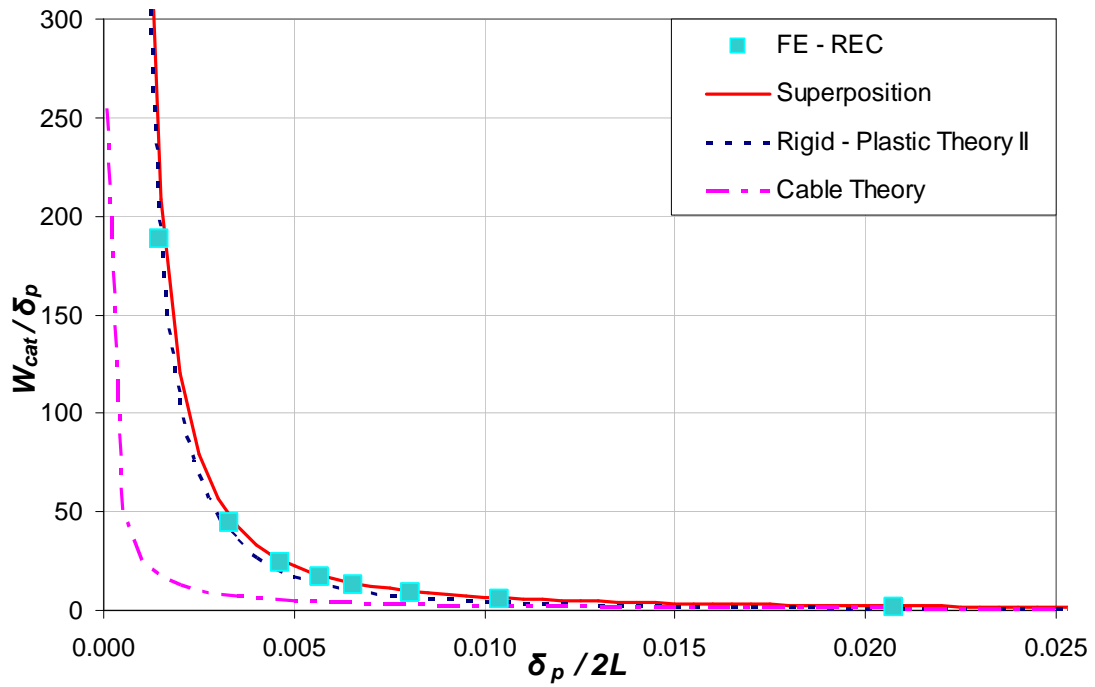


**Figure 5-11** Comparison with FE results (REC Shapes)

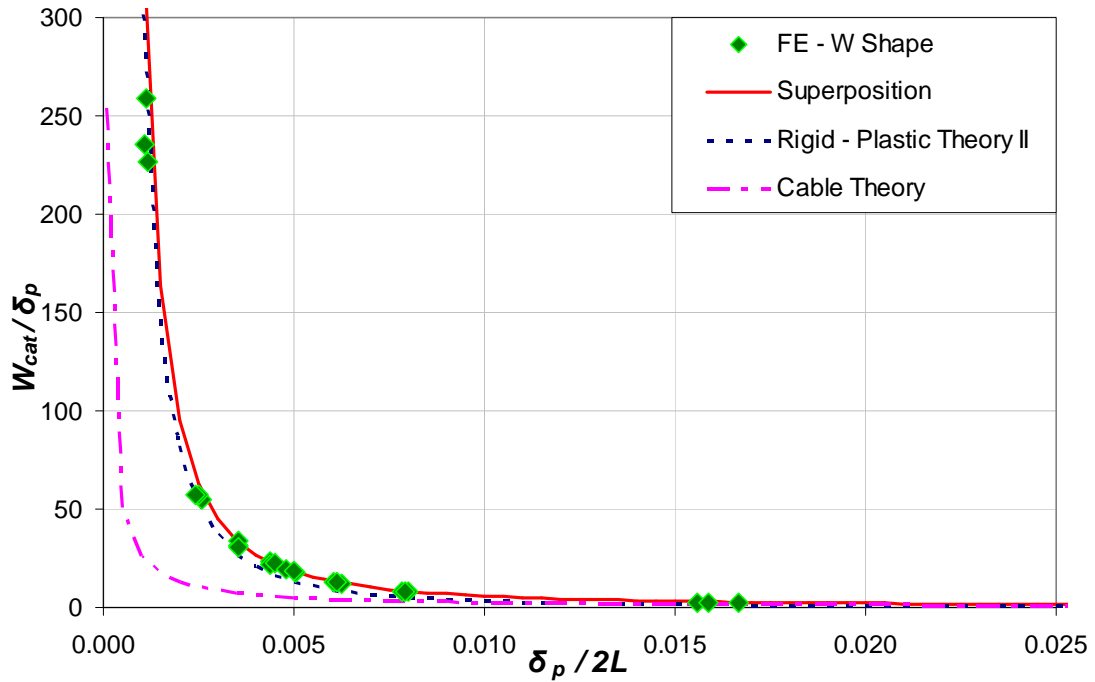


**Figure 5-12** Comparison with FE results (W Shapes)

### 5.3.2 Formulation II

- Rigid – plastic theory:

The onset point of pure cable behavior for a fully fixed beam is independent of the cross-section and occurs when the deflection equals twice as much the nominal depth of the section,  $2d$  (i.e.  $W_{cat} = 2d$ ). Therefore:

$$\frac{W_{cat}}{d} = 2. \quad [5.22]$$

- Cable theory

It has been shown in Section 3.3.2 that the onset point of pure cable behavior is independent of cross-section type and can be written in the form:

$$\frac{W_{cat}}{d} = \frac{1}{\alpha} \sqrt{\frac{\sigma_y}{E}} \cdot \left[ \frac{L}{d} \right]. \quad [5.23]$$

Substitution of  $\alpha = 0.816$  into Equation 5.23 yields:

$$\frac{W_{cat}}{d} = 1.225 \cdot \sqrt{\frac{\sigma_y}{E}} \cdot \left[ \frac{L}{d} \right]. \quad [5.24]$$

Having determined the relationship based on each theory, the superposition equation in this formulation can be given as:

$$\frac{W_{cat}}{d} = 2 + 1.225 \cdot \sqrt{\frac{\sigma_y}{E}} \cdot \left[ \frac{L}{d} \right]. \quad [5.25]$$

Figure 5-13 provides the plots of  $W_{cat}/d$  versus  $L/d$  predicted by Equations 5.22, 5.24 and 5.25 in comparison with FE analysis results from the parametric study as presented in Section 4.4.4. It can be seen that superposition equation adequately represents the trend exhibited by FE analysis results.

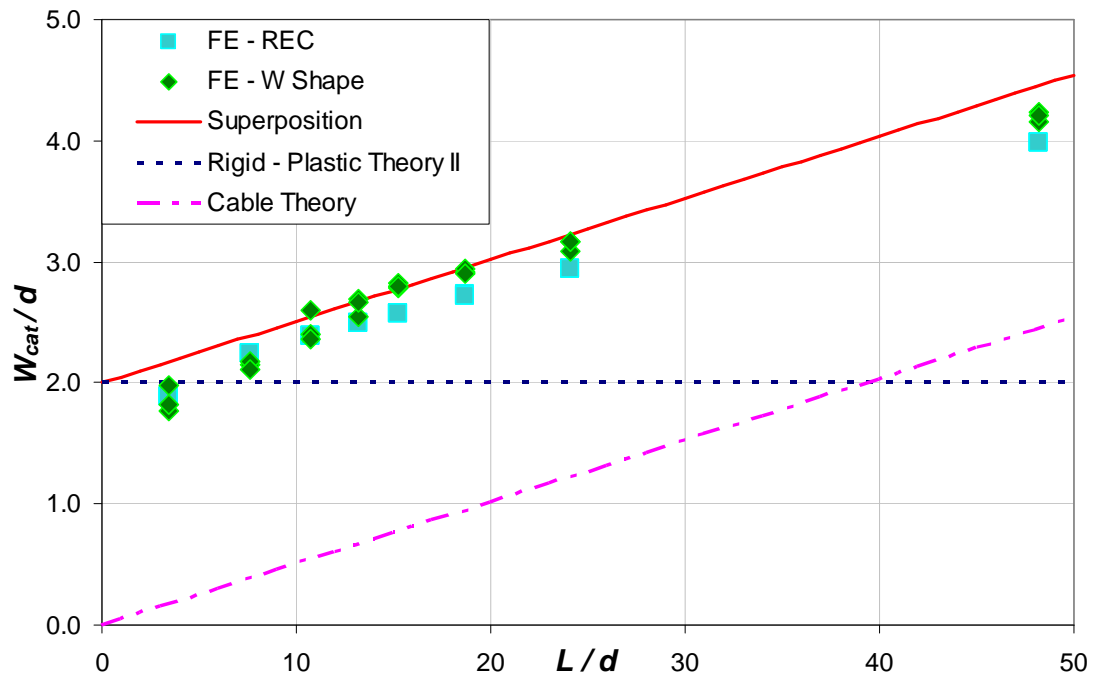


**Figure 5-13** Comparison with FE results (Constant  $L/d$  within each group)

### 5.3.3 Formulation III

- Rigid – plastic theory:

The onset point of pure cable behavior for a fully fixed beam is independent of the cross-section and occurs when the deflection equals twice the nominal depth of the section,  $2d$  (i.e.  $W_{cat} = 2d$ ). Therefore:

$$\frac{W_{cat}}{2L} = \frac{2d}{2L} \quad [5.26]$$

which can be rewritten as:

$$\frac{W_{cat}}{2L} = \frac{1}{\left[ \frac{L}{d} \right]} \quad [5.27]$$

- Cable theory:

It has been shown in Section 3.3.2 that the onset point of pure cable behavior independent of cross-section type and can be written in the form:

$$\frac{W_{cat}}{2L} = \frac{1}{2\alpha} \cdot \sqrt{\frac{\sigma_y}{E}} \quad [5.28]$$

Again, substituting  $\alpha = 0.816$  into Equation 5.28 yields:

$$\frac{W_{cat}}{2L} = 0.6127 \cdot \sqrt{\frac{\sigma_y}{E}} \quad [5.29]$$

Finally, the linear superposition equation for this formulation becomes:

$$\frac{W_{cat}}{2L} = \left[ \frac{L}{d} \right] + 0.6127 \cdot \sqrt{\frac{\sigma_y}{E}} \quad [5.30]$$

$W_{cat} / 2L$  is plotted versus span-to-depth ratio ( $L / d$ ) in Figure 5-14, including FE results from the parametric study (Section 4.4.4) in comparison with predictions produced by Equations 5.27, 5.29 and 5.30. Similar observations are made and it can be seen that W-Shaped beams, in particular, seem to be in better agreement with the prediction given by Equation 5.30 over the entire range of  $L / d$  values.



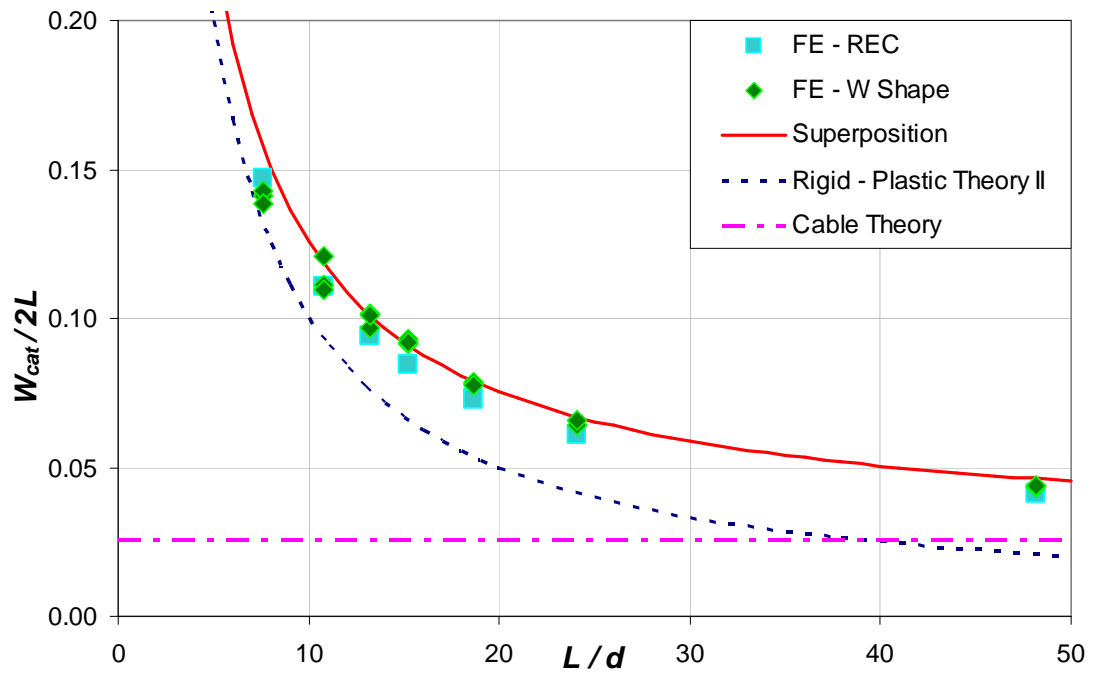


**Figure 5-14** Comparison with FE results (Constant  $L/d$  within each group)

The adequacy of representation of FE results by linear superposition of the theoretical predictions is discussed in following section.

#### 5.4 Discussion

Based on the trends observed in the results of FE parametric study (Section 4.4), theoretical predictions for the onset point of pure cable behavior were formulated and compared to FE analysis results. The comparisons showed that the FE results approached results produced by the rigid-plastic and cable theories for stiff and flexible beams, respectively. In order to cover the entire range of behavior, a new equation is proposed that is obtained by linear superposition of the rigid-plastic and cable equations.

Comparison of FE analysis results with the new equation showed that it can be used to

predict the onset point of pure cable behavior for elastic–perfectly plastic steel beams. Some discrepancies were observed between the proposed equation and FE analysis results. The difference between the two, and possible reasons for this discrepancy are discussed next.

The difference between results from the proposed equation and FE results can be quantified as:

$$Difference(\%) = \frac{Y_{LS} - Y_{FE}}{Y_{FE}} \times 100 \quad [5.31]$$

where  $Y_{LS}$  and  $Y_{FE}$  are  $y$ -coordinates of the proposed equation and FE analysis results at a given  $L/d$  level, respectively. Span-to-depth ratio ( $L/d$ ) was chosen for this analysis due to its common use in practice.

It can be anticipated that the difference will be identical regardless of which formulation is used in comparison. The reason is that each formulation presented in this chapter is a different manipulation of the theoretical onset point of pure cable behavior,  $W_{cat}$ . Thus, the percent differences between proposed equation and FE analysis results for each cross-section type are calculated using Equation 5.31 and are presented in the range of  $L/d$  considered in the parametric study.

Figures 5-15 and 5-16 show plots of Equation 5.31 versus  $L/d$  of the concentrated load case, for rectangular and W-Shaped beams, respectively. It can be seen that the difference is largest for relatively stiff beams and becomes smaller for relatively flexible beams. While this has not been studied in detail in the thesis, it is believed that the difference is largest for relatively stiff beams because the deflection at the onset of pure cable behavior is typically large compared to the span length. Since the rigid-plastic

theory is developed for finite, but not necessarily large deflections, it is believed that it may not give accurate results for very stiff beams.

The shaded region shown in Figures 5-15 and 5-16 covers the range of  $L/d$  between 10 and 30 that is typically encountered in practice. Within this range, the difference between the proposed equation and the FE analysis results falls in a range of 8~15% for rectangular shapes and less than 3% for W-Shapes. Considering that W-Shapes are widely used in practice, this difference can be considered acceptable. While the reason that the difference is larger for rectangular shaped beams than for W-Shaped beams has not been rigorously studied in the thesis, it is believed that it relates to the way the onset point of pure cable behavior,  $W_{cat}$ , was determined, as indicated in Figure 4-34 and explained in Section 4.4.

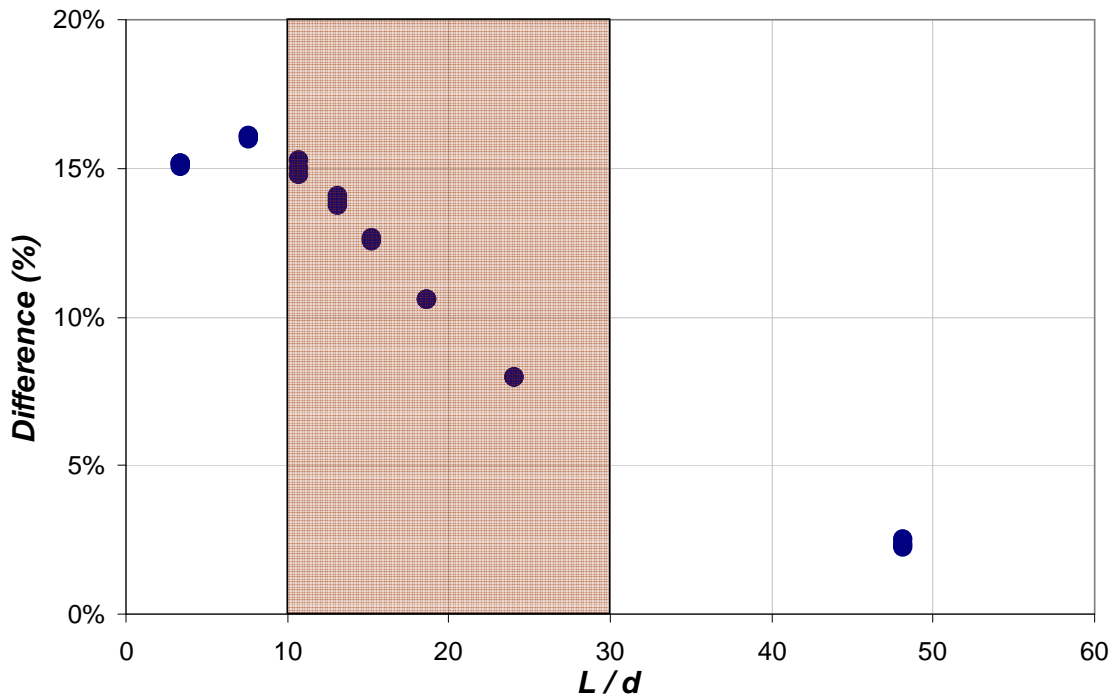


**Figure 5-15** Distribution of the Difference for Rectangular Shaped Beams

(Concentrated Load case)

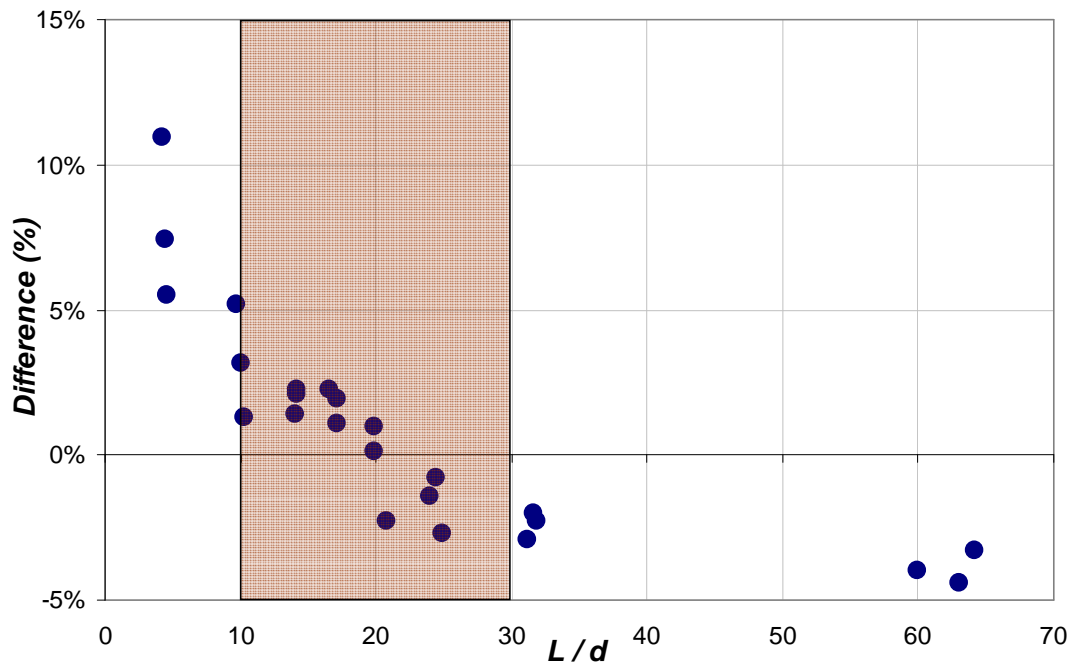


**Figure 5-16** Distribution of the Difference for W-Shaped Beams  
(Concentrated Load Case)

In a similar manner, Figures 5-17 and 5-18 show plots of Equation 5.31 versus  $L/d$  for the distributed load case for rectangular and W-Shaped beams, respectively. The difference is again largest for relatively stiff beams but not necessarily much smaller for relatively flexible beams. However, within the shaded region ( $L/d$  of 10 to 30) the difference ranges from 6% to 10% for rectangular shaped beams and remains within 7% for W-Shaped beams.

The fact that the difference is slightly larger for W-Shaped beams compared to the concentrated load case can be attributed to the discussion made within the context of the preliminary FE analysis (Section 4.3.3.2) that the onset point of pure cable behavior

prediction by the rigid-plastic theory for uniform loading ( $W_{cat} = 2d$ ) is not rigorous but is approximate.

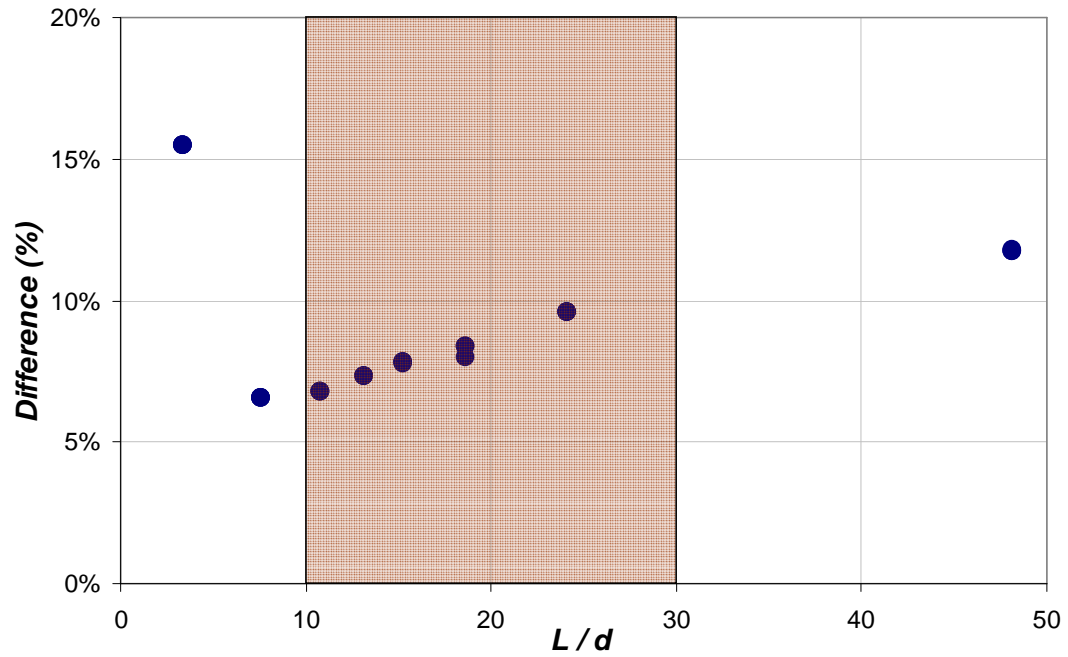


**Figure 5-17** Distribution of the Difference for Rectangular Shaped Beams (Distributed Load Case)

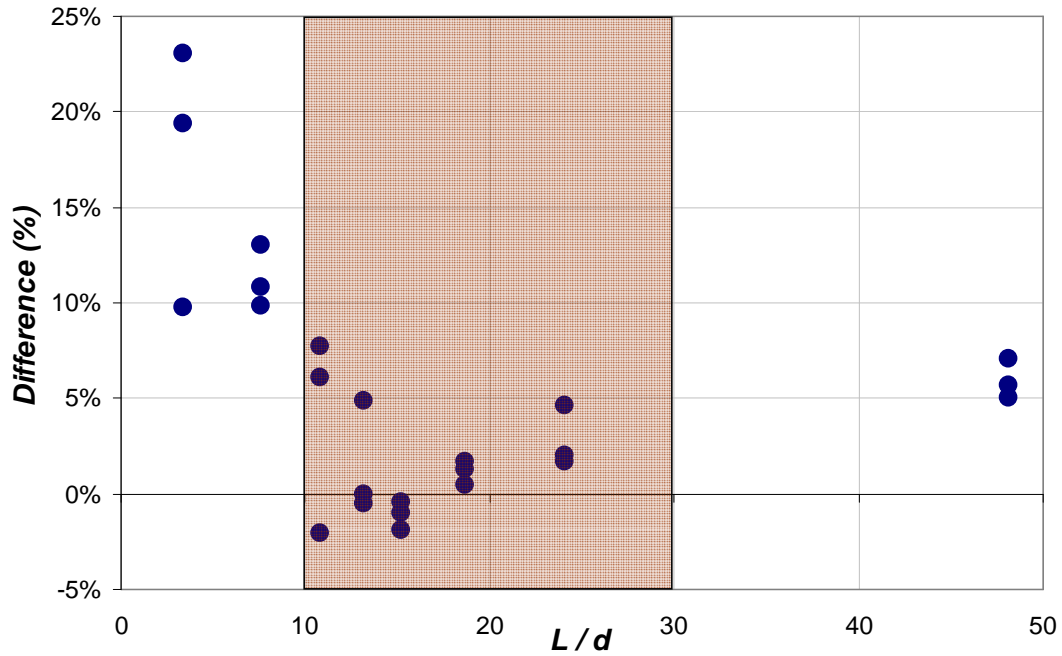


**Figure 5-18** Distribution of the Difference for W-Shaped Beams  
(Distributed Load Case)

## 5.5 Conclusion

An equation is proposed that predicts the midspan deflection at the onset of pure cable behavior,  $W_{cat}$  for elastic–perfectly plastic steel beams with a span-to-depth ratio,  $L/d$ , ranging between 10 and 30. It can be shown that all three formulations presented herein result in the same reduced form of the onset point of pure cable behavior as follows:

For beams fixed at both ends spanning  $2L$  under a concentrated load at midspan:

$$W_{cat} = d + \sqrt{\frac{2 \cdot \sigma_y}{E}} \cdot L \quad [5.32]$$

and for beams fixed at both ends spanning  $2L$  under uniformly distributed load along the length:

$$W_{cat} = 2d + 1.225 \cdot \sqrt{\frac{\sigma_y}{E}} \cdot L \quad [5.33]$$

Equations 5.32 and 5.33 suggest that  $W_{cat}$  is independent of the cross-section type and it can be predicted with knowledge of only  $d$ ,  $L$ ,  $\sigma_y$  and  $E$ . Although previous FE analysis results suggested that the shape of the cross-section has an influence on the onset point of pure cable behavior, the analysis conducted to quantify the difference between FE analysis results and theoretical linear superposition results indicated that the difference is sufficiently small for both rectangular and W-Shaped cross-sections. Therefore, Equations 5.32 and 5.33 can be used independent of the cross-section type.

## Chapter 6. EFFECT OF ELASTIC BOUNDARY CONDITIONS

### 6.1 Overview

The behavior of ductile steel beams undergoing a transition from flexural to cable behavior was described using idealized boundary conditions in the previous chapters. The end supports were assumed to be either fully fixed or pinned. However, it can be anticipated that the boundary conditions of a beam within a building frame may be different from the idealized ones. In particular, conditions at the ends of the beam may result in partial rotational and axial restraints. Beam end restraints can be attributed to two main sources: restraining effects due to the surrounding elements framing into the beam joint and restraining effects provided by the beam-to-column connection itself.

In this chapter, study on the effect of elastic boundary conditions using FE models is described. The study consisted of two main objectives: (1) to determine the effect of elastic boundary restraints on beam behavior and (2) compare frame models to that of beam models.

The beam models used in the analysis are illustrated in Figure 6-1. The beam A–B is isolated from the frame and beam end restraints are modeled using linear–elastic springs.  $k_A$  and  $k_\theta$  are translational and rotational spring constants, respectively, as shown in Figure 6-1. Due to symmetry,  $k_A$  and  $k_\theta$  are the same for both supports.



Nonsymmetrical cases are not considered in this study. In addition, the beam is loaded at midspan as shown in Figure 6-1. The boundary conditions associated with the midspan joint are idealized to be rigid and continuous.

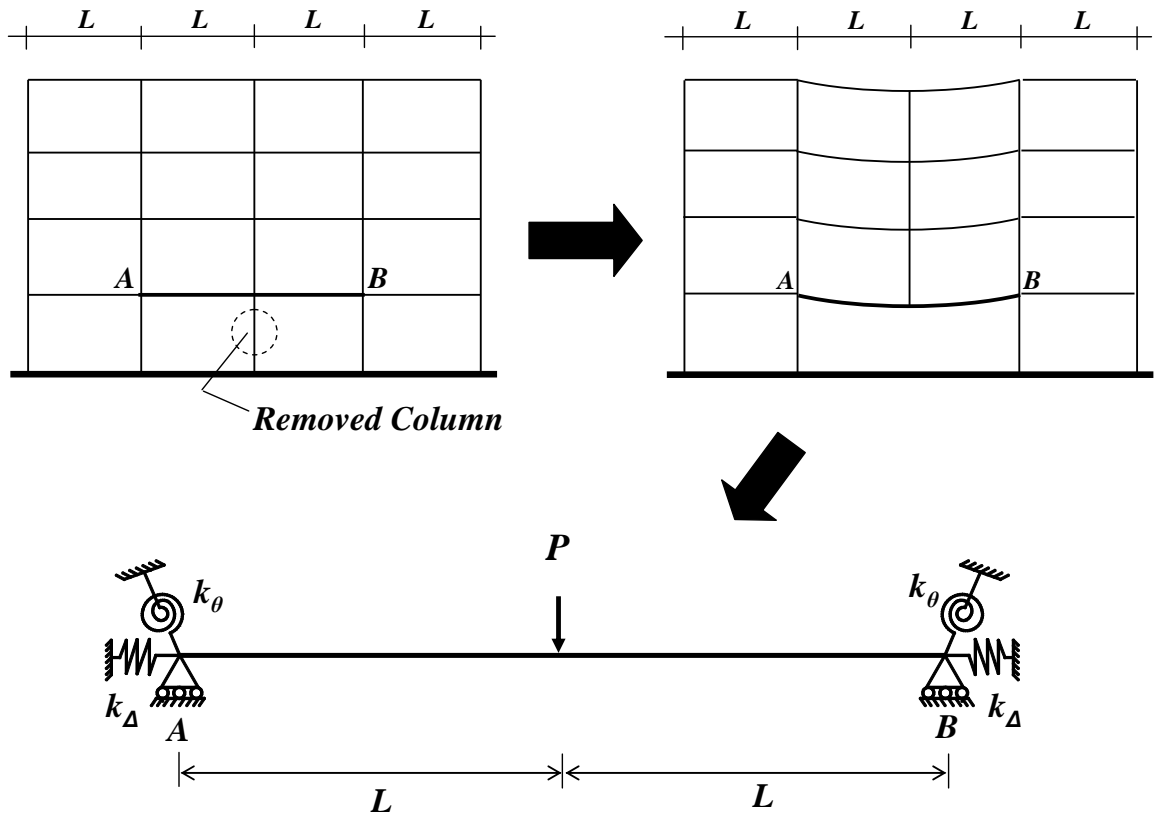


**Figure 6-1** Schematics of Beam Model with Elastic Boundary Conditions

The beams and frames considered in this chapter were also modeled and analyzed using OpenSees (2000). Therefore, all modeling and analysis concepts described in Section 4.2 are valid here as well.

## 6.2 Effect of Elastic Restraint

FE analyses of steel beams with linear–elastic boundary conditions were conducted. Both material and geometric nonlinearity were considered for the beams. First, the effects of translational and rotational restraint were studied separately. For each case, a wide range of spring constant values were used. Then, both were incorporated simultaneously into the models, as illustrated in Figure 6-1, to study their combined effect.

The cross-section of the beam used in the analyses was determined from preliminary design of a two–bay frame, based on the *AISC Manual* (2005) LRFD approach, as presented in Section 6.3. A W14x53 was used for all beam models considered throughout this section. Cross–sections were discretized with fibers as explained earlier in Section 4.2.1 with a constant fiber thickness,  $t_{fiber} = 5 \times 10^{-3}$  inches. An elastic–perfectly plastic steel material with  $\sigma_y = 50$  ksi was used in all models. The number of elements along the beam length was consistently taken as 100.

### 6.2.1 Effect of Translational Restraint

In order to study the effect of partial translational restraint, the beam was modeled as shown in Figure 6-2.

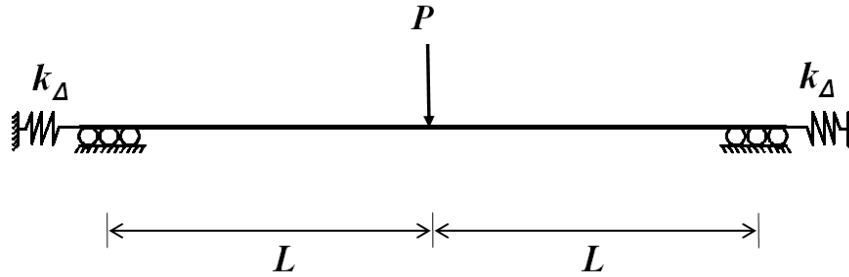


**Figure 6-2** Beam model with translational springs only

A range of spring constant values was considered and three beam models (W14x53) with varying lengths for each  $k_{\Delta}$  were analyzed. Table 6-1 summarizes the input parameters, as well as the resulting midspan displacement at the onset of pure cable behavior,  $W_{cat}$ , and  $W_{cat}/d$ .

**Table 6-1** W14x53 Beam Models with Translational Springs only

No	$k_{\Delta}$ (kip / in)	Length (2L)								
		20 ft			60 ft			100 ft		
		L / d	$W_{cat}$ (in)	$W_{cat} / d$	L / d	$W_{cat}$ (in)	$W_{cat} / d$	L / d	$W_{cat}$ (in)	$W_{cat} / d$
1	0.1	8.63	128.35	9.24	25.90	366.45	26.36	43.17	605.75	43.58
2	1	8.63	128.41	9.24	25.90	349.85	25.17	43.17	547.65	39.40
3	6	8.63	113.65	8.18	25.90	251.05	18.06	43.17	348.50	25.07
4	24	8.63	82.05	5.90	25.90	152.20	10.95	43.17	201.45	14.49
5	100	8.63	50.70	3.65	25.90	85.95	6.18	43.17	112.40	8.09
6	400	8.63	32.85	2.36	25.90	54.20	3.90	43.17	72.85	5.24
7	1600	8.63	24.67	1.77	25.90	41.35	2.97	43.17	57.25	4.12
8	6400	8.63	21.59	1.55	25.90	37.20	2.68	43.17	52.50	3.78
9	25600	8.63	20.64	1.48	25.90	36.15	2.60	43.17	51.25	3.69
10	100000	8.63	20.38	1.47	25.90	35.85	2.58	43.17	50.90	3.66

It can be seen in Table 6-1 that  $W_{cat}/d$  increases with decreasing  $k_{\Delta}$ . This trend is also illustrated in Figure 6-3, in which  $W_{cat}/d$  is plotted versus  $k_{\Delta}$ . The figure also shows that for the same  $k_{\Delta}$ ,  $W_{cat}/d$  is always larger for longer beams than for shorter beams, which is consistent with the observations and results of Chapter 4.

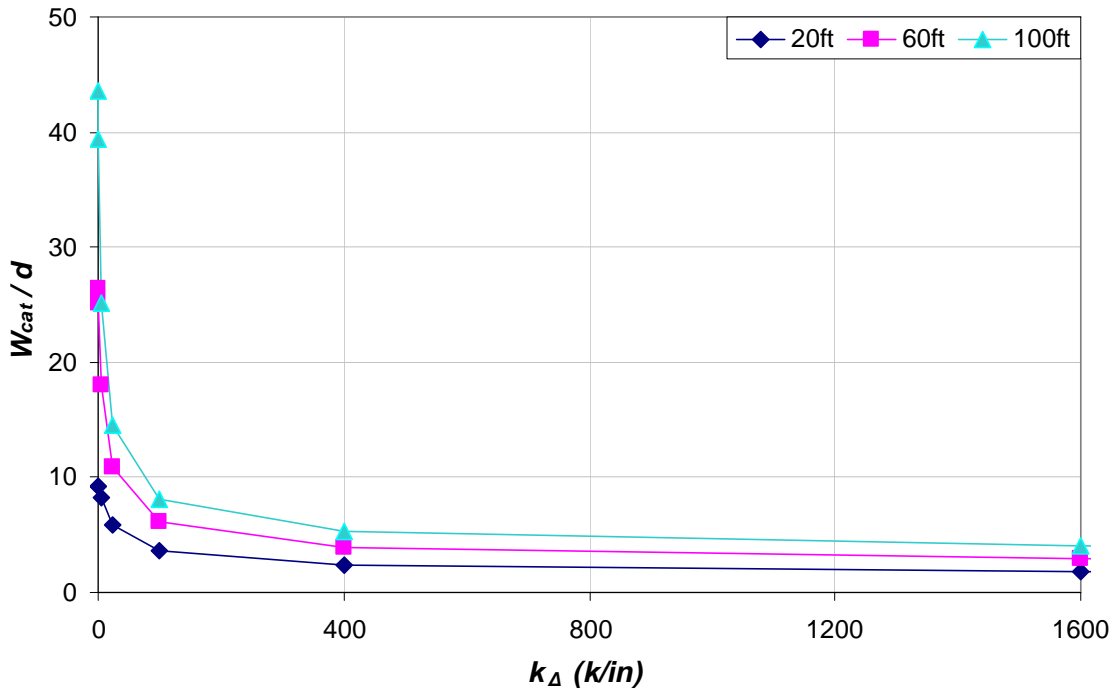


**Figure 6-3** Dependency of  $W_{cat}/d$  on Translational Spring Constant,  $k_{\Delta}$

The results are also given in the form of normalized load versus deflection, normalized axial force versus deflection, normalized moment versus deflection, and normalized  $M-N$  interaction plots in Figures 6-4, 6-5, 6-6, and 6-7, respectively. The figures are given for the 60-ft-long beams only. It should be noted that the external load is normalized by the plastic collapse load,  $P_c$  of a fully fixed beam which in this case is:

$$P_c = \frac{4 \cdot M_p}{L} = \frac{4 \cdot 4253.5}{360} = 47.26 \text{ kips}$$

where  $M_p = 4253.5$  k-in for a W14x53 section (fillets are neglected).

Figure 6-4 shows how the level of axial restraint can significantly affect the behavior. For small values of translational spring constant, it can be seen that no

significant increase in  $P$  beyond  $P_c$  can be achieved until extremely large deflections take place.

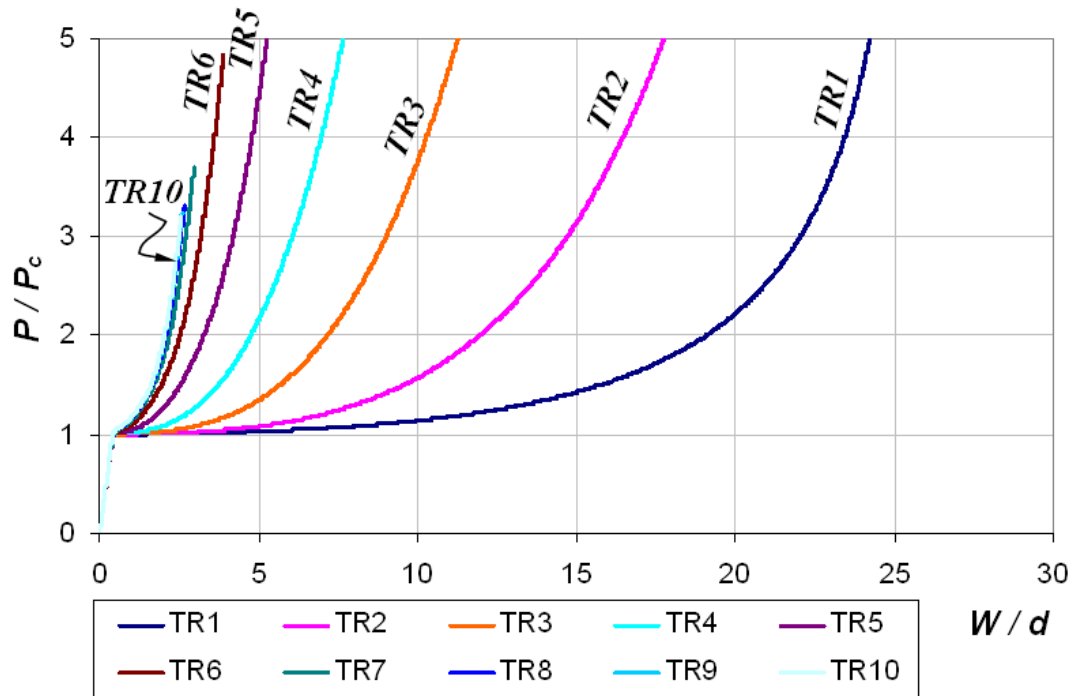


**Figure 6-4** Normalized Load–Deflection Plot (Midspan)

Figure 6-5 shows that for a low level of axial restraint, the beam develops insignificant axial forces even at fairly large deflections. And as a result, the behavior is dominated by flexure, as is seen in Figure 6-6.  $M$ - $N$  interaction plots are provided in Figures 6-7 and 6-8 for midspan and end sections, respectively. Once the mechanism condition is reached, plastic hinges remain on the yield curve under a combination of  $M$  and  $N$  until the behavior is purely dominated by cable action (i.e.,  $N = N_p$ ).

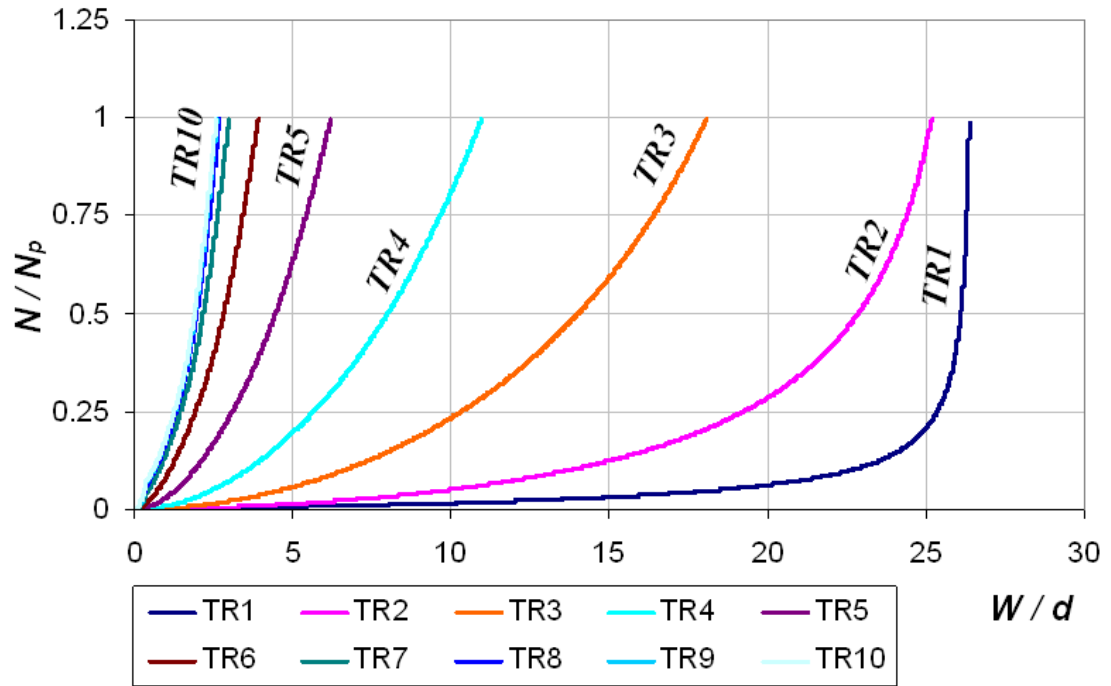


**Figure 6-5** Normalized Axial Force–Deflection Plot (Midspan)

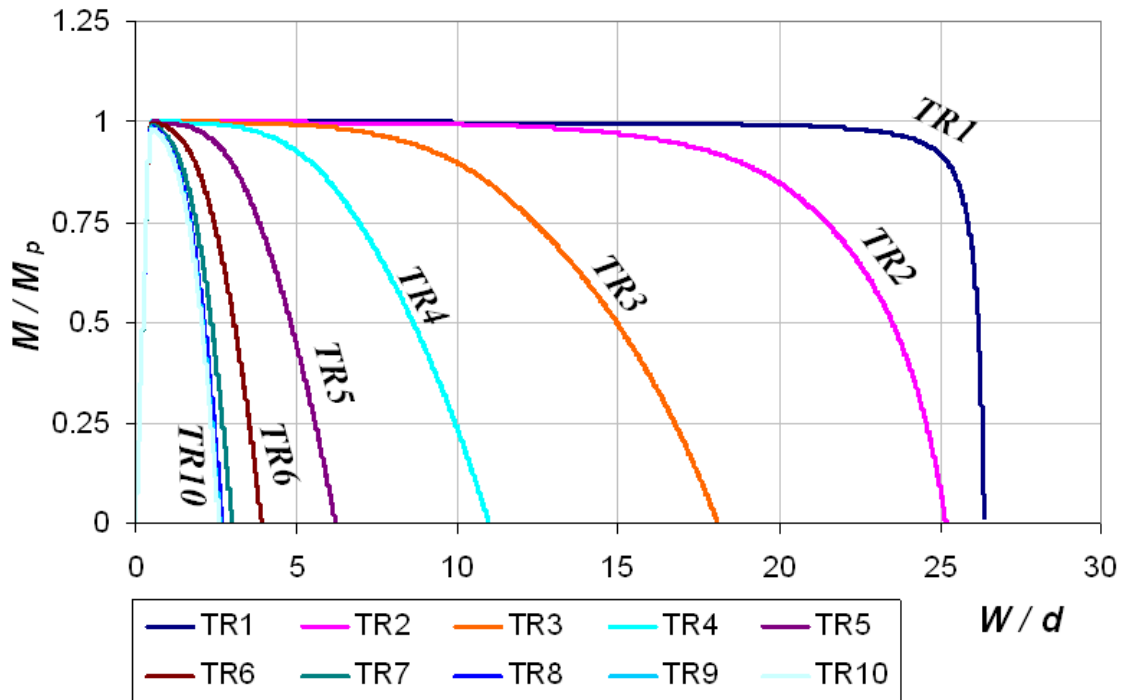


**Figure 6-6** Normalized Moment–Deflection Plot (Midspan)

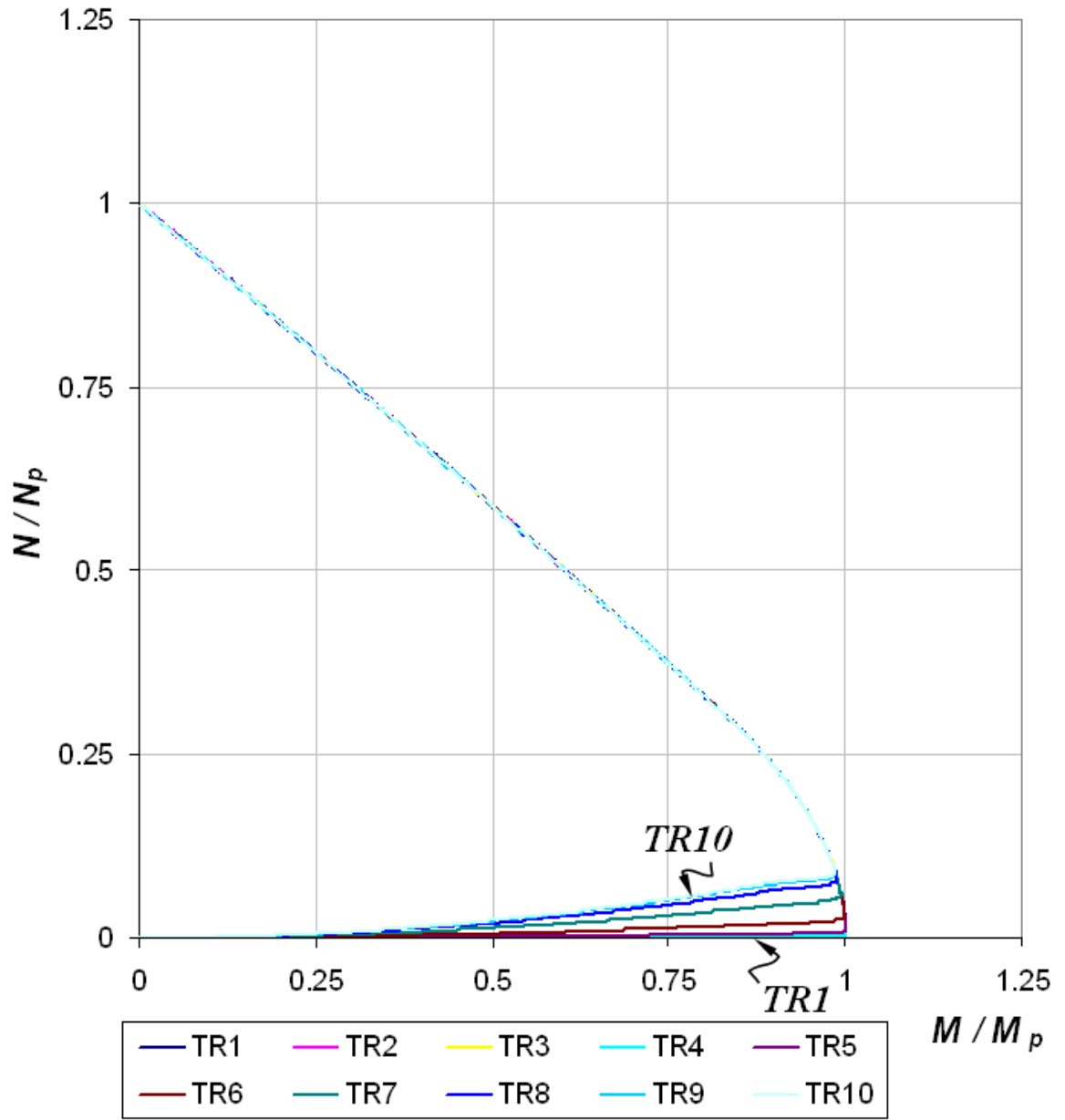


**Figure 6-7** Normalized  $M-N$  interaction (Midspan)

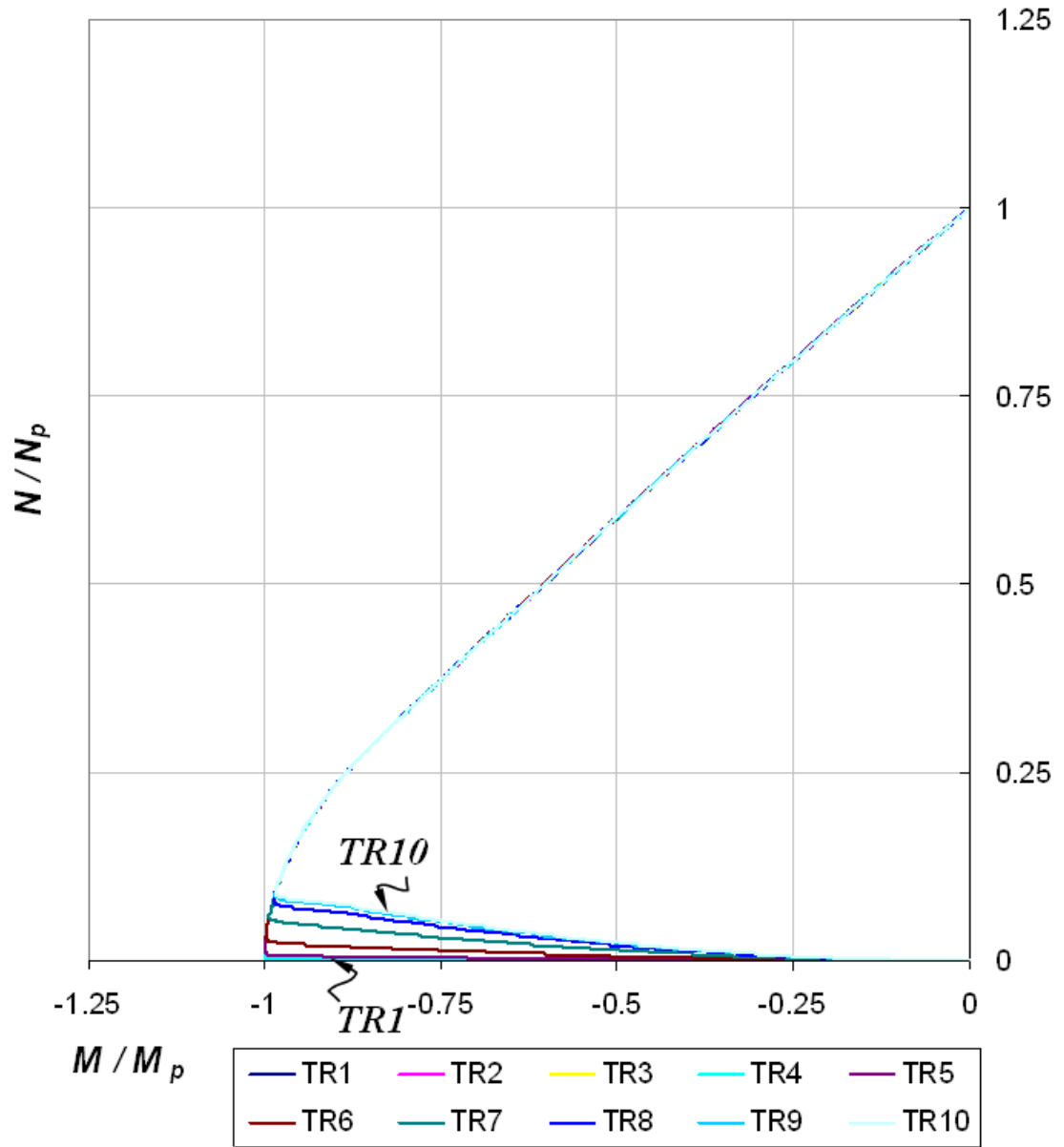
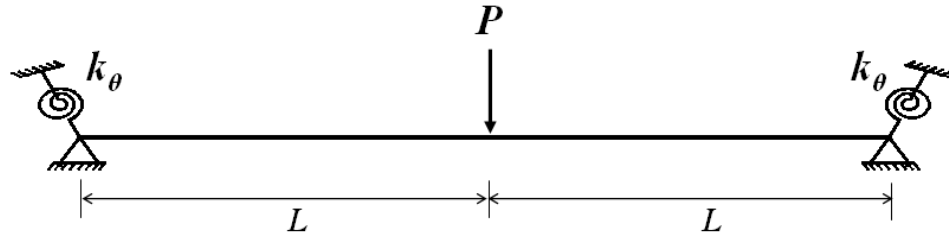


Figure 6-8 Normalized  $M-N$  Interaction (End)

### 6.2.2 Effect of Rotational Restraint

In order to study the effect of partial rotational restraint, the beam with a W14x53 is modeled as shown in Figure 6-8.





**Figure 6-9** Beam with Rotational Springs Only

A range of values for  $k_\theta$  ranging from zero (e.g., pinned) to infinity (fully fixed) at the beam supports was considered and beams with varying lengths were modeled and analyzed for each  $k_\theta$  level.

In Table 6-2, analysis input parameters, as well as the resulting midspan deflection at the onset point of pure cable behavior,  $W_{cat}$ , and  $W_{cat}/d$ , are given. A close examination of the results, along with Figure 6-10, in which  $W_{cat}/d$  is plotted versus  $k_\theta$  reveals that the dependency of  $W_{cat}/d$  on the rotational spring constant,  $k_\theta$  is not as straightforward as it was for the beams with translational springs presented earlier. Figure 6-10 shows that up to a certain level of  $k_\theta$ ,  $W_{cat}/d$  gradually increases and reaches a peak at a  $k_\theta$  level of approximately  $5000 \text{ k-in} / \text{rad}$ . Then, it starts to decrease with increasing  $k_\theta$  and eventually converges to a value which is the one predicted by the fixed-fixed case.

Table 6-2 in comparison Table 6-1 also shows that  $W_{cat}/d$  is relatively less sensitive to  $k_\theta$  than  $k_\Delta$  presented earlier. For example, for beams with a total span length,  $2L$ , of 60 ft,  $W_{cat}/d$  varies between 2.08 and 2.57 for this case (Table 6-2), but varies between 26.36 and 2.58 for beams with translational springs only (Table 6-1).

The results are also graphically presented in the form of normalized load versus deflection, normalized axial force versus deflection, normalized moment versus

deflection and  $M-N$  interaction plots in Figures 6-11 through 6-16. The figures are given for the 20ft-long beams only.

**Table 6-2** W14x53 Beam Models with Rotational Springs only

No	$k_{\theta}$ (k-in/rad)	Length (2L)								
		2L=20 ft			2L=60 ft			2L=100 ft		
		L / d	$W_{cat}$ (in)	$W_{cat} / d$	L / d	$W_{cat}$ (in)	$W_{cat} / d$	L / d	$W_{cat}$ (in)	$W_{cat} / d$
SS	0	8.63	13.93	1.00	25.90	28.90	2.08	43.17	42.75	3.08
1	1	8.63	13.92	1.00	25.90	28.85	2.08	43.17	42.65	3.07
2	100	8.63	13.92	1.00	25.90	28.85	2.08	43.17	42.65	3.07
3	1000	8.63	18.83	1.35	25.90	35.85	2.58	43.17	51.05	3.67
4	5000	8.63	27.41	1.97	25.90	38.15	2.74	43.17	51.35	3.69
5	10000	8.63	27.30	1.96	25.90	38.85	2.79	43.17	51.55	3.71
6	50000	8.63	25.95	1.87	25.90	38.30	2.76	43.17	51.60	3.71
7	100000	8.63	23.56	1.69	25.90	37.95	2.73	43.17	51.25	3.69
8	200000	8.63	22.07	1.59	25.90	37.30	2.68	43.17	51.10	3.68
9	500000	8.63	21.06	1.52	25.90	36.40	2.62	43.17	51.00	3.67
10	1000000	8.63	20.68	1.49	25.90	36.05	2.59	43.17	50.95	3.67
11	5000000	8.63	20.38	1.47	25.90	35.75	2.57	43.17	51.45	3.70
12	50000000	8.63	20.31	1.46	25.90	35.75	2.57	43.17	50.80	3.65
13	100000000	8.63	20.30	1.46	25.90	35.75	2.57	43.17	50.80	3.65
FF	Infinite	8.63	20.29	1.46	25.90	35.75	2.57	43.17	50.90	3.66

\*SS Simply Supported  
\*FF Fixed-Fixed

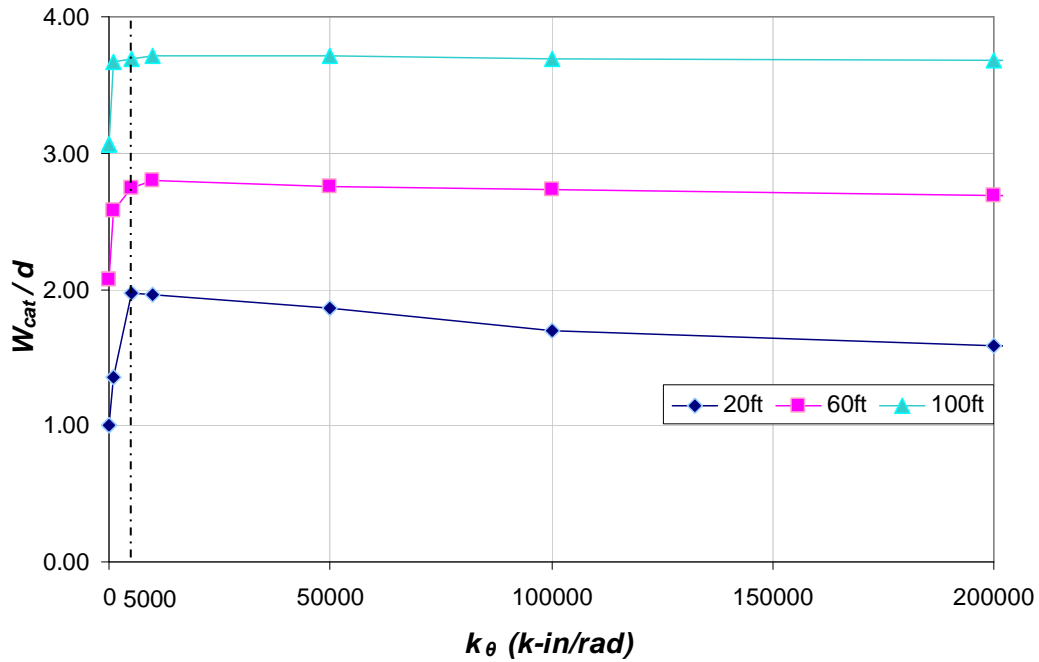


**Figure 6-10** Dependency of  $W_{cat} / d$  on Rotational Spring Constant,  $k_{\theta}$

Again, external force,  $P$  in Figure 6-11 is normalized by the plastic collapse load,  $P_c$  for the fixed-fixed case which in this case is:

$$P_c = \frac{4 \cdot M_p}{L} = \frac{4 \cdot 4253.5}{120} = 141.78 \text{ Kips}$$

Figures 6-12 through 6-14, in particular, show the significance of the level of rotational restraint on the behavior. For models in which  $k_\theta$  is not large enough to develop a plastic hinge (e.g., ROT3 through ROT8), the tendency of the load–deflection curves is to “jump” to the curves that corresponds to models with higher rotational restraints at a certain deflection level. This can be attributed to the fact that those models do not provide enough restraint for the beam to develop flexural plastic hinges at end supports, as shown in Figure 6-14. Therefore, for these low  $k_\theta$  values, the beam acts like a simple beam. As seen in Figure 6-16, with the development of axial forces  $N$ , plastic hinges eventually form at the ends with a combination of  $M$  and  $N$ , and the beam forms a mechanism. As a result, it tends to behave as fixed-fixed and load–deflection curves seem to suddenly shoot towards the one predicted by the fully fixed case.

The plot of  $M$ - $N$  interaction at midspan (Figure 6-15) shows that a plastic hinge forms predominantly by flexure first and follows the yield curve under combined  $M$  and  $N$  in all beam models, regardless of  $k_\theta$  level, as seen in Figure 6-15.

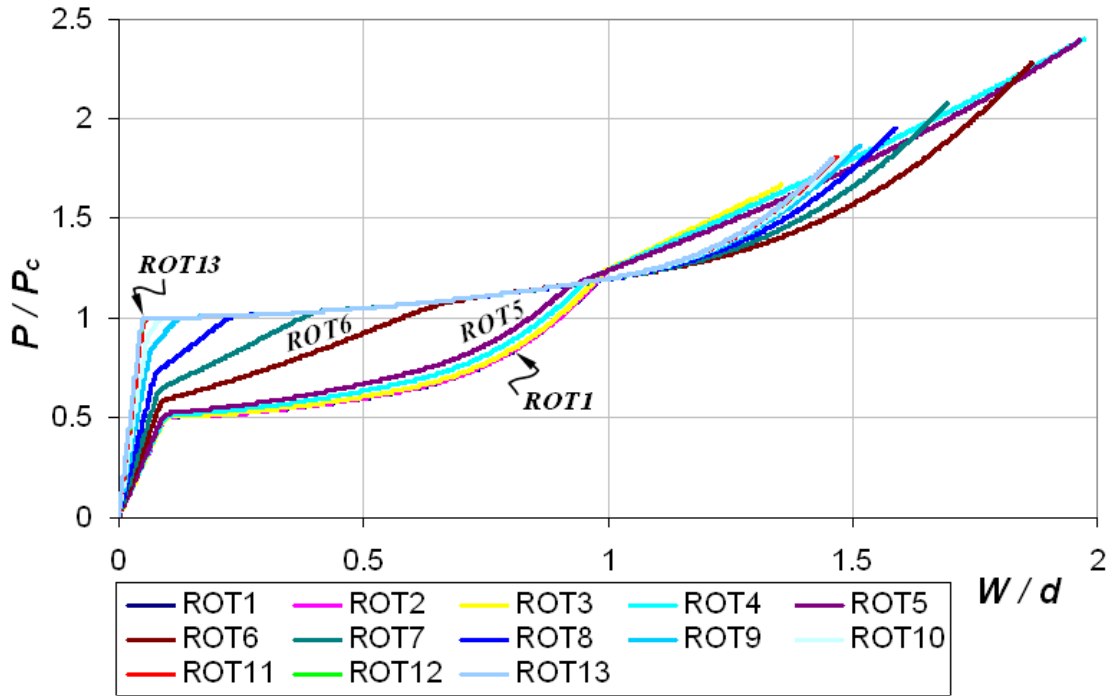


**Figure 6-11** Normalized Load–Deflection Plot (Midspan)

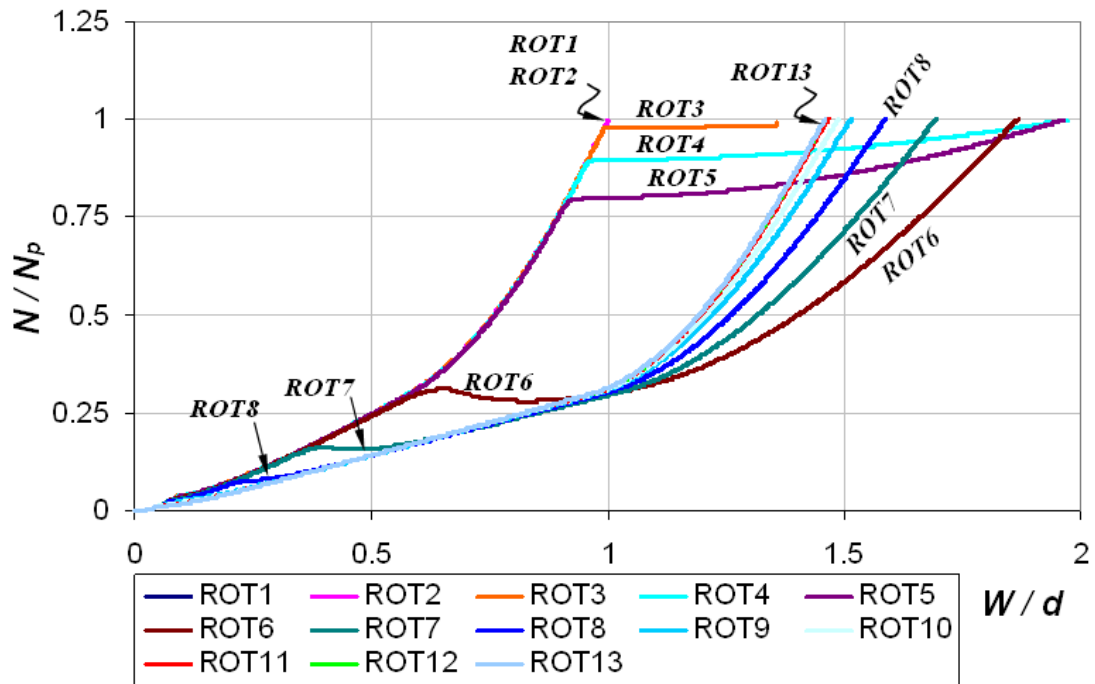


**Figure 6-12** Normalized Axial Force–Deflection Plot (Midspan)

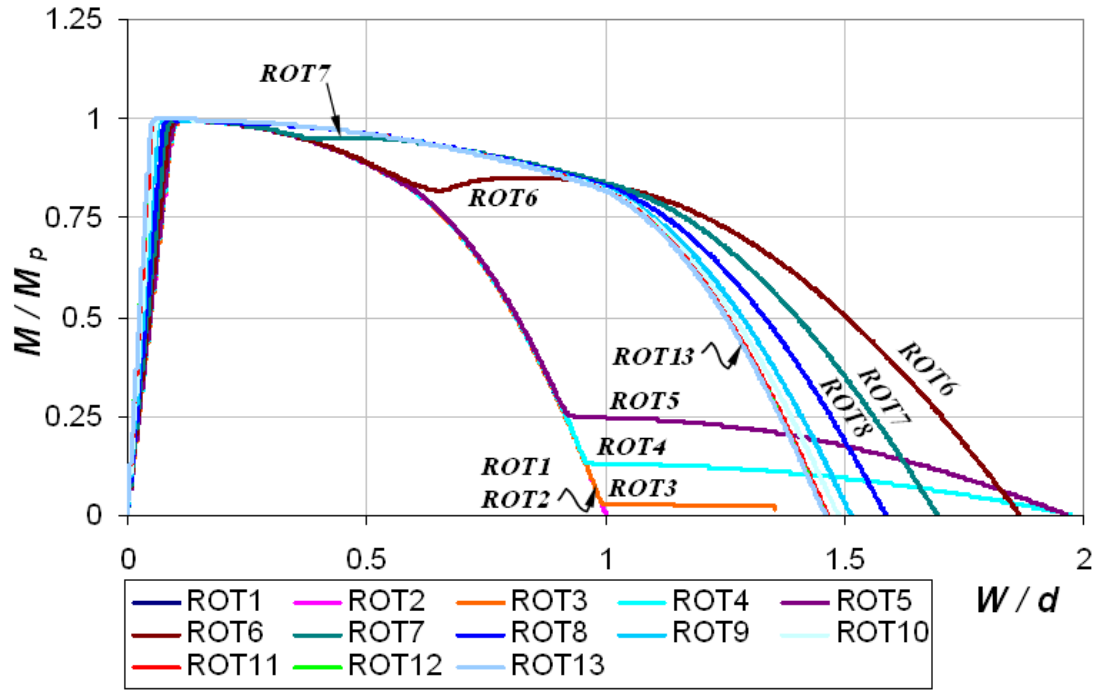


**Figure 6-13** Normalized Moment–Deflection Plot (Midspan)

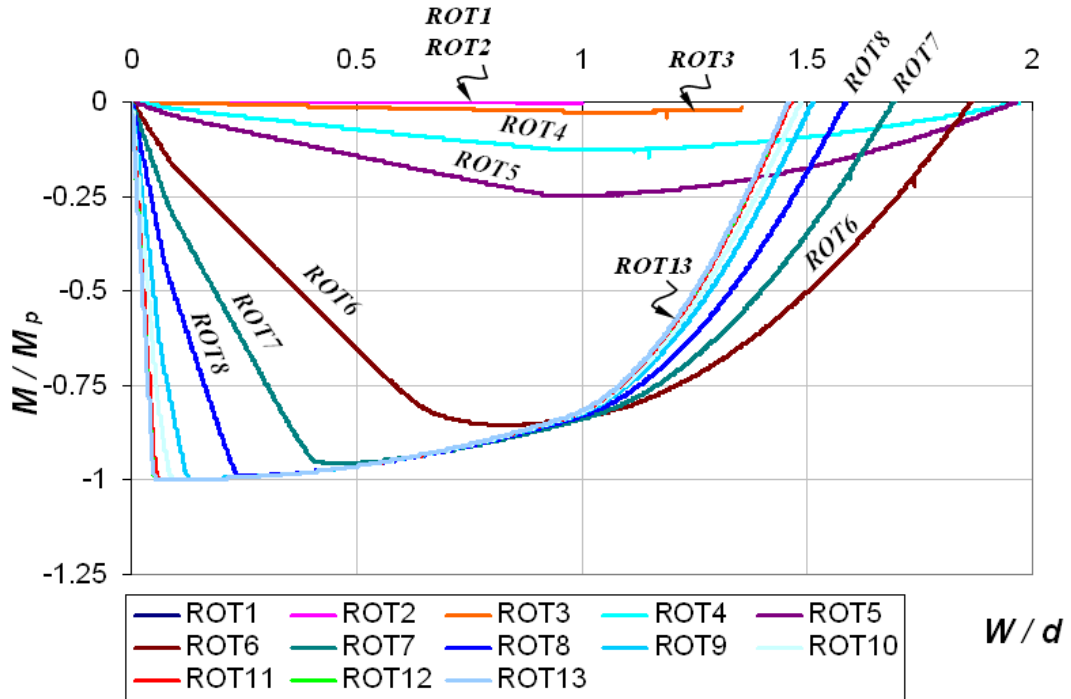


**Figure 6-14** Normalized Moment–Deflection Plot (End)

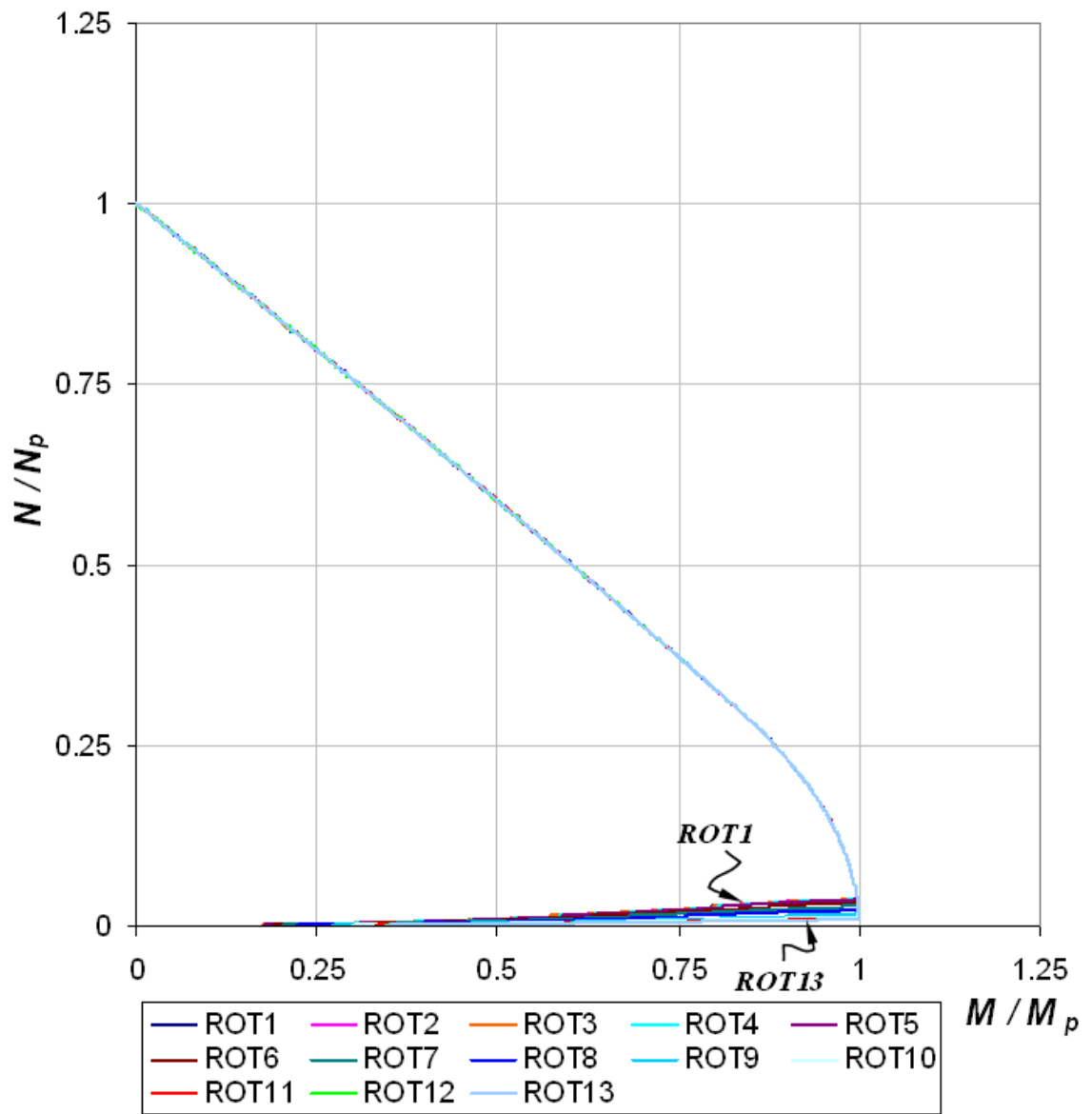


**Figure 6-15** Normalized  $M-N$  Interaction (Midspan)

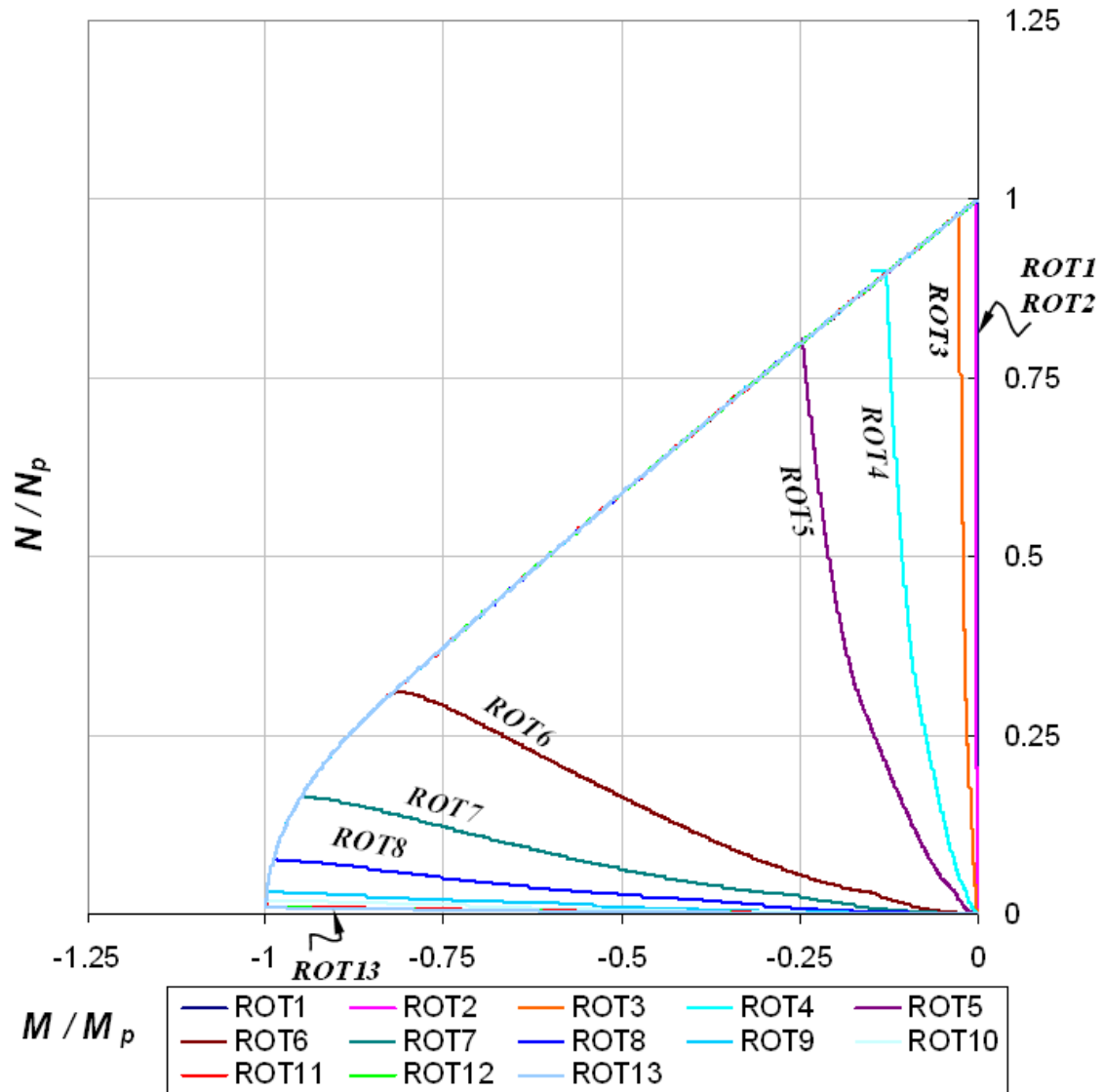


**Figure 6-16** Normalized  $M-N$  Interaction Plot (End)

The effect of rotational restraint can also be related to the connection behavior at the beam supports. The AISC Manual (2005) classifies connections on a moment–rotation ( $M-\theta$ ) behavior model as fully restrained (FR), partially restrained (PR) and simple, as illustrated in Figure 6-17. Dashed lines ( $K_s$ ) set the boundaries for connection behavior idealizations in structural analysis. Connections with stiffness between these two limits are considered as partially restrained (PR). In order to determine how the range

of spring constant considered herein relates to these limits, the moment–rotation response of the spring models are shown in Figure 6-18, along with the AISC regions for connection behavior. It can be seen that a number of representative beam models are covered in all three regions. In fact, the majority of the models (ROT1 through ROT8) fall within the “simple connection” region, which supports the discussion made regarding the sudden jump observed in the normalized internal force–deflection plots (Figures 6-12, 6-13).

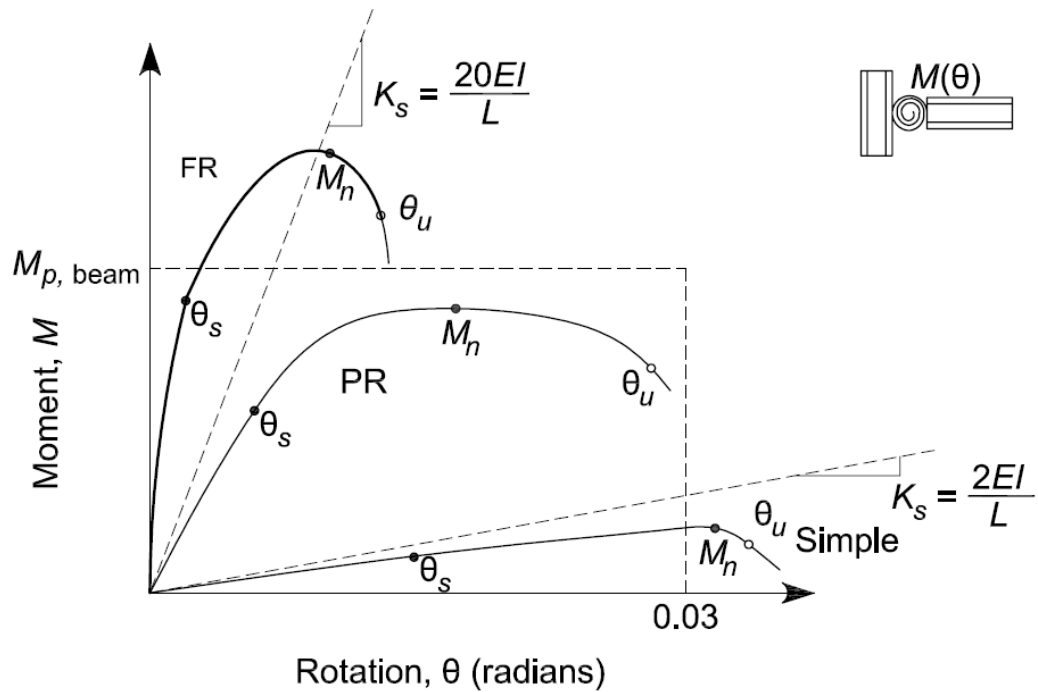


**Figure 6-17** Classification of moment–rotation response of fully restrained (FR), partially restrained (PR) and simple connections (AISC 2005)



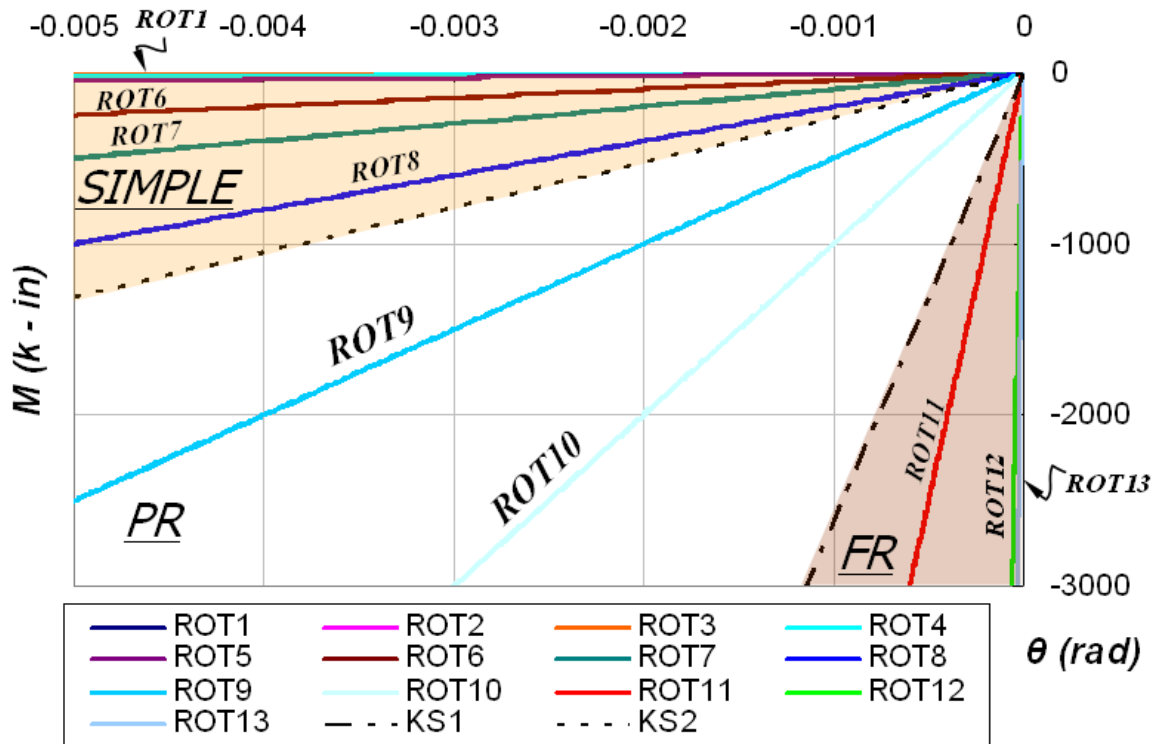


**Figure 6-18** Moment–Rotation Response of Elastic Springs in FE Beam Models

### 6.2.3 Combined Effect of Translational and Rotational Restraints

Individual effects of translational and rotational springs at beam ends provided a great deal of insight into their effect on the behavior. In this section, a W14x53 is modeled as shown in Figure 6-1 to study the combined effect of elastic boundary restraints.

Spring constant combinations were chosen in such a way as to cover combinations of low, intermediate and high spring constants considered in the previous sections. A typical 60-ft-long, elastic–perfectly plastic beam with W14x53 cross-section was modeled and analyzed using the 16 different combinations of linear–elastic spring constants listed in Table 6-3. Labels K11 through K44 denote the beam models analyzed.

Table 6-3 also gives the resulting deflection at the onset of pure cable behavior,  $W_{cat}$  and  $W_{cat}/d$  for each case. It can be seen that  $W_{cat}/d$  is rather more sensitive to the level of axial restraint,  $k_{\Delta}$  than to the level of rotational restraint,  $k_{\theta}$ . In fact, despite the large variation in rotational spring constant, the level of translational spring constant determines  $W_{cat}/d$  which changes only slightly within each group. Additionally, the onset point of pure cable behavior is reached at a relatively reasonable deflection level for the two groups with higher axial restraints as seen in Table 6-3.

**Table 6-3** Beam Models with Combined Spring Constant Cases

<b>Group No</b>	<b>Name</b>	<b><math>k_{\Delta}</math> (kip/in)</b>	<b><math>k_{\theta}</math> (k-in/rad)</b>	<b><math>W_{cat}</math> (in)</b>	<b><math>W_{cat}/d</math></b>
1	K11	1	1	345.67	24.87
	K12	1	5000	353.58	25.44
	K13	1	500000	349.90	25.17
	K14	1	50000000	349.85	25.17
2	K21	24	1	147.66	10.62
	K22	24	5000	154.89	11.14
	K23	24	500000	152.40	10.96
	K24	24	50000000	152.27	10.95
3	K31	400	1	49.27	3.54
	K32	400	5000	56.89	4.09
	K33	400	500000	54.70	3.94
	K34	400	50000000	54.23	3.90
4	K41	25600	1	29.34	2.11
	K42	25600	5000	39.11	2.81
	K43	25600	500000	36.92	2.66
	K44	25600	50000000	36.12	2.60

FE analysis results are also given in the plots of normalized load versus deflection, normalized axial force versus deflection, normalized moment versus deflection in Figures 6-19 through 6-21. It can be seen from these figures that the curves are assembled into four groups, each with the same  $k_{\Delta}$ . Additionally, the significance of the level of axial restraint, rather than the rotational restraint in regard to the onset point of pure cable behavior can also be seen in Figures 6-20 and 6-21. In particular, all the

beams of Group 1 have to exhibit extremely large deflections to reach pure cable behavior.

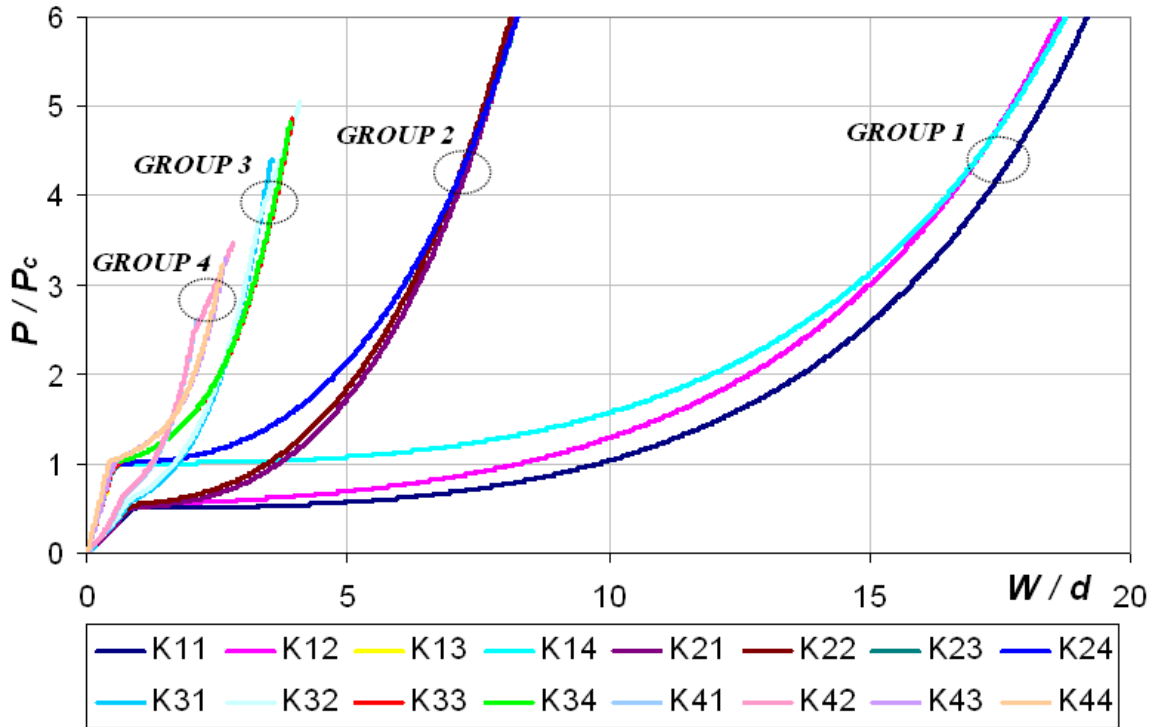
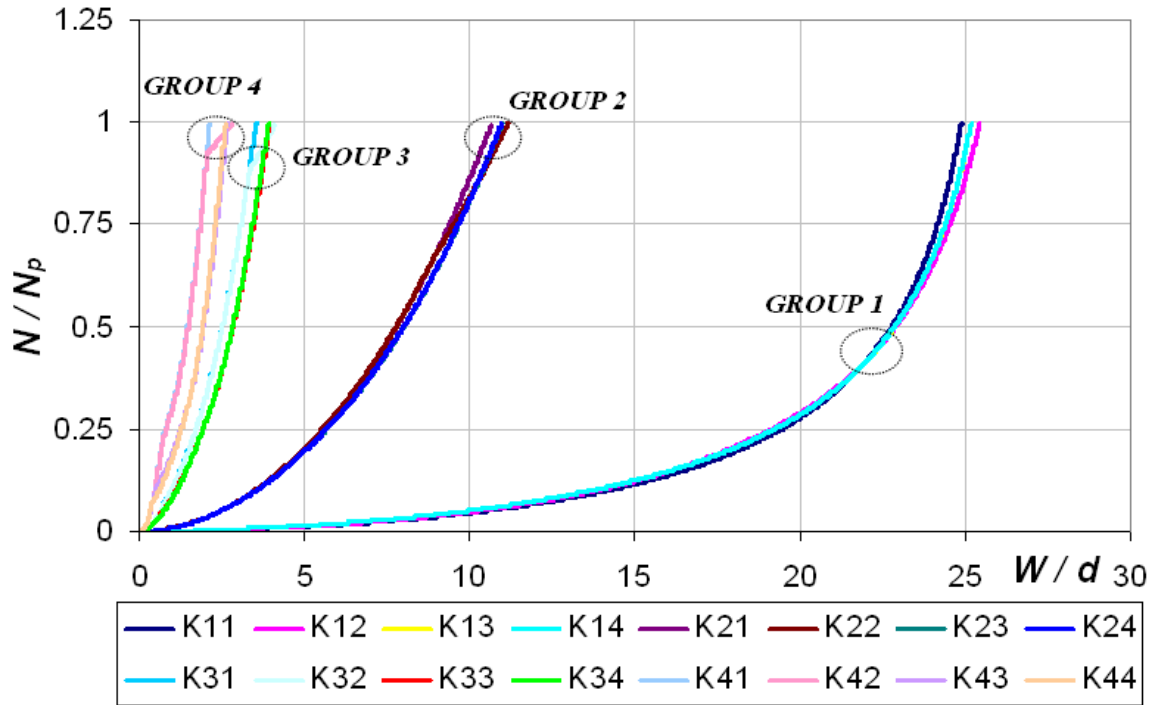
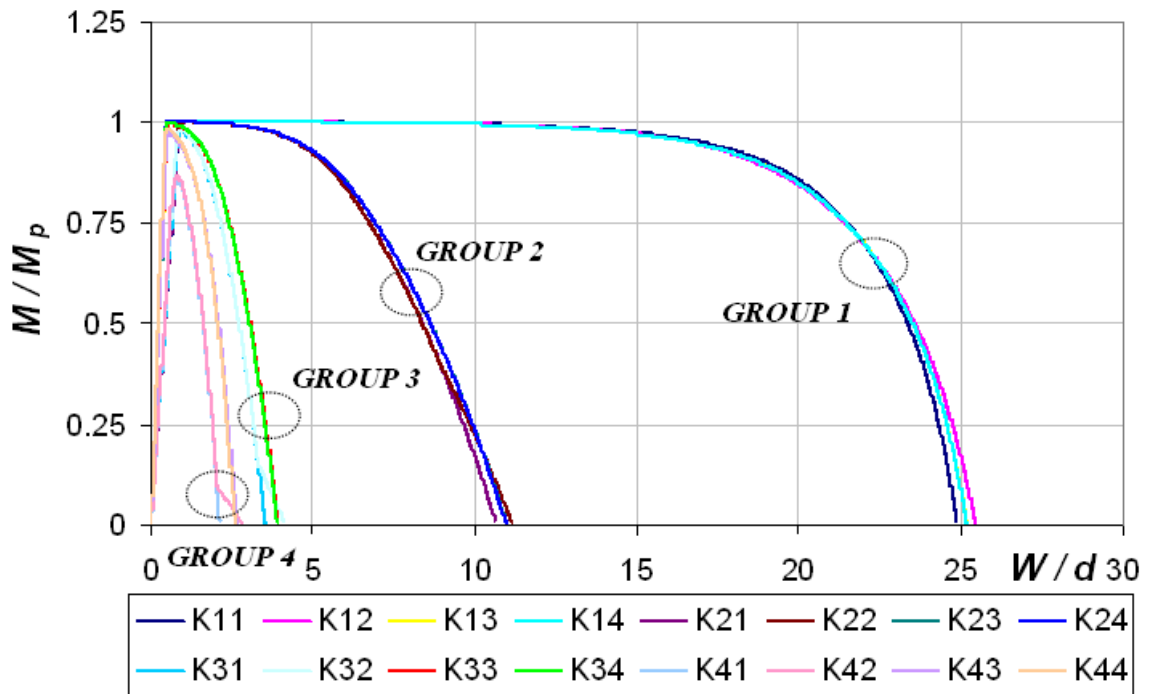


Figure 6-19 Normalized Load-Deflection Plot



**Figure 6-20** Normalized Axial Force–Deflection Plot (Midspan)



**Figure 6-21** Normalized Moment–Deflection Plot (Midspan)

Figures 6-22 and 6-23 show normalized  $M-N$  interaction results for midspan and end sections, respectively. It can be seen that when rotational restraints at supports are low (i.e.  $K_{11}, K_{21} \dots K_{41}$  and  $K_{12}, K_{22} \dots K_{42}$ ), the plastic hinge forms with predominantly axial force,  $N$  (Figure 6-23).

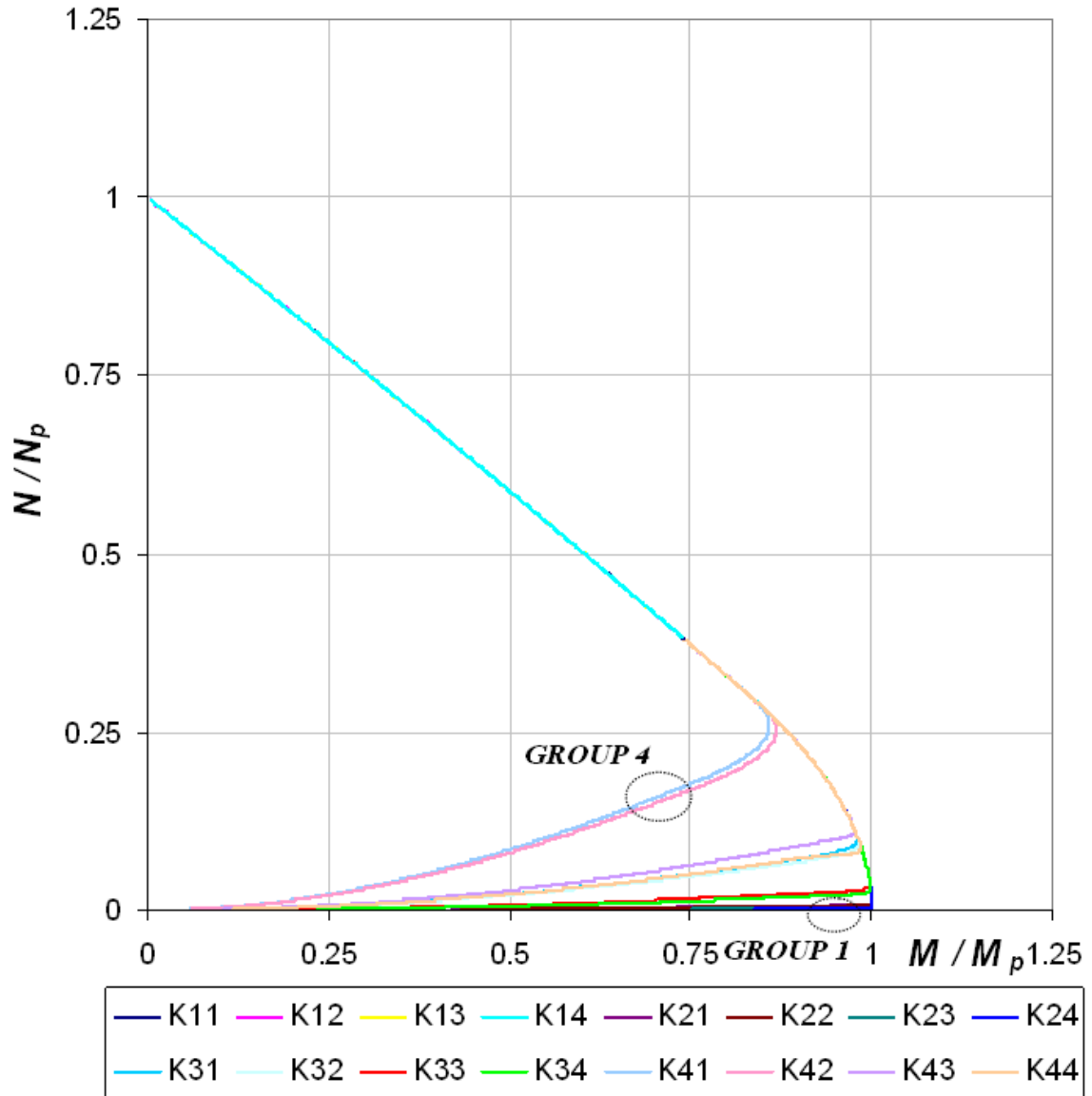


**Figure 6-22** Normalized  $M-N$  Interaction (Midspan)

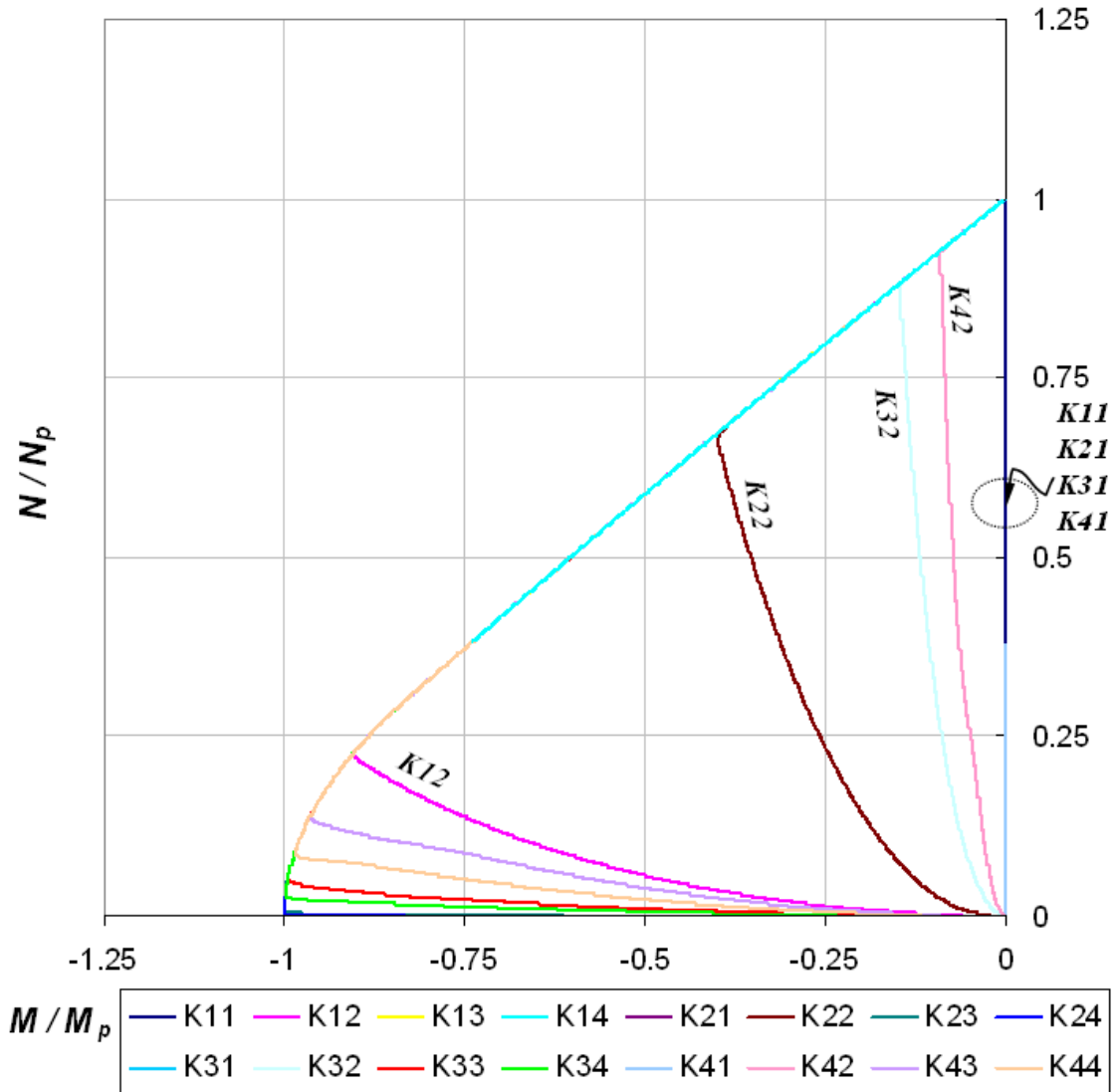


**Figure 6-23** Normalized  $M-N$  Interaction (End)

### 6.3 Relationship between Beam Models and Frame Models

In this section, a description is given of a number of simple FE frame analyses that were conducted using OpenSees to investigate the sources of boundary conditions available within a frame and to relate the results to the beam model studies presented in Section 6.2. First, a preliminary design of a two-bay benchmark frame was performed for gravity loads only. The frame was assumed to be braced. Also, continuous bracing for the

beams due to the existence of a slab was assumed. As illustrated in Figure 6-24, a part of an interior frame in an office building which has symmetry in both directions was considered ( $L=30ft$ ). The AISC LRFD (2005) method was used and typical beam sections were chosen to be W14x53 and W16x100 were chosen for the columns.

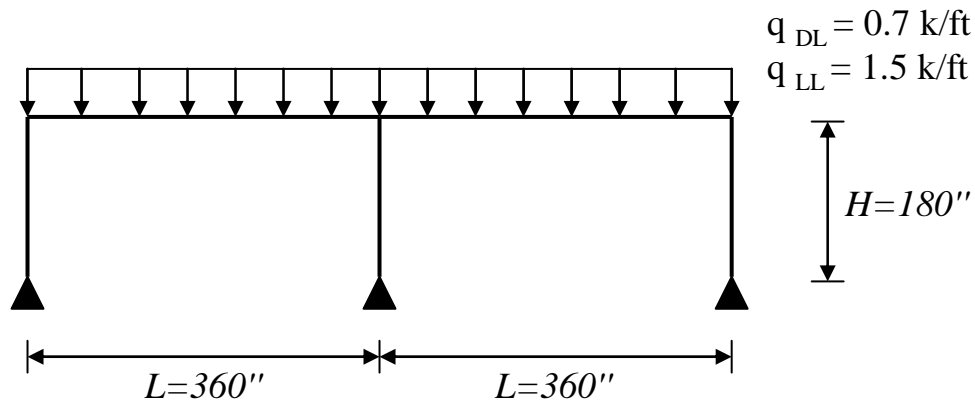


**Figure 6-24** Reference Frame

### 6.3.1 Quantification of Elastic Spring Constants

For the purpose of this study, restraining effects at the beam ends within an actual frame are assumed to be provided by the surrounding members framing into the beam joints. In other words, beam-to-column connections herein are considered to be fully restrained (FR). However, it can be anticipated that the frame given in Figure 6-24 would not provide any significant translational and rotational restraint at the beam supports if the middle column is notionally removed and the remaining frame analyzed under a concentrated load at midspan (Figure 6.25). Instead, one additional bay on each side of the frame was added to the reference frame to study the quantification of boundary restraints.

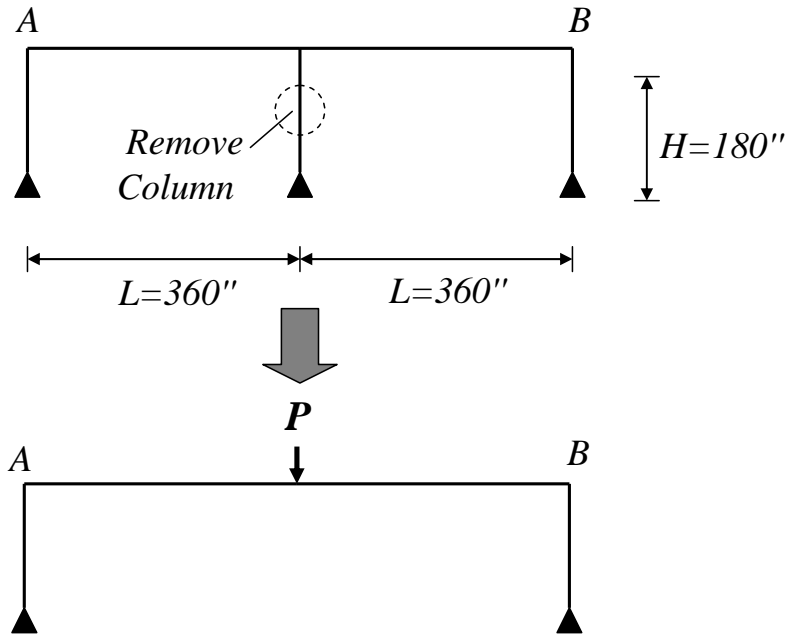


**Figure 6-25** Schematic of Frame Analysis

As illustrated in Figure 6-26, elastic boundary conditions offered by the side frames at joints A and B can be calculated as follows: side frames are isolated from the actual frame and analyzed with arbitrary loads ( $P_A$ ,  $M_A$ ) one at a time in order to obtain translational and rotational spring constants, respectively. A linear-elastic analysis was conducted using OpenSees and the resultant spring constants (i.e. slope of the resultant load-deflection curve) were obtained as:

$$k_{\Delta} = 11.8 \text{ kip} / \text{in}$$

$$k_{\theta} = 393,700 \text{ k-in} / \text{rad.}$$

Due to symmetry, spring constants were taken to be the same at A and B.



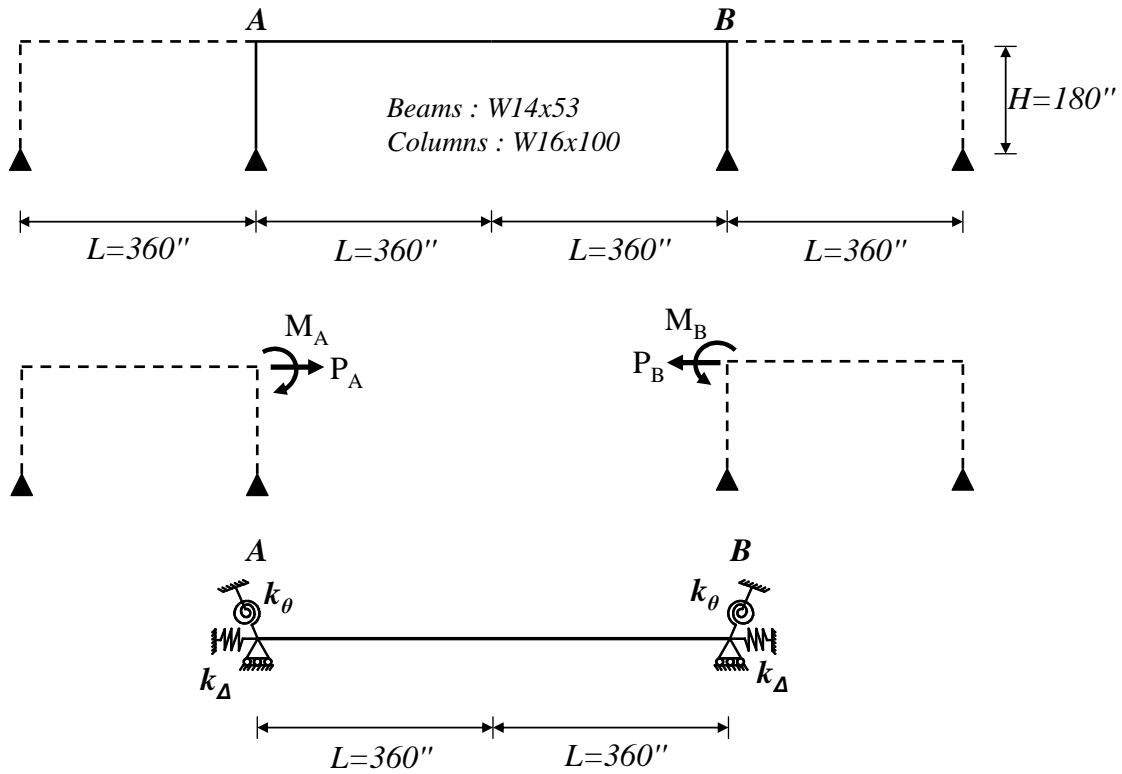


**Figure 6-26** Schematic for the Quantification of Linear-Elastic Spring Constants

### 6.3.2 Comparison between Frame and Beam Models

Having determined the linear-elastic spring constants, nonlinear static analyses of the frame and the beam A-B were conducted under a concentrated load at midspan separately, as illustrated in Figure 6-27. It should be noted that material nonlinearity was not included in the members other than for the beam A-B in the frame analysis, as noted in Figure 6-31.

W14x53 beam A-B was again discretized with fibers with a typical thickness of  $t_{fiber}=5 \times 10^{-3}$  inches and an elastic-perfectly plastic steel material ( $\sigma_y=50$  ksi) was used. The number of elements along the beam length was also taken as 100.

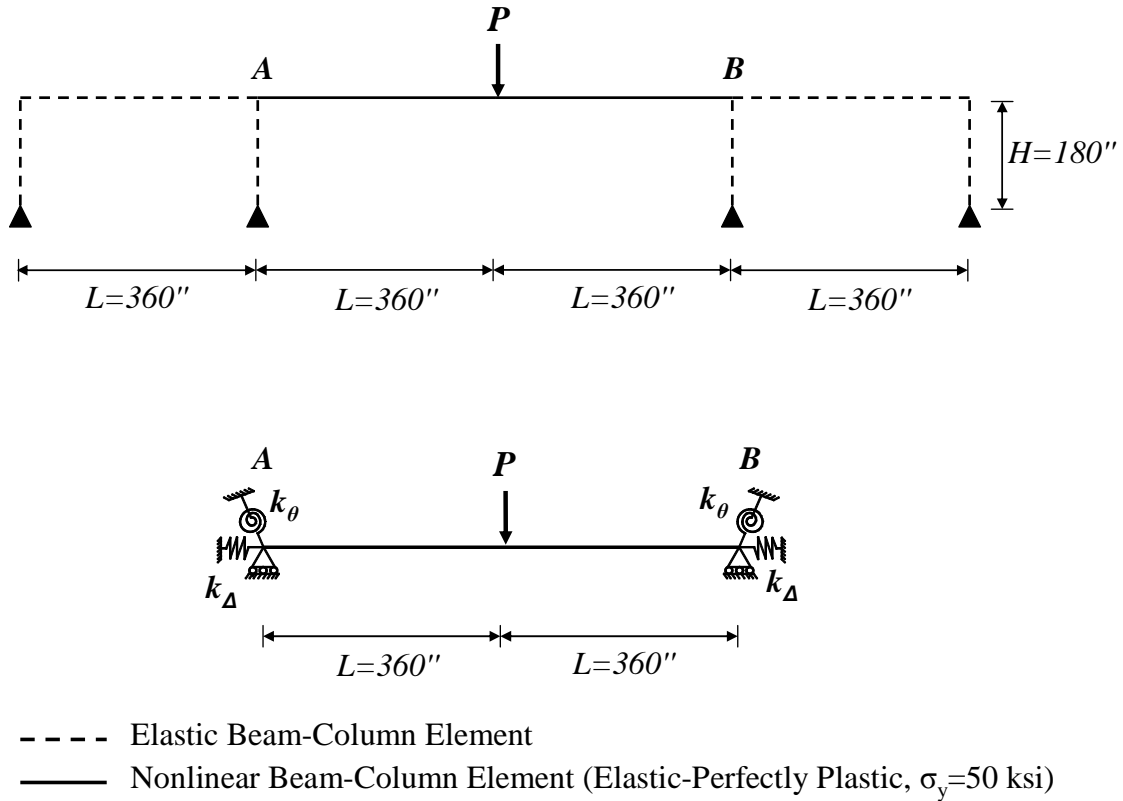


**Figure 6-27** Frame and Beam Models

FE analysis results are presented in the form of normalized load versus normalized deflection, normalized axial force versus normalized deflection, normalized moment versus normalized deflection, and  $M-N$  interaction plots in Figures 6-28 through 6-32 for the beam A–B in each case. In Figure 6-28, the external load,  $P$ , is normalized by the plastic collapse load,  $P_c$ , of a W14x53 beam with fixed ends spanning  $2L=60ft$  as typical.

It can be seen in Figures 6-28 through 6-32 that the behavior exhibited by the beam model with elastic springs is in excellent agreement with the beam behavior within the frame. It can be seen from the normalized axial force–deflection plot given in Figure

6-30 that the beam within the frame exhibits a slight compression in the elastic regime, as anticipated, and then axial tension forces due to large deflections start to dominate the behavior. This can also be seen in the normalized  $M-N$  interaction curves as both midspan and end sections, which follow the yield condition perfectly once the flexural plastic hinge is formed (Figures 6-31 and 6-32, respectively).

The results show that it is possible to model and analyze the beam above a notionally removed column in a given frame with adequate representation of boundary conditions. Nevertheless, it should be noted that the results are limited to the frame considered herein, and are not necessarily to be generalized at this point.

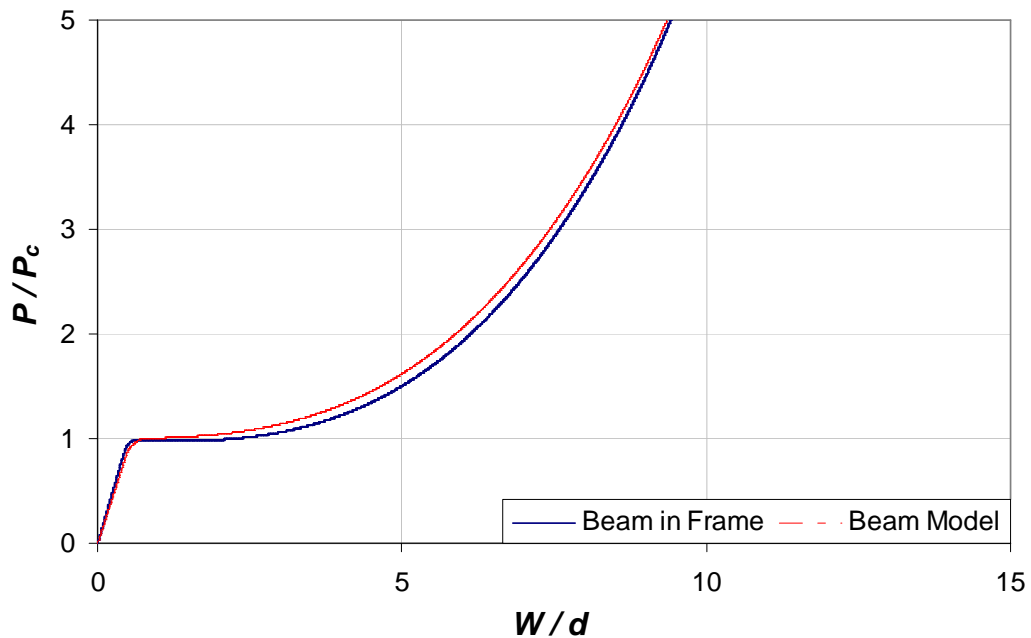


**Figure 6-28** Normalized Load–Deflection Plot (Beam Midspan)

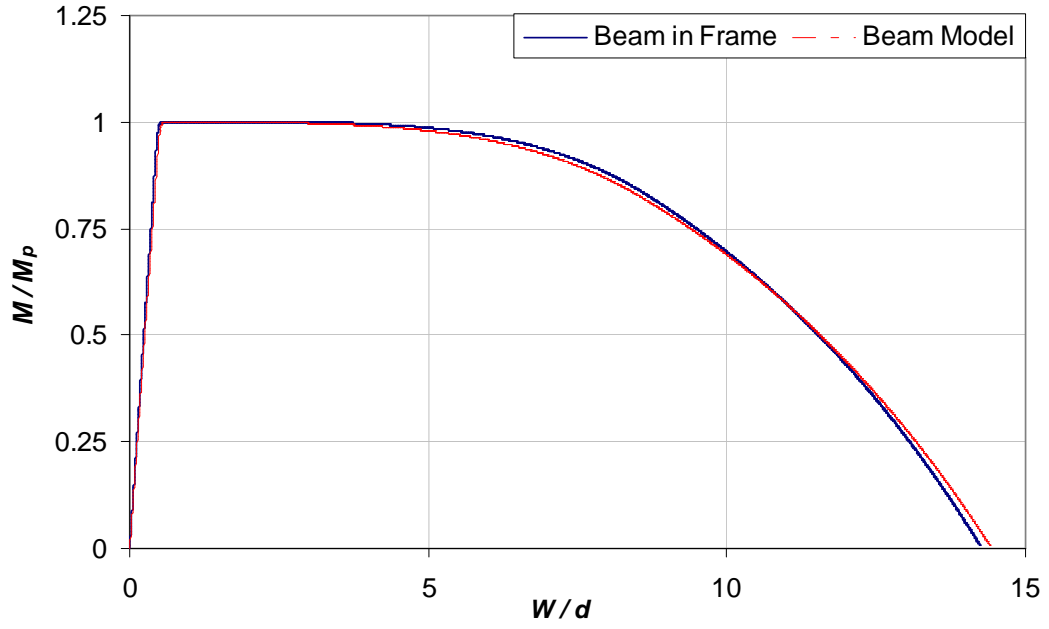


**Figure 6-29** Normalized Moment–Deflection Plot (Beam Midspan)

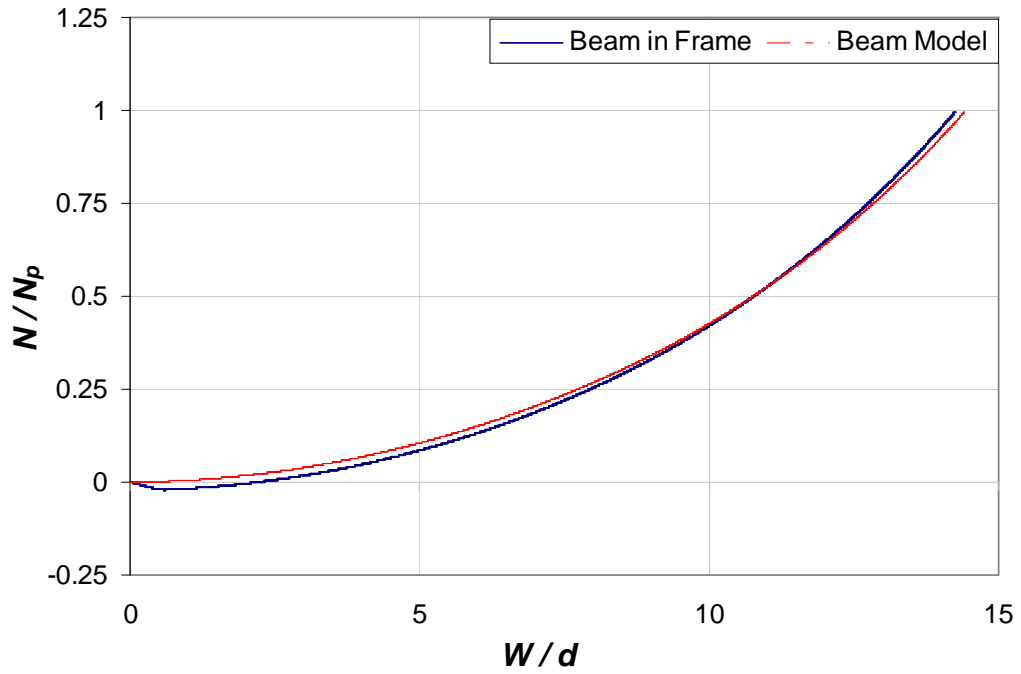


**Figure 6-30** Normalized Axial Force–Deflection Plot (Beam Midspan)

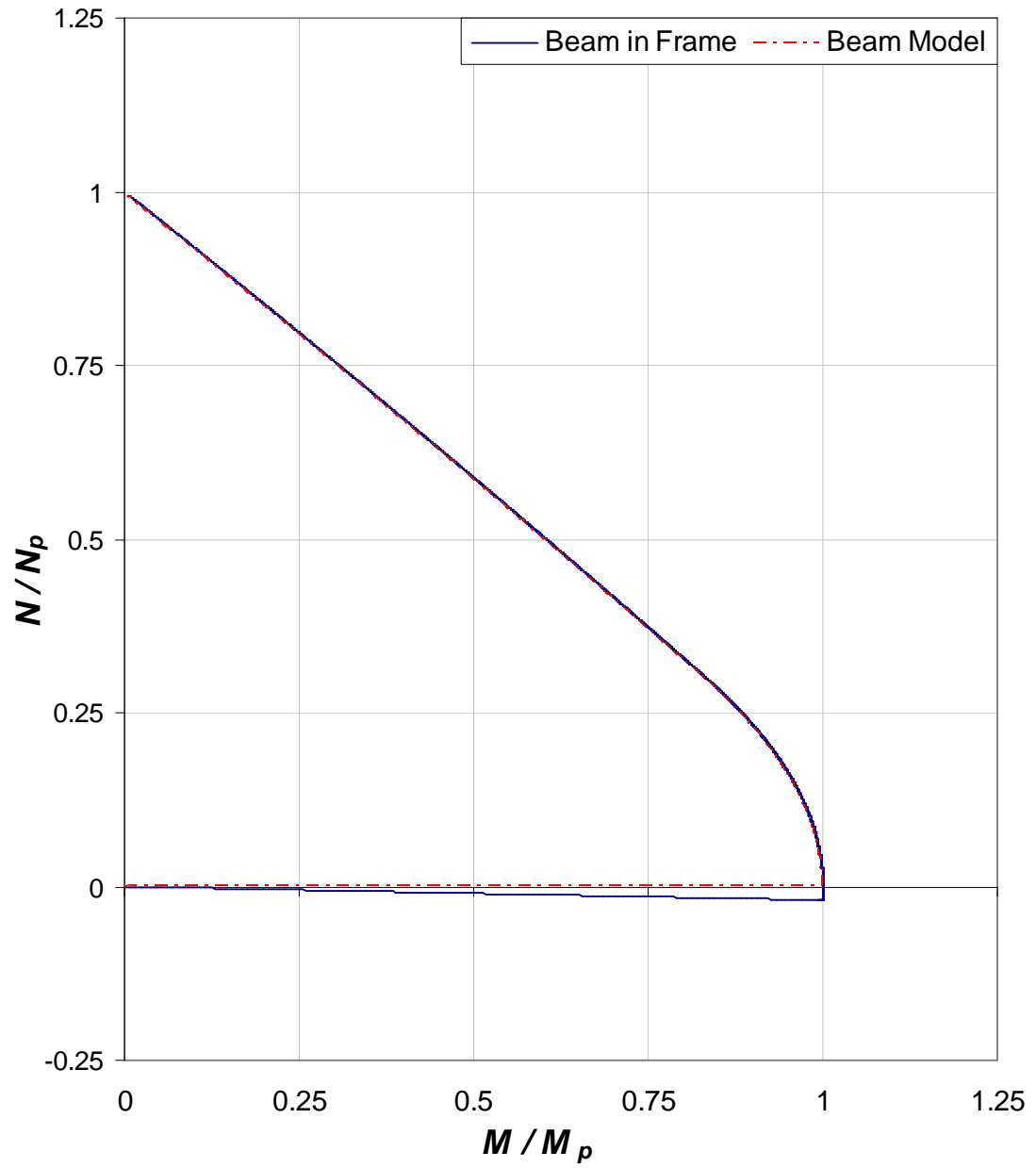


**Figure 6-31** Normalized  $M$ - $N$  Interaction (Beam Midspan)

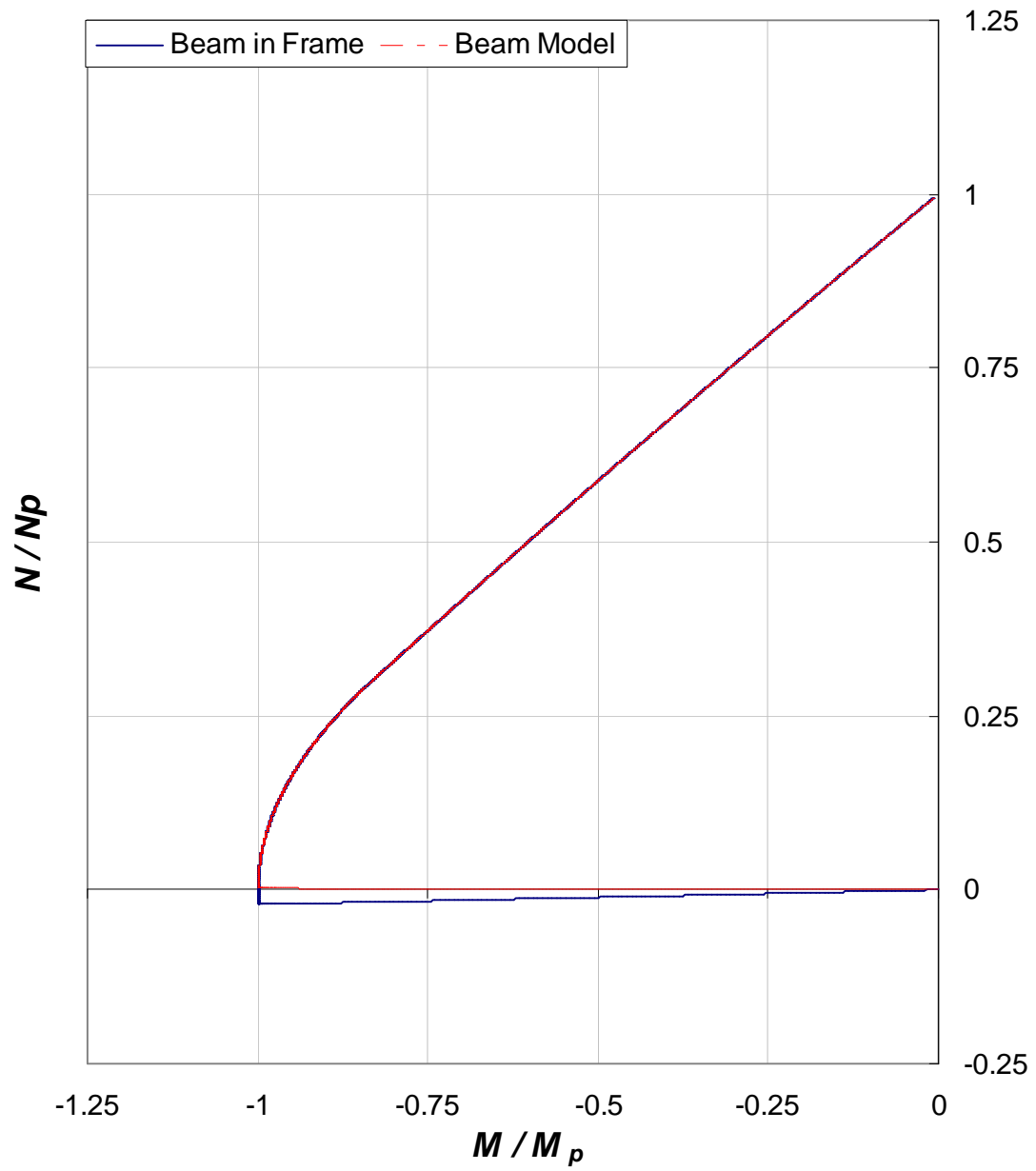


**Figure 6-32** Normalized  $M-N$  Interaction (Beam End)

## 6.4 Summary and Conclusions

Studies of the effect of elastic boundary conditions on the beam response, along with simple frame studies conducted herein provided the following findings:

- The dependency of the deflection at the onset of pure cable behavior on axial restraint is significantly larger than the dependence on rotational restraint. Therefore, if the beam ends are not sufficiently restrained axially, it is impractical to take advantage of the cable behavior described in this thesis as a load-resisting mechanism.
- Evaluation of linear–elastic boundary conditions that are offered at the beam joints within a given frame, and comparison with corresponding beam models, showed an acceptable agreement for use in future frame studies. However, it should be noted that general statements can not be made at this time due to the limited data produced.

## Chapter 7. SUMMARY, CONCLUSIONS AND RECOMMENDATIONS FOR FUTURE STUDY

### 7.1 Summary

In addressing the propensity of steel building structures to experience progressive collapse due to extreme loading conditions (e.g., blast), current design guidelines propose the use of a threat-independent approach that is commonly referred to in the literature as “the missing column scenario”. Under this scenario, a column from a given story is assumed to be removed and the resulting structure is analyzed to determine if it could sustain the loads by activating one or more alternate load-carrying mechanisms, with the idea of mitigating the potential for progressive structural collapse. This study specifically focused on the ability of ductile steel beams to carry loads by transitioning from flexural behavior to cable-like behavior. Theoretical fundamentals of this behavior were described for rectangular and W-shaped steel beams with idealized boundary conditions and presumed fully ductile behavior. Two theoretical analysis approaches were used to model the beam behavior: rigid-plastic analysis and cable analysis. The main factors affecting the behavior, such as material and geometric properties as well as boundary conditions were described and corroborating nonlinear finite element (FE) analyses were presented and compared to the theoretical results. *Open System for Earthquake Engineering Simulation*, OpenSees was used in the FE analysis studies. Based upon theoretical and FE



analysis results, a set of equations were proposed that can be used to predict the deflection at the onset of pure cable behavior.

Additionally, the effect of elastic boundary restraints on the beam behavior was studied using FE analysis. An approach to evaluate the boundary restraints offered by the surrounding members in a given frame was also presented. It is shown that axial restraints have a much more significant effect on the behavior than rotational restraints.

## 7.2 Conclusions

Conclusions for this study can be summarized as follows:

- Rigid-plastic and cable theories serve as bounds to the behavior of ductile steel beams undergoing a transition from a flexural to cable-like behavior.
- Comparisons of FE analysis results with the theoretical results revealed that modeling the behavior using rigid-plastic theory is appropriate for very stiff beams, whereas modeling with the use of cable theory is appropriate for very flexible beams. In the general case, neither theory can alone accurately predict the behavior.
- FE analysis parametric studies showed that the midspan beam deflection at the onset of pure cable behavior,  $W_{cat}$ , is especially sensitive to the deflection at the onset of flexural mechanism formation.
- Expressions for  $W_{cat}$  were developed and compared with theory, and equations were proposed for use in the range of span-to-depth ratio,  $L/d$ , from 10 to 30.
- Studies on the effect of boundary conditions indicated that the onset point of pure cable behavior is predominantly affected by translational restraints.

### 7.3 Recommendations

Despite a number of assumptions made in the development of theory in this study, it is believed that a profound understanding of the behavior established a solid foundation for future investigations. The following recommendations for future study are made:

- It is recommended that beam models be investigated for:
  - Evaluation of ductility demands in regards to accommodating respective displacements.
  - Nonlinear behavior incorporation at boundary conditions.
  - Material strain hardening effect.
  - Nonlinear-dynamic analysis.
- Due to the lack of experimental results in the literature, it is also recommended that medium-scale laboratory testing be performed for idealized boundary conditions to corroborate the results obtained in this study.
- It is recommended that further frame analyses (*2D / 3D*) be conducted to understand the global behavior with regard to how the beam behavior described in this study would interact within a frame.
- It is also recommended that all sources of anchorage possibilities such as those that exist in an actual building structure be investigated due to the significant dependency of the behavior to the lateral stiffness provided at each floor.
- It is recommended that the equations proposed in this study be compared to and their applicability be investigated for, development of the Tie Force Method used in current progressive collapse design guidelines.

## REFERENCES

- AISC (2005) Steel Construction Manual 13<sup>th</sup> Edition, *American Institute of Steel Construction*, Chicago, IL
- ASCE (2005) ASCE / SEI 7-05: Minimum Design Loads for Buildings and Other Structures, *American Society of Civil Engineers*, Reston, VA
- Bazant, Z. P., Verdure, M., (2007) “Mechanics of Progressive Collapse: Learning from World Trade Center and Building Demolitions”, *ASCE Journal of Engineering Mechanics*, 133(3), 308
- Breen, J., (1980), “Developing Structural Integrity in Bearing Wall Buildings,” *PCI Journal*, 25(1), 42-73
- British Standard Institution (BSI) (2000), BS5950: Part 1, *Structural Use of Steelwork in Building*, London, UK
- Burnett, E.F.P., (1975), “The Avoidance of Progressive Collapse: Regulatory Approaches to the Problem” Report No. NBS-GCR-75-48, *National Bureau of Standards*, Washington, DC
- Byfield M., Paramasivam, S. (2007), “Catenary Action in Steel-Framed Buildings”, *Structures & Buildings*, 160(5), 247-257
- Creasy, L. R., (1972), “Stability of Modern Buildings” *The Structural Engineer*, London, 50(1), 3-6
- De Souza, R. M. (2000). “Force-Based Finite Element for Large Displacement Inelastic Analysis of Frames” Ph.D. Thesis, Univ. of California, Berkeley, CA

- Dusenberry D.O. (2002), “Review of Existing Guidelines and Provisions Related to Progressive Collapse”, *Workshop on Prevention of Progressive Collapse*, National Institute of Building Sciences, Washington D. C
- Ellingwood B. R., Smilowitz R., Dusenberry D. O., Duthinh D., Lew H. S., Carino N. J., (2007), Best Practices for Reducing the Potential for Progressive Collapse in Buildings, Report No: NISTIR-7396. *National Institute of Standards and Technology*, Technology Administration, *US Department of Commerce*
- Foley C. M., Martin K., Schneeman C., (2007), Robustness in Structural Steel Framing Systems, Report, *American Institute of Steel Construction (AISC)*, Chicago, IL
- General Services Administration (GSA), (2003), “Progressive Collapse Analysis and Design Guidelines for New Federal Office Buildings and Major Modernization Projects” Washington, D.C
- Gustafson, K. (2009) “Meeting the 2009 IBC Structural Integrity Requirements”, *AISC North American Steel Construction Conference (NASCC)*, Phoenix, AZ, Conference Proceedings, AISC <<http://www.aisc.org/>>
- Haythornthwaite, R. M. (1957), “Beams with Full End Fixity” *Engineering*, 183, 110-12
- Hamburger, R., Whittaker, A. (2004) “Design of Steel Structures for Blast-Related Progressive Collapse Resistance” *North American Steel Construction Conference (NASCC)*, Long Beach, CA, Conference Proceedings AISC <<http://www.aisc.org/>>
- Horne, M. R. (1979) “Plastic Theory of Structures” Pergamon Press, Oxford, England, 66-68
- Izzuddin, B. A. (2005) “A Simplified Model for Axially Restrained Beams Subject to

- Extreme Loading’’ *International Journal of Steel Structures*, 5, 421–429
- Jones N. (1989) “Structural Impact” *Cambridge University Press*, Cambridge, Great Britain, 276-290
- Khandelwal, K., and El-Tawil, S. (2007). “Collapse Behavior of Steel Special Moment Resisting Frame Connections” *ASCE Journal of Structural Engineering*, 133(5), 646–655.
- Khandelwal K., El-Tawil S., Kunnath S. K., Lew H. S. (2008)“Macromodel-Based Simulation of Progressive Collapse: Steel Frame Structures” *ASCE Journal of Structural Engineering*, 134(7), 1070-1079
- Khandelwal K., El-Tawil S; Kunnath S. K., Lew H. S. (2008)”Macromodel-Based Simulation of Progressive Collapse: RC Frame Structures’’ *ASCE Journal of Structural Engineering*, 134(7), 1079-182
- Krauthammer, T., Hall, R. L., Woodson, S. C., Baylot, J. T., Hayes, J. R., and Sohn, Y. (2002) “Development of Progressive Collapse Analysis Procedure and Condition Assessment for Structures” *National Workshop on Prevention of Progressive Collapse in Rosemont, Ill.* Multihazard Mitigation Council of the National Institute of Building Sciences, Washington, D.C
- Marchand, K. A., Alfawakhiri F., (2004) Facts for Steel Buildings 2: Blast and Progressive Collapse, *American Institute of Steel Construction (AISC)*, Chicago, IL
- McKenna, F., Fenves, G. L., and Scott, M. H. (2000) “Open System for Earthquake Engineering Simulation (OpenSees)” Univ. of California, Berkeley, CA, <<http://opensees.berkeley.edu>>

- Mohamed, O. A. (2006), “Progressive Collapse of Structures: Annotated Bibliography and Comparison of Codes and Standards”, *ASCE Journal of Performance of Constructed Facilities*, 20(4), pp. 418–425
- Nair, R. S. (2004) “Progressive Collapse Basics” *Modern Steel Construction*, American Institute of Steel Construction (AISC), 44(3), 37– 42
- Neuenhofer A., Filippou F. C (1998) “Geometrically Nonlinear Flexibility-Based Frame Finite Element” *ASCE Journal of Structural Engineering*, 124(6), 704–711
- Powell, G. (2005) “Progressive Collapse: Case Studies Using Nonlinear Analysis” *ASCE Structures Congress*, New York, NY, American Society of Civil Engineers (CD-ROM)
- Scott M., H., Fenves G. L., McKenna F., Filippou F. C. (2008) “Software Patterns for Nonlinear Beam-Column Models” *ASCE Journal of Structural Engineering*, 134(4), 562–571
- Weisstein, E. W. (2009), “Catenary” Retrieved from *MathWorld*, a Wolfram Web Resource, June 25: <http://mathworld.wolfram.com/Catenary.html>
- Unified Facilities Criteria (UFC) (2005) “Design of Buildings to Resist Progressive Collapse”, *Department of Defense*, Washington, D.C

## **APPENDICES**

## APPENDIX A: Notation

$a$	Distance between centroid and neutral axis of cross-section, in
$A$	Cross-sectional area of member, in <sup>2</sup>
$A_w$	Web area, the overall depth times the web thickness, $(d \times t_w)$ , in <sup>2</sup>
$b$	width of rectangular cross-section, in
$b_f$	Flange width, in
$d$	Full nominal depth of the section, in
$d_w$	Nominal web depth, in
$E$	Modulus of Elasticity of steel, 29000 ksi
$f$	Shape function
$I_x$	Moment of inertia about principal axis, in <sup>4</sup>
$k_A$	Linear-Elastic translational spring constant, kip / in
$k_\theta$	Linear-Elastic rotational spring constant, kip-in / rad
$l$	Plastic hinge length
$L$	Length (e.g., beam, bay), in (ft)
$L'$	Actual length in deformed configuration
$M$	Bending moment, kip-in
$M_p$	Plastic Bending Moment, kip-in
$M_{pf}$	Plastic Bending Moment calculated using the flanges only (about major axis)
$N$	Axial force, kips



$N_p$	Plastic Axial Force, kips
$N_{pw}$	Plastic Axial Force calculated using the web only
$P_c$	Plastic collapse load of member, kips
$P$	Point load on member, kips
$q$	Uniformly distributed load along the member
$q_c$	Uniformly distributed plastic collapse load of member
$Q$	Shear Force, kips
$s$	Mean transverse spacing, in (ft)
$S_x$	Elastic section modulus taken about the principal axis, in <sup>3</sup>
$t_{fiber}$	Thickness of fiber
$t_w$	Beam web thickness, in
$w$	shape function of deformed shape configuration
$W$	Midspan transverse deflection, in
$W_{cat}$	Midspan Transverse deflection at pure catenary formation
$\dot{W}$	Transverse deflection rate (with respect to time)
$Z_x$	Plastic section modulus about the principal axis, in <sup>3</sup>
$\delta_p$	Midspan deflection at the onset of flexural mechanism, in
$\varepsilon$	Axial strain
$\dot{\varepsilon}$	Axial strain rate (with respect to time)
$\kappa$	Curvature
$\dot{\kappa}$	Curvature rate (with respect to time)
$\sigma_y$	Yield stress, ksi

- $\eta$  Depth fraction represents the location of neutral axis from bottom of cross-section
- $\theta$  Rotation angle at beam supports
- $\Delta L$  Change in length

## APPENDIX B: Typical Input Files in OpenSees

### B.1: Centrally Loaded Beam Fixed at Supports

```
wipe all;

#---Units: kip, in---#

#-----Define the Model Builder-----#

model basic -ndm 2 -ndf 3;

#-----File Directory-----#

file mkdir W30x124;

#-----Define nodes-----#

for {set i 0} {$i<101} {incr i} {

set nodeTag [expr $i+1]

set xdim [expr $i*7.2]

node $nodeTag $xdim 0

}

#-----Define Boundary Conditions-----#

fix 1 1 1 1;

fix 101 1 1 1;

#-----Geometric Transformation-----#

geomTransf Corotational 1;

#-----Define Materials-----#

uniaxialMaterial ElasticPP 1 29000 0.00172413;
```

#-----Define Fiber Section-----#

#Section W30x124#

set SecTag 1

set d 30.2;

set tw 0.585;

set bf 10.5;

set tf 0.93;

set nfdw 5688;

set nftw 1;

set nbf 1;

set nftf 186;

set dw [expr \$d-2\*\$tf]

set y1 [expr -\$d/2]

set y2 [expr -\$dw/2]

set y3 [expr \$dw/2]

set y4 [expr \$d/2]

set z1 [expr -\$bf/2]

set z2 [expr -\$tw/2]

set z3 [expr \$tw/2]

set z4 [expr \$bf/2]

section fiberSec \$SecTag {

#        nFIJ nFJK   yI zI   yJ zJ   yK zK   yL zL

patch quadr 1 \$nbf \$nftf \$y1 \$z4 \$y1 \$z1 \$y2 \$z1 \$y2 \$z4

```

    patch quadr 1 $nftw $nfdw $y2 $z3 $y2 $z2 $y3 $z2 $y3 $z3
    patch quadr 1 $nfbf $nftf $y3 $z4 $y3 $z1 $y4 $z1 $y4 $z4
}
#-----Define Elements-----#
for {set k 0} {$k<100} {incr k} {
    set eltag [expr $k+1]
    set inode [expr $k+1]
    set jnode [expr $k+2]
    element nonlinearBeamColumn $eltag $inode $jnode 3 1 1
}
#-----Define Recorders-----#
recorder Node -file W30x124/Node51.out -time -node 51 -dof 2 disp;
recorder Node -file W30x124/Node1.out -time -node 1 -dof 3 disp;
recorder Element -file W30x124/ForceE51-S1.out -time -ele 51 section 1 force;
recorder Element -file W30x124/DefE51-S1.out -time -ele 51 section 1 deformation;
recorder Element -file W30x124/ForceE1-S1.out -time -ele 1 section 1 force;
recorder Element -file W30x124/DefE1-S1.out -time -ele 1 section 1 deformation;
#-----Define Load Case-----#
pattern Plain 1 Linear {
    load 51 0 -230.4474 0
}
#-----Define Analysis Objects-----#
constraints Plain;

```

```
numberer Plain;  
system BandGeneral;  
test NormDispIncr 1.0e-3 10;  
algorithm Newton;  
integrator DisplacementControl 51 2 -0.02;  
analysis Static  
analyze 5000;  
loadConst -time 0.0;  
puts "Done!"
```

## B.2: Fixed Beam with Uniformly Distributed Load along the Length

```
wipe all;

#---Units: kip, in---#

#-----Define the Model Builder-----#

model basic -ndm 2 -ndf 3;

#-----File Directory-----#

file mkdir W30x124_DistL;

#-----Define nodes-----#

for {set i 0} {$i<101} {incr i} {

  set nodeTag [expr $i+1]

  set xdim [expr $i*7.2]

  node $nodeTag $xdim 0

}

#-----Define Boundary Conditions-----#

fix 1 1 1 1;

fix 101 1 1 1;

#-----Geometric Transformation-----#

geomTransf Corotational 1;

#-----Define Materials-----#

uniaxialMaterial ElasticPP 1 29000 0.00172413;

#-----Define Fiber Section-----#
```

```

set SecTag 1

set d 30.2;

set tw 0.585;

set bf 10.5;

set tf 0.93;

set nfdw 5688;

set nftw 1;

set nfbf 1;

set nftf 186;

set dw [expr $d-2*$tf]

set y1 [expr -$d/2]

set y2 [expr -$dw/2]

set y3 [expr $dw/2]

set y4 [expr $d/2]

set z1 [expr -$bf/2]

set z2 [expr -$tw/2]

set z3 [expr $tw/2]

set z4 [expr $bf/2]

section fiberSec $SecTag {

    #      nfIJ nfJK  yI zI  yJ zJ  yK zK  yL zL

    patch quadr 1 $nfbf $nftf  $y1 $z4  $y1 $z1  $y2 $z1  $y2 $z4

    patch quadr 1 $nftw $nfdw  $y2 $z3  $y2 $z2  $y3 $z2  $y3 $z3

    patch quadr 1 $nfbf $nftf  $y3 $z4  $y3 $z1  $y4 $z1  $y4 $z4

```



```

}

#-----Define Elements-----#

for {set k 0} {$k<100} {incr k} {

set eltag [expr $k+1]

set inode [expr $k+1]

set jnode [expr $k+2]

element nonlinearBeamColumn $eltag $inode $jnode 3 1 1

}

#-----Define Recorders-----#

recorder Node -file W30x124_DistL/Node51.out -time -node 51 -dof 2 disp;

recorder Node -file W30x124_DistL/Node1.out -time -node 1 -dof 3 disp;

recorder Element -file W30x124_DistL/ForceE51-S1.out -time -ele 51 section 1 force;

recorder Element -file W30x124_DistL/DefE51-S1.out -time -ele 51 section 1
deformation;

recorder Element -file W30x124_DistL/ForceE1-S1.out -time -ele 1 section 1 force;

recorder Element -file W30x124_DistL/DefE1-S1.out -time -ele 1 section 1 deformation;

#-----Define Load Case-----#

pattern Plain 1 Linear {

load 1 0 -2.24 0

for {set m 1} {$m<100} {incr m} {

set Nodetag [expr $m+1]

load $Nodetag 0 -4.48 0

```

```
}  
load 101 0 -2.24 0  
}  
#-----Define Analysis Objects-----#  
constraints Plain;  
numberer Plain;  
system BandGeneral;  
test NormDispIncr 1.0e-1 10;  
algorithm Newton;  
integrator DisplacementControl 51 2 -0.01;  
analysis Static  
analyze 10000;  
loadConst -time 0.0;  
puts "Done!"
```

### B.3: Beam with Linear-Elastic Boundary Conditions

```
wipe all;

#---Units: kip, in---#

#-----Define the Model Builder-----#

model basic -ndm 2 -ndf 3;

#-----File Directory-----#

file mkdir W30x124.wSPrings;

#-----Define nodes-----#

for {set i 0} {$i<101} {incr i} {

  set nodeTag [expr $i+1]

  set xdim [expr $i*7.2]

  node $nodeTag $xdim 0

}

node 102 0 0;

node 103 720 0;

equalDOF 1 102 2;

equalDOF 101 103 2;

#-----Define Boundary Conditions-----#

fix 102 1 1 1;

fix 103 1 1 1;

#-----Geometric Transformation-----#
```

```

geomTransf Corotational 1;

#-----Define Materials-----#

uniaxialMaterial ElasticPP 1 29000 0.00172413;

uniaxialMaterial Elastic 2 320;

uniaxialMaterial Elastic 3 4451000;

#-----Define Fiber Section-----#

#Section W30x124#

set d 30.2;

set tw 0.585;

set bf 10.5;

set tf 0.93;

set nfdw 5668;

set nftw 1;

set nfbf 1;

set nftf 186;

set dw [expr $d-2*$tf]

set y1 [expr -$d/2]

set y2 [expr -$dw/2]

set y3 [expr $dw/2]

set y4 [expr $d/2]

set z1 [expr -$bf/2]

set z2 [expr -$tw/2]

set z3 [expr $tw/2]

```

```

set z4 [expr $bf/2]

section fiberSec 1 {

    #          nfIJ nfJK  yI zI  yJ zJ  yK zK  yL zL

    patch quadr 1 $nfbf $nftf  $y1 $z4  $y1 $z1  $y2 $z1  $y2 $z4

    patch quadr 1 $nftw $nfdw  $y2 $z3  $y2 $z2  $y3 $z2  $y3 $z3

    patch quadr 1 $nfbf $nftf  $y3 $z4  $y3 $z1  $y4 $z1  $y4 $z4

}

#-----Define Elements-----#

for {set k 0} {$k<100} {incr k} {

set eltag [expr $k+1]

set inode [expr $k+1]

set jnode [expr $k+2]

element nonlinearBeamColumn $eltag $inode $jnode 3 1 1

}

element zeroLength 101 102 1 -mat 2 3 -dir 1 6;

element zeroLength 102 103 101 -mat 2 3 -dir 1 6;

#-----Define Recorders-----#

recorder Node -file W30x124.wSP/Node51.out -time -node 51 -dof 2 disp;

recorder Node -file W30x124.wSP/Node1.out -time -node 1 -dof 1 3 disp;

recorder Node -file W30x124.wSP/Node101.out -time -node 101 -dof 1 3 disp;

recorder Element -file W30x124.wSP/TRSpringForce101.out -time -ele 101 force;

recorder Element -file W30x124.wSP/TRSpringDEF101.out -time -ele 101 deformation;

recorder Element -file W30x124.wSP/TRSpringForce102.out -time -ele 102 force;

```

```

recorder Element -file W30x124.wSP/TRSpringDEF102.out -time -ele 102 deformation;

recorder Element -file W30x124.wSP/ForceE1.out -time -ele 1 globalForce;

recorder Element -file W30x124.wSP/ForceE100.out -time -ele 100 globalForce;

recorder Element -file W30x124.wSP/ForceE51-S1.out -time -ele 51 section 1 force;

recorder Element -file W30x124.wSP/ForceE1-S1.out -time -ele 1 section 1 force;

recorder Element -file W30x124.wSP/DefE1-S1.out -time -ele 1 section 1 deformation;

recorder Element -file W30x124.wSP/DefE51-S1.out -time -ele 51 section 1
deformation;

#-----Define Load Case-----#

pattern Plain 1 Linear {

load 51 0 -224.046 0

}

#-----Define Analysis Objects-----#

constraints Lagrange;

numberer Plain;

system BandGeneral;

test EnergyIncr 1.0e-3 10;

algorithm Newton;

integrator DisplacementControl 51 2 -0.01;

analysis Static

analyze 10000;

loadConst -time 0.0;

puts "Done!"

```